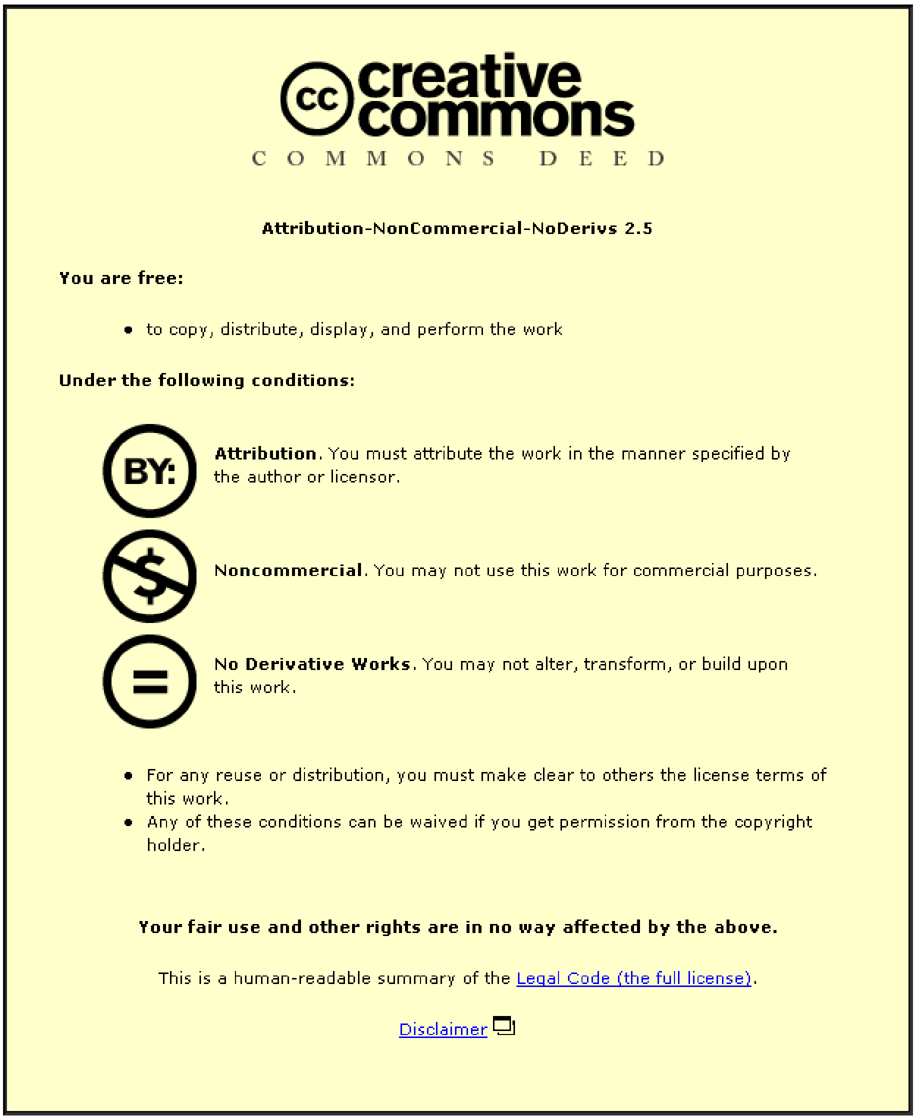

Characterisation of Flow Structures Inside an Engine Cylinder Under Steady State Condition

Saud A. Binjuwair

B.Sc., M.Sc.

Doctoral Thesis

Submitted in partial fulfilment of the requirements for the award of
Doctor of Philosophy of Loughborough University

School of Aeronautical, Automotive, Chemical and Materials Engineering
Department of Aeronautical and Automotive Engineering,
Loughborough University, UK

May 2013

I dedicate this thesis to my parents, my wife and my sons.

Abstract

The in-cylinder flow of internal combustion (IC) engines, formed during the intake stroke, is one of the most important factors that affect the quality of air-fuel mixture and combustion. The inducted airflow through the inlet valve is primarily influenced by the intake port design, intake valve design, valve lift and valve timing. Such parameters have a significant influence on the generation and development of in-cylinder flow motion. In most combustion systems the swirl and tumble motions are used to aid the air-fuel mixing with the subsequent decay of these bulk flow motions generating increased turbulence levels which then enhance the combustion processes in terms of rate of chemical reactions and combustion stability. Air motion formed inside the engine cylinder is three-dimensional, transient, highly turbulent and includes a wide spectrum of length and time scales. The significance of in-cylinder flow structures is mainly reflected in large eddy formation and its subsequent break down into turbulence kinetic energy. Analysis of the large scale and flow motions within an internal combustion engine are of significance for the improvement of engine performance. A first approximation of these flow structures can be obtained by steady state analysis of the in-cylinder flow with fixed valve lifts and pressure drops.

Substantial advances in both experimental methods and numerical simulations provide useful research tools for better understanding of the effects of rotational air motion on engine performance. This study presents results from experimental and numerical simulations of in-cylinder flow structures under steady state conditions. Although steady state flow problem still includes complex three-dimensional geometries with high turbulence intensities and rotation separation, it is significantly less complex than the transient problem. Therefore, preliminary verifications are usually performed on steady state flow rig. For example, numerical investigation under steady state condition can be considered as a precondition for the feasibility of calculations of real engine cylinder flow.

Particle Image Velocimetry (PIV) technique is used in the experimental investigations of the in-cylinder flow structures. The experiments have been conducted on an engine head of a pent-roof type (Lotus) for a number of fixed valve lifts and different inlet valve configurations at two pressure drops, 250mm and 635mm of H_2O that correlate with engine speeds of 2500 and 4000 RPM respectively. From the 2-D in-cylinder flow measurements, a tumbling vortex analysis is carried out for six planes parallel to the cylinder axis. In addition, a swirl flow analysis is carried out for one horizontal plane perpendicular to the cylinder axis at half bore downstream from the cylinder head (44mm).

Numerically, modelling of the in-cylinder flow is proving to be a key part of successful combustion simulation. The numerical simulations require an accurate representation of turbulence and initial conditions. This Thesis deals with numerical investigation of the in-cylinder flow structures under steady state conditions utilizing the finite-volume CFD package, STAR CCM+. Two turbulence models were examined to simulate the turbulent flow structure namely, Realizable k-ε and Reynolds Stress Turbulence Model, RSM. Three densities of generated mesh, which is polyhedral type, are examined. The three-dimensional numerical investigation has been conducted on the same engine head of a pent-roof type (Lotus) for a number of fixed valve lifts and both valves are opened configuration at two pressure drops 250mm and 635mm of H_2O that is equivalent to engine speeds of 2500 and 4000 RPM respectively.

The nature and modelling of the flow structure together with discussions on the influence of the pressure drop and valve lift parameters on the flow structures are presented and discussed. The experimental results show the advantage of using the planar technique (PIV) for investigating the complete flow structures developed inside the cylinder. It also highlighted areas where improvements need to be made to enhance the quality of the collected data in the vertical plane measurements. Based on the comparison between the two turbulence models, the RSM model results show larger velocity values of about 15% to 47% than those of the Realizable k-ε model for the whole regions. The computational results were validated through qualitative and quantitative comparisons with the PIV data obtained from the current investigation and published LDA data on both horizontal and vertical cross sections. The calculated correlation coefficient, which is above 0.6, indicated that a reasonable prediction accuracy for the RSM model. This verifies that the numerical simulation with the RSM model is a useful tool to analyse turbulent flows in complex engine geometries where anisotropic turbulence is created.

List of Publications from Current Work

1. S. Binjuwair, S. Ibrahim, G. Wigley, and G. Pitcher, ‘Numerical and particle image velocimetry characterisations of flow structures under steady state condition’. World Journal of Engineering 2013, 10 (3).
2. S. Binjuwair and S. Ibrahim, ‘Numerical Analysis of Flow Structure inside a Single Cylinder of a 4 Valve Head under Steady State Condition’. Submitted to SAE International, February 2013, 13ICE-0023.
3. S. Binjuwair, S. Ibrahim, G. Wigley, and G. Pitcher, ‘In-Cylinder Flow Structure Analysis by Particle Image Vleocimetry under Steady State Condition’. SAE Technical Paper 2102-01-1975, 2012.
4. S. Binjuwair, S. Ibrahim, G. Wigley, and G. Pitcher, ‘Numerical Analysis of Flow Structure inside a Single Cylinder Engine under Steady State Condition and validate the outcomes with LDA data’. Saudi International Conference (SIC06), London, UK, 14-16 October, paper number 89-119, 2012.
5. S. Binjuwair, G. Wigley, S. Ibrahim, A. Wood and G. Pitcher, ‘Experimental Analysis of In-Cylinder Flow Structure Using PIV’. Saudi International Conference (SIC05), Coventry, UK, 23-26 June, paper number 84, 2011.
6. S. Binjuwair, G. Wigley, and S. Ibrahim, ‘Experimental Analysis of In-Cylinder Flow Structure Using PIV’. Proceedings of the technical meeting of the Combustion Institute, KAUST, Saudi Arabia, January, pp1-3, 2011.
7. G. Pitcher, S. Binjuwair, T. Picton, A. Wood, G. Wigley and D. Hollis, ‘LDA and PIV Analyses and Comparison of In-Cylinder Flow Structures under Steady Flow Conditions’. 15th Int. Symp on Applications of Laser Techniques to Fluid Mechanics, Lisbon, Portugal, 05-08 July, Paper number 1801-1809, 2010.

Acknowledgements

First and foremost, praises and thanks to the God, the Almighty, for granting me the capability to proceed successfully and his blessings throughout my research work to complete the research successfully. This thesis appears in its current form due to the assistance and guidance of several people. I would therefore like to offer my sincere thanks to all of them.

I would like to express my deep and sincere gratitude to my research Supervisors Dr. Salah Ibrahim and Dr. Graham Wigley for their constant encouragement, helpful, advice, and guidance throughout my research work. I am obligated to them for the skills, computational, experimental and analytical, acquired during my association with them. I would like to thank Graham Pitcher for his friendship and assistance during my research. I would also like to extend my gratitude to my sponsor King Abdulaziz City for Science and Technology (KACST).

Finally, I am extremely grateful to my parents for their love, prayers, caring and to my wife and my sons who provided inspiration and constant support all along, without whom I would be unable to complete my research. I am indebted to them for their love, understanding, prayers, and the sacrifices made to make my effort a success.

Contents

Chapter 4 Experimental Set-Up and Instrumentation 68

Chapter 5 The Governing Equations and Numerical Model 92

Chapter 6 Experimental Analysis of In-cylinder Flows: Results and Discussions 110

List of Figures

List of Tables

Nomenclature

Abbreviations

2-D	2-Dimensional
3-D	3-Dimensional
AFR	Air-Fuel Ratio
AVT	Active Valve Train
BDC	Bottom Dead Centre
CID	Charge Injection Device
CMOS	Complementary Metal Oxide Semiconductor
CCD	Charge-Coupled Device
CFD	Computational Fluid Dynamics
CO_2	Carbon Dioxide
CO	Carbon Monoxide
CPU	Central Processing Unit
DNS	Direct Numerical Simulation
FDM	Finite Difference Method
FVM	Finite Volume Method
FOV	Field of View
FFT	Fast Fourier Transform
GDI	Gasoline Direct Injection
GM	General Motors
GHG’s	Green House Gases
HC	Hydrocarbons
IC	Internal Combustion
IVC	Inlet Valve Closing
IVO	Inlet Valve Opening
LDA	Laser Droppler Anemometry
LES	Large Eddy Simulation
LTA	L-Type Adaptor
LIF	Laser Induced Fluorescence
NO_X	Oxides of Nitrogen

NVO	Negative Valve Overlap
NSA	Stationary Swirl Number
Nd: YAG	Neodym Yttrium Aluminium Garnet
PCC	Partial Cell in Cartesian Coordinator
PDE	Partial Differential Equation
PTU	Programmable Timing Unit
PRV	Pressure Relief Valve
PIV	Particle Image Velocimetry
PTV	Particle Tracking Velocimetry
RANS	Reynolds Averaged Navier-Stokes
RMS	Root Mean Square
RNG	Renormalization Group
RSM	Reynolds Stress Model
SCORE	Single Cylinder Optical Research Engine
SI	Spark-Ignition
TDC	Top Dead Centre
TKE	Turbulence Kinetic Energy
TTA	T-Type Adaptor
VVT	Variable Valve Timing

Notation

A	Area of inlet port	m^2
$\mathrm{A_v}$	Valve curtain area	m^2
a	Sound speed	m/s
a	Flow acceleration	m/s^2
B	Cylinder bore	m
C	Correlation coefficient	
C_d	Discharge coefficient	
C_f	Flow coefficient	
C_m	Flow coefficient at certain crank angle	
$C_{1\varepsilon}, C_{2\varepsilon}, C_{3\varepsilon}$	Constants	
D_k	Turbulent diffusivity	m^2/s
d_{PID}	Particle Image diameter	µm

d_{diff}	Diffraction limited image diameter	µm
D_v	Valve seat diameter	m
E_w	Turbulent kinetic energy spectrum	m^3/s^2
$\vec{f}$	External body forces	N
f#	Lens f-number	
f	Focal length	m
I_t	Turbulence intensity	%
L_v	Valve lift	m
l_t	Turbulence length scale	m
M	Magnification factor	
$\dot{m}$	Mass flow rate	kg/s
$\dot{m}_{ideal}$	Ideal mass flow rate	kg/s
N	Number of vectors	
n	Relative index of refraction	
P	Pressure	N/m^2
P_{atm}	Atmospheric pressure	N/m^2
P_k	Production of turbulence kinetic energy	
p	Static pressure	N/m^2
Q	Volumetric flow rate	m^3/s
R_{air}	Air gas constant	J/K mol
Re	Reynolds number	
R	Radial distance from centre of cylinder	m
S	Stroke	m
SR	Swirl ratio	
TR	Tumble ratio	
S	Strain rate tensor	
T	Temperature	K
T	Torqe	Nm
U	Mean axial velocity	m/s
$U_{(i)}$	Radial velocity	m/s
U_s	Velocity lag	m/s
$\bar{u}$	Mean velocity	m/s
u_i	Instantaneous velocity in the *x* direction	m/s
u_{RMS}	Root mean square velocity in x-direction	m/s

$\vec{u}$	Velocity vector	m/s
V_{in}	Inlet velocity	m/s
v_{RMS}	Root mean square velocity in y-direction	m/s
w_{RMS}	Root mean square velocity in z-direction	m/s
X	Axial displacement	m
Y	Distance in y-direction	m
Z	Mach index	

Greek Symbols

α	Crank angle	Degree
γ	Specific heat ratio	
Δt	Numerical time step	s
ΔZ	Depth of filed	m
∇	Operator referred to as grad or del	
ε	Turbulence dissipation rate	m^2/s^3
θ	Scattering angle	degree
k	Turbulence kinetic energy	m^2/s^2
λ	Wavelength	µm
μ	Fluid dynamic viscosity	kg/m s
μ_t	Turbulent viscosity	kg/m s
ν	Kinematic viscosity	m^2/s
ρ	Density	kg/m^3
ρ_p	Seeding particle density	kg/m^3
σ_k	Turbulent Schmidt number	
$\overset{=}{\tau}$	Stress tensor	N/m^2
τ_p	Particle response time	s
τ_t	Flow mixing time scale	s^{-1}
ϕ	General scalar	
ω	Engine speed	rad/s

Definitions

STAR CCM+	Commercial CFD code

Superscripts

·	Rate
–	Mean
=	Tensor
→	Vector
#	Number

Subscripts

atm	Atmosphere
d	Discharge
$diff$	Diffraction
f	Flow
in	Inlet
i, j	Components of vector
k	Turbulence kinetic energy
PID	Particle image diameter
p	Particle
RMS	Root mean square
t	Turbulent
v	Valve
w	Wavelength

Chapter 1

Introduction

1.1: Motivation

There is a tangible significance of the internal combustion (IC) engine applications day-to-day. Internal combustion engines are used in cars, Trucks, ships, trains, and aircrafts. No one imagine modern society without these machines. However, the engine performance, in terms of efficiency and pollutants emissions has an impact extending to the environment. Local and global environmental concern include increased concentrations of carbon monoxide (CO) hydrocarbons (HC), Nitrogen Oxides (NO_x), which are the potential for climatic warming is a threat. Figure 1.1 shows causes of climate change. This indicates that transport emissions are considered a cause of Green House Gases (GHG's) and account for around 32% of all UK Carbon Dioxide (CO_2) emissions (SMMT, 2011).

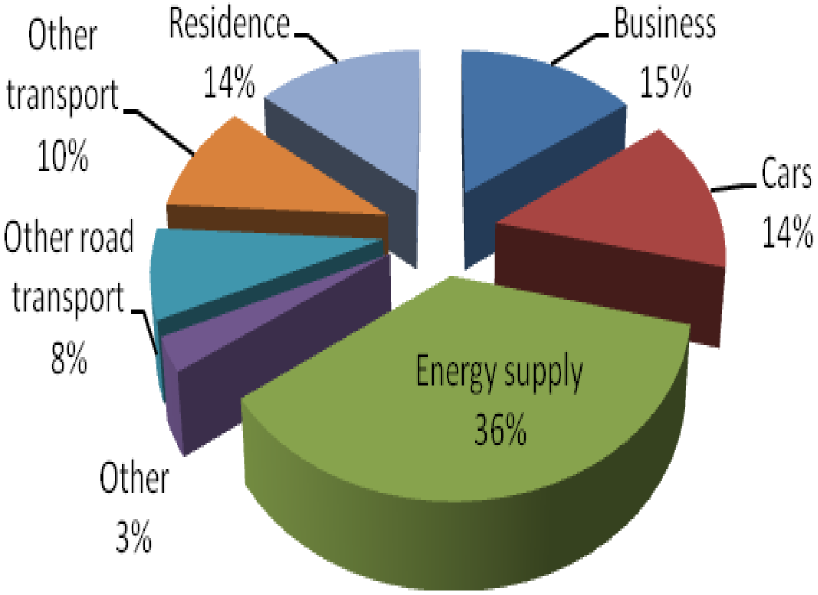

Figure 1.1: UK CO_2 emissions by sources, 2009 (SMMT, 2011)

A new European legislation on CO_2 emission targets was set for vehicle manufacturers, which are 130 g/km CO_2 to be achieved by 2015 and 95 g/km CO_2 to be achieved by 2020, subject to assessment. These increasingly stringent emissions legislation beside to customers' demand to have vehicles with reduced emission and fuel consumption, due to emissions based vehicle taxing and unstable fuel prices, are forcing vehicles manufacturing to produce vehicles with improved fuel economy and reduced exhaust emissions. Figure 1.2 shows the average new car CO_2 emissions reduction that had been achieved up to 2010 (SMMT, 2011). One key area of the engine performance development that can be improved to meet such demands is through analysing and improving the in-cylinder flow characteristics. In-cylinder flow is essential to the air/fuel mixing process as concluded by Bevan and Ghandi (2005). The outcome of the study by those authors demonstrated that the improved air/fuel mixing rate is a significant factor that shortens combustion duration and improve combustion efficiency, which in sequence would improve engine efficiency.

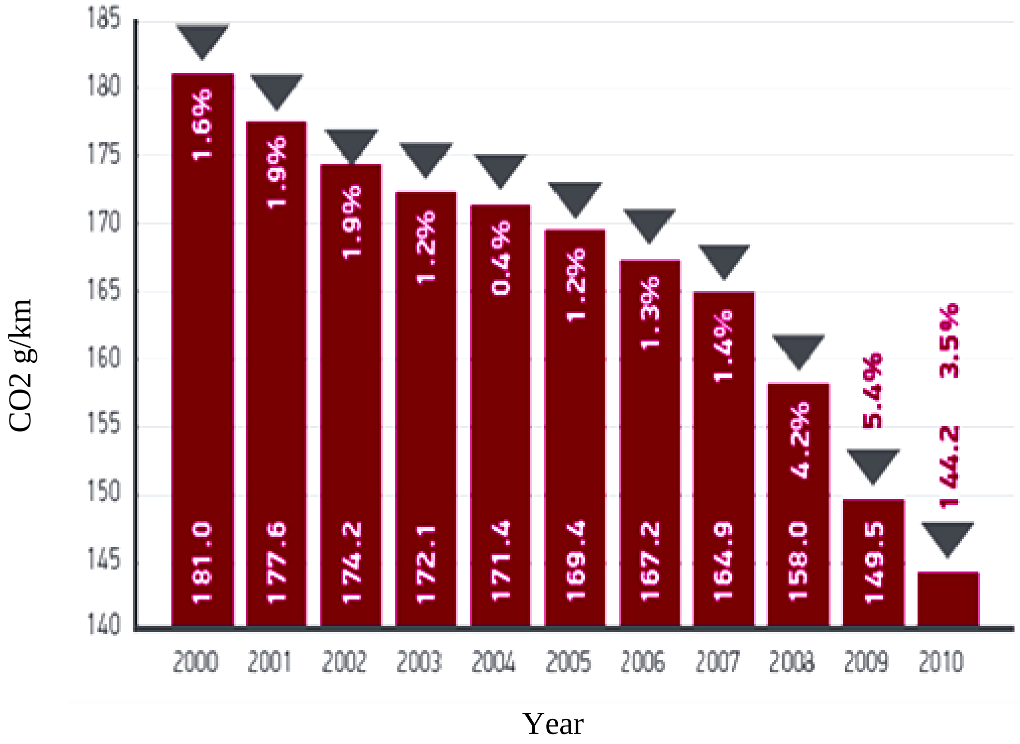

Figure 1.2: Emissions average new cars CO_2 emission reduction, 2000-2010 (SMMT, 2011)

Knowledge of in-cylinder flows plays a significant role in both the gasoline direct injection (GDI) technology and diesel engine operation. Figure 1.3 shows the Mitsubishi GDI operating policies for first mass-produced GDI engine introduced by Mitsubishi in 1996 (Mitsubishi, 2005). At high load, the engine operates in the homogeneous charge phase. The time of fuel injection is during the induction stroke. This allows time for the fuel and air to mix within the cylinder before ignited by the spark. However, at low loads the engine operates in a stratified charge mode. In this operating mode, the fuel is injected into the cylinder as the piston approaches Top Dead Centre (TDC) and the curved piston crown guides the fuel spray towards the spark plug. This creates a rich zone of the mixture at the spark plug. The quality of air/fuel mixing during stratified charge operation is often poor due to the short duration of the fuel injection. This represents the significance of the in-cylinder flow to the mixing process in the engine operations, in particular, when engine operates in homogenous charge phase at high load.

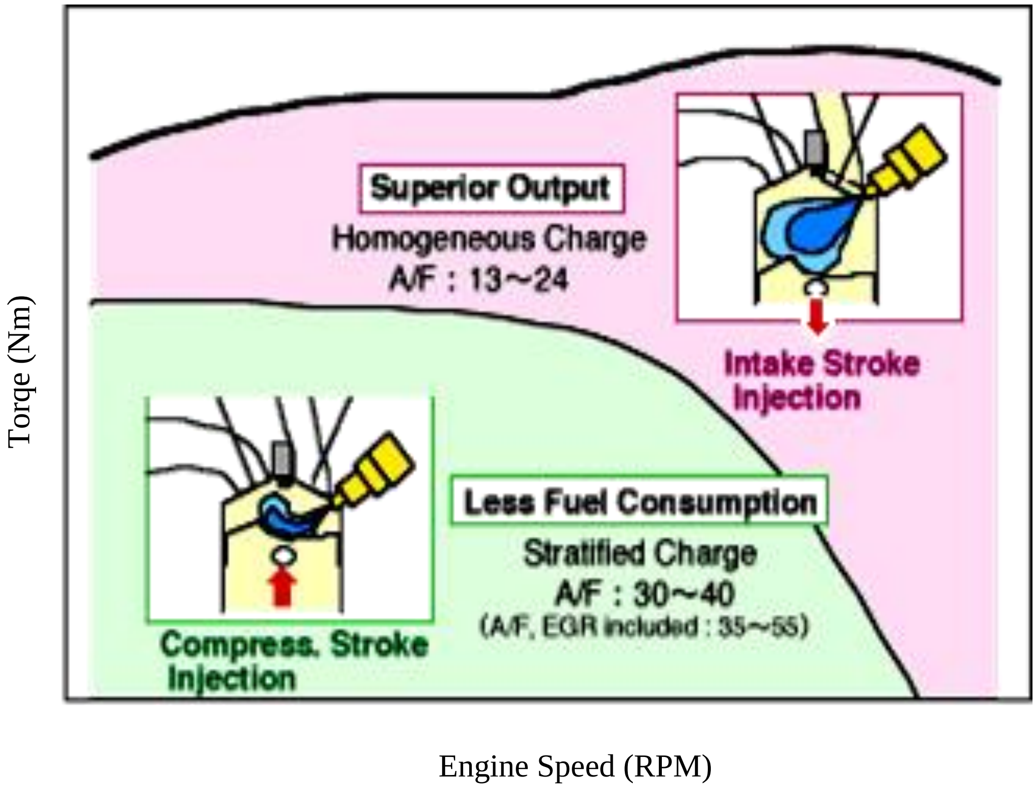

Figure 1.3: Combustion characteristics in GDI engine (Mitsubishi, 2005)

The enhancement of combustion efficiency of diesel engine operation could, also, be achieved by improved knowledge of in-cylinder flows. It is essential in diesel engine operation to have a complete air/fuel mixing in the short time available before the start of combustion. Thus enhanced turbulence level inside the cylinder is one of the most important factors that would lead to increase mixing rate and therefore enhance the combustion efficiency in diesel engine.

In-cylinder flow structures of an IC engine are complex and vary significantly among different engine design types. Generally, turbulence characteristics of the flow add value to the flow structure. Moreover, heat transfer is influenced by the in-cylinder flow structure (Heywood, 1988). Therefore, it is essential to understand the flow structure inside the cylinder in order to improve combustion process and thus enhance IC engines performance. Flow structure investigations inside the cylinder can be characterised either experimentally or numerically. Optical engines along with the optical diagnostics are developed technologies that enable researchers to investigate the flow structures and fuel mixture inside engine’s cylinders. In addition, computer simulations (Computational Fluid Dynamics, CFD) codes are developed to support the numerical simulation of IC engines, which has become an integral part of the IC engines development process due to its capability for obtaining detailed information for the interpretation and analysis of in-cylinder flow fields in IC engines. These codes offer the opportunity to perform repetitive parameter studies with defined boundary conditions in order to investigate various configurations.

Practically simulating and predicting the flow mixing phenomena relevant to IC engines is greatly depends on accurate prediction of the turbulence inside the engine cylinder. As it is also demonstrated in this investigation, the shortcomings of the classical turbulence models are the primary factors for poor predictions, for instance an assumption of the local isotropy of turbulence, particularly as applied by standard two-equation eddy viscosity (k-ε) turbulence model (Launder and Spalding, 1994). In addition, to local isotropy assumption, this model utilizes a single length and time scale to represent a whole spectrum of turbulence length and time scales. In recent history, several turbulence modelling approaches have been developed to account for the turbulence effects in practical situations. The current investigation is performed with the hypothesis that some of such turbulence modelling deficiencies can be addressed by employing higher and developed turbulence models such as both realizable k-ε (Durbin, 1996; Shih *et al.*, 1995) and Reynolds stress (RSM) models (Thakur and Shyy, 1999; Launder *et al.*, 1975) as RANS models.

The main aim of this investigation is to characterise the in-cylinder flow behaviour of a single cylinder pent roof head under steady state conditions. A combined numerical and experimental study has been carried out. In the experimental study, Particle Image Velocimetry (PIV) was employed to analyse the flow structures formed within the cylinder utilizing an air flow rig. From the two-dimensional in-cylinder flow measurements, tumble flow analysis is examined on six vertical planes, situated every 30°, and swirl flow analysis is observed on a plane situated 44mm downstream from the flame face. The influence of different number of PIV image pairs measurements was discussed. In the numerical study, Computational Fluid Dynamics (CFD) Package STAR CCM+ was used in order to evaluate the capability of a developed RSM model to predict the turbulent in-cylinder flow motion for a 4 valve cylinder head. The investigations have been conducted for three valves opened configurations and fixed valve lifts (2mm, 5mm, 8mm) at two pressure drops of 250mm and 635mm of H_2O that are representative of engine speeds of 2500 and 4000 RPM respectively. The spatial development of the swirling and tumbling structures are presented and discussed. The strength of the rotating motions inside the cylinder is quantified by a dimensionless swirl ratio. The main objectives of the current investigations are listed in the following Section.

1.2: Objectives of the Present Research Work

The main objectives of this research work are:

i) Contribute to the understanding of in-cylinder flow structures and turbulence generation in IC engines. A combined numerical and experimental study has been carried out to examine the structure of the flow field from a 4 valve cylinder head under steady state conditions. The PIV experiments as a planar measurement technique were utilised, where local air velocities can be measured directly and a whole picture of the flow structures developed inside the cylinder head can be visualised. This provides further evidence of the value of experimental and computational techniques for modern engine development.

ii) Create a correlation resource in order to test the assumption of a close correspondence between the steady-state port flow measurement and motored engine condition. This adds value to the steady state port flow measurement associated with the optical diagnostic as a method for future engine design and diagnostic work.

iii) Create a long term vision for achieving higher efficiency and environmentally acceptable emissions levels. One key area of the engine performance development that can be improved to meet such demands is through analysing and improving the in-cylinder flow characteristics. For instance, modern spark ignition engine design, particularly with direct injection, has led to the requirement to control the flow formation of the charge being developed in the engine cylinder, which results in guidance of the fuel mixture for stratified operation and improve the combustion speed and stability.

iv) Assess the accuracy and possible error sources from using these techniques. For example, in the PIV vertical measurements, high flare from reflected laser light produced considerable noise in the raw images. This was eliminated by using a thinner liner and perfectly configures the experimental set-up.

To achieve the specific objectives above, the following tools and engine specifics are used:

i) Particle Image Velocimetry (PIV) experimental technique is used for flow measurements. The data obtained are used for model validation.

ii) The finite-volume Computational Fluid Dynamic (CFD) package, STAR CCM+ is used in order to calculate the detailed flow velocities and structure inside a single-cylinder engine.

iii) The Reynolds Stress Turbulence Model, RSM, is used to evaluate its capability for predicting the turbulent in-cylinder flow field for a complex cylinder head.

iv) The Lotus single cylinder engine with a pent-roof type is used in this study.

v) A number of fixed valve lifts at two pressure drops 250mm and 635mm of H_2O equivalent to engine speeds of 2500 and 4000 RPM, respectively, are examined, and conclusions are drawn.

1.3: Outline of the Thesis

The overview of past experimental and numerical investigations of in-cylinder flows are addressed in the first part of Chapter 2. The remaining section of that chapter reviews the optical diagnostic techniques and research optical engine. Furthermore, the development of an optically accessible engine and the measuring methodology is described. The practical background of conducting Particle Image Velocimetry (PIV) is described in Chapter 3. Apart from the basic principles of this measuring technique, this chapter deals with the various options that have to be made to set up reliable experiments.

Chapter 4 deals with the experimental set-up of steady-state port flow measurements associated with PIV technique and swirl motion meters. First, the steady air flow rig and measuring conditions are described. Then, the PIV measurements set-up for both the horizontal and vertical planes are described. Finally, the source of error and bias in measurements is discussed and presented. An introduction to the governing equation and numerical model used for this investigation are described and presented in Chapter 5. The description of turbulence and selection of turbulence models was discussed. Furthermore, general descriptions of the computational methods that are employed, the generation of the computational mesh and initial and boundary conditions are described and discussed.

The experimental analysis of the in-cylinder flow structure under steady-state conditions utilising PIV is presented in Chapter 6. The measuring conditions are described. The PIV results are presented and the flow structures are analysed. Chapter 7 deals with the numerical analysis of the in-cylinder flow structures under steady-state conditions. The comparison between two turbulence models, namely, the Realizable k-ε and Reynolds stress models (RSM) have been presented. The nature of the flow structure together with discussions on the influence of the pressure drop and valve lifts parameters on the flow structures are discussed. The numerical simulation results are validated by comparison with the experimental-acquired data in Chapter 8.

Finally, the conclusions are drawn in Chapter 9. Furthermore, recommendations for future work are given.

Chapter 2

Overview of Past Research

2.1: Previous Research of Flows in Engine's Cylinders

Comprehensive knowledge of the flow structure inside an engine's cylinder is essential to optimize the mixture preparation and the combustion process. The in-cylinder flow structure taking place during the intake stroke can be classified as having either organised or disorganized structure. The disorganised structures are simply filling the cylinder with undefined flow moving. While the organised structures have defined rotational flow structures and formed by means of the inlet port design, inlet valves assembly and cylinder head and piston geometry. In addition, valve lift is considered to have a significant influence on the generation and development of in-cylinder flow motion (Mahrous, 2007).

Most of flow structure investigations (Pitcher and Wigley, 2008; Stansfield *et al.*, 2007; Thomas, 2006; Vucinic *et al.*, 2001) focus on the organised structures that can be initially prepared during the intake process. These structures can be characterised as swirl and tumble motions or a combination of both. Figure 2.1(*a*) illustrates the swirl motion that is the rotational motion around the axis parallel to the axis of the cylinder, whereas the tumble motion (it is also referred to as tumbling vortex or barrel swirl) is defined as a large-scale eddy that rotates around an axis perpendicular to cylinder axis as illustrated in Figure 2.1(*b*). In most combustion systems the swirl and tumble motions are used together to obtain the preferred air-fuel mixing field. It is also used to gain rapid air-fuel mixing by rising turbulence levels and enhanced combustion processes. Swirl motion occurs more in diesel engines where high swirl intensities are required, whereas tumble motions can be found in gasoline engines with pent roof designs.

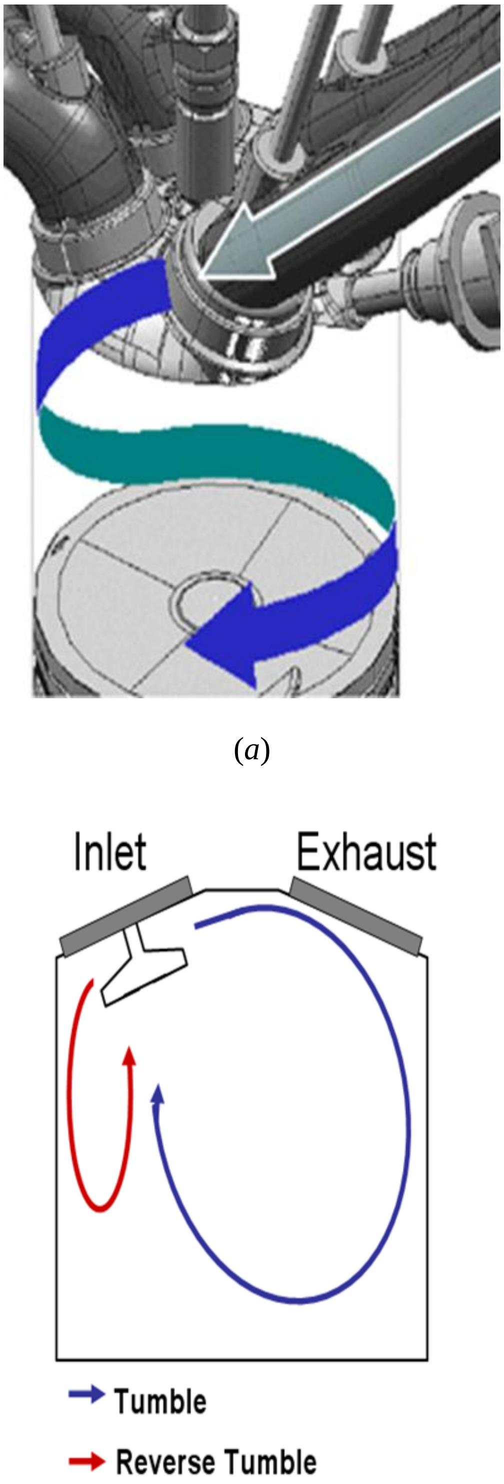

(*a*)

(*b*)

Figure 2.1: Organised structures inside engine cylinder *a*) Swirl motion and *b*) Tumble motion (Stansfield et al., 2007)

There are several generation methods of rotational flows. Tumble motion can be generated by the induction of a large amount of the flow over the top of the inlet valve, which is sucked down and rotated by the influence of the cylinder wall and piston design. Li *et al.* (2004) produced a strong tumbling flow by partially shrouded the lower periphery of the inlet valve. On the other hand, the helical inlet ports or tangential ports are used to generate swirl motion. In the case of using helical inlet ports, the swirl is formed inside the inlet port prior to induction inside the cylinder. In the second case, the inlet ports are designed to guide the flow that penetrates inside the cylinder with substantial tangential momentum about the cylinder axis and swirl flow develops as the cylinder walls redirect this momentum. Moreover, early opening of one of the intake valves can also generate swirl. Mahrous *et al.* (2007) applied higher degrees of variable negative valve overlap (NVO) to investigate numerically its effect on the mixture preparation process and the actual in-cylinder conditions at the end of the compression stroke. Consequently, modifications of in-cylinder swirl and tumble motions were obtained.

The decay of the rotational motions into turbulence during the compression stroke is different. Tumble structure is distorted and degraded as a result of the influence of piston movement. The breakdown of large-scale structures of the tumble enhances turbulence level at the end of the compression process. However, swirl motion persists with a weak angular momentum during the compression stroke as demonstrated by Vucinic *et al.* (2001). Kang *et al.* (1998) also deduced that turbulence intensity is enhanced doubled by the tumble eddies that persisted through the compression stroke compared with that of weak tumble. The influence of piston shape and cylinder head on the in-cylinder tumble motion has been previously investigated experimentally by Xavier and Alain (1997). It was found that preserving the tumble angular momentum and reducing the tumble distortion process are the significant effects of a concave piston design. Huang *et al.* (2005) also proved experimentally that the flat-crown piston induces higher tumble ratio and turbulence intensity than the slightly concave piston. Both the rotational flows and the turbulence characteristics of the flow are keys for the optimum intake assemble design.

A significant number of investigations of rotating flows inside the cylinder and its effects on turbulence generation have been carried out (Kang *et al.*, 1999; Kang *et al.*, 1998; Hill and Zhang, 1994). Flow structures analysis, carried out by Kang *et al.* (1998), presented that tumble motion does not affect the integral time scale, but the integral length scale is considerably increased by the break-down of tumble large-scale motion into small-scale eddies when the piston approached top dead centre (TDC) (Kang *et al.*, 1999). Hill and Zhang (1994) stated that the rotational motion is one method of increasing the rate of combustion and of allowing operation with leaner mixtures and with higher compression ratios. However, undesirable higher heat loss occurs due to the effect of rotational motion on heat convection transfer to the cylinder wall. A second disadvantage is a decrease in volumetric efficiency owing to extra pressure loss (depending on the method of generating the rotational motion) during the intake process. It is evident from study of Xavier and Alain (1997) that the cyclic fluctuations of the mean velocities at TDC are nearly twice as large without swirl. It has also been demonstrated that the swirl motion is effective in restraining cyclic variations with a flat piston while the tumble motion is effective in enhancing these variation and turbulence intensity.

Vucinic *et al.* (2001) also found that the core of the valve vortex moves closer to the cylinder wall when reducing valve lift as shown in Figure 2.2. Ismail *et al.* (2008) showed that increasing the valve lift and test pressure raise the air flow rate and the discharge coefficient in both intake manifold system and exhaust manifold system, but after a maximum valve lift per diameter ($0.25L_v/D_v$), air flow rate is stable without increasing.

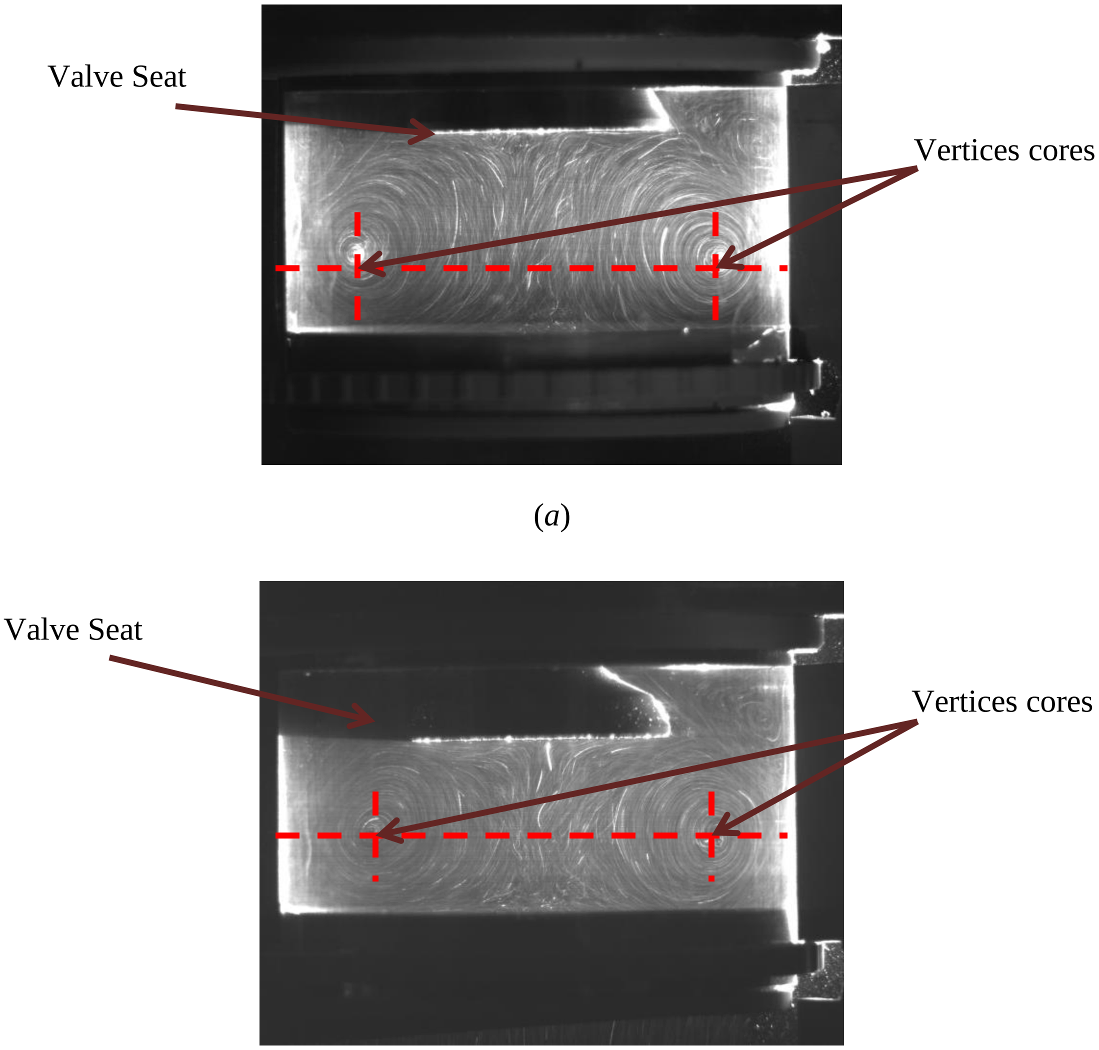

(*a*)

(b)

Figure 2.2: Movement of tumble vortex closer to the cylinder wall with reducing valve lift *(a)* 5mm and *(b)* 10mm (Vucinic *et al.*, 2001)

It was proved that the radial and axial velocities components that are formed close to surrounded area of the intake valve are about 10 times the mean piston speed, which was obtained by using Laser Doppler Anemometry (LDA) during the intake process in a motored model engine with transparent walls and single valve located on the cylinder axis (Heywood, 1988).

In summary, a fundamental limitation on the performance of any engine is when the flow through the intake valves reach choking event. Choking occurs when the velocity through the inlet valve turn out to be the sonic velocity at the minimum valve flow area; after this point, the mass flow into the cylinder will not increase if the cylinder pressure falls (John, 2001). Choking is identified by the Mach number.

2.2: Characterisation of Intake Valve Flow

The valve and the intake port design primarily influence airflow induction through the inlet valve. Intake valve lift, valve geometry, valve surrounded area and valve timing are parameters that have a significant influence on the generation and development of in-cylinder fluid motion (Mahrous, 2007). The challenge is to achieve the optimum performance by means of adjusting the above-mentioned parameters, Figure 2.3 shows source of flow losses in the port.

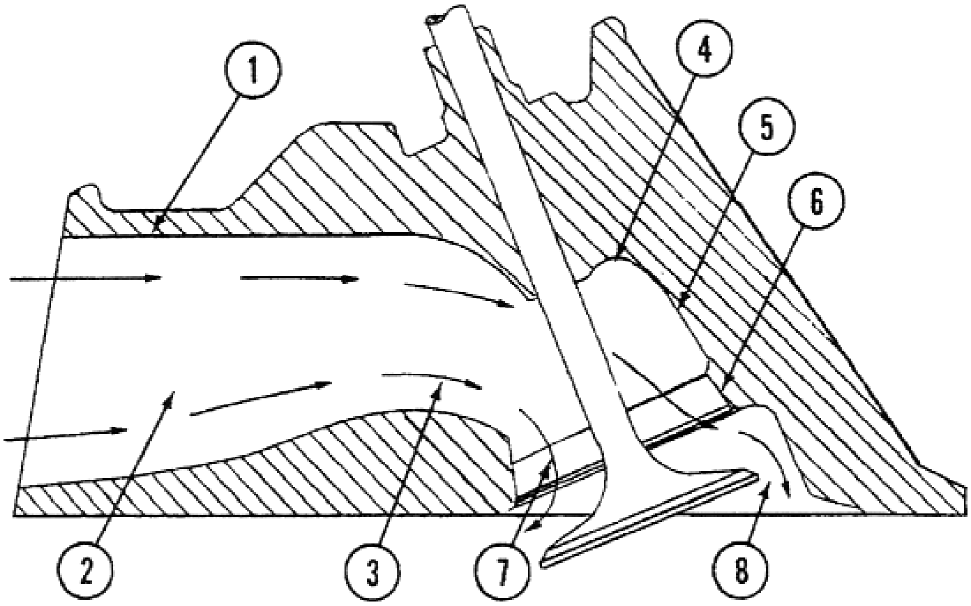

Source of flow loss	% of loss
1- Wall friction	4
2 - Contraction at push-rod	2
3- Bend at valve guide	11
4- Expansion behind valve guide	4
5- Expansion 25 degrees	12
6- Expansion 30 degrees	19
7- Bend to exit valve	17
8- Expansion exiting valve	31

Figure 2.3: Source of flow losses in the port (Ismail *et al.*, 2008)

The flow structure through the inlet valve varies along with altering the valve lifts and has three different stages as shown in Figure 2.4. At low valve lift, the flow streams close to the valve head and seat. While at intermediate lift, the flow separates from the valve head and at high lift, the flow separates from the inner edge of the valve seat (Heywood, 1988).

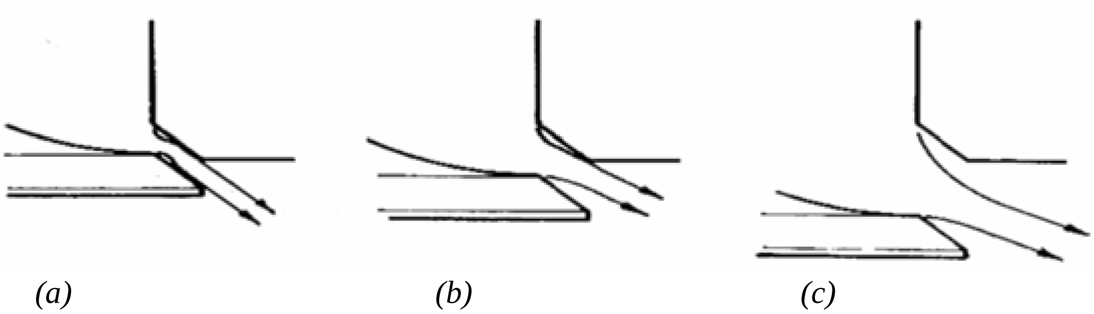

Figure 2.4: Three air flow structures through the inlet valve: *(a)* low lift *(b)* intermediate lift *(c)* high lift (Heywood, 1988)

2.2.1: Non-dimensional Flow Characterisations: Inlet Valve

The performance of the inlet port and valve assembly in terms of the inducted airflow capacity inside the cylinder can be evaluated under the steady flow test condition by using flow rig test. The flow breathing capacity through the inlet valve can be evaluated by several parameters such as:

- Discharge coefficient
- Flow coefficient
- Mean flow coefficient
- Mach index
- Reynolds number

Discharge coefficient

The discharge coefficient (C_d) is defined as the ratio of actual mass flow rate, $\dot{m}$ to ideal mass flow rate, $\dot{m}_{ideal}$, of both intake and exhaust system as calculated by Equation 2.1. The coefficient of discharge are widely used to check the flow efficiency through various engine components such as valves, ports and ducts and can be measured under steady flow conditions for various pressures and valve lift per diameter (L_v/D_v) ratios.

$$C_d = \frac{\dot{m}}{\dot{m}_{ideal}} \tag{2.1}$$

A real gas flow effects are included to calculate the ideal mass flow rate as defined in equation 2.2, where P is pressure , T is temperature, R_{air} is universal gas constant for air, and γ is the specific heats ratio. The value of the discharged coefficient and the choice of reference area are linked together, the reference area of discharge coefficient is the valve inner curtain area $A_{vc}=\pi D_v L_v$, where L_v is the valve lift and D_v is the valve diameter as shown in Figure 2.5. It was found (Heywood, 1988) that high values for the discharged coefficient could be obtained at low lifts when the flow remains close to the valve head and seat. While at intermediate lifts, the flow separates from the valve head at the inner edge of the valve head. A sudden decrease in discharged coefficient occurs at this point as illustrated in Figure 2.6.

$$\dot{m}_{idea} = \frac{A_V P_{atm}}{\sqrt{R_{air} T}} \sqrt{\frac{2\gamma}{\gamma - 1} \left(\frac{P}{P_{atm}} \right)^{2/\gamma} \left(1 - \left(\frac{P}{P_{atm}} \right)^{\frac{\gamma-1}{\gamma}} \right)} \tag{2.2}$$

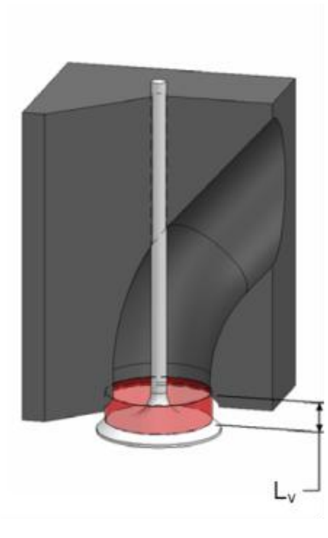

Figure 2.5: Reference area for the discharge coefficient

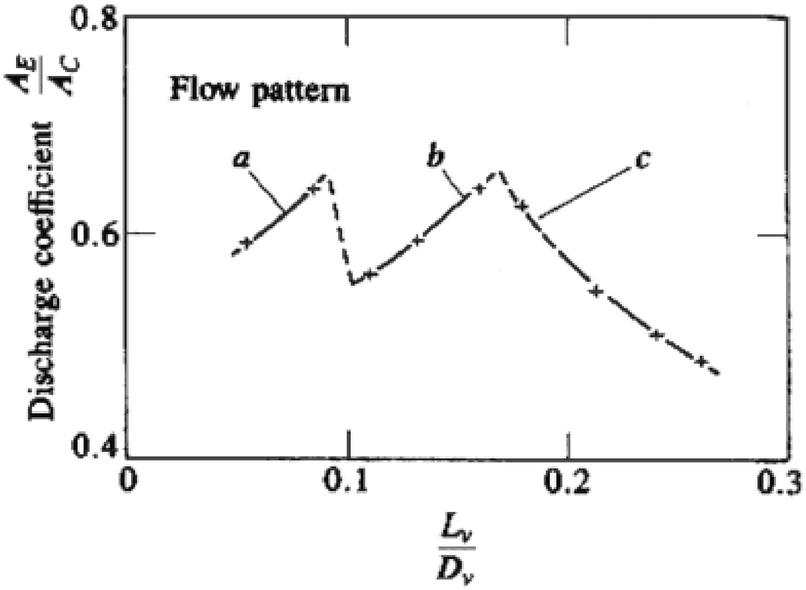

Figure 2.6: Discharge coefficient values through the inlet valve (Heywood, 1988)

The Flow coefficient

The flow coefficient (C_f) is defined as the ratio of the actual mass flow rate, $\dot{m}$, to ideal mass flow rate, $\dot{m}_{ideal}$, of both intake and exhaust system as calculated by Equation 2.1, which is similar to the discharge coefficient but the reference area is the valve inner seat area $A_{vs} = \pi(D_v)^2/4$ as shown in Figure 2.7. The flow coefficient has a capability of comparisons at high lift values in the contrast to the discharge coefficient.

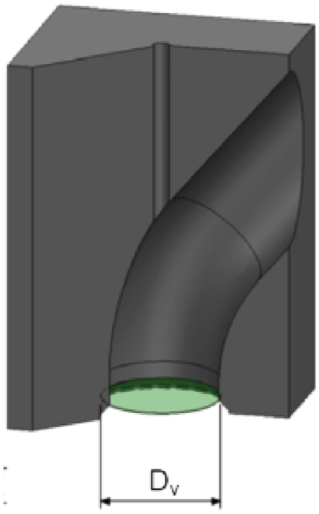

Figure 2.7: The reference area for the flow coefficient

Mean flow coefficient

The mean flow coefficient is a measure of the total flow performance by integrating the flow coefficient over a certain range of crank angles. There are a number of different approaches to define and calculate the mean flow coefficient. Ricardo (1993) identified the intake process period to start at the intake valve open (IVO) and finishes at the intake valve close (IVC) and it can be calculated from Equation 2.3, where α_1 and α_2 are the valve opening and closing angles, respectively. While Hongming (2001) assumed that the intake process period occurs between top dead centre (TDC) and bottom dead centre (BDC) for 180° crank angle degrees with assumption that the flow velocity in the valve gaps is proportional to piston speed and it is calculated by Equation 2.4, where C_m is the mean flow coefficient at certain crank angle.

$$\overline{C}_f = \frac{\int_{\alpha 1}^{\alpha 2} C_f \, d\alpha}{\alpha_2 - \alpha_1} \tag{2.3}$$

$$\overline{C}_f = \left[\frac{1}{\pi} \int_0^{\pi} \left(\frac{C(\alpha)}{C_m} \right)^3 \frac{1}{C_f^2} \, d\alpha \right]^{\frac{1}{2}} \tag{2.4}$$

Mach index

The Mach index of an intake system, also known as the gulp factor, is the mean effective flow velocity in the port throat divided by sonic speed. It was showed by Heywood (1988) that when the Mach index is great than or equal 0.5, the volumetric efficiency of an intake valve decreases rapidly. The equation for Mach index, Z, is calculated by Equation 2.5, where B is the cylinder bore, S is the stroke, *a* is the speed of sound, and ω is the rotational speed of the engine.

$$Z = \left(\frac{B}{D_V}\right)^2 \left(\frac{2S\omega}{n}\right)\left(\frac{1}{a}\right)\left(\frac{1}{\overline{C}_f}\right) \tag{2.5}$$

Reynolds number

The Reynolds number identify the flow behaviour through the port, valve gap or inside the cylinder either become a turbulent or laminar and it is the ratio between inertial and viscous forces as calculated by Equation 2.6, where ρ is the density, V is characteristic velocity, d is characteristic diameter and μ is dynamic viscosity. It is essential to ensure the flow through the valves will be turbulent by calculating the Reynolds number, which is required for engine simulation. Ricardo (1993) has revealed that the non-dimensional properties of the port flow become independent of pressure drop when the Reynolds number of the port exceed 60,000 for low valve lift and 90,000 for high valve lift.

$$R_e = \frac{\rho V\, d}{\mu} \tag{2.6}$$

In the current investigation, a rapid prototyped of the pent-roof Lotus engine head is mounted on a steady flow rig and tested at different pressure drops. The preliminary tests are conducted to measure volumetric flow rate. The volume flow rate is converted to a mass flow rate, which for conventional use would be used to calculate the discharge and flow coefficients for the cylinder head.

2.3: Overview of Measurements of In-Cylinder Flows

Most of the previous experimental investigations aim to visualize the tumble or swirl flow structures and calculate the equivalent tumble or swirl flow quantities inside the engine cylinder by utilizing different techniques. The flow structure has to be accessed either by using non-intrusive optical techniques such as Laser Doppler Anemometry (LDA) and

Particle Image Velocimetry (PIV) or based on intrusive techniques. There are two principal intrusive methods associated with the steady flow rig for measuring the rotational flows, namely paddle wheel anemometer and torque meter.

The first intrusive method is using the paddle wheel anemometer to measure the angular velocity of the flow. Figure 2.8 illustrates that the paddle wheel anemometer is aligned with the cylinder axis (Heywood, 1988). The second method employs the torque swirl meter to measure the torque generated by the flow straightened out by a honeycomb element as shown in Figure 2.9. The steady flow rig test is used to identify the rotational motions generating characteristics of the intake valve and port at fixed valve lift (Heywood, 1988). The tumble adaptor should be employed to measure the tumble motion.

There are two types of tumble adaptor namely the T-type adaptor (TTA) and the L-type adaptor (LTA) associated with paddle wheel and impulse meter as shown in Figure 2.10. The swirl and tumble measurements can also be obtained from the optical techniques either the LDA or PIV measurements. It should take in consideration that the tumble motion measurements can be obtained from the vertical plane, while the swirl motion from the horizontal plane. A dimensionless rotational motion number (i.e. tumble and swirl ratios) can be calculated from the measurements to identify the rotational motion level inside the engine cylinder.

In the current investigation, two different intrusive methods associated with the airflow test rig are used to obtain the swirl measurements of the intake port of the rapid prototyped cylinder head. The first method is utilizing the paddle swirl meter to measure the angular velocity of the flow. The second method employs the impulse torque swirl meter as described in Section 4.1.3.

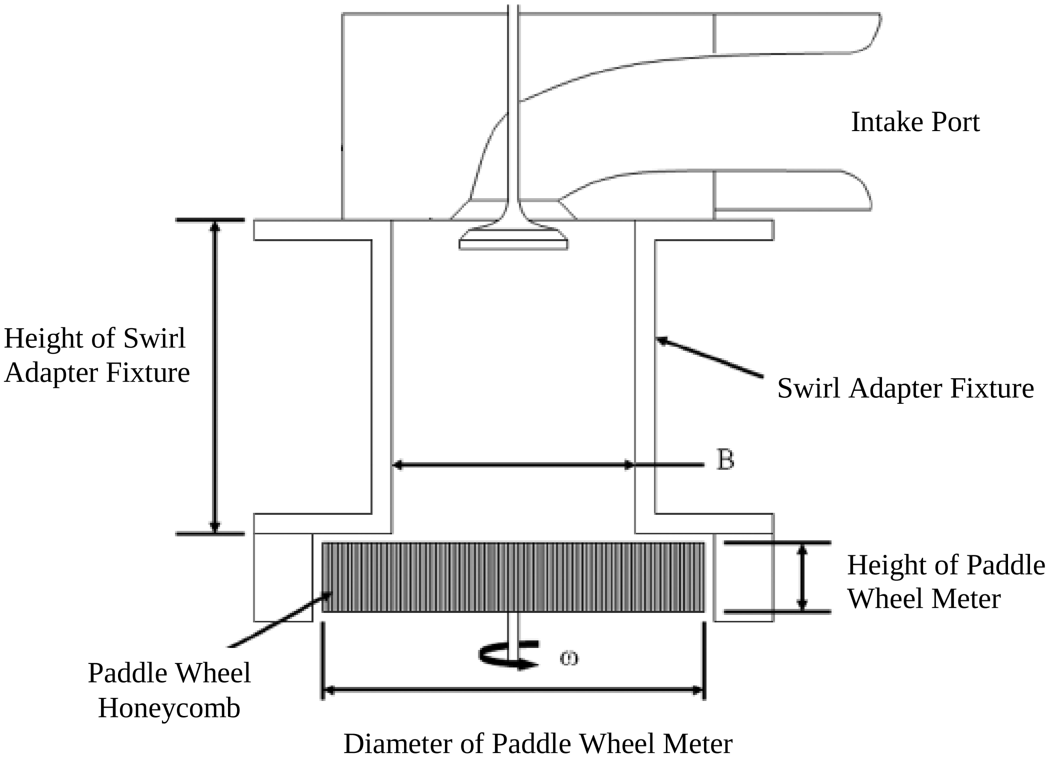

Figure 2.8: Swirl meter test set-up

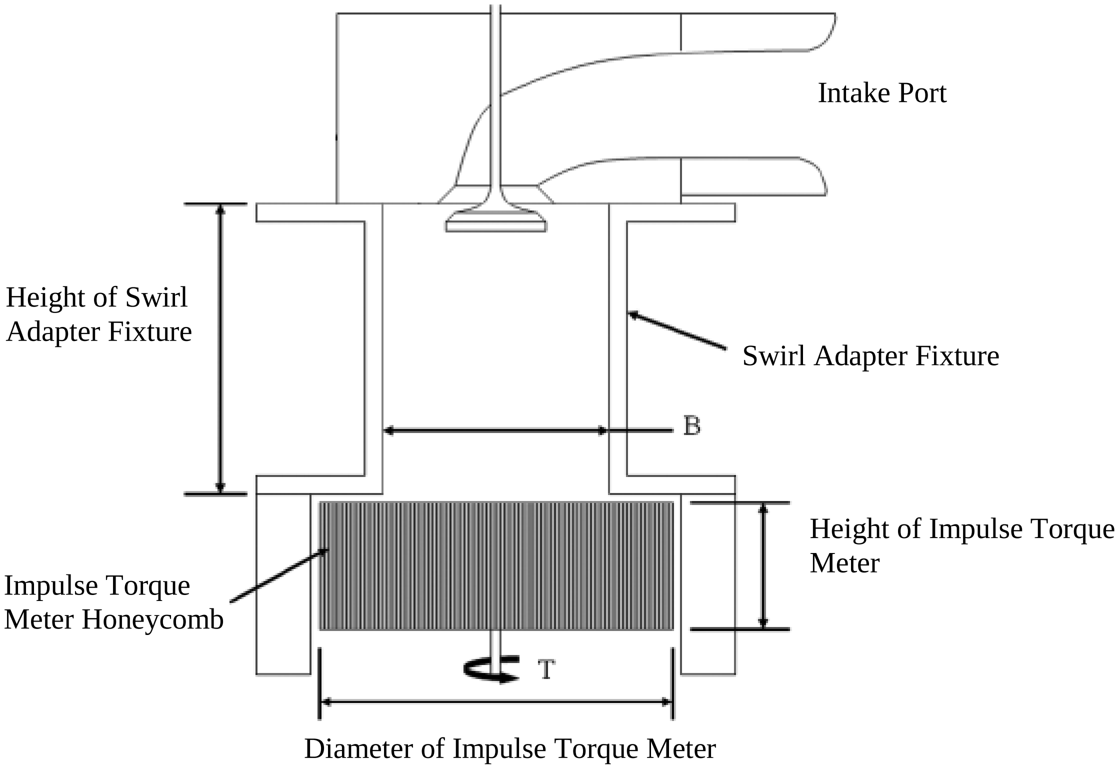

Figure 2.9: Impulse-type torque meter test set-up

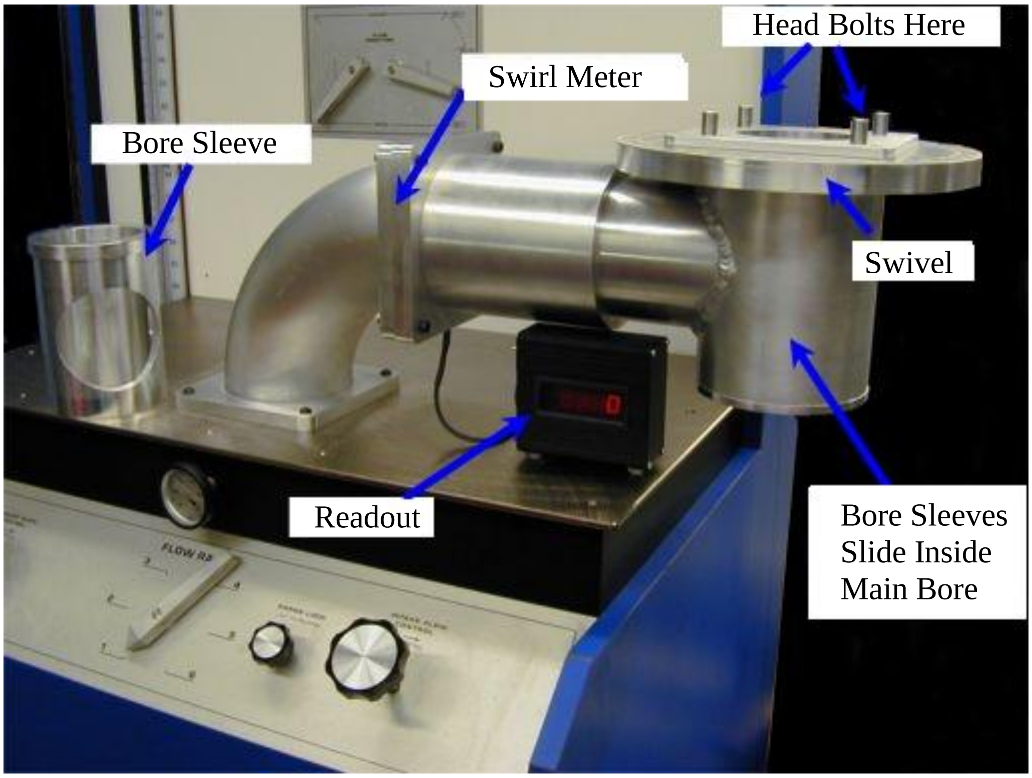

Figure 2.10: Configuration of tumble adaptor L-type tumble adaptor (Hongming, 2001)

2.3.1: Tumble and Swirl Ratios

Tumble (TR) and swirl (SR) ratios are used to define the rotational motion levels inside an engine cylinder. The simplest method of obtaining the swirl and tumble ratios, assumes solid body rotation to calculate the angular velocity for the full vector field. The centre of the rotation has been taken (Pitcher *et al.*, 2008) to be the centre of the cylinder. The angular velocity is divided by the mean angular velocity of the engine as shown in Equation 2.7.

$$SR(i) \quad OR \quad TR(i) = \frac{\sum_{n=1}^{N} \frac{U(i)_n}{R(i)_n}}{N\omega} \tag{2.7}$$

The second method is a weighted version of the simplest equation where the angular velocity is weighted by the engine speed as shown in Equation 2.8. It assumes that the angular velocity is equivalent to a rotating plate with a non- homogeneous mass distribution.

$$SR(i) \quad OR \quad TR(i) = \frac{\sum_{n=1}^{N} U(i)_n R(i)_n}{\omega \sum R(i)_n^2} \tag{2.8}$$

The third method is based on the angular momentum. Both swirl and tumble ratios were calculated based on the angular momentum as shown in Equation 2.9 (Pitcher *et al.*, 2008).

$$SR \quad OR \quad TR = \frac{8\sum_{n=1}^{N}(V_{yn}X_n - V_{xn}Y_n)}{N\omega B^2} \tag{2.9}$$

Where *U(i)* is the radial velocity, V_y is the velocity component in y-direction, V_x is the velocity component in x-direction, *Y* is the distance in y-direction, *X* is the distance in x-direction, *R* is the radial distance from the centre of cylinder, *N* is the number of vectors, ω is angular engine speed and *B* is the cylinder bore.

2.4: Overview of Previous Modelling of In-Cylinder Flows

Numerical simulation based on Computational Fluid Dynamics (CFD) codes is considered as another approach for gaining insight into the engine in-cylinder flow. The multidimensional modelling of numerical simulation has become a significant technique due to its capability for obtaining detailed information for the interpretation and analysis of in-cylinder flow fields in IC engines. It was shown that an accurate modelling of the flow in-cylinder is a key part of successful combustion simulation (Hai-Wen *et al.*, 2008; Fujimoto *et al.*, 1995; Fujimoto *et al.*, 1993; Takenaka *et al.*, 1990). In contrast to the experimental investigations, the numerical simulations linked with the advanced and high supper-processors, narrow down the range of the cost and time associated with building prototype engines. Figure 2.11 shows the numerical simulation process that can be approached to gain the optimum simulation.

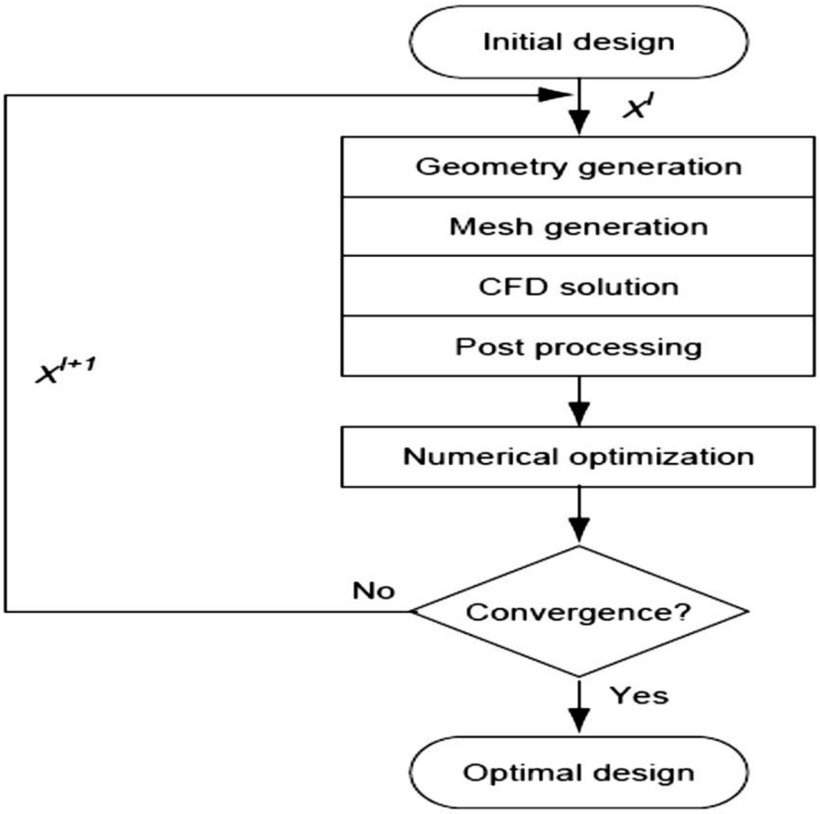

Figure 2.11: Numerical simulation processes (Hai-Wen *et al.*, 2008)

The challenges of using numerical simulation of the in-cylinder flow structure is derived from the complicated engine geometry associated with a moving piston and multiple moving valves as well as the difficulty of mesh generation and the large amount of information that is generated with each calculation. Furthermore, the numerical simulations require an accurate prediction of the turbulence modelling and initial conditions in particular in terms of describing the air motion at the start of the calculations (Heywood, 1988). Moreover, air motion formed inside the engine cylinder is three-dimensional, highly turbulent and includes a wide spectrum of length and time scales. Generated turbulence inside engine cylinder is playing a vital role in the complete engine cycle process, directly influencing the general flow structure, as well as the air/fuel mixture and the combustion stability. The main factors of importance to the in-cylinder flow structure are the large eddy formation and its subsequent break down into turbulent kinetic energy, which acts as an enhancement to the combustion characteristics. Analysis of the large scale and the fluctuation motions within an internal combustion engine are of significance for the improvement engine performance.

Several computational studies have shown that differences in the coefficients of the term in the standard k-ε turbulence model have an influence on flow field predictions. Higher order turbulence models may provide better accuracy. Both mesh refinement and use of higher order differencing schemes may improve significantly the accuracy of the predictions. Bella *et al.* (2003) carried out a numerical analysis of the flow characteristics in the intake system of a high performance engine, where they analysed the structure of the air motion during the intake phase at 12000 RPM. It demonstrated that the code's predictive capability was improved by using the Re-Normalization Group (RNG) k-ε turbulence model instead of a standard k-ε for both a medium and high valve lift. The turbulent motions of in-cylinder flow was analysed numerically by Nomura *et al.* (2008). A developed Partial cell in Cartesian coordinator (PCC) method was applied to reduce the input data preparation works by using Cartesian coordinate and partial cells for a geometry. In general, good agreement for the turbulence intensities and the flow patterns with experimental results was found. The CFD results show 10 to 30% smaller values than those of LDA in whole regions. Nomura *et al.* (2008) presented the numerical simulation of intake port valve for both steady state and transient condition with moving valves and piston. It was shown that finite element method would provide a good capability for analysis of a complex shape region like an intake port and valve. Moreover, the comparison between the experiment and simulation in a steady state case (Takenaka *et al.*, 1990) showed a good agreement for the flow pattern and absolute value of the velocities and flow rate. It was suggested that the agreement could be further enhanced by a mesh refinement. Richter *et al*. (1999) found that calculations and measurements do not agree well and they recommended that this disagreement could be recovered by improving the boundary conditions.

Payri *et al*. (2004) investigated that three-dimensional flow calculation of the intake and compression strokes of a four-valve direct-injection engine with different three pistons shapes. The predicted turbulent velocities compared reasonably well with the experimental radial and tangential turbulent components measured near TDC. However, for the re-entrant piston, it was found that the strong turbulence velocity fluctuations were not adequately predicted due to the poor performance of the k-ε model in the presence of strong shear stresses. In general, this study showed that CFD predictions of in-cylinder flow yield reasonably accurate results that allow improving the knowledge of the airflow characteristics during the intake and compression strokes. Choi *et al*. (2003) analysed the in-cylinder flow fields both experimentally by PIV and numerically by Star-CD CFD code. In the CFD analysis, the standard high Reynolds k-ε and RNG k-ε model were adopted with tetrahedral, hexahedral and hybrid meshes to determine the turbulence model dependencies. A comparison of the PIV with CFD results suggested that the standard high Reynolds k-ε model was to be more appropriate turbulence model for low speed operations than the RNG k-ε model.

As far as RANS models are concerned, there is no agreement in the literature as to which model performs better. The significant shortcomings of the standard k-ε model are isotropic turbulence concept and unrealistic representation of the normal stresses. It is also in the standard k-ε model the eddy viscosity is identified from a single turbulence length scale to calculate turbulent diffusion that occurs only at the specified scale, whereas in reality all scales of motion will contribute to the turbulent diffusion (Bradshaw, 1975). Comparisons presented by (Celik *et al.*, 1987; Leschziner, 1991) confirm the above arguments. In recent history, several turbulence models approaches have been developed to account for the turbulence effects in practical situations.

The realizable k-ε model developed by Shih *et al*. (1995) is similar to RNG version of the k-ε models in terms of anisotropic turbulence assumption that accounts for the Reynolds stress in three directions; it does a better simulation when anisotropic effects dominate the physics when compared to the standard k-ε model. Moreover, a critical coefficient of the model, C_μ, is identified as function of mean flow and turbulence properties, rather than assumed to be constant as in the standard k-ε model. The Reynolds Stress Models (RSM) is the second moment closure model that computes directly the Reynolds stress. The application of RSM to three dimensional, turbulent flows is rare in the literature, possibly having to solve six additional non-linear partial differential equations. RSM models were applied in a study by Yang *et al.* (1998). This study indicated better insight into the application of a RSM model to capture the in-cylinder flow of complex engine cylinder geometry.

More recently, a substantial effort has been put into advancing the prediction of turbulence modelling in compressible flows by the Large Eddy Simulation (LES) technique. In LES approach all important turbulence scales are resolved and only turbulence on the smallest scales requires additional modelling. An early overview of a successful LES approach for engine applications was reported by (Celik *et al.*, 1999; Haworth, 1998) who presented computations on a simplified piston-cylinder assembly. However, theoretical limitations make the use of the LES approach in practical applications debatable. The first problem is that the isotropic turbulence in the near wall region is restricted to very small scales that require a very fine mesh and large computational resources (Sagaut, 2002). The second problem concerns the inflow boundary condition. Lund *et al.* (1998) showed that a long development period may be required to reproduce the correct mean and turbulence statistics in case of estimating nonphysical inflow boundary conditions, such as a constant velocity inflow or random fluctuations. Klein *et al.* (2003) stated that one way to decrease this dependency is to use physically reasonable inflow boundary conditions.

The choice of the technique in the current investigation was, on one hand, determined by the following factors: complexity of geometry, highly unsteady processes in the engine cylinder. On the other hand, determine the computational resources that are required to apply the technique. It was shown in a study by Goryntsev *et al.* (2009) that the LES technique has the potential to simulate such highly unsteady and complex phenomena accurately in the engine cylinder. However, in the current investigation, there was a lack of the computational resources to apply the LES.

The numerical flow simulations presented in this investigation are obtained by using, as a research tool, a commercial code so-called STAR CCM+ (CD-ADAPCO, 2012). The CFD simulations are performed using a polyhedral mesh type due to the complexity of the cylinder head geometry. The mesh is generated with the STAR CCM+, version 5.06.010. Two turbulence models have been applied in the current study, namely, the Realizable k-ε (Durbin, 1996; Shih et al., 1995) and Reynolds stress models (RSM) (Thakur and Shyy, 1999; Launder, 1989; Gibson et al., 1978).

Optical diagnostic techniques play a significant role in the development of internal combustion (IC) engines. These techniques enhance the analysis of the flow structure and combustion process inside the cylinder. Overview of optical diagnostic techniques and research optical engines are presented in the following Section.

2.5: Overview of Optical Diagnostic Techniques and Research Optical Engines

A key advantage with such techniques compared with conventional instruments is that the measurements can be performed non-intrusively. Moreover, the parameters for instance temperature, pressure, velocity, and species concentration can be measured with high spatial and temporal resolution (Kohse-Hinghaus *et al.*, 2002). The optical access to the traditional opaque cylinder is required in order to enable researchers to apply the optical diagnostic techniques. There are different ways for optical access to the cylinder and it differs according to the desired measurements and available fund. In the flowing section, review of previous optical diagnostic techniques and optical access methods are described and explained.

2.5.1: Review of Previous Research Optical Engines

An internal combustion engine that allows for optical access to the combustion chamber is classified as an optical engine. Early applications of the optical access was a transparent acrylic resin that was assembled on the extended part of the cylinder and a quartz window was installed at top of the extended piston, which enclosed a mirror inclined 45^o to observe the motion of in-cylinder fluid (Charoenphonphanich *et al.*, 1996). The standard Bowdich layout was utilised by Richter *et al.* (1999) as shown in Figure 2.12, a quartz cylinder has height 80mm was mounted that allows access to almost all of the combustion chamber. Part of the inside cylinder was painted black in order to reduce undesired scattered light to reach the camera. In the second case of the experiment, when advanced piston crown design was installed, some problems were appeared due to the complex shape of the piston crown. Windows could not be placed in an arbitrary manner of the piston. Therefore, an endoscope rod inserted in the spark plug hole as shown in Figure 2.13. Huang *et al.* (2005) used a transparent cylinder that was made of Plexiglas and a section of aluminium cylinder. A chromed metal liner is inserted between the Plexiglas cylinder and the crankcase. An elongated hollow cylindrical aluminium frame was used instead of the original piston. The top end of the cylindrical frame is screwed with the piston head.

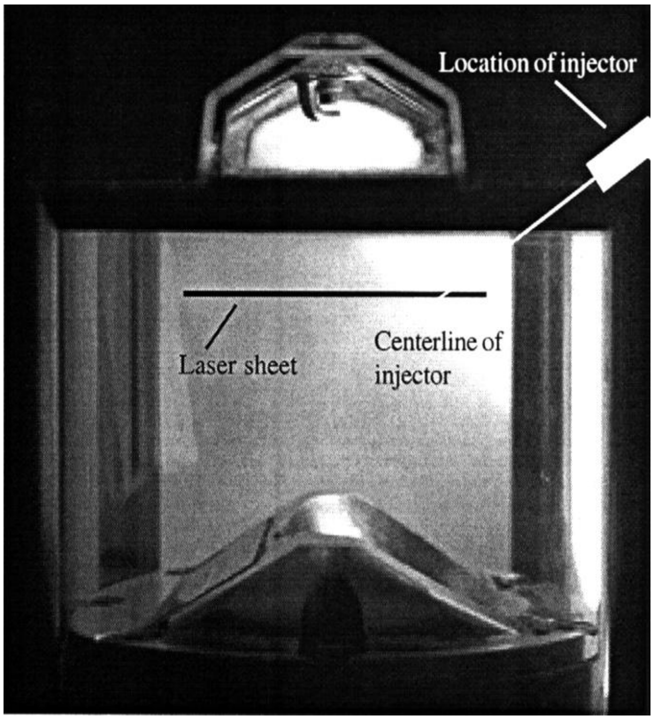

Figure 2.12: Optical access with 80mm quartz liner (Richter *et al.*, 1999)

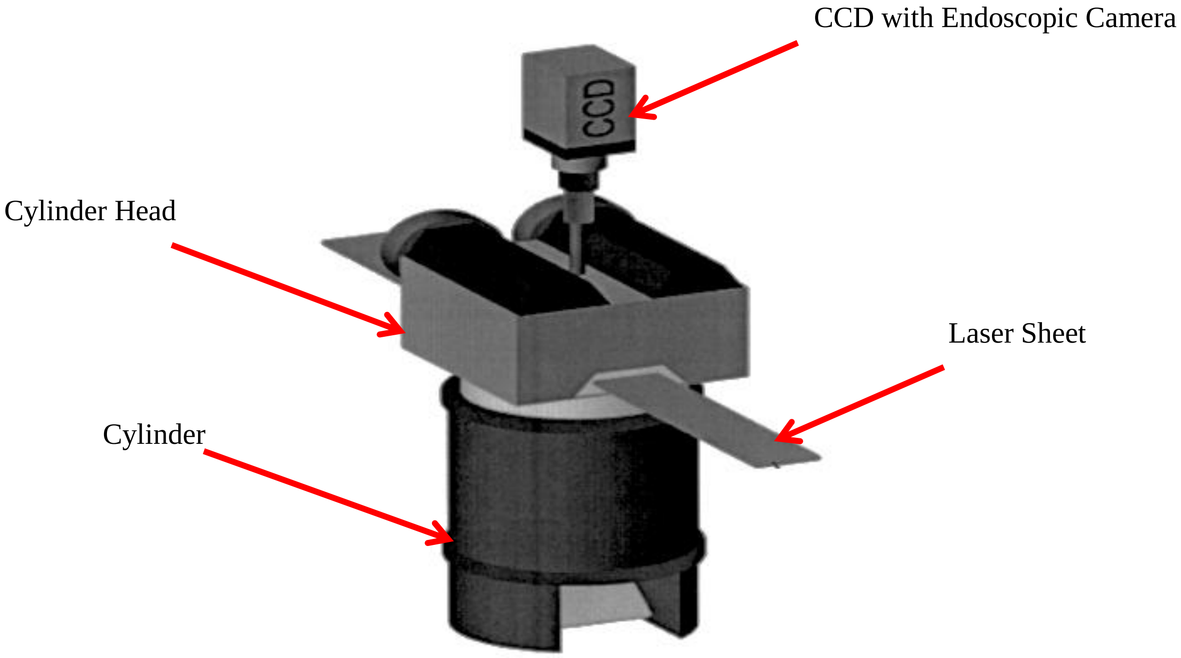

Figure 2.13: Optical engine with the endoscope mounted in the spark plug hole (Richter *et al.*, 1999)

Full optical cylinder liner that provides a large optical access to the combustion chamber can be used as shown in Figure 2.14, such optical engines modification is costly. However, the high cost can be managed by identify the interest area of investigation, for example, optical probes can be used to investigate a certain area of interest utilizing the spark plug hole to gain optical access to the combustion chamber. The optical probes include two fibre optic bundles. One bundle delivers the light source while the second bundle carries the scatter light to an endoscopic camera. The drawbacks of using the fibre optic probes are the influence of the heat and pressure limitations that could damage it. Furthermore, the view of endoscopic camera is restricted as shown in Figure 2.15.

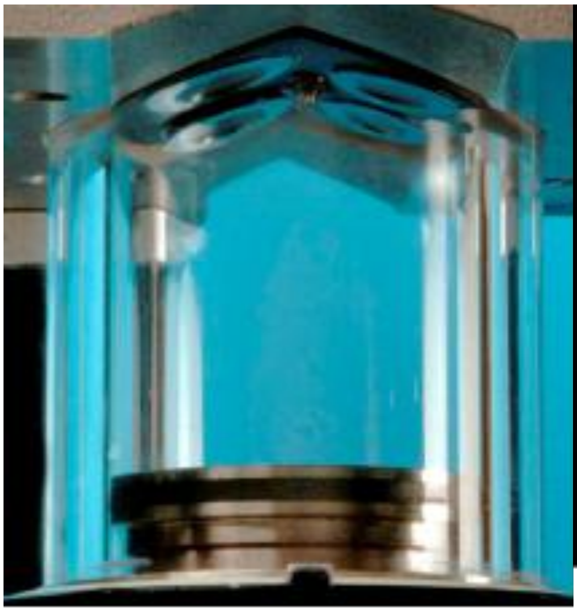

Figure 2.14: Lotus SCORE fully optical cylinder liner

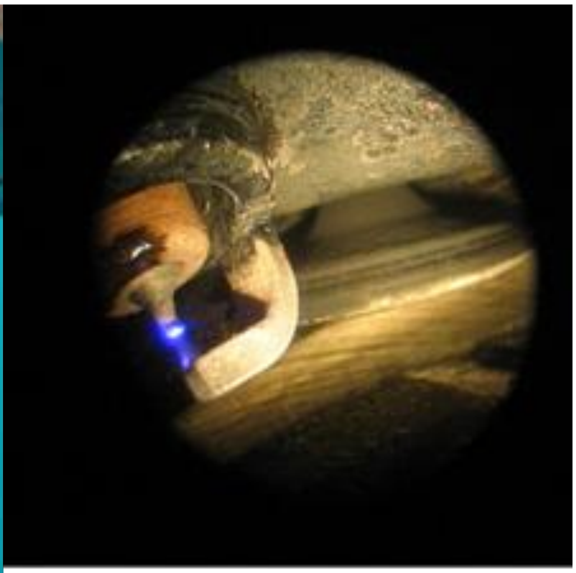

Figure 2.15: Endoscopic image of the Hotfire thermodynamic engine

Dierksheide *et al.* (2001) presented and compared Endoscopic PIV measurements through 8mm optical access on an IC engine with the measurements using standard optical access through a large window for the same interest area. It was demonstrated that the use of endoscopic devices, both for the illumination of the light-sheet plane and for the recording of the PIV images has proved to be successful for the investigation of in-cylinder flow structure development in IC engines. It was noticeable that the amount of information about the in-cylinder flow structures were increased when using endoscopic devices as illustrated in Figures 2.16 and 2.17.

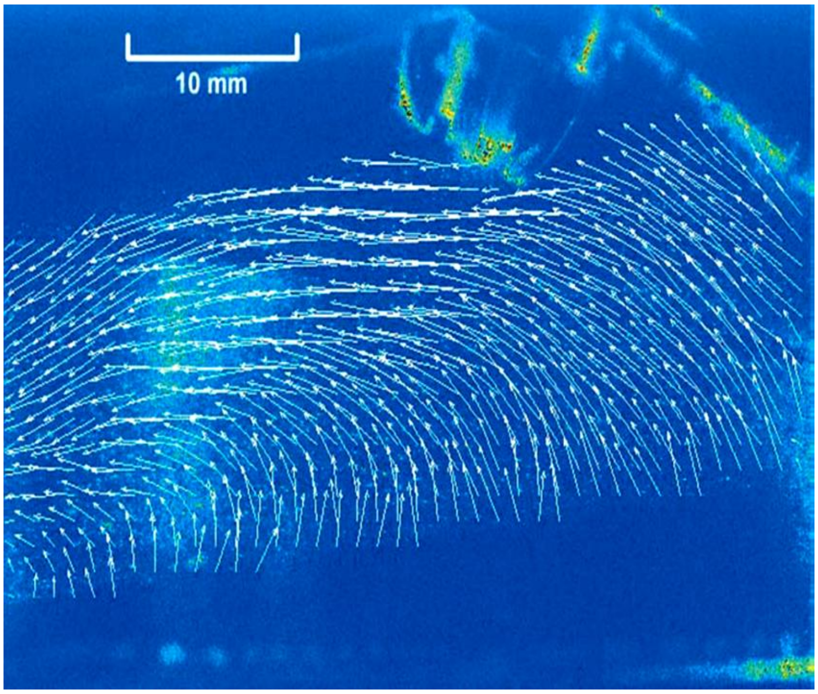

Figure 2.16: Tumble flow via large window (Dierksheide *et al.*,2001)

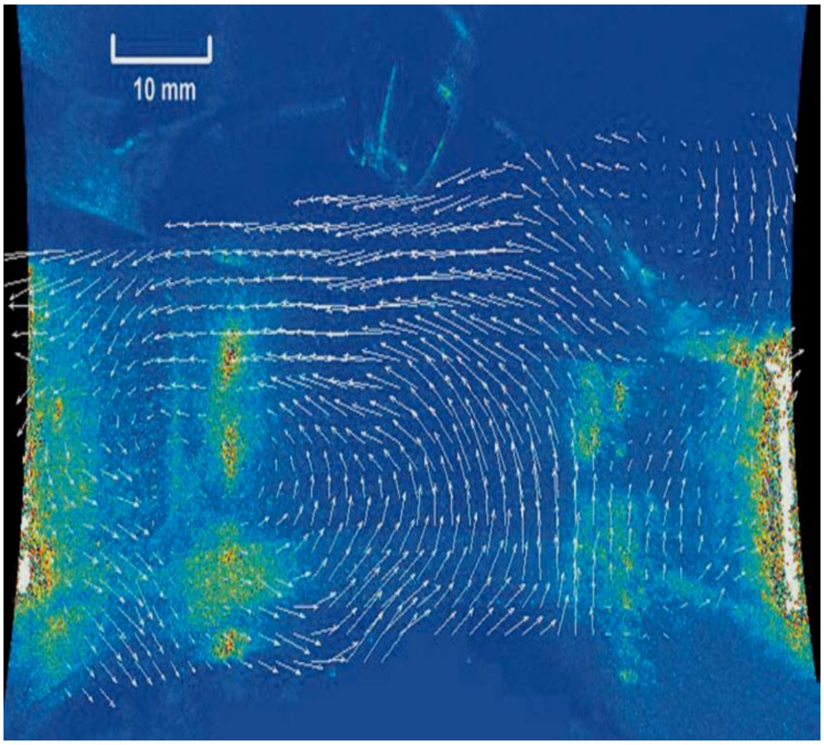

Figure 2.17: Tumble flow via endoscopic (Dierksheide *et al.*,2001)

A significant number of factors such as physical and thermal properties should take in consideration when optical access material is selected. For example, the Perspex is used for non-firing running, while the quartz is used for cylinder liner due to its hardness property. Sapphire as well, which is more expensive than quartz and more durable, is used for small windows such as those within the piston crown. The thermal properties of the optical components have a significant impact on the heat losses through the cylinder walls. Table 2.1 shows the optical engine material properties.

Table 2.1: Optical engine material properties

Material type	**Chemical Species**	**Thermal Conductivity ($W.m^{-1}.K^{-1}$)**	**Refractive Index**	**Tensile Strength**
Quartz (also known as fused silica)	Silicon Dioxide (SiO_2)	1.4 at 0°C	1.46	48 MPa
Sapphire	Aluminium Oxide (Al_2O_3)	41.9 at 20°C	1.77	400 MPa
Perspex (known as Plexiglas, Lucite or Acrylite)	Poly Methyl Meth Acrylate	0.19 at 20°C	1.49	70 MPa

Research optical engines suffer from several restrictions, such as the balance difficulty of a single cylinder, which owing to the added mass of the elongated piston and limits engine speeds. Furthermore, the running operation of optical engines is short due to the low heat transfer rates through the optical components and lack of cooling for the cylinder liner. Moreover, the optical wall must be cleaned from combustion products. The following Section gives an example of the advanced optical research engine. It should mention that the optical research engine has not been used in the current investigation due to limitation of time. It is essential to correlate detailed data of in-cylinder flows obtained under steady state in the current investigation with data from motored engine to test the assumption of a close correspondence between both conditions. This adds value to the steady state port flow measurement associated with the optical diagnostic as a method for future engine design and diagnostic work.

Lotus single cylinder optical research engine (SCORE)

Lotus Single Cylinder Optical Research Engine (SCORE) was designed for the purpose of optical diagnostics. It was installed in a test cell at Loughborough University. The cylinder liner is made from fused silica and a sapphire window inserted in the piston crown in order to provide full optical access to the combustion chamber as shown in Figure 2.18. The thickness of the cylinder liner is 15 mm that allowed a maximum secured operating pressure of 60 bar. The cylinder bore is 88.0 mm and the stroke is 82.1 mm. In order to provide optical access directly into the pent roof of the combustion chamber, the top of the liner is designed to be a curved profile as the inverse of which is machined into the cylinder head. A hydraulic ram applying 10 bar pressure is used to allow the cylinder liner to be removed, cleaned and refitted (Stansfield, 2008).

The piston is manufactured from aluminium for low weight and has a cavity in the middle allowed positioning the 45° mirror. A 45° mirror could be positioned between the upper and lower piston crowns allowed illumination or imaging through the piston window. Engine run time is limited by the temperature and purity of the optical liner. A thermocouple is located on the cylinder head and an Omega OS102 infrared temperature sensor was pointed at the cylinder liner to measure the outer cylinder wall temperature. The engine will shut down when the cylinder's outer wall temperature reached 100°C. In case of running the engine without firing, the engine run time was 7-10 minutes, while when the engine was fired, the 100°C limit was reached after less than 3 minutes at 2000 RPM and 2.7 bar IMEP.

The single cylinder engine mounted on crankcase contained both primary and secondary balance shafts, which, in combination with the lightweight elongated piston, allowed engine operation at speeds of up to 5000 RPM. Lotus' Active Valve Train (AVT) is implanted to actuate four valves. The AVT is an electro-hydraulic system capable of varying the timing, duration, and lift of each of the individual valves. It also allowed different lift profiles to be operated and made multiple valve openings during one engine cycle. The intake system is designed using the Lotus Engine Simulation (LES) software code (Lotus Software Manual, 2001). A SciTech atomizer was used to produce oil droplets of approximately 1µm diameter into the intake air for PIV and LDA techniques.

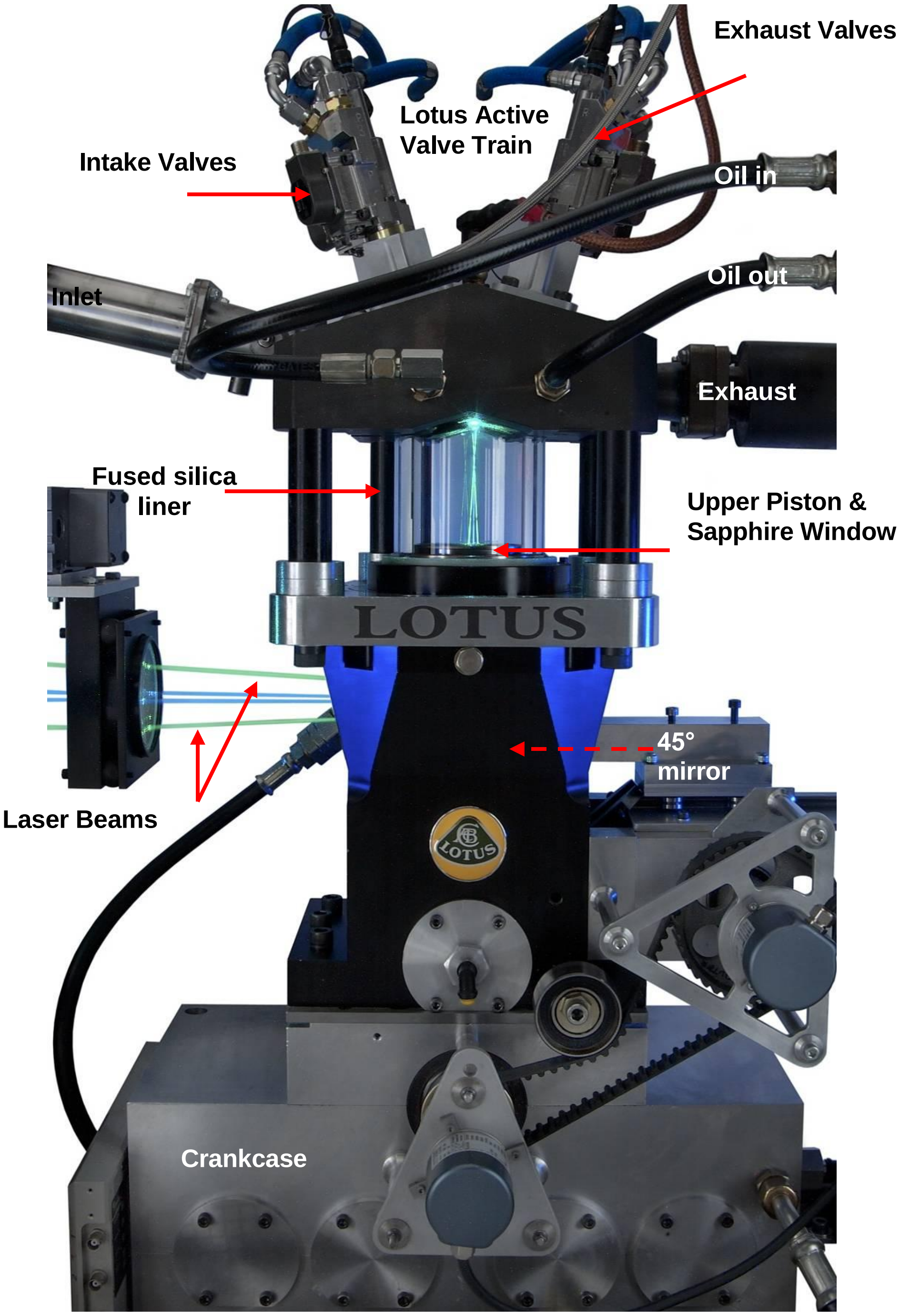

Figure 2.18: Single cylinder optical research engine (SCORE)

The cylinder head is designed with a central injector mounted at 10° to the vertical between valves 3 and 4 as shown in Figure 2.19. This reduces any reliability difficulties associated with fuel washing lubricating oil off the bore. The spark plug is positioned near central as for a typical spray-guided configuration.

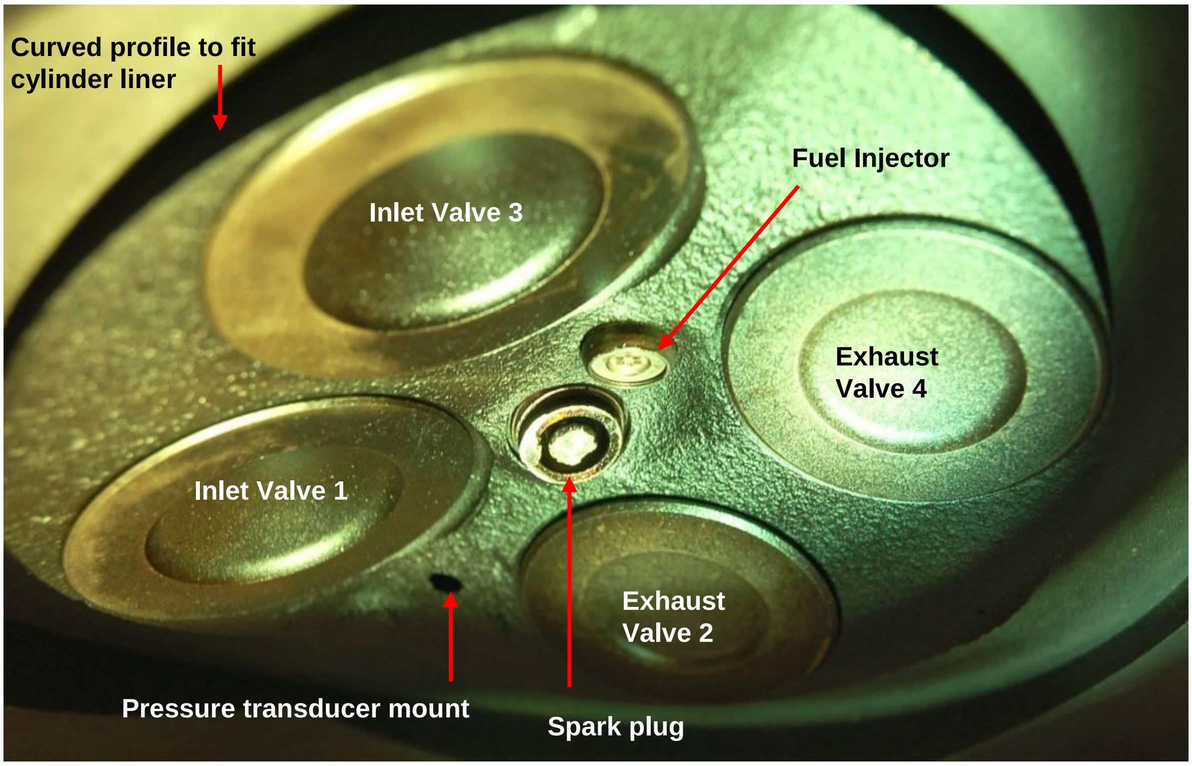

Figure 2.19: Lotus SCORE combustion cylinder

The fuelling system had a low-pressure automotive fuel pump, which drew fuel from a 10L tank and passed it through a pressure relief valve (PRV) set to 3.5 bar, to feed a three-cylinder Siemens Automotive GDI pump. A second PRV set the output pressure in the line that can be measured by a pressure transducer in the fuel line.

A water-cooled pressure transducer is placed in the cylinder head to measure the instantaneous in-cylinder pressure. The DSP unit is used to record and monitor the main operating parameters. Furthermore, PC running LabView software ensured engine operational parameters. These operating parameters are oil pressures and temperatures, inlet and exhaust temperatures, in-cylinder pressures and cylinder head temperatures.

2.5.2: Review of Optical Diagnostics

The purpose of the optical diagnostics system is to obtain non-intrusive visualization and measurement of in-cylinder processes with high temporal and local resolution. The optical diagnostic system is mostly popular in fluid dynamics and is made up of several components such as light source, particles seeding device, a detector and an optical arrangement that refer to devices for altering a beam of light, for instance, lenses, mirrors, active or adaptive optics and diffractive optics.

The classification of the optical diagnostics system is based on the incident light source, the duration of the incident light and the method of light scattering. The first classification according to the incident light source can be simple imaging techniques when the basic flash lamp is used or can be advanced techniques when the laser is used, the significance of using the laser as a light source is for three primary reasons. The first reason is due to the laser has a spatial coherence allows for diffraction-limited light sheet dimensions. The second reason is that the laser can be tuned to a particular wavelength for atomic or molecular excitation or filtering. The third reason is when the laser is pulsed with high energies in short time compared to the development of flow features (Kohse-Hinghaus *et al.*, 2002). Laser diagnostic tool permits for detailed analysis in-cylinder processes such as fuel injection and flow structure, atomization and mixing, ignition and combustion.

The second classification of the optical diagnostic is by the method of the light scattering. Seeded particles are penetrated through the flow to scatter the light. The scattering process can be classified as elastic scattering or inelastic scattering. The elastic scattering can be obtained when the frequency of excited photon is the same as the incident light beam. While non-elastic scattering causes that, the wavelength of the scattered photon is longer than the wavelength of the incident light.

The third method for classifying optical diagnostics is by the duration of the incident light such as the double-pulse of laser light, that is used to illuminate a plane that is applied by the PIV technique, while two continuous crossed laser beams, that is used to illuminate a point, which is applied by the Laser Doppler Anemometry (LDA) technique. In the Mie scattering on fuel droplets, a copper vapour laser combined with high-speed filming can be applied. While, laser-induced fluorescence (LIF) can be used for spray and fuel vapour analysis. This section presents the general features of each optical technique in order to illustrate their capabilities and limitations.

Light scattering

The light scattering is defined as the alteration of the direction and intensity of a light beam that is scattered by seeded particles, the alteration being due to the combined effects of reflection, refraction, and diffraction. A more fundamental definition that involves absorption, which is considered one of the light interactions, that results of the photons collision and then the energy of exited photon is dispersed either by random atomic motion or in form of thermal energy instead of remitting a photon. Light scattering occurs when the bound electron cloud in the material removes energy from the light beam (photon by photon), and then reemits the energy (photon by photon) without otherwise altering it (Zhao, 1998; Zhao *et al.*, 1993). The intensity of the scattered light is influenced by several parameters such as the wavelength (λ), the scattering angle (θ), the seeded particle diameter (d), and the relative index of refraction (n) of the particle and the medium.

It is stated that the more refractive indices of the seeded particles differ from the surrounded medium, the more light will be scattered by the seeded particles. However, if there is no difference in refractive indices, no light will be scattered (Jay, 1987). Many of diagnostic techniques have being developed based on the light scattering, for instance, an elastic scattering such as Rayleigh scattering and Mie scattering or inelastic scattering such as Raman scattering and laser induced fluorescence for both the qualitative and quantitative measurements of the combustion-related factors.

It is deduced that the Rayleigh scattering technique is mainly attractive due to the simple experimental arrangement and its high signal strength that allows instantaneous single-pulse measurements as well as in 2-D images. Rouland (1997) initiated the application of the Rayleigh scattering to combustion investigations. Filtered Rayleigh scattering is used to study high-speed flows and temperature imaging (Rouland, 1997). The Rayleigh scattering technique should be employed in very clean situations due to Mie interferences and spuriously scattered laser beam.

The scattering caused by seeded particles larger than that are used in Rayleigh scattering, is called Mie scattering. The Mie scattering can be a very strong process depending on particle concentration, and particle size and is a potential source of interference. Seeded particles for engine flow field measurements are of the order of 1μm diameter. In this region, Mie scattering regime dominates for visible light wavelengths. The difficulty of implement a Mie scattering in engines is due to strong reflections caused by the walls and windows. However, this difficulty can be recovered by darken the head and use coated optical ports. Otherwise, inelastic light beam interaction can help to eliminate these problems. For instance, fluorescence is the preferred fuel diagnostic in engines because of the sufficient signal/noise ratio in many situations (Kohse-Hinghaus *et al.*, 2002).

Raman scattering is based on the inelastic scattering. The different types of spectra of Raman scattering depend on the energy exchange between photons and the rotational or vibrational energy states of the molecule. The Raman scattering signal is order of magnitude smaller than Mie. Thus, it is difficult to use Raman spectroscopy when there are walls and windows reflections or when there are presence of particles or fluorescent emissions. However, this is sorted by utilizing the modern laser light sources and conditioning beside to the high performance detection system, Raman scattering is ideally suited to combustion diagnostics and has been widely applied. The drawback of Raman scattering is the very low cross-section compared to Rayleigh scattering approximately three orders of magnitude lower that influence 2-D Raman temperature measurement. The design of Raman experiment requires a very careful selection of the laser source and a critical consideration of the optical properties of filters and the efficiency of the detector (Zhao *et al.*, 1993).

Imaging techniques

The light detection technologies play a significant role in the development of optical flow field diagnostics. Detectors are photosensitive elements that respond to light and are called photo-detectors. The main purpose of the photo-detector is to get an image of the interest region with high resolution by utilizing the lens techniques to focus the targeted region of scattered light into a light sensitive surface. A film was used as an early image technique. Photons strike a photographic film and then the striking of the photons on the film cause a chemical reaction. Currently, developed imaging techniques such as photodiode and intensified charge injection device (CID), a Complementary Metal Oxide Semiconductor (CMOS) and charge-coupled device (CCD) cameras are used.

CCD is an integrated-circuit chip that produces a current flow proportional to the instantaneous light intensity. CCD cameras are capable to accumulate signal over time. They are more suitable for measurement of low light intensities if the size of the photosensitive area is small. The CCD can provide a suitable signal-to-noise ratio even when individual elements in the array are extremely small. Both the photodiode and CCD suffer from threshold and saturation limitations. CMOS cameras compared with CCD cameras have a lower resolution and lower sensitivity. However, CMOS cameras are capable of much higher repetition rates and are often used in high-speed PIV measurements (Kohse-Hinghaus *et al.*, 2002).

Particle Image Velocimetry (PIV)

PIV is a significant flow measuring technique that has ability to capture planer two dimensional velocity fields with high temporal and spatial resolution. The basic principle of PIV technology based on that the flow is illuminated with a double-pulsed laser-sheet and then the light scattered from particles, which were seeded in the flow, is recorded with a camera, which is positioned perpendicular to plane of the sheet as shown in Figure 2.20. The recorded images with defined time of the illuminated field are processed to measure the displacement of the particle between the first and subsequent exposure and from that, the velocity field is derived. The choice of seeded particles and the way of their penetration in the flow are significant aspects of the PIV technique to obtain the high-quality recordings of the particle positions throughout the region. Consequently, the particles should be seeded in the flow with sufficient concentration and proper size. Moreover, the out-of-plane particles motion must be restricted to be a within the laser-sheet to avoid unpaired particle images and noise increasing. One of the specialists of the PIV technique so-called Ronald Adrian (Rouland, 1997) defined the advanced PIV as:

> *"The accurate, quantitative measurement of fluid velocity vectors at a large number of points simultaneously"*

In the following review of PIV technique is provided which gives better insight on the flow measuring method which is also used in the current investigation and will be discussed in Chapter 3.

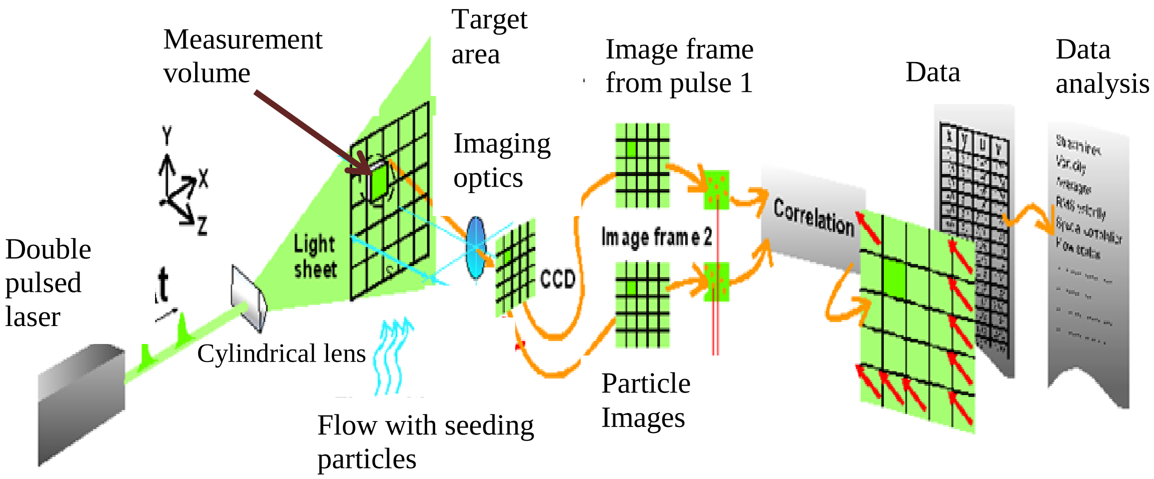

Figure 2.20: Principle of Particle Image Velocimetry (PIV) (Courtesy of Dantec Dynamics)

Early PIV techniques used a laser with mechanical shutter to illuminate the flow and attempted to capture both images on one frame of photographic film. Kohse-Hinghaus *et al.* (2002) applied in his PIV investigation a double-exposure of the film using a double-plus ruby laser with a time interval between exposures of 2.5µs yielded a velocity measurement to approximately 1% for 102 mm/s flow field. Reuss (1993) and Stucky *et al.* (1994) also used PIV on wet film images with autocorrelation techniques. During post processing, it was impossible to know which particle image captured from which laser beam. The main modification of these studies was the way in which the directional ambiguity of autocorrelation was overcome. Reuss (1993) used an image shifting technique, whereas Stucky *et al.* (1994) used a two-colour PIV system.

One of PIV technology development is evolution from a film based image detection system to one based on a CCD detector, which employs a cross-correlation to remove the directional ambiguity. Reeves *et al.* (1996) applied cross-correlation processing to resolve the directional ambiguity and improve the tolerance to out-of-plane motion. They used larger seeding particles (4-10μm) to scatter more light and address the flare issues. Bevan and Ghandi (2005) applied PIV to investigate the influence of three different port geometries. They attempted to correlate large-scale tumble, turbulence, and kinetic energy to the combustion duration, but were incapable to find a conclusive correlation. Investigation by Josefsson *et al.* (2001) utilized PIV and LDA techniques to compare turbulent length scale measurements in a four-valve, optical engine motored at 1200 RPM. Turbulence intensity and the turbulent length scale were calculated and found to be in good agreement for both techniques, but there was slight variations in the calculated length scale values because of the cyclic variation was not taken in consideration.

Li *et al.* (2001, 2002) applied PIV to measure the flow field in an optical engine. They calculated the mean and fluctuating velocity component, turbulent length scales, vorticity and strain rate distributions. They also investigate later the benefits of higher tumble geometries. Li *et al.* (2001) used PIV also to measure swirl structures in a single-cylinder Hydra engine with a Ford Zetec head. The measurement conducted at a single engine speed of 1200 RPM and Only one crank angle position. Swirl motion was generated by blocking one of the two inlet valves with a rubber bung. They applied small interrogation area (32x32px) with high seeding levels in order to measure turbulent integral length scale and strain rate. A filtering technique, which applies FFT, was used to choice a cut-off frequency to distinct low frequency cyclic variation from high frequency turbulence. The integral length scale was found to be in the range of 6-10 mm. In addition to the swirl plane measurements, Li *et al.* (2002) also applied PIV to measure tumble plane on the central symmetry plane and a parallel plane underneath one of the inlet valves at two engine speeds of 1200 RPM and 600 RPM. The tumble structure was formed early in the compression stroke and moved underneath the exhaust valves until the tumble vortex disappeared at 50° BTDC. Similar structures were observed at both engine speeds.

Huang *et al.* (2005) applied PIV to investigate the effect on the air motion of installing a tumble plate in the intake system of optical engine operating at 1500 RPM. They found that tumble had deteriorated by 90° BTDC compression and swirl motion was generated in the cylinder. Moreover, they found that the existence of plate improves engine performance at low loads, but the active throttling at high loads dramatically reduced engine performance. Nomura *et al.* (2002, 2008) applied PIV and LDA techniques to investigate the flow field for a two-valve head on steady flow rig. They compared the results of PIV and LDA data. They found that PIV data showed the same tendencies for mean velocities and turbulence intensities. One of the PIV technique features is the capability to collect large amount of flow data in a short time compared with LDA, but the data that is generated during such measurements and processing of image data requires huge and fast computers. The PIV technique can be extended to collect data in three dimensions utilizing stereo PIV as have been shown by Choi *et al.* (2000) and Petschenig *et al.* (2010).

Laser Doppler Anemometry (LDA)

The LDA is another optical diagnostic technique classified as a point measurement technique capable of measuring fluid velocities. LDA utilise the Eulerian approach that measures the velocity of flow particles as they pass the point of measurement (it is known as measurement volume). The LDA technique based on a continuous laser beam that is split into two beams and they then crossed, to form a measurement volume as shown in Figure 2.21. An interference fringe pattern is formed at the measurement volume as illustrated in Figure 2.22. The signal from seeded particles, penetrated in the flow, is measured as they scatter light from the fringe pattern. The intensity of the scattered light in time has a fundamental frequency that can be measured by knowing the space between the fringes, and then the speed of the particle can be determined.

The LDA measurement technique has several advantages over most other techniques such as calibration is not required and it is sensitive to direction. For instance, it measures a vector quantity not a scalar, and it can be applied in harsh environments, for example, combustion systems, without any damage to the sensor. The main disadvantage, however, is that LDA requires much time to record the temporal flow-field development in a complete plane (Pitcher *et al.*, 2010).

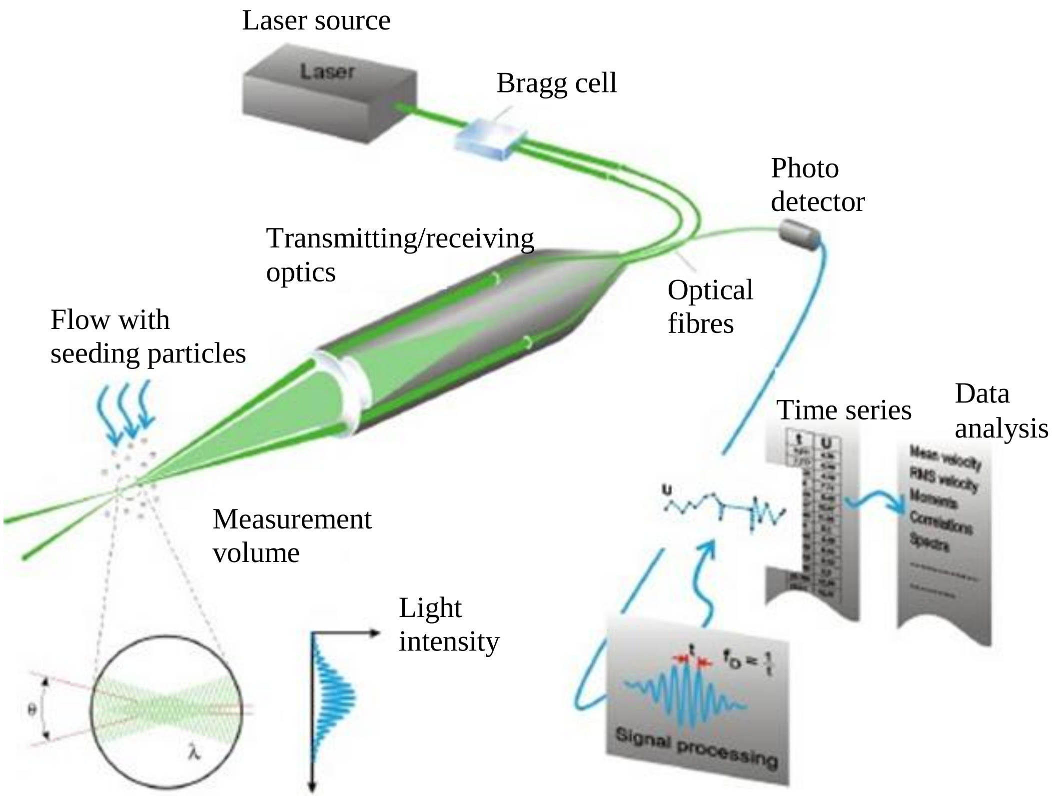

Figure 2.21: Principle of Laser Doppler Anemometry (LDA) (Courtesy of Dantec Dynamics)

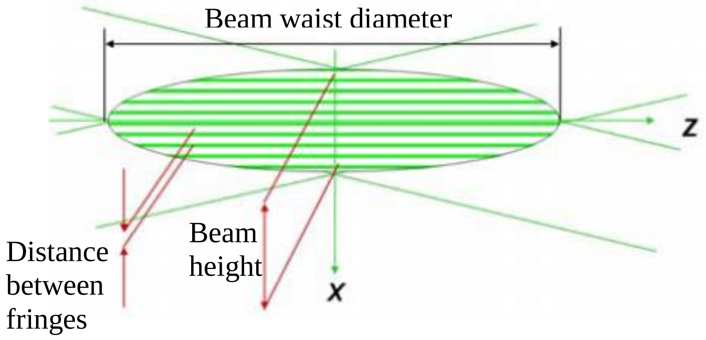

Figure 2.22: Fringe pattern (Courtesy of Dantec Dynamics)

Early investigation applied LDA measurements in motored engines was by Cole and Swords (1979), who conducted measurements near the spark plug of a modified Ricardo E6 engine at 800 RPM in 1979. They measured 2D velocity components by using 1.3W Argon ion laser mounted on a frame that had ability to translate horizontally and rotated by 90°. The photomultipliers were positioned perpendicular to the incident beams on the same optical table to reduce the time required for alignment (Cole and Swords, 1979). Gasparetti *et al.* (1996) examined the effect of valve lift, in a motored research engine, using a combination of LDA airflow measurements and simultaneous laser vibrometry measurements of the valve position. This arrangement allowed the effect of valve to be studied at engine speeds up to 4000 RPM. 1-D LDA system was applied by Gold *et al.* (2000) to measure the in-cylinder airflow in an optical engine. LDA data were recorded for two tumble planes and four swirl planes during the induction and compression strokes. They found that a nearly homogeneous charge was formed at TDC under both injection strategies, but higher cyclic variability occurred with late injection onto open valves, due to a change in the shear forces across the valve gap and a reduction in available mixing time. Węclas *et al.* (1998) utilised LDA and oil streak techniques on a steady flow rig to also study the variations in the flow field with different valve lifts. The LDA system comprised a 400mW Argon ion laser in the backscatter arrangement. Measurements were recorded for 3mm and 5mm valve lifts. The work demonstrated that symmetric cylinder geometries do not necessarily produce symmetric airflow fields.

Miles *et al.* (2001) investigated a flow filed of direct injection Diesel engine operating at 900rpm and 1.2bar IMEP using LDA technique and CFD simulation. They compared the LDA data with CFD simulation of the induction, compression, and expansion stroke. They found that predicted mean angular momentum was agreed with the measured value to within 5%, however, the instantaneous and distribution of angular momentum was significantly less accurate. *Xu et al.* (2003) also applied LDA to compute the in-cylinder air motion and recommended the reduction in tumble motion at part load could be compensated for by closing one valve. A developed application for LDA system have been approached by Esirgemez and Olcmen (2005), who developed a LDA probe contained within a spark plug. The LDA control volume could be traversed 50 mm for in-cylinder flow analysis of production engines. Li *et al.* (2001) also calculated turbulence intensity using LDA in a four–valve SI engine, and showed that, when approaching TDC, the turbulence intensity increased due to break up of the large scale tumble structures near the cylinder liner. Hong and Chen (1997) also applied CFD simulation and a two point LDA system to measure the integral length scale and a single point LDA system to measure integral time scale measured. The comparison between the measured data was performed to investigate the turbulence of single cylinder engine motored at 500 RPM. They found that both techniques were reliable, as the in-cylinder turbulence was not completely isotropic by TDC. The predicted results of CFD using k-ε turbulence model were the compared and found to be reasonable for the studied conditions (Hong and Chen, 1997).

The experimental techniques used in this work for the investigations of the in-cylinder flow structures under steady state conditions are Particle Image Velocimetry (PIV) and swirl motion meters. A rapid prototyped cylinder head is used, which is a replica of an engine head of a pent-roof type (Lotus). The steady air flow rig (SuperFlow- SF660E) is used to measure the air flow and quantify in-cylinder air motion at steady flow conditions. A detailed discussion of PIV technique and measurements set up for both the horizontal and vertical planes are presented and described in Chapter 3 and Chapter 4 respectively.

Chapter 3
PIV: Acquisition system, Processing and Analysis

3.1: Introduction

The objectives of the experimental investigation described in this thesis are twofold. Firstly, the experiments should provide enough information for studying the in-cylinder engine flow phenomena. Secondly, this information must allow for an appropriate validation of numerical simulation results. Such a validation is described in Chapter 8 for the steady-flow rig, based on the results of the experiments reported in Chapter 6. Experimental analysis of internal combustion engine performance can be approached with a wide range of techniques. For the purpose of the current study, detailed flow data must be acquired. As described in the previous Chapter, PIV experimental data must not only yield a qualitative presentation, but also quantitative information is required since it must serve as a validation resources. Therefore, this Chapter will focus on the characteristics of PIV and its specific application to present investigation, while the specific choices made for the presently conducted measurements are discussed in Chapter 4. There are many parameters relevant to the PIV measurements technique, which are available to adjust and optimise.

The following Sections outline the PIV process adopted here with detailed discussions on each step of this process. Firstly, the PIV acquisition system is described, followed by the description of data pre-processing and post-processing. Finally, optimisation of the PIV setup is discussed together with explanation of the limitations of this measurement technique.

3.2: The PIV Acquisition System

The acquisition process is actually collecting the raw images and is considered to be the most significant step in data collection. It is widely known that a fruitful exploit of one's time is to spend more time on setting up the experiment, rather than make poor quality data look better than it really is by post-processing (Westerweel, 1993). It is essential that the physical test rig set-up and flow field of interest are accurately identified prior to the PIV acquisition considerations which includes providing sufficient optical access and adding of the most suitable seeding to the flow. Beside to accurately setting up the actual flow conditions of interest, the PIV hardware must also be accurately set up. The light sheet illuminating the flow must be correctly aligned at the field of view (FOV) and the thickness of the sheet should be optimised for the experiment. The camera should be positioned and calibrated and the focal parameters are optimised to ensure the best quality image. Another significant parameter that must be optimised is the inter-frame time settings. Three fundamental aspects can identify the success of a PIV acquisition system (Adrian and Westerweel, 2011):

i. The generation and distribution of the seeding particles,
ii. Flow illumination and
iii. The CCD camera and lens combination.

3.2.1: Tracer Particles

Undoubtedly, scattering particles play a significant role in most of the laser techniques such as PIV. The PIV technique is often used to measure the velocity of a flow. However, it is more accurate to describe it as measuring the velocity of particles seeded within the flow. As such, it is significant that the velocity of the seeding particles is the same as the velocity of the flow. The main requirements for scattering particles in order to obtain satisfactory results in an optical flow measurement are:

i. Ability to follow the flow by optimizing its size and density,
ii. The seeding particles should be large enough to scatter sufficient light,
iii. Non-toxic, non-volatile, non-corrosive, chemically-inactive and cheap.

The most important requirement is that the ability of seeding particles to follow the flow, in particular, under the highest frequencies of the flow fluctuations that might be reaches up to 10 kHz in engines (Lorenz and Prescher, 1990). It is critical to the success of the PIV measurements, because the particle displacement is deducing the movement of flow. The fluid dynamic behaviour of particles seeded in a moving fluid depends on the particle size and shape that has an influence on the relative density of the particle to the fluid. The ability of seeding particles to follow the flow can be evaluated in terms of two parameters:

- Particle response time, which was defined as in Equation 3.1 by Elghobashi (1994).
- Velocity lag, which was identified by Raffel *et al.* (1998; 1996) as in Equation 3.2.

Mellling (1997) investigated the limitations of using such defined equations to calculate both parameters in his research engine. He stated that using Equations 3.1 and 3.2 in order to calculate the particle response time and velocity lag based on the density of the particles seeding that must be higher than the gas or the surrounding flow.

In engine research, the particle response time should be faster than the smallest scale of turbulence under investigation in order to be able to follow the flow. In general, in engine PIV measurements, this will be the integral length scale. Olive oil droplets of 3.09µm diameter are capable of following 1 kHz fluctuations and 1.0µm diameter droplets are capable of following 10 kHz fluctuations. This is sufficient to follow typical engine integral length scales, which typically fall within this region (Melling, 1997).

$$\tau_p = \frac{\rho_p}{\rho_f} . \frac{{d_p}^2}{18\upsilon} \tag{3.1}$$

$$U_s = {d_p}^2 \frac{(\rho_p - \rho_f)}{18\mu} a \tag{3.2}$$

Where, the subscripts p and f refer to the seeding particles and domain fluid respectively and

τ_p is particle response time (s),

ρ_p is seeding particle density (kgm^{-3}),

ρ_f is fluid density (kg.m^{-3}),

d_p is seeding particle diameter (m),

υ is fluid kinematic viscosity (m^2.s^{-1}),

U_s is velocity lag (ms^{-1}),

μ is fluid dynamic viscosity (kg.m^{-1}s^{-1})

a is flow acceleration (m.s^{-2}).

The light scattering properties of small sized particles are influenced by the ratio of the refractive index of the particle to that of the surrounding medium, the particle's size and shape and scattering angle, so it is not easy to anticipate their general behaviour. Adrian (1986) stated that the intensity of scattered light increases proportional to the square of the particle diameter and better scattering might be yield when have high ratios of the particle refractive index to the fluid refractive index, which is often the case when measuring in air. The parameters of some common seeding particles are shown in Table 3.1.

Table 3.1: Particle parameters and performance in an oscillating flow (Wigley, 2008)

Particle	**Density Ratio (to Air)**	**Refractive Index**
Alcohol	667	1.36
Water	832	1.33
Nylon	850	1.45
Latex	875	1.59
Silicon Oil	900	1.47
Aluminium Oxide	3310	1.76
Titanium Dioxide	3500	2.7

It is essential that to ensure a correct quantities and homogeneously disseminated of seeding particles are seen in each interrogation area. This indicates to have an optimal signal to noise ratio. In case of too few particles contribute to the correlation peak, this leads to low signal peak. Likewise, if the density of particles seeding is too high, the particles overlap will increase the signal noise. Both cases represent a poor signal to noise ratio and may cause the correlation to identify a false vector.

Several studies investigated the required minimum number of particle captured per integration area to achieve a reliable correlation. Raffel *et al.* (1998) suggested that 5 particles were required to achieve 95% valid detection. Hollis (2004) targeted 8 particles per integration area, but it required a minimum of 5 to accept the vector. La Vision Company (DaVis. 7.2 Manual, 2011) in the other hand stated that good results can be obtained with 3 particles per interrogation area. In case of real engine measurements, seeding particles must be capable to exist in the harsh conditions such as the high pressures and temperatures experienced at TDC compression that approximately reaches 25 bar and

475°C, respectively, according to Lotus research engine, and must not excessively smeared or damage the optical components.

In the current investigation, Seeding particles are generated by means of a pressure atomiser jet (Model 9306 Six-Jet; TSI) and were fed into the cylinder through the intake port. Olive oil is used as the liquid to produce the seeding particles with a diameter of approximately 1µm. In the RMS velocity measurement, SciTech pressure atomiser is used to generate a fine cloud and high density of oil droplets particles with a diameter of approximately 0.5 µm.

3.2.2: Flow Illumination

A frequency doubled pulsed laser unit is used as a source of illumination in PIV technique. The laser supplies double pulses of 532nm wavelength unlike Continuous Wave laser that emits a constant beam as would be required in LDA technique. PIV lasers comprise of two laser pump cavities that produce one pulse each. Such laser types allow the energy to accumulate within the cavities before a ‘Q-switch’ opens to emit a high intensity pulse with approximately 3-5ns. A series of mirrors and prisms built in the laser head unite are used to align the pulses from each pump cavity.

The type of pulsed laser employed is a Neodym Yttrium Aluminium Garnet laser (Nd: YAG). It is a solid-state laser in which the beam is generated by Nd^{3+} ions, which are merged in the Yttrium-Aluminium-Garnet (YAG) crystals. The fundamental wavelength output of the Nd:YAG laser is frequency doubled to 532nm. The beam delivered from the laser is formed in a light sheet via light sheet optics that consists of converging and diverging lenses. Firstly, the converging lens focus the beam into the field of view and the diverging lens then forms the light sheet. This was practically assessed by observing the sheet at very low laser power (Adrian and Westerweel, 2011). A schematic of the PIV laser head is shown in Figure 3.1.

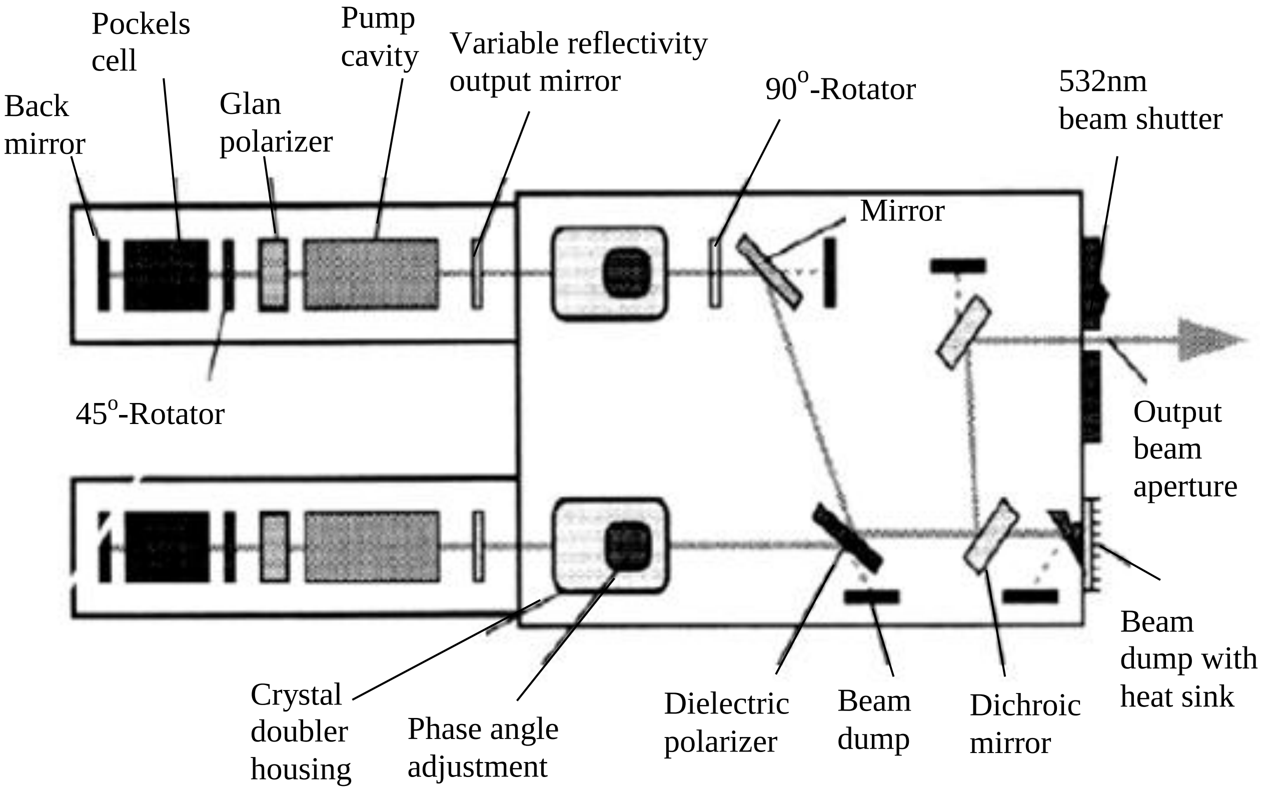

Figure 3.1: Laser head schematic (Raffel *et al.*, 1998)

The laser sheet preserves the Gaussian intensity profile of the original beam. This means that the intensity drops to half its maximum value at the laser sheet edges. The thickness of the sheet is controlled by adjusting the distance between the converging and diverging lenses that alters the position of the diverging lens relative to the focal point of the beam. The optimal thickness of the sheet is usually selected to be as small as possible.

The significance of light sheet thickness is to eliminate the scattering of particles out of plane motion and restraining the number of particles in the light sheet that leave the field of view after the first image. An investigation related to the out-of-plane motion assessment was carried out, which suggested that the out-of-plane motion should be less than 30% of the laser sheet thickness, although this can be difficult to achieve in highly turbulent IC engines (Raffel *et al.*, 1998). The laser specification is provided in Table 3.2.

Table 3.2: PIV laser specification

Laser	New Wave Solo 120
Laser Power (532nm)	120 mJ
Laser Power (256nm)	20 mJ
Max Repetition Rate	15 Hz
Pulse Width	3-5 ns
Divergence	<3 mrad
Power Requirement	1000 watts
Operating Temperature	10°C - 30°C

3.2.3: Recording

Double frame cameras are essential in the modern PIV technique. The scattered light from the particles distributed within the flow filed is recorded. An accurate recording of the flow field requires careful consideration of the camera parameters and selection of the camera lens parameters. These parameters and the distance of the object from the camera define the field of view. In the current investigation, a high-resolution double frame CCD camera (LaVision: Flowmaster 3S) is used. The camera has an image spatial resolution of 1280 X 1024 pixels and the acquisition frequency was 4 Hz. The specification of the camera is provided in Table 3.3. The recording process is onto an electronic Charged Coupled Device (CCD) array built in the housing of camera.

Table 3.3: Camera specification

Camera	Flowmaster 3S
Sensor	Sony ICX 085
Pixel (H x V)	1280 x 1024 pixels
Pixel Size (H x V)	6.7 µm x 6.7 µm
CDD Array size (H x V)	8.6 mm x 6.9 mm
Fill Factor	60% With Micro lens
Dynamic Range	12 bit
Double Frames per Second	4
Minimum Interframe Time	300 ns
Operating temperature	-12°C

The CCD array consists of an arrangement of light sensitive chips 1280 pixels in row and 1024 pixels in column as shown in Figure 3.2. These CCD pixels register light intensity instead of emitting light. Each pixel collects the light in the form of charged electrons. The charge represents the digital intensity at each pixel. The data is transferred from column to adjacent column of the CCD array when the double frames were illuminated. Data on the active column is then transfer to a PCI frame-grabber card in the PC whilst another column collects the current illuminated image. In this way, the camera can operate in double frame single exposure mode, as is required for the cross correlation algorithm to be performed. The CCD camera allows very short inter-frame times between each of the frame pair due to efficient data transference between the chip columns, thus this is synchronized well with the dual head pulsed laser. The CCD sensor can burn-out due to high exposure, resulting in reducing data quality. Thus, a filter must be used to cover the camera lens. In high-speed PIV measurements, which require a high repetition rate, CMOS cameras are recommended to be used as most of functions are integrated into the chip and the charge can be transferred immediately off the chip (Litwiller, 2001).

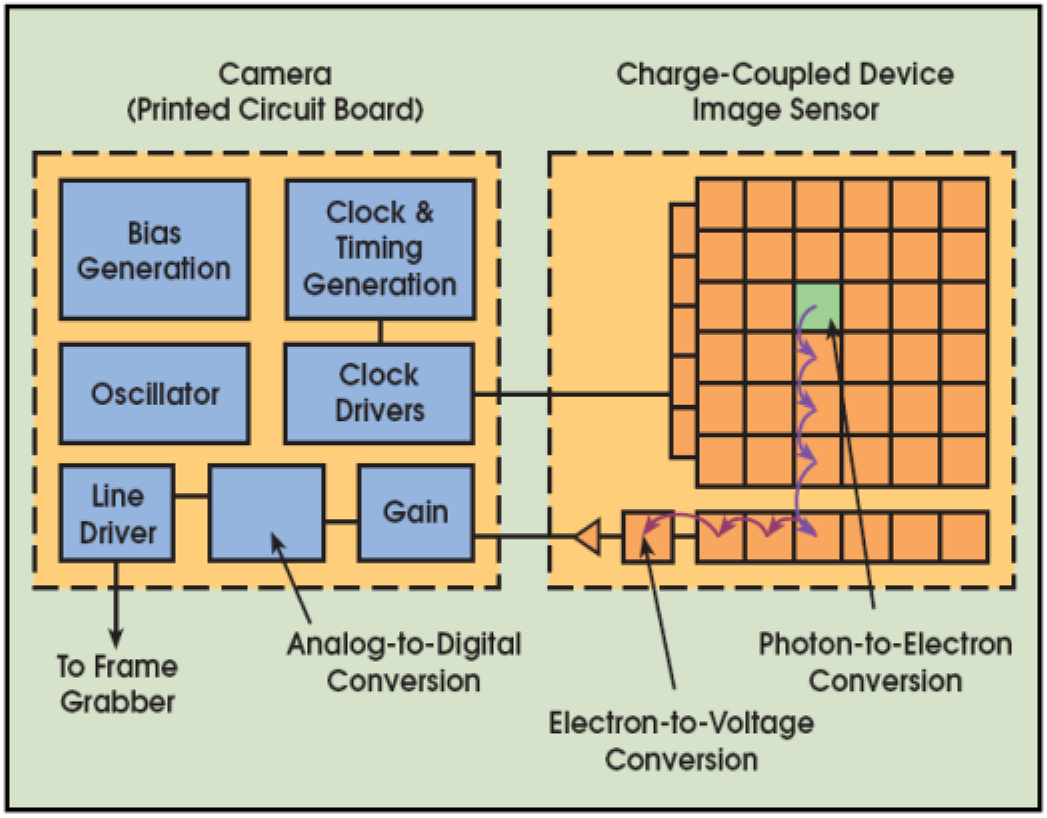

Figure 3.2: CCD sensor operation (Litwiller, 2001)

A number of dependant parameters can determine the recording set-up. Lens parameters such as focal length and aperture are significant factors controlling the image resolution, image size, and the range of the scattering pattern. The focal length of the lens is the distance between the scattered light and the location of the lens. While the aperture is, a physical constraint that limits the amount of the light that lens captures as shown in the Figure 3.3. The ratio between the focal length and the diameter of the aperture is known as the f-number. Another important parameter is the depth of field, which is the distance between nearest and outmost points of focused field that ensures the image remains in. It is a significant to have most of seeding particles remaining in focus. This can be attaining when the laser sheet thickness is smaller than focal depth, so a depth of field should be selected practically somewhat larger than the laser sheet thickness (Adrian and Westerweel, 2011). The depth of field, ΔZ, is defined by Equation 3.3 where M is the magnification factor, f# is the lens f-number and λ is the wavelength (μm):

$$\Delta Z = 4(1+M^{-1})^2 f\#^2 \lambda \tag{3.3}$$

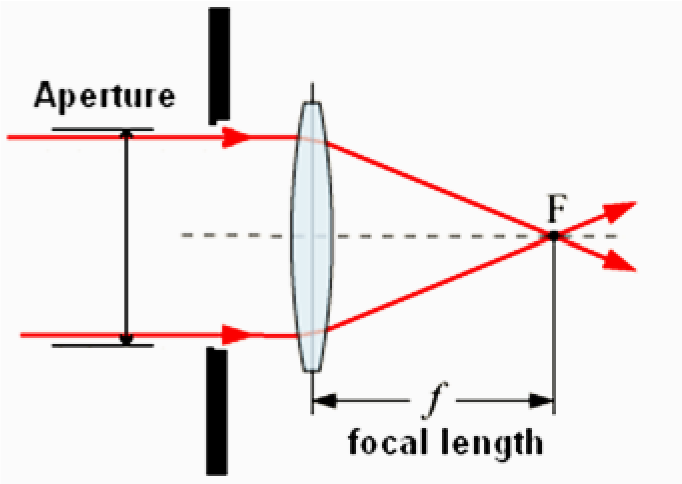

Figure 3.3: Camera focal length and aperture

The influence of f-number is obvious on the depth of the field and the amount of light passing through the lens. When the f-number is reduced, it allows much light to pass through the lens. However, the depth of the field will be reduced as shown in Figure 3.4.

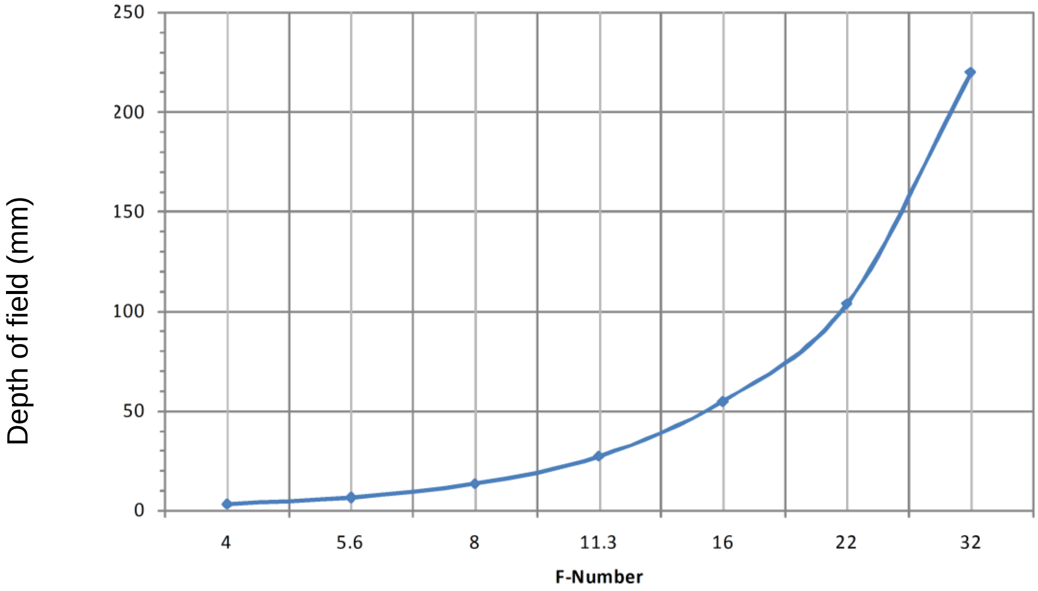

Figure 3.4: The effect of f-number on the depth of field (Image to chip magnification: 10:1, 532 nm light) (Stansfield, 2008)

The particle image diameter, d_{PID}, is another important parameter in recording process and is defined in Equation 3.4 where d_{diff} is diffraction limited image diameter (μm) and is calculated from Equation 3.5. A strong bias to the integer values so-called "Peaking-locking" that occurs when particle image diameter is smaller than one pixel. Such phenomena is related to the size of the tracer particles, the sub-pixel peak fitting algorithms, insufficient resolution to describe the particle image and image interpolation algorithms (Astarita and Cardone, 2005). Westerweel *et al.* (1997) has revealed that when the particle image diameter is equal or greater than two pixels, allows the Gaussian curve fitting used in the correlation process to be accurately locate the centre of the particle and eliminates the peak locking effect as can be seen in Figure 3.5. Westerweel *et al.* (1997) also found that where Gaussian fitting schemes are employed, the optimum particle image diameter is two pixels. Finally, even though the given equations can be utilized to estimate the optimum set-up, the hands-on trial and error was an essential to optimise the configuration.

$$d_{PID} = (M^2 d_p^2 + d_{diff})^{1/2} \qquad (3.4)$$

$$d_{diff} = 2.44\,(1+M)\,f\#\,\lambda \qquad (3.5)$$

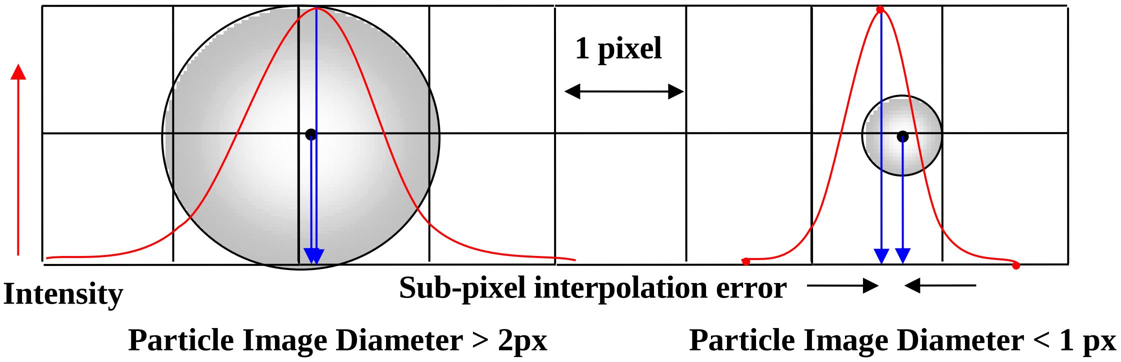

Figure 3.5: The 'Peak locking' effect

With the illumination and image system correctly aligned and the flow uniformly seeded, the significant operating parameter is the selection of the inter-frame time. The inter-frame time, Δt, is the period between the first and second illuminations of the scattered flow and defines the distance moved by the seeding particles. The inter-frame time along with the laser and camera timing is controlled and set by the user using a Programmable Timing Unit (PTU) that is integrated with the DaVis software. The optimum inter-frame time is deduced with take in consideration both the interrogation area size and an estimate of the flow velocity. Keane and Adrian (1990; 1991; 1992) found that the inter-frame time should allow for a displacement of seeding particle around one-quarter of the interrogation area size.

3.3: Processing

The processing and calculation of the vector field from the raw images can be approached by using DaVis software (DaVis. 7.2 Manual, 2011) as pre- and post-processing techniques. It is generally advised that it is an essential to improve the raw images by providing optimum PIV hardware set-up rather than conducting unjustified pre- or post-processes for the raw images and vector validations. In the beginning, camera calibration process should be performed via DaVis 7.2 software which is necessary for identify the size of field of view and in order to correct the image distortion that is caused by the cylinder liner. A flat calibration plate with appropriate marks size (crosses), that is covered the complete field of view, is used as shown in Figure 3.6. The calibration plate was located at the centre of the cylinder perpendicular to the camera and parallel to the laser sheet. Several image correction processing steps might be applied in order to improve the raw image and prepare it for vector calculations.

Figure 3.6: Calibration plate

The first step of image processing is to subtract a background image. The main purpose of subtracting the background image is to eliminate intensity fluctuations in the background that were caused by reflections and then to increase the signal to noise ratio during the correlation process. Chan (2000) and Westerweel (2000b) stated that where unavoidable background reflections appeared; subtracting the background image can be beneficial pre-processing tool that results in an increase in signal to noise ratio and henceforth data quality. DaVis software (DaVis. 7.2 Manual, 2011) offers different techniques for subtracting background image. The first technique is only subtracting the reference image from source images. However, reference image subtraction would not account for the problematic accumulating on the liner. Thus, the second technique can be alternatively applied so called subtracting sliding minimum, average or maximum over number of source images. These specify a number of images, typically 3-5 images, from the start of the dataset, and calculated either the minimum, average or the maximum intensity at each pixel location and then this produces a new image that was then subtracted from the middle image of the specified images. The process continued for all images of the datasets. An example of such techniques is a dynamic background subtracting as shown in Figure 3.7.

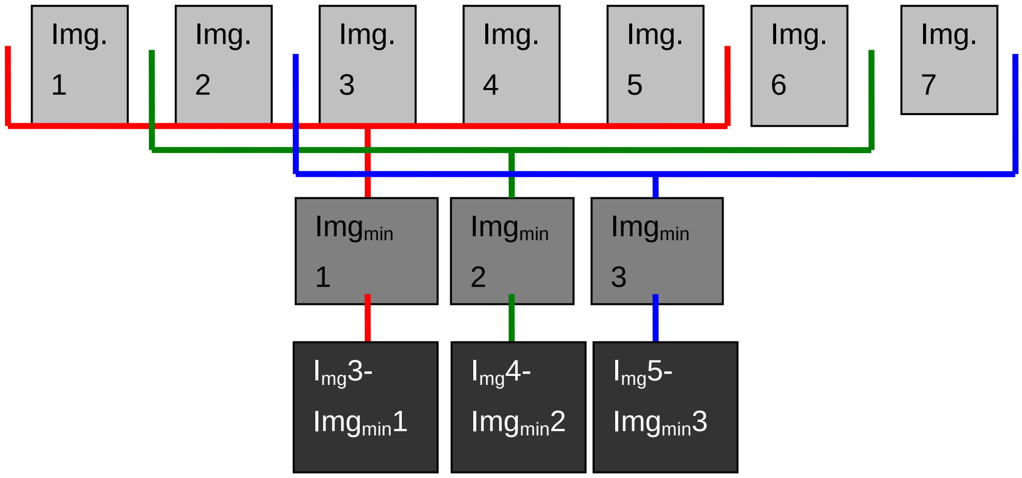

Figure 3.7: Dynamic background subtraction

Further image corrections for yielding accurate results can be applied, for instance, applying masks to eliminate regions of the image that are unnecessary for processing that can reduce computational time. Moreover, image correction process such as particle intensity normalization can be applied in order to improve the particle image quality for the correlation process. This increases contrast between seeding particles and background image that allows DaVis softwar to identify easily particles in images. The de-warping and rectangle extracting correction processes can also be applied to modify image based on calibration image (i.e. remove the lens effect) and allows only the cylinder area to be extracted respectively.

3.3.1: Vector Calculation and Analysis

In the vector calculation process, it is required to determine the data range and the correlation mode. There are two ways of the evaluation of the images; one is auto-correlation that based on single frame/ double exposure technique. The second is across-correlation algorithm that is widely used for the images evaluation to determine the particle displacement within each interrogation area. The cross-correlation relays on double frame/double exposure technique and it has higher and unambiguous correlation peak compared to the auto-correlation function. Recorded image is divided in so-called interrogation areas that must be square and its dimensions has an integer power of two, i.e. 16x16, 32x32, 64x64 or 128x128 pixels etc. due to the Fast Fourier Transform (FFT) used in the correlation. Each interrogation area is evaluated by cross correlation function and thus the evaluation yields one velocity vector for each interrogation window. The multi-pass filter with decreasing window size is available to allow for using a much smaller final interrogation window size to improve the spatial resolution of the vector field and produces less erroneous vectors.

The cross-correlation based on the alignment of interrogation area from the second image with the corresponding area from the first image as shown in Figure 3.8. When the image shift is matching to the particle displacement between images, the greatest overlap is detected as seen in Figure 3.8*(c)*. This produces a peak in the correlation map as in Figure 3.9. The location of the detected peak represents the distance of the moved particle within the interrogation area and therefore the required displacement of the flow. The displacement is then divided by the time step to yield one vector for that interrogation area. The process is repeated for each interrogation area to generate a completely two-dimensional flow field. In case of the image shift is not identical between images, the accidental overlap occurs and then a noise peak detected as shown in Figure 3.8*(d)*. This noise (accidental overlap) causes outlying data. The quality of the data is measured by the Q ratio. The Q ratio is the ratio of the largest peak to the largest noise peak. The vector is invalid and will be removed if the signal to noise ratio is lower than a user defined value (typically Q ratio= 1.5 - 2.0).

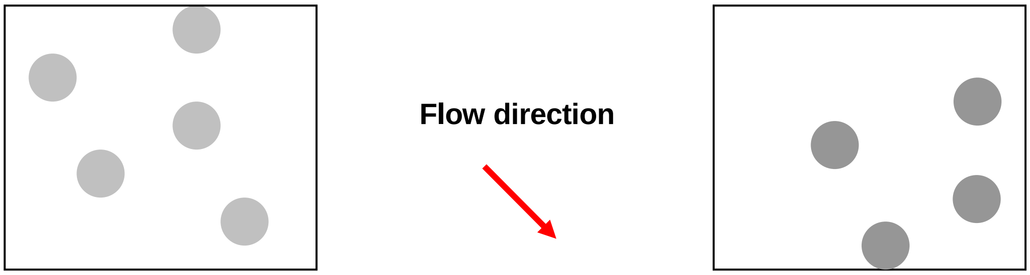

a) Interrogation Area from Image 1 *b)* Interrogation Area from Image 2

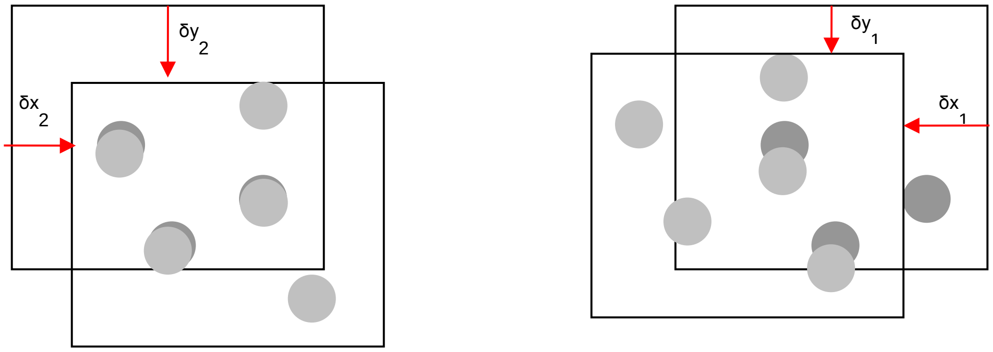

c) Image shift equal to particle shift:
High overlap: Correlation peak at (δx_2, δy_2)

d) Image shift NOT equal to particle shift:
Unexpected overlap: Noise at (δx_1, δy_1)

Figure 3.8: Cross-correlation process

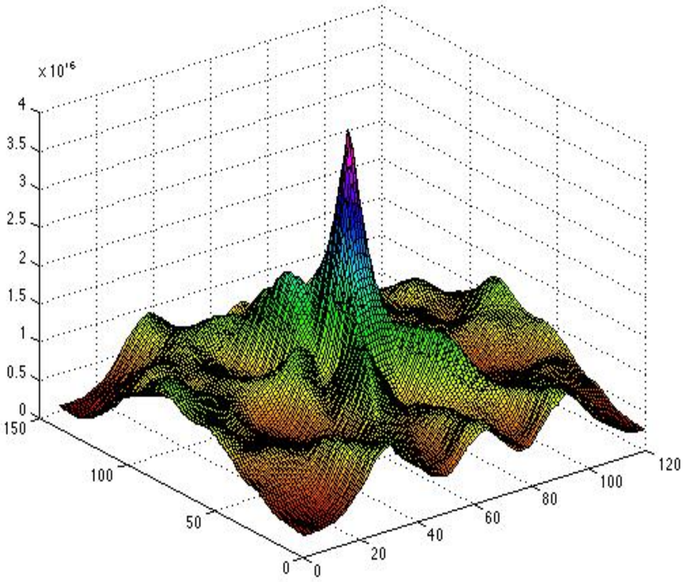

Figure 3.9: Cross correlation peak and elimination of extraneous vectors

High density of vector can be obtained by applying a multi-pass cross correlation. This consists of an iteration loop of initial filter pass with large interrogation area size in order to produce a coarse vector, and then a further filter passes with a smaller interrogation area size. This helps to achieve a high-resolution vector field. Hollis (2004) applied an initial cell size of 64x64, and a high-resolution cell size of 32x32. He found that the multi-pass technique would commonly yield data of a higher quality (Hollis, 2004). Another way of enhancing the vector density is an overlap the interrogation areas. Overlapping the interrogation areas is given by a percentage value, for example, 50% overlapping means increasing the vector density by factor of four.

Once the vector field is calculated in the pre-processing stage, vector validation algorithms can be applied to eliminate false vectors in a post-processing stage. Firstly, a median filter can be applied to compute a median vector from the neighbouring vectors. It is based on comparing the middle vector with the median vector deviation of the neighbouring vectors. The centre vector is rejected when it is outside the allowed range of the average vector deviation of the neighbour vectors. Westerweel (2000b) suggested that the best check of vector validity is to compare it with the neighbour vectors. If a vector deviates from its neighbours, there is a high possibility that the vector is spurious due to failure to meet flow continuity principle. An additional vector post-processing step can be used by applying allowable vector range to restrict the filtered vectors to a specified velocity range. This requires previous knowledge about the measured flow. Figure 3.10 shows the influence of applying the image correction process for instance subtracting sliding background, the multi-pass filter and vector validation algorithm on the vector field calculation in case of the vertical plane image.

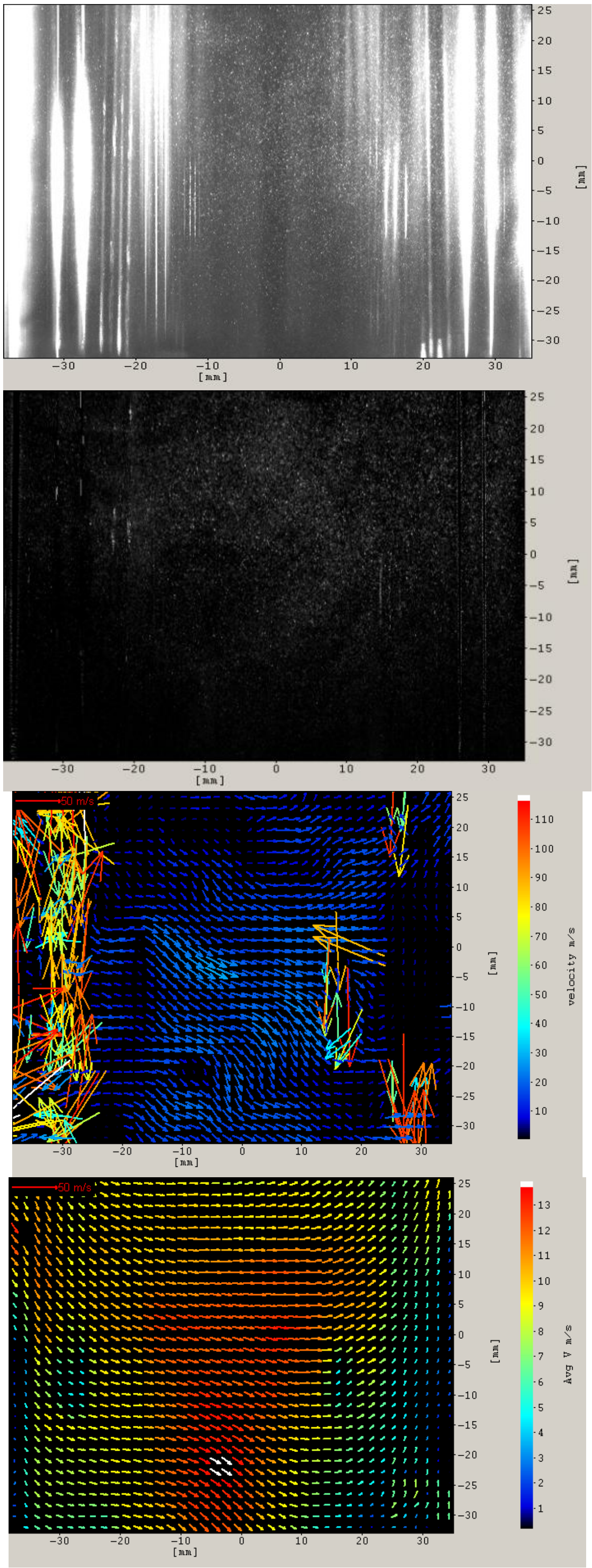

Raw image
1280 by 1024 pixels

Subtract sliding background

Vector processing:
Multi-pass cross correlation
1st Pass:128 x 128pixel
2nd Pass: 64 x 64pixel

50% Overlap

Mean flow field
(50 Pair images)

Figure 3.10: PIV process

3.4: Summary

In this Chapter, the principle of Particle Image Velocimetry (PIV) technique and its application were discussed. Clearly, this measurement technique is capable of providing detailed information of the in-cylinder flow structures. Nevertheless, its application to gain reliable results is not straightforward, in particular not for complex flow cases. There are many parameters relevant to the PIV measurements technique, which are available to adjust and optimise. It is required that the physical test rig set-up and flow field of interest are accurately identified prior to the PIV acquisition considerations which includes providing sufficient optical access and adding of the most suitable seeding to the flow. Beside to accurately setting up the actual flow conditions of interest, the PIV hardware must also be accurately set up. The light sheet illuminating the flow must be correctly aligned at the field of view (FOV) and the thickness of the sheet should be optimised for the experiment that is usually selected to be as small as possible. The camera should be positioned and calibrated. A number of dependant parameters can determine the recording set-up. Lens parameters such as focal length and aperture are significant factors controlling the image resolution, image size, and the range of the scattering pattern. Another significant parameter that must be optimised is the inter-frame time settings. The optimum inter-frame time is deduced with take in consideration both the interrogation area size and an estimate of the flow velocity. The application of this technique to steady flow rig is described and discussed in Chapters 4 and 6 respectively.

Chapter 4

Experimental Set-Up and Instrumentation

4.1: Experimental Apparatus and Set up

This section describes and discusses the experimental set-up used in this work for the investigations of the in-cylinder flow structures under steady state conditions utilizing Particle Image Velocimetry (PIV) and swirl meters. A rapid prototyped cylinder head is used, which is a replica of an engine head of a pent-roof type (Lotus). The steady air flow rig (SuperFlow- SF660E) is used to measure the air flow and quantify in-cylinder air motion at steady flow conditions. Two different methods are applied to quantify the swirl ratio. Firstly, the paddle swirl meter is used to record angular velocity of intake flow of the rapid prototyped cylinder head at a target distance about half a bore of the cylinder liner (B/2=44mm) from the cylinder head. Secondly, a torque swirl meter is used to record the swirl generated torque and then swirl ratios is calculated at the same horizontal plane. The PIV measurements set up for both the horizontal and vertical planes are presented and described in the following sections.

The experiments were conducted for a number of fixed valve lifts and different inlet valve configurations at two pressure drops, 250mm and 635mm of H_2O that correlate with engine speeds of 2500 and 4000 RPM, respectively. From the two-dimensional in-cylinder flow measurements, a tumble flow analysis is carried out for six planes parallel to the cylinder axis. In addition, a swirl flow analysis is carried out for one horizontal plane perpendicular to the cylinder axis at half bore downstream from the cylinder head (44mm).

The following Sections present detail description of rapid prototype cylinder head, airflow test rig, swirl motion meters, PIV system, PIV horizontal plane measurements set-up and PIV vertical plane measurements set-up.

4.1.1: Rapid Prototype Cylinder Head

In the current investigation, a rapid prototyped of the pent-roof LOTUS engine head is used. Both the exhaust valves and the injector hole of the rapid prototyped cylinder head are blocked as shown in Figure 4.1*(a)*. For the horizontal plane measurements, an additional hole in the top of the rapid prototyped cylinder head is bored to allow for the endoscopic access. The valve holder opening mechanism has two adjustable wheels that allow 1mm displacement of the valve for each revolution as illustrated in Figure 4.1*(b)*.

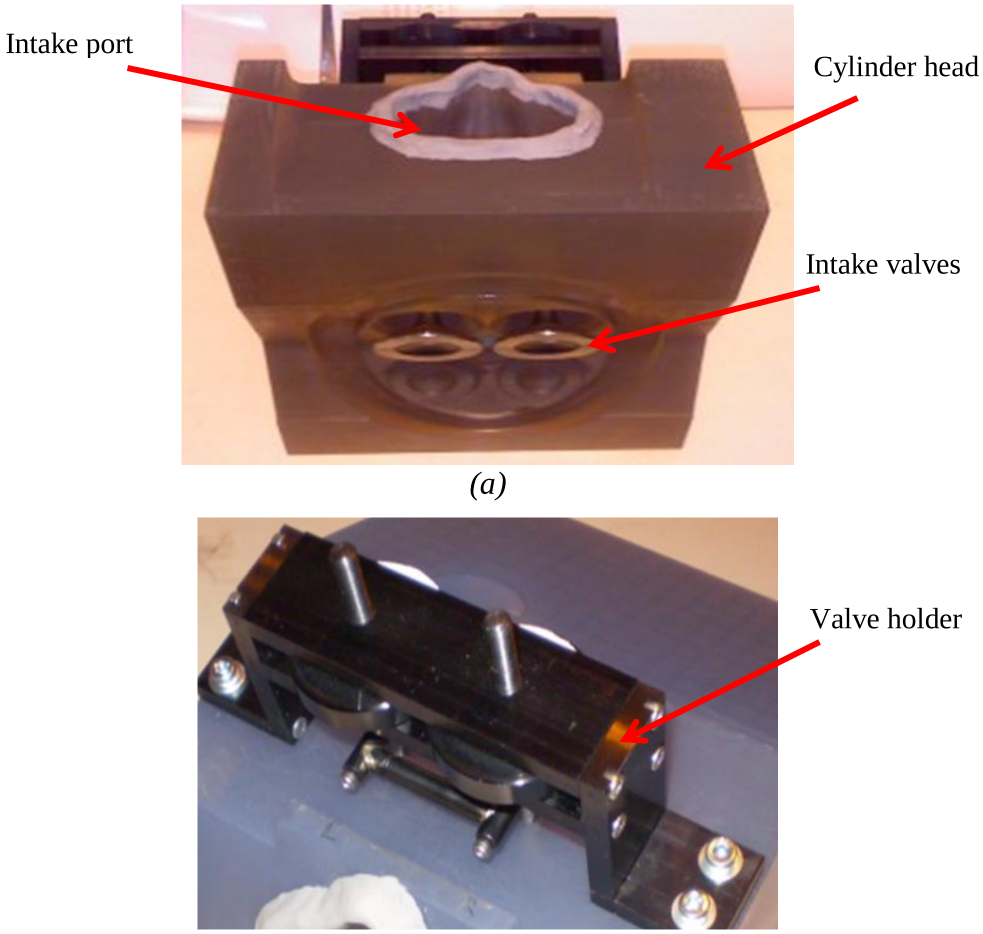

(a)

(b)

Figure 4.1: *(a)* Rapid prototyped cylinder head and *(b)* Valve holder

Two sets of 2-D PIV measurements in the vertical planes are attempted. In the first measurement set, the transparent cylinder is made of fused silica with a bore of 88mm, a wall thickness of 15mm and a length of 82.1mm while in the second measurement set, an acrylic plastic cylinder of the same bore and length but with a wall thickness of 6mm is used. The way of seeding particles is also changed, in the first measurement set up, seeding particles are generated by means of a pressure atomiser jet (Model 9306 Six-Jet ;TSI) and were fed into the cylinder through the intake port. Olive oil is used as the liquid to produce the seeding particles with a diameter of approximately 1µm. In the second PIV measurement set up, SciTech pressure atomiser is used to generate a fine cloud and high density of oil droplets particles with a diameter of approximately 0.5 µm. These changes in cylinder are implemented in an attempt to reduce optical flare from the cylinder and to measure RMS velocity.

The 2-D PIV measurements are conducted to visualise and analyse the flow characteristics for a horizontal plane at the half bore location (44mm) downstream from the cylinder head and for six vertical planes (0^o, 30^o, 60^o, 90^o, 120^o and 150^o) as illustrated in Figure 4.2. The measurements were taken for two pressure drops, 250mm and 635mm of H_2O that correlate with engine speeds of 2500 and 4000 RPM, respectively. and for number of valve lifts (2mm, 5mm, 8mm and 10mm) for three intake valve configurations; *(a)* both inlet valves are opened, *(b)* right inlet valve only is opened and *(c)* left inlet valve only is opened. In the following Sections, the detailed experimental measurements set up for both horizontal and vertical planes are presented. The PIV measuring area is set as rectangular shape with 58.5mm x 74mm in the vertical plane and 84mm x 76mm for the horizontal plane.

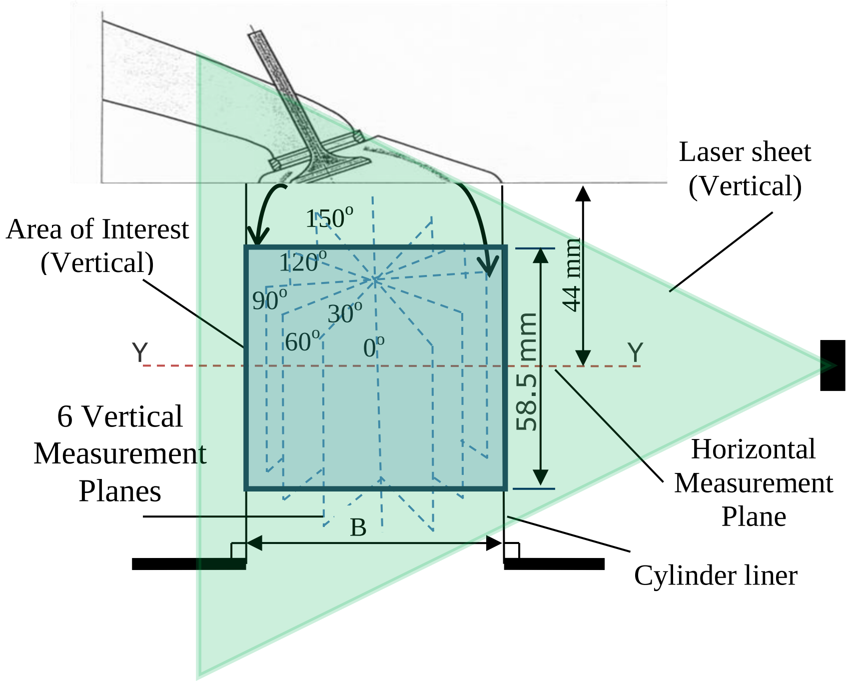

(a)

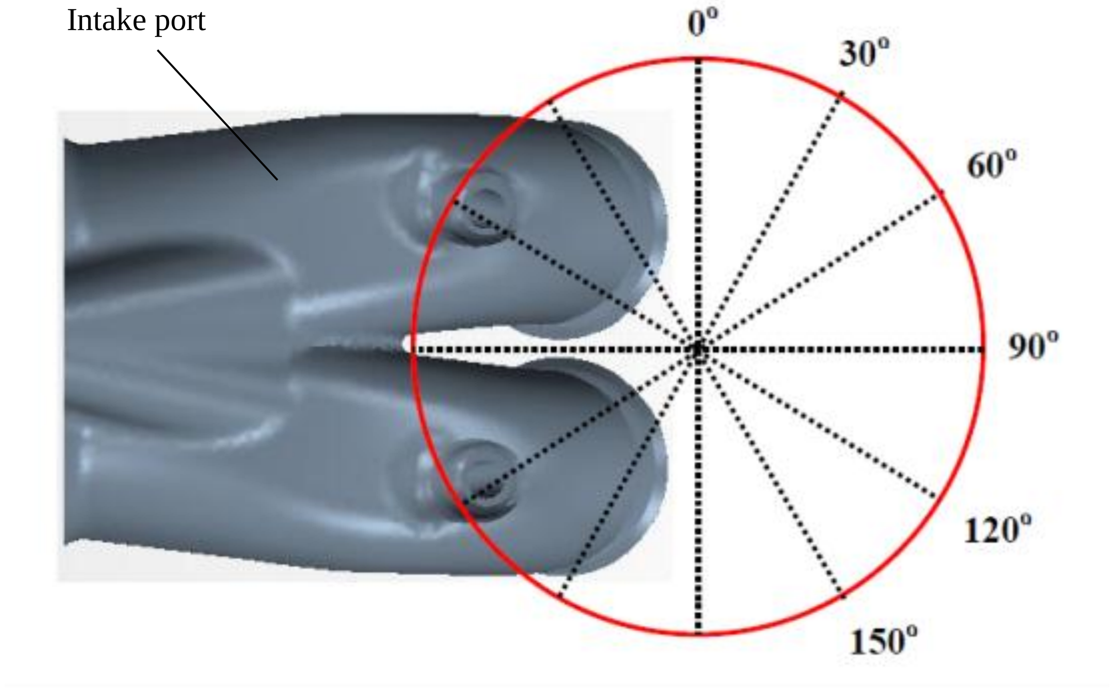

(b)

Figure 4.2: PIV measuring planes through glass liner *(a)* Side view and *(b)* Top view section Y-Y

4.1.2: Airflow Test Rig

The airflow test rig is used to pull air from the bottom of the cylinder at the required pressure drop across the valves. In the current investigation, the airflow test rig is a SuperFlow SF600E, as shown in Figure 4.3. This is primarily used in automotive applications to measure volumetric flow rate related to the inlet and exhaust ports of the engine against pressure drop. It contains six vacuum pumps and orifice plates of varying size with a throttle for the vacuum pumps to set the pressure drop across the valves. The throttle is adjusted so that a constant pressure drop is observed for all valve lifts (2 on Figure 4.3).

The airflow rig is a calibrated system for volumetric flow rate measurement and must therefore be checked before each series of measurements. A calibration plate allows the system to be checked for a known low flow and high flow rate. The calibration data plat as shown in Figure 3.4 presents the flow scale values for the six flow ranges used for both the intake and exhaust modes. The volumetric flow rate through the test object is measured on an inclined manometer (3 on Figure 4.3) as a percentage of the total for the orifice being used. Both barometric pressure and ambient temperature are recorded with each measurement, allowing the volume flow rate to be converted to a mass flow rate, which for conventional use would be used to obtain the discharge and flow coefficients for the cylinder head. There are many other applications for the air flow bench, when associated with the proper instrumentation, for instance swirl, tumble and combined air motion measurements, either with an intrusive device placed in the cylinder such as swirl meter and impulse swirl meter or with laser based diagnostics such as Laser Doppler Anemometry (LDA) and Particular Image Velocimetry (PIV).

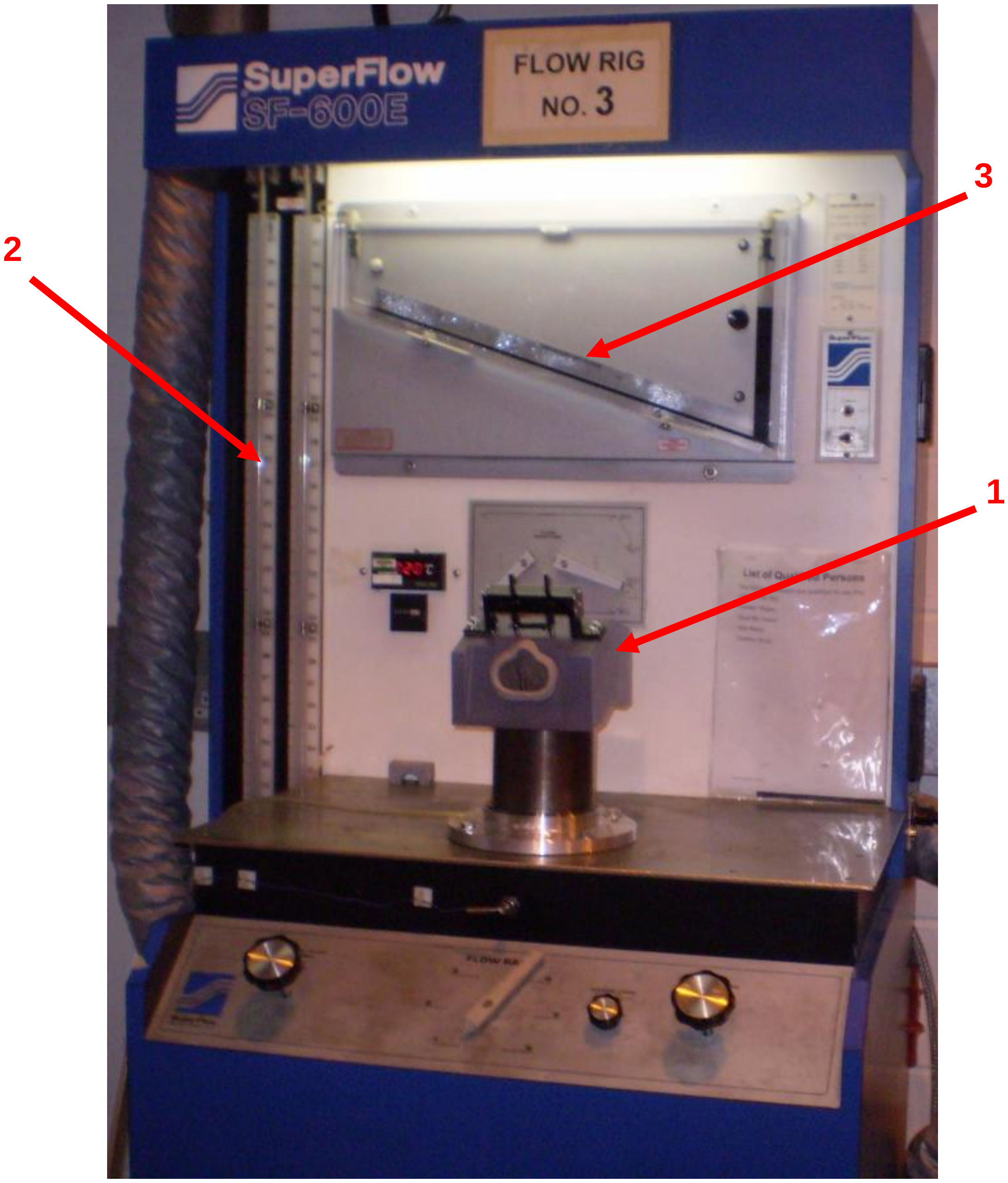

Figure 4.3: SuperFlow SF600E. 1-Cylinder head being tested, 2-Pressure manometer, 3-Percentage flow manometer

An airtight attachment between the flow bench and the test object is essential. In the current case, the adapter is fabricated as shown in Figure 4.5. There are four holes to allow for pressure drop measurements. Furthermore, to obtain accurate volumetric flow rate (CFM) readings, the sharp edge of the cylinder head port should be radius with plasticine to ensure there is no turbulence at the port entrance as seen in Figure 4.6. Once the test object is mounted on the bench, the appropriate flow direction should be selected either a sucked or blown modes. The appropriate flow range can be set for a particular test.

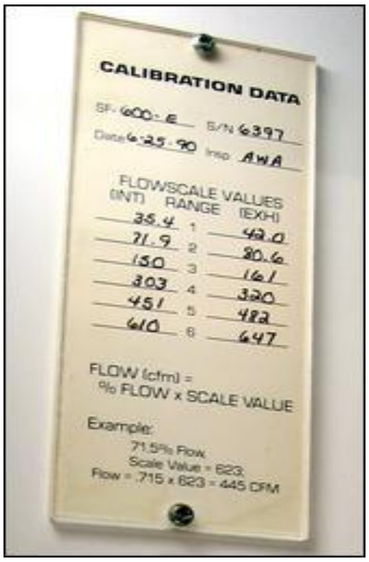

CALIBRATION DATA

SF- 600-E S/N 6397

Date 6-25-90 Insp. AWA

FLOWSCALE VALUES

(INT)	RANGE	(EXH)
35.4	1	42.0
71.9	2	80.6
150	3	161
303	4	320
451	5	482
610	6	647

FLOW (cfm) =
% FLOW x SCALE VALUE

Example:
71.5% Flow
Scale Value = 623
Flow = .715 x 623 = 445 CFM

Figure 4.4: Calibration data plate

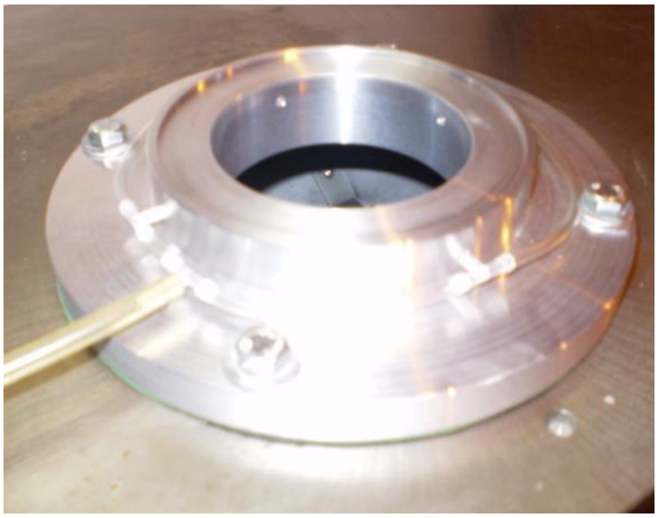

Figure 4.5: Adapter part with the holes for presser drop measurement

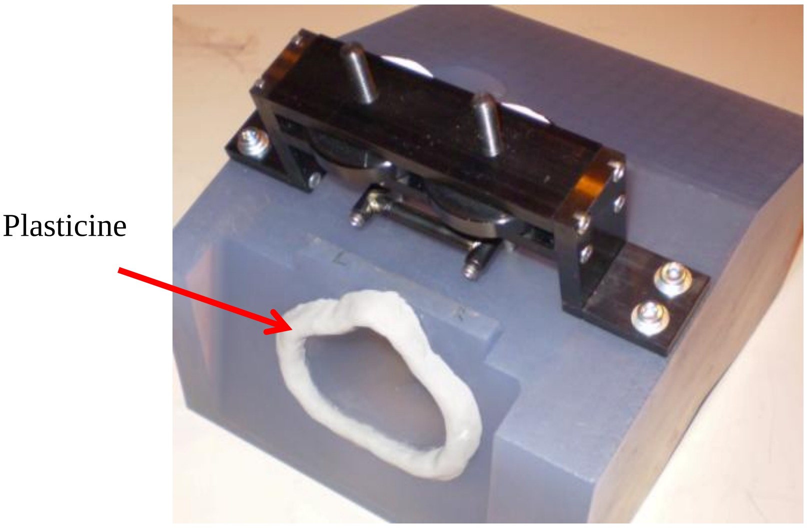

Figure 4.6: A plasticine around the port edge

4.1.3: Swirl Motion Meters

In the current investigation, two different intrusive methods associated with the airflow test rig are used to obtain the swirl measurements of the intake port of the rapid prototyped cylinder head. The first method is utilising the paddle swirl meter to measure the angular velocity of the flow as illustrated in Figure 4.7. The second method employs the impulse torque swirl meter to measure the torque generated by the flow straightened out by a honeycomb element as shown in Figure 4.8.

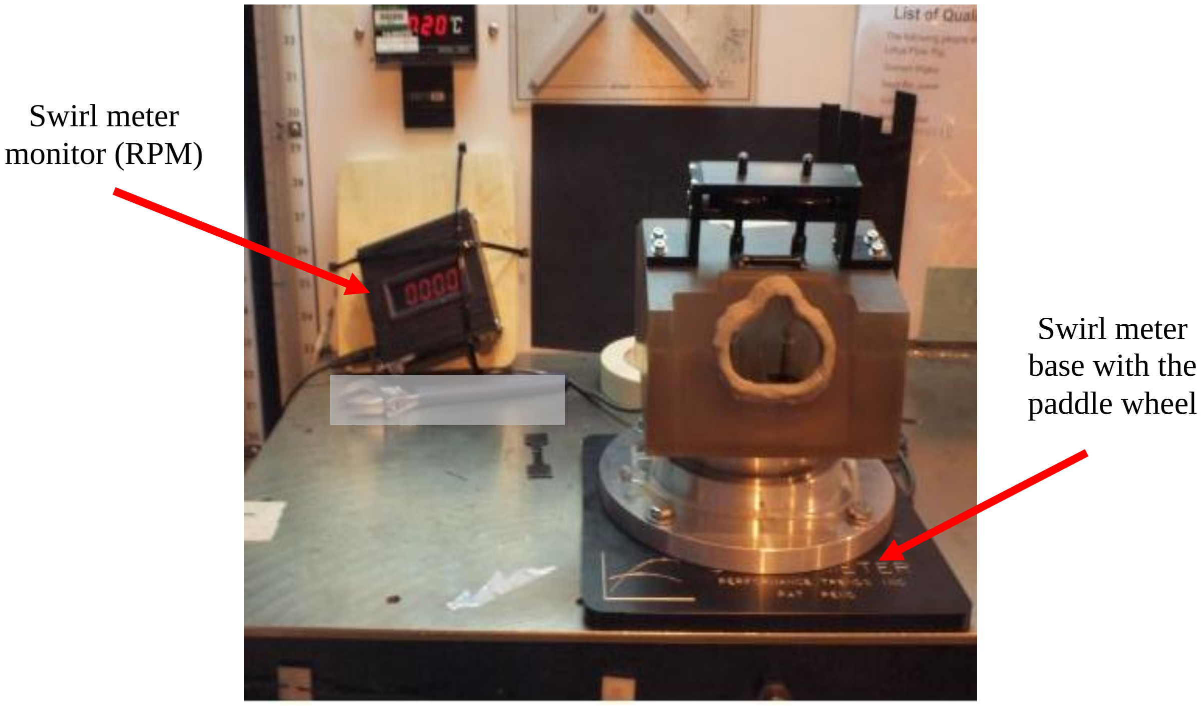

Figure 4.7: Swirl meter measurement

Figure 4.8: Torque meter measurement

4.1.4: PIV System

The PIV system consisted of double pulsed Nd:YAG laser, a high-resolution CCD camera, particles seeder and a PIV processing software (LaVision's DaVis 7.2 software). Table 4.1 shows the apparatuses of PIV system used in the current investigation.

Table 4.1: Apparatuses of PIV system

Laser source	Nd : YAG (New Wave SOLO 120 XT)
CCD Camera (pixel)	1280px X 1024px (Flowmaster 3S)
Atomiser (first set-up)	Atomiser jet-Model 9306 Six-Jet; TSI
Atomiser (second set-up)	SciTech pressure atomiser
PIV software	Davis 7.2 software

Light source

A frequency doubled, pulsed Nd: YAG laser (New Wave Research: Model SOLO 120 XT) is used as a source of illumination in the current investigation. The laser supplies double pulses of 532nm wavelength with energies up to 120mJ per pulse. The time separation between pulses is set to 10µs for the flows measured here. The laser beams are formed into a planar laser sheet of 1mm thickness using a cylindrical lens with a focal length of -20mm.

The laser beams are aligned for the horizontal plane at the targeted depth from the cylinder head (B/2=44mm) by using marked plate as shown in Figure 4.9. Whereas, the laser beam for the vertical plane are aligned at the centre of the cylinder liner by using the special tool that allows for the light sheet to pass through at the targeted plane as shown in Figure 4.10. The alteration in orientation between the horizontal and vertical planes was made by rotating the lens through 90^o.

Figure 4.9: A plate was used for horizontal plane alignment

Figure 4.10: Tools was used for vertical alignment

Camera

A high-resolution Charged-Couple Device (CCD) camera (LaVision: Flowmaster 3S), that records images on a double frame is utilised at a working distance of 50cm for vertical planes and 7.4cm for horizontal plane. The camera has an image spatial resolution of 1280 X 1024 pixels and the acquisition frequency is 4 Hz. The camera is fitted with a Nikon 60mm, F/2.8 lens for the vertical planes. While it is fitted with a Nikon 28mm, F/2.8 lens with the endoscope for the horizontal plane. The PIV measuring area for the horizontal plane is 84mm x 75.5mm and for the vertical plane is 73.5mm x 58.5mm. The influence of background light from the surface reflection is eliminated by painting most of the surrounding parts with a black. The significant parameters of the camera are calculated in Table 4.2. In the horizontal plane measurements, the camera is mounted on the made structure that is fixed on the airflow test rig base at a position perpendicular to the laser sheet. While in the vertical planes case, the camera is positioned on the traverse at the same level of the PIV laser source at a position perpendicular to the laser beam sheet as shown in Figures 4.18 and 4.19, respectively.

Table 4.2: Calculated parameters for recording set-up for both vertical and horizontal experimental set-up

Pixels on chip	1280px X 1024px
Pixel size	6.70 µm X 6.70 µm
CDD Array size	8.6 mm X 6.9 mm
Imaged Area Size	Vertical (58.5mm X 73.5mm) Horizontal (84mm X 75.5mm)
Lens	Vertical (Nikon 60mm, F#2.8) Horizontal(Nikon 28mm, F#2.8)
Focal length	Vertical (50cm) Horizontal (7.4cm)
Depth of field	Vertical (1.698mm) Horizontal (2.447mm)
Magnification factor	Vertical (0.11) Horizontal (0.09)
Double frame per second	4
Acquisition frequency	4 Hz
Depth of filed	Vertical (1.6mm) Horizontal (2.4mm)

Seeding particles

Uniformity and the density of particle distribution are significant factors in order to obtain optimal PIV raw image which leads to better estimates of the velocity field. In addition, the tracer particle size is a trade-off; a small particle size is desirable in order to improve the flow tracking while a large particle size is desirable in order to improve the light scattering intensity. Thus, a compromise between the tracer particle sizes is required to tackle this situation.

Seeding particles are generated by means of a pressure atomiser jet (Model 9306 Six-Jet ;TSI) and were fed into the cylinder through the intake port. Olive oil is used as the liquid to produce the seeding particles with a diameter of approximately 1µm. In the RMS velocity measurement, SciTech pressure atomiser is used to generate a fine cloud and high density of oil droplets particles with a diameter of approximately 0.5 µm. The seeding atomiser is supplied through a distributor, which is made of a honeycomb structure box as shown in Figure 4.11, in order to generate uniform oil droplets. Seeding density and drop size are controlled by adjusting the supply pressure of air to the atomiser, which is set to be 2bar.

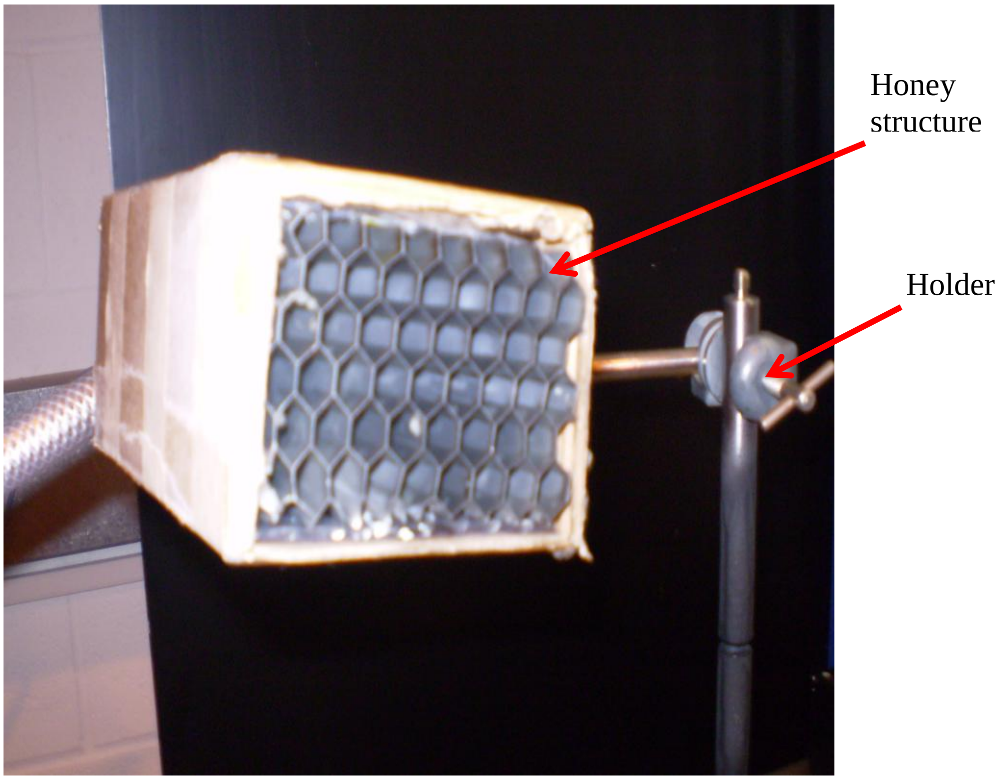

Figure 4.11: Honey structure box distributor

The PIV software

In this study, LaVision's DaVis 7.2 software is used for data collection and control of the laser and camera system. In the current investigation, originally 50 image pairs were taken for mean velocity measurement. However, as the RMS velocity measurement was later required, this was increased to 1200 image pairs. In the beginning, calibration of the camera process via DaVis 7.2 software was performed in order to correct the image distortion that is caused by the cylinder liner in the vertical plane measurement. In the vertical plane measurements, a flat calibration plate with appropriate size, that covers the complete field of view, is used. The calibration plate is located at the centre of the cylinder perpendicular to the camera and parallel to the laser sheet as shown in Figure 4.12. It was ensured that the image was focused and the reference point (0, 0) of the x-y scaling is specified and marked at the cylinder centre. In the horizontal plane measurement, the flat calibration plate is positioned at the targeted plane around 44mm distance from the cylinder head as shown in Figure 4.13.

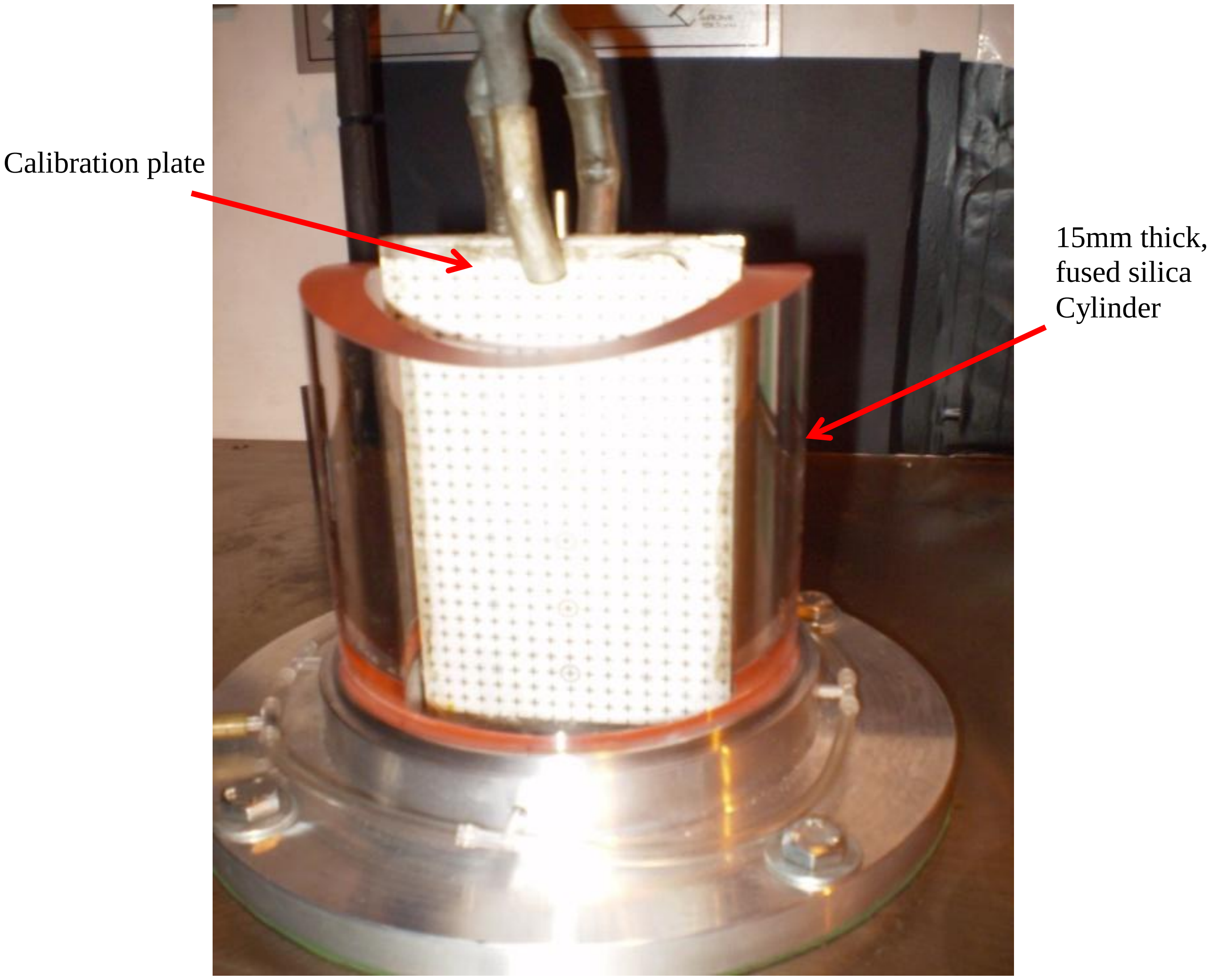

Figure 4.12: Location of flat calibration plate for vertical plane measurements.

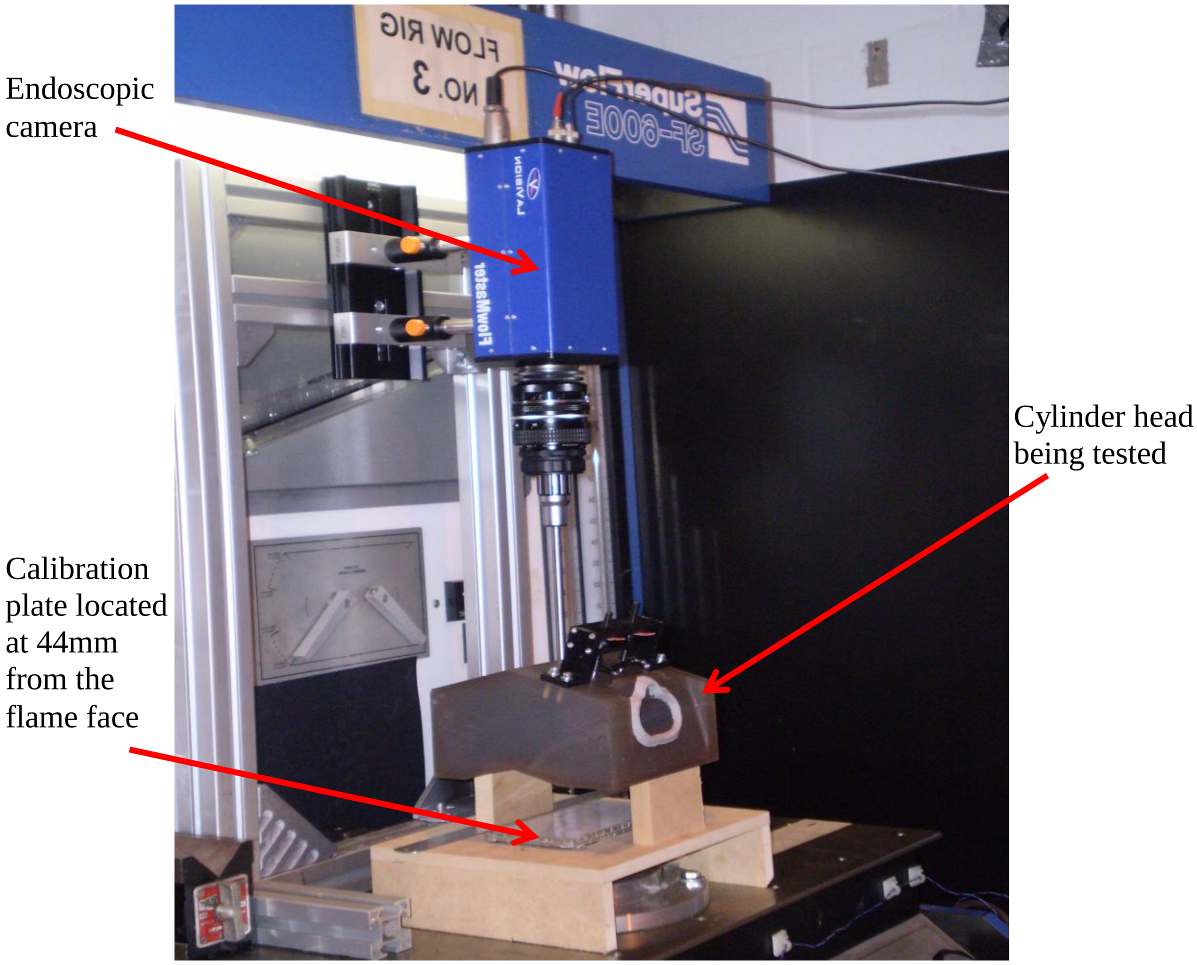

Figure 4.13: Location of flat calibration plate for horizontal plane measurements.

Several image correction-processing steps are applied in order to improve the raw image and prepare it for vector calculations. The first step was to subtract a background image that was applied in order to eliminate intensity fluctuations in the background that were caused by reflections. Figures 4.14 *(a)* and 4.14 *(b)* show a raw image and corrected image after the subtraction process for the vertical plane. Further image correction processes are conducted on the vertical plane images by activating the particle intensity normalisation with scale length (4 pixels) to improve the particle image quality by enhancing the contrast between individual particles and background noise. Figures 4.15 *(a)* and 4.15 *(b)* show a raw image and corrected image after the background subtraction for the horizontal plane. Additional image correction processes are conducted on the horizontal plane images. Figure 4.16

illustrates de-warp correction process that are applied for the horizontal image to correct for aberrations generated by the endoscope lens.

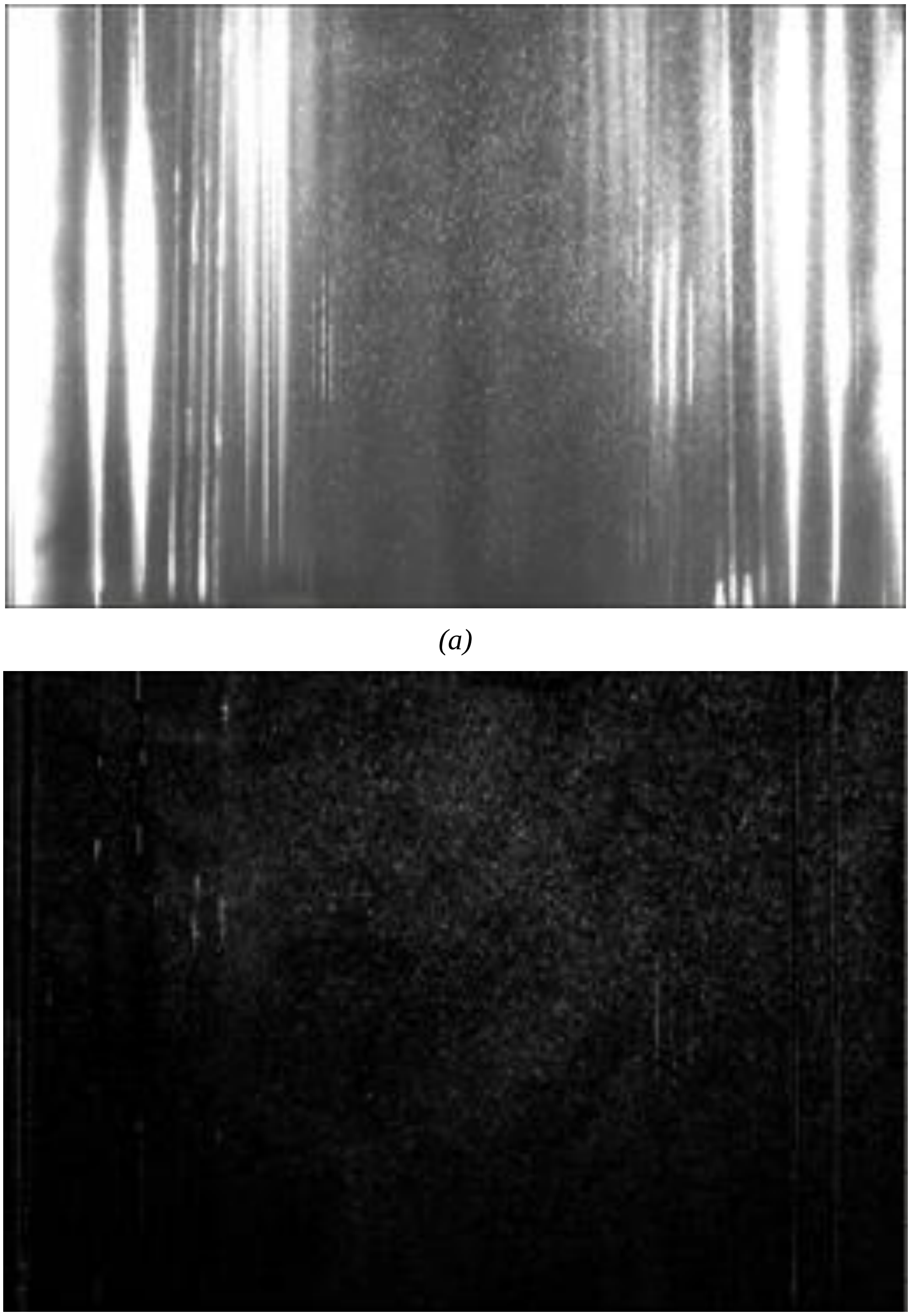

(a)

(b)

Figure 4.14: *(a)* Vertical raw image and *(b)* Corrected image after subtracting the background for the vertical plane

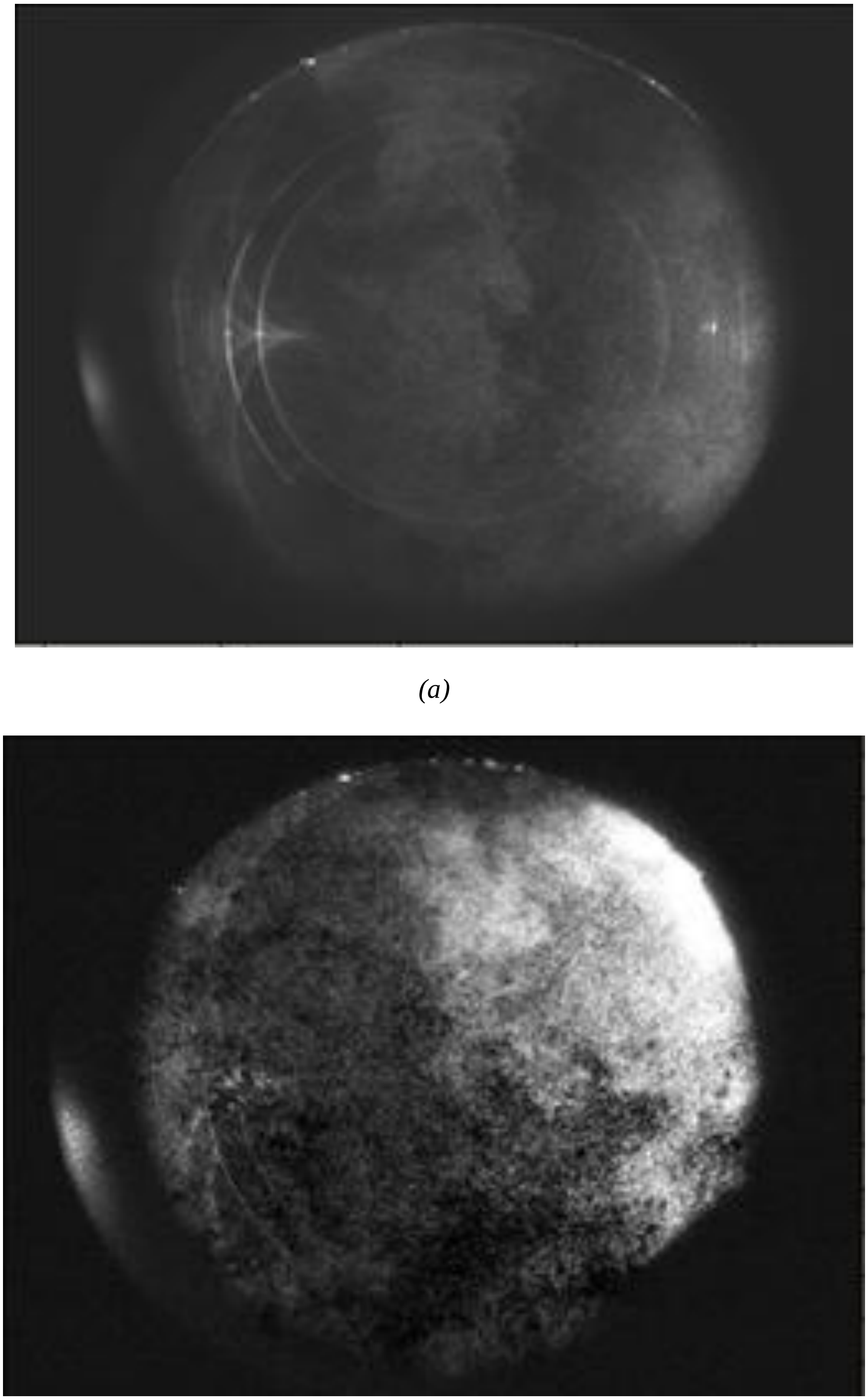

(a)

(b)

Figure 4.15: *(a)* Horizontal raw image and *(b)* Corrected image after subtracting the background for horizontal plane

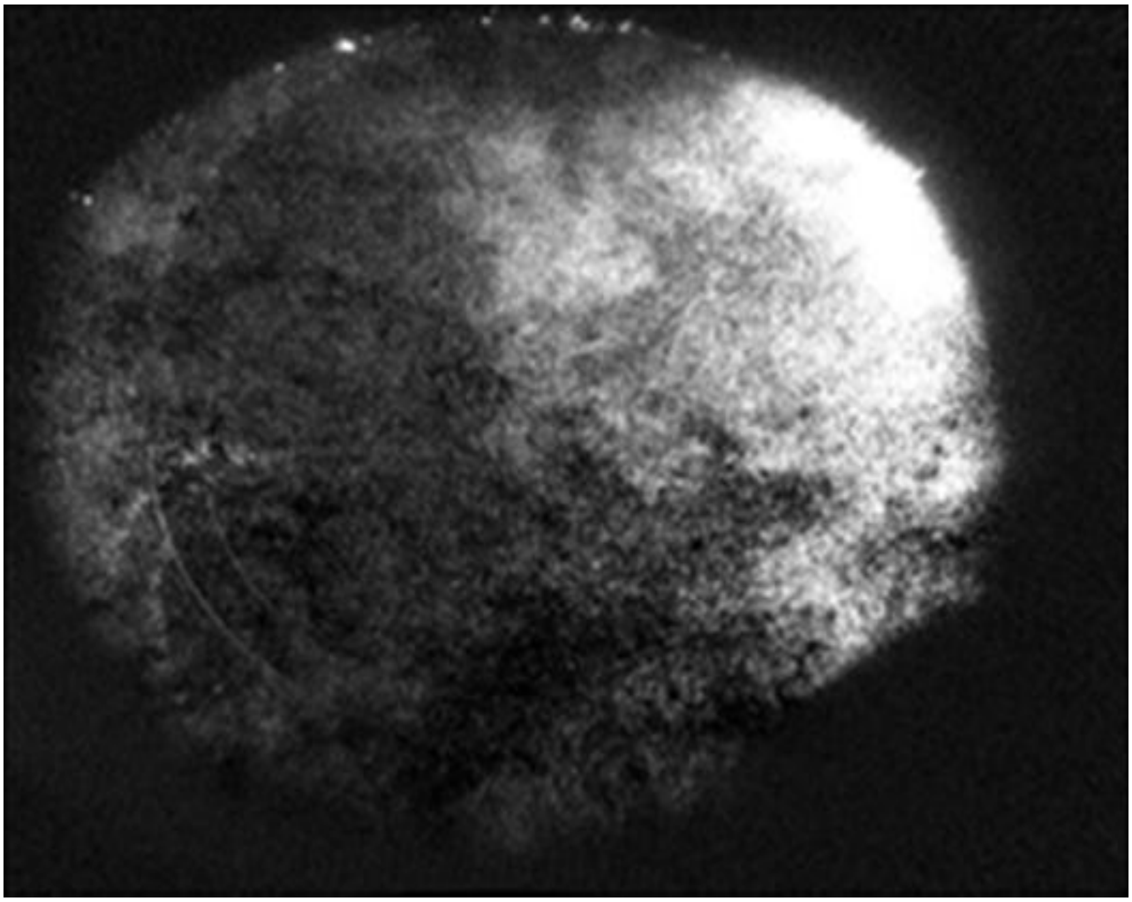

Figure 4.16: Corrected image with the de-warp and rectangle extracting correction process for the horizontal image

The data are processed by using cross correlation method with a decreasing interrogation window size in order to obtain two-dimensional vector maps. The cross correlation function relays on double frame/double exposure technique and it has higher and unambiguous correlation peak. Images are divided in so-called interrogation windows and then each interrogation is evaluated by cross correlation function and thus the evaluation will yield one velocity vector for each interrogation window.

The multi-pass filter with decreasing window size is applied to allow for using a much smaller final interrogation window size to improve the spatial resolution of the vector field and produces less erroneous vectors. An initial pass with 128x128 pixels was used with two passes, and then 64x64 pixels is used with two passes. An overlapping the interrogation windows size by 50% is applied to increase the vector density.

Vector validation algorithms are applied to eliminate false vectors in a post-processing stage. In the beginning, a median filter was applied to compute a median vector from the neighbouring vectors and compares the middle vector with the median vector ±deviation of the neighbouring vectors. The centre vector is rejected when it is outside the allowed range of the average vector deviation of the neighbour vectors as seen in Figure 4.17. An additional vector post-processing step is used by applying allowable vector range to restrict the filtered vectors to a specified velocity range (m/s).

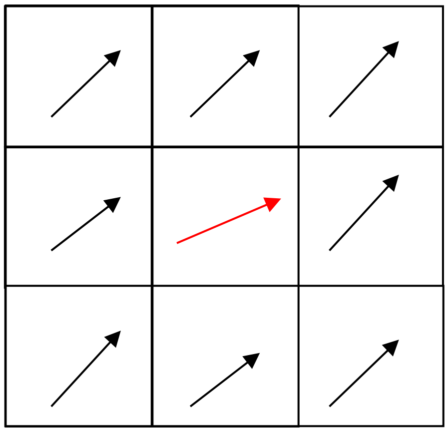

Figure 4.17: Central vector validity

4.1.5: PIV Horizontal Plane Measurements Set up

The experimental apparatus for the horizontal plane are shown in Figure 4.18. The air flow test bench (1 on Figure 4.18) is used to pull air from the bottom of the cylinder at the required pressure drop across the valves. Nd:YAG laser used as a light source (6 on Figure 4.18). The laser beam is aligned in the horizontal plane at the targeted height from the cylinder head half bore i.e. of 44mm. The camera and its endoscope (4 on Figure 4.18) are mounted above the cylinder head (8 on Figure 4.18) on a gantry at a position perpendicular to the laser sheet. A laser safety filter (11 on Figure 4.18) is used to prevent the light scattering toward the control area. The PIV measurements are conducted on a transparent cylinder made of fused silica (7 on Figure 4.18).

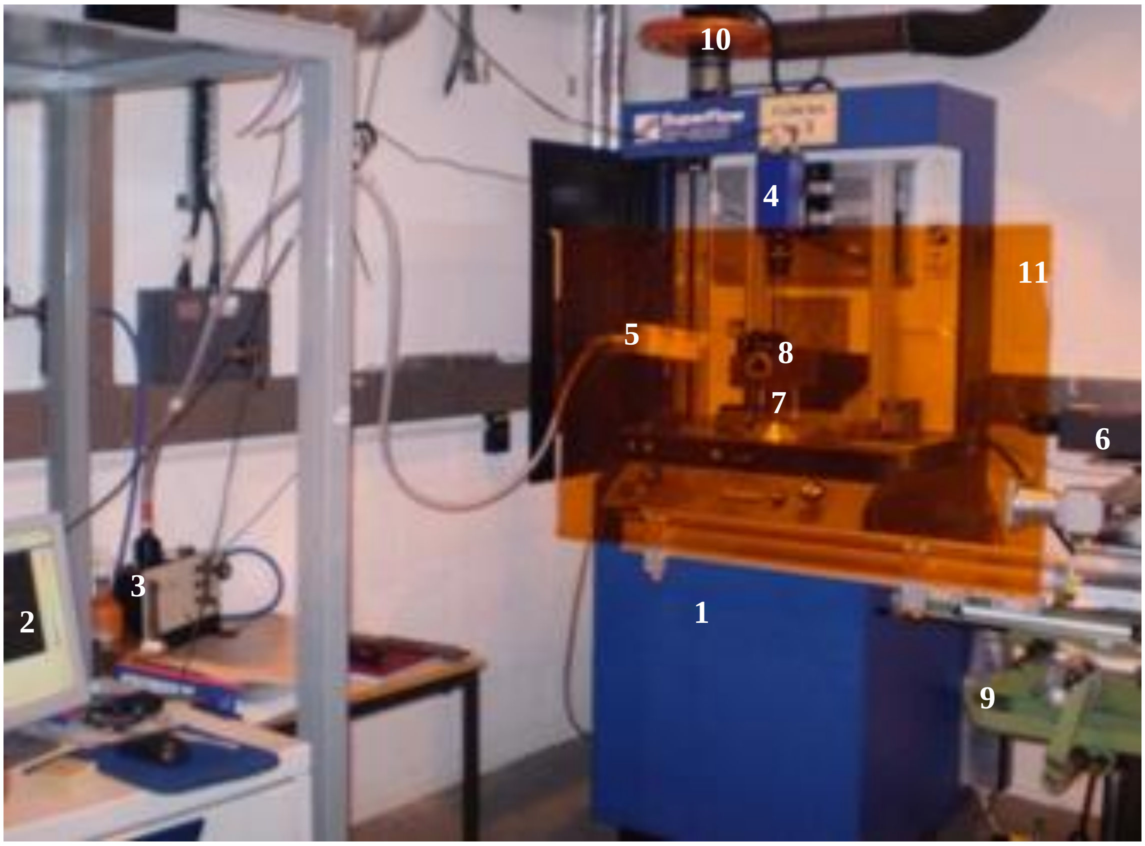

1- Air flow bench
2- Personal computer
3- Atomiser jet
4- Endoscopic camera
5- Honey structure distributor
6- PIV laser
7- Transparent cylinder
8- Cylinder head being tested
9- Traverse
10- Vacuum fan
11- Safety laser filter

Figure 4.18: Experimental apparatus for horizontal plane

4.1.6: PIV Vertical Plane Measurements Set up

The experimental set-up for the PIV measurements in the vertical plane is shown in Figure 4.19. A Nd:YAG laser is used as a light source (1 on Figure 4.19). The high-resolution CCD camera (2 on Figure 4.19) is positioned normal to the laser sheet. The laser beam is aligned at the centre of the cylinder liner at the targeted plane. PIV measurements are conducted with a 15mm thick transparent cylinder made of fused silica (3 on Figure 4.19) for six vertical planes (0^{o}, 30^{o}, 60^{o}, 90^{o}, 120^{o}, 150^{o}). Selection of vertical planes positions from one to another was made by rotating the cylinder head and liner to the required angle referenced to the camera and laser head positions. The measurements have been taken for two pressure drops of 250 mm and 635 mm of H_2O, equivalent to engine speeds of 2500 and 4000 RPM respectively and for a number of fixed valve lifts (2mm, 5mm, and 8mm) for different intake valve configurations. When measuring the turbulence characteristics, the number of captured image pairs was increased to be 1200 image pairs. The PIV measuring area was set as a rectangular shape with 60mm x 72mm in the vertical plane and located at 26mm downstream from the flame face.

1- PIV laser
2- Camera
3- Transparent cylinder
4- Honeycomb structure distributor
5- Cylinder head being tested

Figure 4.19: Experimental apparatus for vertical planes

High flare from reflected laser light produced considerable noise onto the raw images and several steps are utilised to improve the quality of the raw images. The first step was to ensure the laser beam alignment with the centre of the cylinder by using an alignment tool to minimise off axis reflections. Secondly, the SciTech atomiser was used to guarantee a high enough density of seeded particles with size of nominally 0.5µm, which were distributed uniformly inside the area of interest by using a distributor (4 on Figure 4.19). The influence of background light from surface reflections is eliminated by painting most of the surrounding parts black, such as the valve heads and cylinder adaptor part on the flow rig. In addition a piece of black cloth was used to cover the cylinder sides that were facing the laser and camera sides to act as a laser beam stop, “light dump”. The raw images obtained for both the old and the new PIV measurements are shown in Figure 4.20. The 15mm thick, fused silica liner was replaced with a 6mm thick acrylic liner. The effect of these preliminary steps had a significant influence on eliminating the reflections, Figure 4.20 *(b)*.

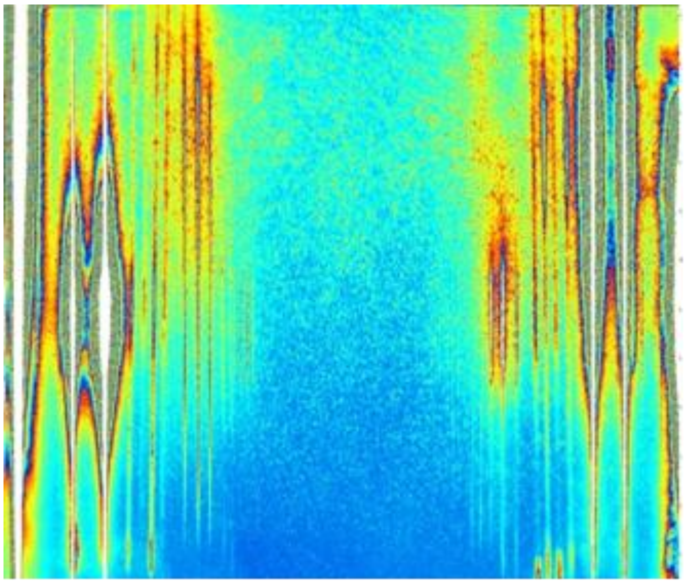

a-Fused silica liner (15mm thickness)

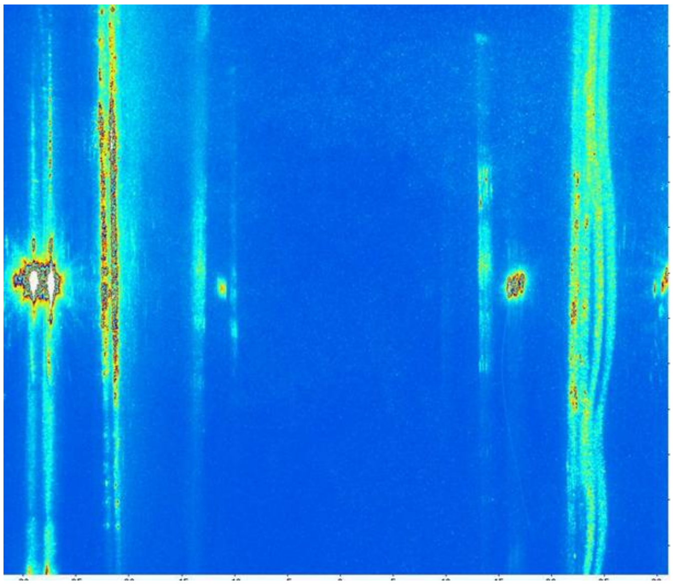

b-Acrylic plastic liner (6mm thickness)

Figure 4.20: Vertical plane raw images of PIV measurements

4.2: Sources of Error and Bias in Measurements

The use of steady flow port and optical diagnostic techniques to perform flow measurements results in an estimation of the fluid properties. There is a slightly discrepancy between the measured values were obtained from both measurements as a result of number of random errors and bias in the measurements. An understanding of these errors is necessary to accurately configure the experiments. One of the main causes of error would be the manufacturing tolerance of the rapid prototyped head. A slight discrepancy in surface finishing quality on intake port would have significantly affected the flow coefficients. The second source of error is plasticine used around the sharp edge of the intake port entrance in order to eliminate separation. These errors unfortunately are difficult to quantify its influence on the results. Table 4.3 and Table 4.4 shows uncertainty analysis on flow field measurements by means of both steady flow port and PIV measurements respectively. The calibration of air-flow rig was provided by manufacturing stated that a mass flow rate accuracy of 3% and repeatability of 1%. In PIV measurements, when the combined uncertainties are considered, the expanded uncertainty in velocity is ±0.054 m/s.

Table 4.3: Steady flow port sources of error

Source of Error	**Absolute uncertainty**
Temperature gauge reading	$\pm 1^{o}$C
Flow percentage reading	An error of around ±0.5% is estimated in the calculation of flow rate
Pressure drop reading	An error of around ±5mm is estimated. This represents a 3.9% error at the lowest pressure drop value and a 0.8% error at the highest pressure drop value.
Valve lift actuated by basic mechanism	An error of around ±0.1mm is estimated in the valve lift. This represents a 20% error at lowest valve lift and a 1% error at highest valve lift.

Table 4.4: PIV measurements sources of error

Source of Error	**Absolute uncertainty**	**Possible Action**
Alignment of Laser beam at the field of view (FOV)	when the angle between the laser sheet and the calibration plate deviates at most 2^o the uncertainty is about ±0.011 mm/pixels	Check alignment more regularly
Laser power fluctuation	The detection of particle will be affected; the maximum uncertainty could be in the length of particle diameter is about ±0.0071μm.	This can be reduced up to 1/10 of particle diameter if the experimental condition is well controlled
Image distortion by lens	The image could be distorted by the aberration of lens. The distortion of the image is less than 0.5% of total length. The uncertainty is about ±0.0056 pixels.	This can be eliminated by applying de-warp correction process.
Calibration plate position	The uncertainty of located the calibration at the targeted plane is about ±0.5mm.	Check and align the calibration plate with the laser sheet more regularly.
Image distance of reference points using Calibration plate	The distance of the reference points were measured on the image plane. The location of the reference points were detected from a single point of image, the uncertainty is about ±0.5 pixels.	
Sub-pixel error	The uncertainty of sub-pixel depends on the diameter of tracer particle, noise level of the image and particles concentration. Particle image size ~2pixels, Smaller: particle no longer resolved (peak locking effect) Larger : random noise increase noise in data (seeding density, camera noise) The estimated uncertainty is about ±0.03 pixels.	Configuring the experimental hardware to ensure the particle image diameters are greater than two pixels can eliminate this error.

4.3: Summary

In this Chapter, the PIV measurements set up for both the horizontal and vertical planes used in this work for the investigations of the in-cylinder flow structures under steady conditions are presented and discussed. A detail description of rapid prototype cylinder head, airflow test rig, swirl motion meters and PIV system were described. Moreover, the uncertainties of measurement were approximated and optimisation of the measurement technique was presented. High flare from reflected laser light produced considerable noise onto the raw images and several steps are utilised to improve the quality of the raw images. The alignment of the laser beam is essential to minimise off axis reflections. The influence of background light from surface reflections is eliminated by painting most of the surrounding parts black, such as the valve heads and cylinder adaptor part on the flow rig. In addition a piece of black cloth was used to cover the cylinder sides that were facing the laser and camera sides to act as a laser beam stop, “light dump”. The 15mm thick, fused silica liner was replaced with a 6mm thick acrylic liner. The effect of these preliminary steps had a significant influence on eliminating the reflections. The experimental analysis is discussed in Chapter 6.

Chapter 5

The Governing Equations and Numerical Model

5.1: Introduction

The second aim of this thesis is to conduct numerical simulation for the in-cylinder flow structures of an internal combustion engine under steady flow conditions. The computation of the in-cylinder engine flow field requires detailed mathematical description of all significant properties of the process by means of solving a number of algebraic equations. Using computational fluid dynamic (CFD) for studying practical engine flow consists of geometry creating, mesh generation, setting-up physical sub-models, solve algebraic equations and post-processing resulting data. The numerical flow simulations presented in this investigation are obtained by using, as a research tool, a commercial code so-called STAR CCM+ (CD-ADAPCO, 2012). The CFD simulations are performed using a polyhedral mesh type due to the complexity of the cylinder head geometry. Mesh sensitivity tests are assessed by increasing the computational mesh density as following: low mesh number with 700 thousand cells, medium mesh number with 1 million cells and a fine mesh with 3.7 million cells. The mesh is generated with the STAR CCM+, version 5.06.010. Two turbulence models have been applied in the current study, namely, the Realizable k-ε (Durbin, 1996; Shih *et al.*, 1995) and Reynolds stress models (RSM) (Thakur and Shyy, 1999; Launder, 1989; Gibson *et al.*, 1978). The computational time, using a Linux PC contains 3.16GHz dual Intel Core processors; having 8 Gb of RAM, was about 48 hours and 430 hours for Realizable k-ε and Reynolds stress models (RSM) respectively. This clear as a result of RSM model is seven equations model, which requires solving transport equations for all turbulent stresses in three dimensions.

The three-dimensional simulation are conducted on the single cylinder engine head of a pent-roof type (Lotus), described in Section 4.1.1 for a fixed both valves lifts of (2mm, 5mm, 8mm) at two pressure drops 250mm of H_2O and 635 mm of H_2O that correlates with engine speeds of 2500 RPM and 4500 RPM respectively. First, the Realizable k-ε model was applied, then the RSM model was used with the quadratic pressure strain sub-model for pressure strain. The obtained results for the flow field are validated against the PIV experimental results. This Chapter provides an introduction to the numerical model used for this thesis. In addition, general descriptions of the computational methods that are employed, the generation of the computational mesh and initial and boundary conditions are presented and discussed.

5.2: The Governing Equations

The governing equations of fluid dynamics have a significant role in CFD. These equations can be written in two forms; the partial differential equation or the integral equation. The governing equations are transformed into algebraic equations using a discretisation method in time and space. Discretisation of the partial differential equation form of the governing physical equations leads to Finite Difference Method (FDM), whereas discretisation of the integral equation form of the governing physical equations leads to Finite Volume Method (FVM). The latter is preferred and used here because of dealing with complex geometries in multi-dimensional problems, as the integral formulations do not count on any special mesh structure. Furthermore, the FVM is locally conservative based on a balance approach, which is true because the values of the conserved variables are conserved from one discretisation cell to its neighbour, within the volume, and not at nodes or surfaces.

In general, multidimensional flow problems can be solved by computational fluid dynamics (CFD) technique with basic equations representing mass conservation (continuity), momentum and energy. In addition, as regards to turbulence modelling, additional transport equations are required to represent time-averaged flow fluctuations. The application of these principles yields a set of partial differential Navier-Stokes equations in terms of time and space. The first principle results in the continuity Equation 5.1. This equation represents the conservation of mass in a control volume for a compressible flow (Robert *et al.*, 2003; Angermann, 1996; Atthey, 1974).

$$\frac{\partial \rho}{\partial t} + \nabla \cdot (\rho \cdot \vec{v}) = 0 \tag{5.1}$$

The conservation equation for momentum is derived using Newton’s law which is based on the principle that the temporal change of the momentum equals to sum of all external forces acting on the control volume considered.

$$\frac{\partial}{\partial \mathrm{t}}(\rho\vec{v}) + \nabla \cdot (\rho\vec{v} \cdot \vec{v}) = -\nabla p + \nabla \cdot \bar{\bar{\tau}} + \rho\vec{f} \tag{5.2}$$

Where the operator ∇ referred to grad or del, which represents the partial derivative of a quantity with respect to the direction in the chosen coordinate system. In the Cartesian coordinates, ∇ is defined to be: $\nabla = \frac{\partial}{\partial x}\vec{i} + \frac{\partial}{\partial y}\vec{j} + \frac{\partial}{\partial z}\vec{k}$,$\nabla = \frac{\partial}{\partial \mathrm{x}}, \frac{\partial}{\partial y}, \frac{\partial}{\partial z}$; $\vec{v} = u, v, w$ and ρ is the density, p represents the pressure, $\bar{\bar{\tau}}$ is the stress tensor defined as in Equation 5.3 and $\vec{f}$ is the external body forces. The second term of the momentum equation on the left-hand side is the convective term and the second term on the right-hand side is the diffusion term.

$$\bar{\bar{\tau}} = -\rho \begin{bmatrix} \overline{\acute{u}\acute{u}} & \overline{\acute{u}\acute{v}} & \overline{\acute{u}\acute{w}} \\ \overline{\acute{u}\acute{v}} & \overline{\acute{v}\acute{v}} & \overline{\acute{v}\acute{w}} \\ \overline{\acute{u}\acute{w}} & \overline{\acute{v}\acute{w}} & \overline{\acute{w}\acute{w}} \end{bmatrix} \tag{5.3}$$

5.2.1: Description of Turbulence

Turbulence does not have a specified definition but it is possible to be described according to the common features of the disturbed flows. As it is known, turbulent flows include a wide spectrum of features where the most important are highly unsteady, three-dimensional which consists of vortices (eddies) with a wide range of scales of motion, diffusivity, high Reynolds number and dissipative in nature. Turbulent flow motions can be found in most industrial applications. There are many definitions for turbulence and turbulent flows. For instance, turbulence is known as a chaotic motion that exists at high Reynolds numbers, which means the inertial force is much higher than the viscous force. In more detailed Bradshaw (1996) stated the following definition of turbulence:

> *"Turbulence is a three dimensional time-dependent motion in which vortex stretching causes velocity fluctuations to spread to all wavelengths between a minimum determined by viscous forces and a maximum determined by the boundary conditions of the flow".*

In this section, the phenomenon of turbulence will be discussed in more detail.

Spectral Definition of Turbulent Flows

Turbulence is categorised by a multitude of scales in time and space. It has a wide spectrum of vortex sizes with a corresponding spectrum of fluctuation frequencies. It is important to notice that turbulent flows are characterised with a continuous spectrum. The largest vortices have low frequencies and its sizes are on the same order of magnitude as the flow domain and are affected by the boundaries and the mean flow. On the other hand, the viscosity of the fluid and their high frequency fluctuations determines the smallest vortices. The difference between the largest and smallest eddies, which is represented in the width of the spectrum, are influenced proportionally by the Reynolds number. The large vortices extract kinetic energy from the mean motion and feed it to the large-scale turbulent motion.

The cascade process can be described as the energy is passed down to smaller and smaller vortices due to the vortex stretching until viscosity causes the dissipation of the vortices. The turbulent kinetic energy spectrum E_w (k_w) vs. wave number k_w is plotted in Figure 5.1, where $k_w = 2\pi/\lambda$ (Maltsev, 2004; Pope, 2000).

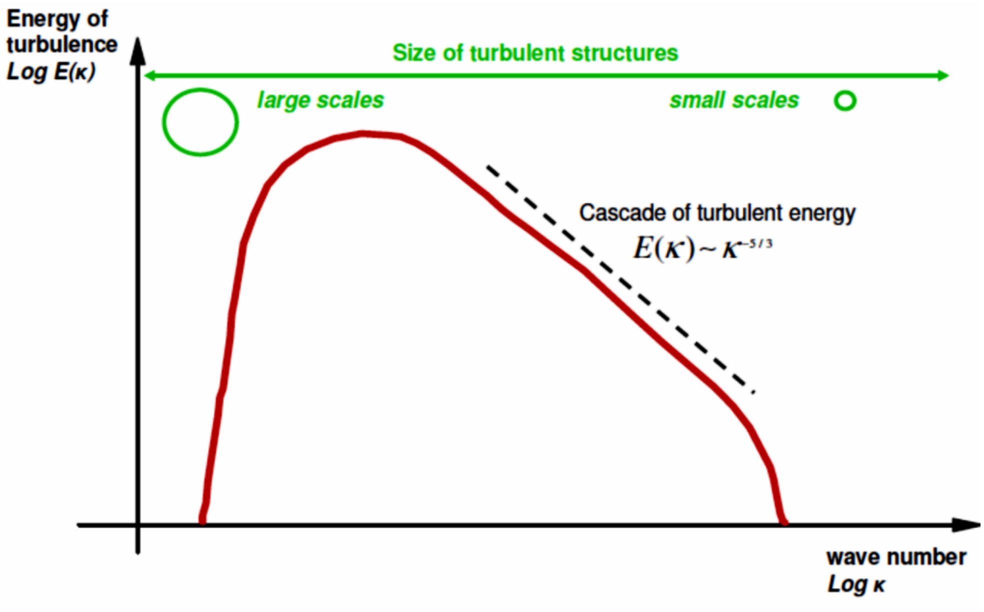

Figure 5.1: Schematic for turbulent kinetic energy spectrum

The physical dimensions of turbulence are described by turbulence length scales. A number of turbulence length scales exist to define the various stages of eddy dissipation. The largest of these scales is known as the integral length scale (l_t.). This represents the largest distance between two points at which the flow velocity is correlated. Since the size of the large vortices depends on the flow domain and the geometry. Thus, the integral length scale in engine geometry is of similar magnitude to the valve lift during the intake stroke, and then it expands to the bore of the cylinder during compression stroke. The preferred flow direction of the mean flow is imposed on the large-scale turbulent motion, which makes the flow strongly anisotropic. With the cascade process, the direction sensitivity of the flow is diminished, and in high Reynolds number flows, the small-scale dissipative motion is isotropic. Based on the scale invariance of the eddy dissipation rate, the characteristic length associated to the larger integral vortices and the time scale can be derived as:

$$l_t = \frac{k^{3/2}}{\varepsilon} \tag{5.4}$$

$$\tau_t = \frac{k}{\varepsilon} \tag{5.5}$$

Where k is the turbulence kinetic energy, ε is the turbulence dissipation rate, and τ_t is the flow mixing time scale.

Turbulence Models

Modelling of turbulence is still a challenge when solving practical flow problems. Turbulent flow requires too much computational effort to solve the governing transport equations exactly to the smallest scales. Turbulent flow is characterised by fluctuating components fields and is required to set-up a turbulence model. Since such fluctuations are of small scale and high frequency, they are very numerically expensive to simulate directly in practical problems. Instead, the instantaneous governing transport equations can be time averaged, resulting in adapted equations that are numerically less expensive to resolve. However, the obtained equations contain additional unknown variables, and turbulence models are required to solve these variables in terms of known quantities. Several turbulence models are available and the complexity of different turbulence models may vary depends on the details that are required. Complexity is due to the nature of Navier-strokes equations which are unsteady and nonlinear partial differential equations. A number of different approaches can be used to compute the turbulent flows. In order to resolve the "all" flow scales in both space and time coordinates, the Direct Numerical Simulation (DNS) (Moin *et al.*, 1998) can be applied. The DNS model solves the full instantaneous three-dimensional Navier–Stokes equations without applying any modelling for turbulent motion and offers detailed information over all flow parameters. The possibility of applying DNS in practical industrial applications is restricted due to limitations of current computer capacity. The second approach is Large Eddy Simulation (LES) (Sagaut, 2002; Deardorff, 1982) model that is based on filtering rather than averaging process in which the large-scale structures are calculated directly without approximation, while only the small-scale turbulence needs to be modelled. This approach demands high resolution computational grids in order to resolve flow scales with small time steps. The third approach is Reynolds-Averaged Simulation (RANS) models that are considered one of most practical approaches that have been commonly used to predict various engineering turbulent flows in industrial applications. Such models are based on using a set of Reynolds averaged governing transport equations, with the Reynolds averaged Navier-Stokes (RANS) modelling approach a series of turbulence models can be used includes the following:

- Spalart-Allmaras Model (Spalart and Allmaras, 1992)
- $k-\varepsilon$ Models
    - Standard $k-\varepsilon$ Model (Bella *et al.*, 2003; Launder and Spalding, 1974, 1972)
    - Renormalization-Group (RNG) $k-\varepsilon$ Model (Bella *et al.*, 2003; Choudhury, 1993)
    - Realizable $k-\varepsilon$ Model (Durbin, 1996; Shih *et al.*, 1995)
- $k-\omega$ Models
    - Standard $k-\omega$ Model (Wilcox, 1998)
    - Shear-Stress Transport (SST) $k-\omega$ Model (Menter, 1994)
- Reynolds Stress Model (RSM) (Thakur and Shyy, 1999; Launder, 1989; Gibson *et al.*, 1978)

As far as RANS models are concerned, there is no agreement in the literature as to which model performs better. Number of previous studies used RANS models for modelling of the flow in-cylinder was reported in section 2.2.3 (Nomura *et al.*, 2008; Payri *et al.*, 2004; Bella *et al.*, 2003; Choi *et al.*, 2003 ; Richter *et al.*, 1999; Yang *et al.*, 1998; Leschziner, 1991; Takenaka *et al.*, 1990).

Selection of Turbulence Models

It is known that no single turbulence model is universally accepted as being superior for all problems. There are number of considerations has to be taken in account prior to choice the turbulence model such as:

i. The physics encompassed in the flow
ii. The level of accuracy required
iii. The available computational resources

Take above consideration in account, along with understanding the capabilities and limitations of the various models available, the following models were considered, and investigated further to found which model was best suited for modelling in-cylinder flow structures. RANS based turbulence models are cheaper than other turbulence models since they provide good results with coarser meshes. In the following sections, Examples of RANS based turbulence models are described.

The Eddy Viscosity k-ε models

The eddy viscosity k-ε turbulence models introduce two additional equations to represent the transport of turbulence through a flow. These two variables are the turbulence kinetic energy (k) and its dissipation rate (ε) (Xu *et al.*, 1998; Lien, 1996; Durbin, 1996; Shih *et al.*, 1995; Launder and Spalding, 1974). A general formulation is given by Equations 5.6-5.7:

$$\frac{D\rho k}{Dt} = D_k + P_k + G_k - \rho\varepsilon \tag{5.6}$$

$$\frac{D\rho\varepsilon}{Dt} = D_\varepsilon + C_1\frac{\varepsilon}{k}(P_k + C_3 G_k) - C_2\rho\frac{\varepsilon^2}{k} \tag{5.7}$$

The k-ε model takes in account the distribution of turbulent viscosity μ_t to solve the turbulence. The limitation of such models is an assumption of the local isotropy of turbulence. The turbulent viscosity μ_t and normal shear stress are defined, respectively, by the following equation:

$$\mu_t = \rho C_\mu \frac{k^2}{\varepsilon} \tag{5.8}$$

$$k = \frac{1}{2}\rho\overline{\acute{u}_\imath \acute{u}_\imath} \tag{5.9}$$

Where ρ is density and D_k , P_k and G_k are diffusion, production and buoyancy terms, respectively, in the k equation. D_ε is the diffusion term in the ε equation. C_1 , C_2 and C_3 are universal constants in the k-ε model and C_μ is the critical coefficient of the model. There are different variant of the k-ε turbulence model, namely:

- Standard k- ε (Bella *et al.*, 2003; Launder and Spalding, 1974, 1972)
- Standard Low-Reynolds number (Lien *et al.*, 1996)
- Realizable k- ε (Durbin, 1996; Shih *et al.*, 1995)
- Realizable k- ε Two-Layer (Xu *et al.*, 1998)

The Realizable k-ε Model

The realizable k- ε model developed by Shih (Shih *et al.*, 1995) is one of the more successful recent developments of RANS models. A new transport equation is used in this model for the turbulence dissipation rate ε. Moreover, in contrast to the standard model, the critical coefficient of the model, C_μ, is expressed as a function of mean flow and turbulence properties (see Equation 5.13), rather than assumed to be constant. Realizable models have been implemented with a two-layer approach, which allows them to be used with fine meshes that resolve the viscous sub-layer. The transport integral equations for realizable k-ε model are:

$$\frac{d}{dt}\int_V \rho k dV + \int_A \rho k(\mathbf{v})\ .d\mathrm{a} = \int_A \left(\mu + \frac{\mu_t}{\sigma_k}\right)\nabla k.\ \mathrm{da} + \int_V [G_k - \rho(\varepsilon)]\,dV \tag{5.10}$$

$$\frac{d}{dt}\int_V \rho \varepsilon dV + \int_A \rho \varepsilon(\mathbf{v})\ .d\mathrm{a} = \int_A \left(\mu + \frac{\mu_t}{\sigma_k}\right)\nabla \varepsilon\,.\,\mathrm{da} + \int_V \left[G_{\varepsilon 1} + \frac{\varepsilon}{k}(C_{\varepsilon 1}) - \frac{\varepsilon}{k+\sqrt{\nu\varepsilon}} C_{\varepsilon 2}\rho(\varepsilon)\right] dV \tag{5.11}$$

Where,

$$G_k = \mu_t S^2 - \frac{2}{3}\rho k \nabla\,.\,\mathbf{v} - \frac{2}{3}\mu_t(\nabla.\ \mathbf{v})^2 \tag{5.12}$$

$$C_\mu = \frac{1}{4 + A_s U^{(*)}\dfrac{k}{\varepsilon}} \tag{5.13}$$

Where:

$$U^{(*)} = \sqrt{\boldsymbol{S}\!:\!\boldsymbol{S} - \boldsymbol{W}\!:\!\boldsymbol{W}}$$

Where S is the modulus of the mean strain rate tensor and **W** is the rotation rate tensor defined as:

$$S = |\boldsymbol{S}| = \sqrt{2\boldsymbol{S}\!:\!\boldsymbol{S}^T}$$

Where **S** is the strain rate tensor can be calculated as:

$$\boldsymbol{S} = \frac{1}{2}(\nabla\,\mathbf{v} + \nabla\,\mathbf{v}^T)$$

$$A_s = \sqrt{6}\cos\phi$$

$$\phi = \frac{1}{3}\operatorname{acos}(\sqrt{6}W)$$

$$\boldsymbol{W} = \frac{S_{ij}S_{jk}S_{ki}}{S^3}$$

The model coefficients are defined as follows:

$$C_{\varepsilon 1} = max\left(0.43, \frac{\eta}{5+\eta}\right)$$

$$\eta = \frac{Sk}{\varepsilon}$$

$C_{\varepsilon 2} = 1.9$, $\sigma_k = 1.0$,and $\sigma_\varepsilon = 1.2$.

Some of field Operators are identified as following:

Gradient of a scalar quantity:

$$\nabla\phi = \frac{\partial\phi}{\partial x}\mathrm{i} + \frac{\partial\phi}{\partial y}\mathrm{j} + \frac{\partial\phi}{\partial \mathrm{z}}\mathrm{k}$$

Divergence of vector quantity:

$$\nabla\cdot\mathbf{v} = \frac{\partial \mathrm{v}_x}{\partial \mathrm{x}} + \frac{\partial \mathrm{v}_y}{\partial y} + \frac{\partial \mathrm{v}_z}{\partial z}$$

Scalar (inner, dot) product of two vectors, whose result is a scalar:

$$\mathrm{a}\cdot\mathrm{b} = a_i b_i$$

Scalar (inner, double-dot) product of two tensors, whose result is a scalar:

$$\mathbf{S}:\mathbf{T} = S_{ij}T_{ji}$$

Trace of a tensor quantity:

$$tr\,(\mathbf{T}) = T_{ii}$$

The Reynolds stress model (RSM)

The Reynolds stress model (RSM) (Thakur and Shyy, 1999; Launder, 1989; Gibson *et al.*, 1978), also known as a second moment closure model, accounts for anisotropy of the turbulence. It is considered a developed model of RANS models series to close the RANS equations of motion. The RSM model is seven equations model, which requires solving transport equations for all turbulent stresses in three dimensions. In three-dimensional simulations, six Reynolds stress equations are unique of the nine shear stress components due to the Reynolds stress is symmetric. In addition to the six Reynolds equations, a dissipation equation is required. The Reynolds stress equations are derived by multiplying the instantaneous Navier-Stokes equations by a fluctuating property (Sarkar *et al.*, 1990). In the resulting equations, the terms of equations required to be modelled are the diffusion term, the dissipation term and the pressure-strain term (Speziale *et al.*, 1991). There are three different Reynolds stress transport turbulence models based on modelling the pressure strain term namely liner pressure strain of Gisbon and Launder (1978) quadratic pressure strain and liner pressure strain two-layer. A general formulation is given by Equations 5.14-5.17.

$$\frac{D\left(\rho\overline{\acute{u}_\imath\acute{u}_\jmath}\right)}{Dt} = D_{ij} + P_{ij} + \Phi_{ij} - \varepsilon_{ij} + F_{ij} \qquad (5.14)$$

Where D_{ij}, P_{ij}, φ_{ij}, ε_{ij} and F_{ij} are turbulent diffusion, turbulent production, pressure strain, turbulent dissipation and body forces. The turbulent diffusion is adopted, such that as in STAR CCM+ (Lien and Leschziner, 1994):

$$D = \left(\mu + \frac{\mu_t}{\sigma_k}\right)\nabla\bar{\bar{\tau}} \qquad (5.15)$$

Where the turbulent Schmidt number is σ_k =0.82 and the turbulent viscosity is computed as in Equation 5.8. The turbulent production and dissipation rate are defined as follows:

$$P = -\rho(\bar{\bar{\tau}}\,.\,\nabla\mathbf{v}^T + \nabla\mathbf{v}\,.\,\bar{\bar{\tau}}) \qquad (5.16)$$

$$\begin{gathered}\frac{d}{dt}\int_V \rho\varepsilon dV + \int_A \rho\varepsilon(\mathbf{v})\ .d\mathrm{a} = \\ \int_A \left(\mu + \frac{\mu_t}{\sigma_\varepsilon}\right)\nabla\varepsilon\,.\,\mathrm{da} + \int_V \left\{\frac{\varepsilon}{k}\left[C_{\varepsilon1}\big(tr(\boldsymbol{P})\big) - C_{\varepsilon2}\rho\varepsilon\right]\right\}dV\end{gathered} \qquad (5.17)$$

The model coefficients are defined as follows: $C_{\varepsilon1}$ = 1.44, $C_{\varepsilon2}$ = 1.83.

5.3: The Numerical Model

Three-dimensional numerical simulations of the in-cylinder flow structures were performed for the same condition as the 2D-PIV measurements on the airflow rig. The Reynolds Stress Turbulence Model (RSTM) with a quadratic formulation of the pressure strain model was applied to calculate the flow fields. The discretised equations were derived based on the Finite Volume Method (FVM) (Robert *et al.*, 2003) and the segregated flow model (Demirdzic *et al.*, 1993) was applied to solve the flow equations for each component. The Semi-Implicit Method for Linked Equation (SIMPLE) (Lea and Watkins, 1997) method was utilized as the calculation algorithm. The applied convection scheme was a second order upwind difference method. The flow computational domain consisted of four main areas: the intake port, the area around the intake valves, the pent-roof cylinder head and the cylinder volume. The cylinder head prototype from CAD files are shown in Figure 5.2.

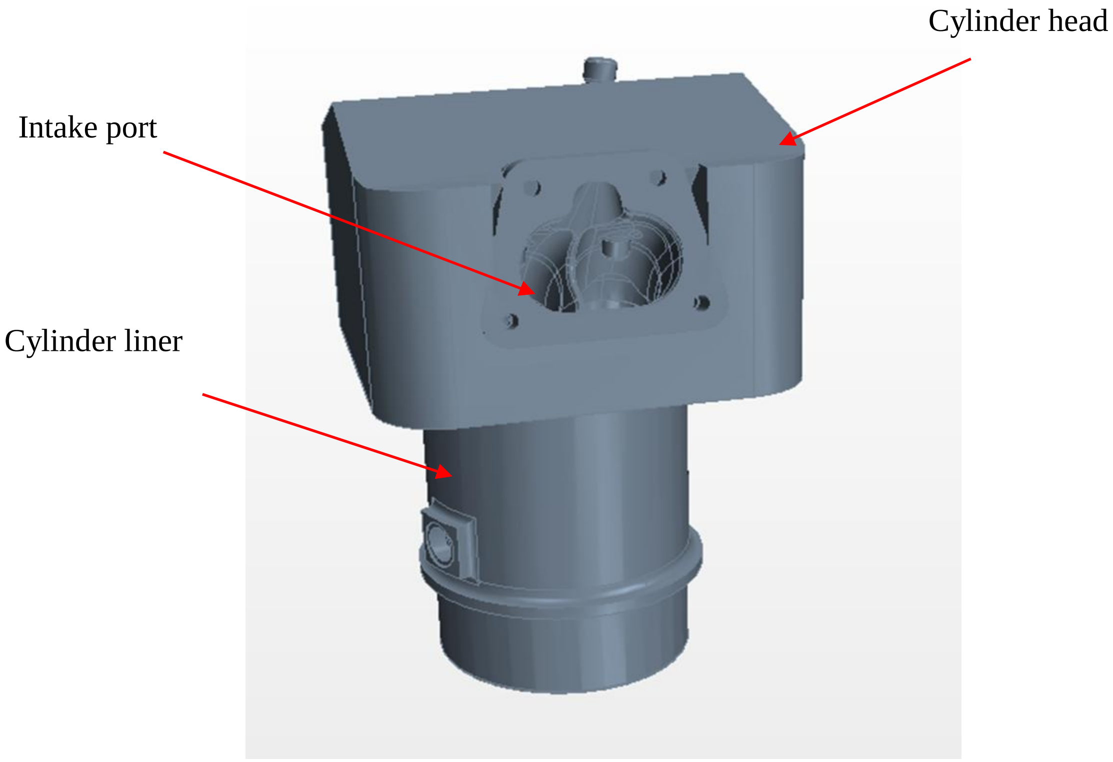

Figure 5.2: Prototype of the cylinder head

The flow computational domain reproduced the shape of the flow rig as can be seen in Figure 5.3. The airflow enters the flow domain at an inlet velocity boundary that was specified at the intake port. Lea and Watkins (1997) reported that the computations became more accurate when a uniform profile was assumed at the inlet. In the current investigation, a developed uniform flow at the inlet boundary is assumed. Thus, the inlet boundary was extended in a direction normal to the local face by 63mm that was also recommended by a previous study (Osei-Owusu, 2008) focusing on the optimal length of the extruded part of the intake port on the same cylinder head. The airflow then passes through the valve curtain into the cylinder volume, which is considered the most critical region due to the high velocities gradients generated in this region. The exhaust port was blocked and the cylinder liner was extended in a normal direction to the outlet face by 250mm in agreement with Watkins *et al.* (1990) in order to avoid any the outlet reversal flow. The extrusion of both inlet and outlet boundaries is a demand to ease the computation and quicken convergence (Yang *et al.*, 1998).

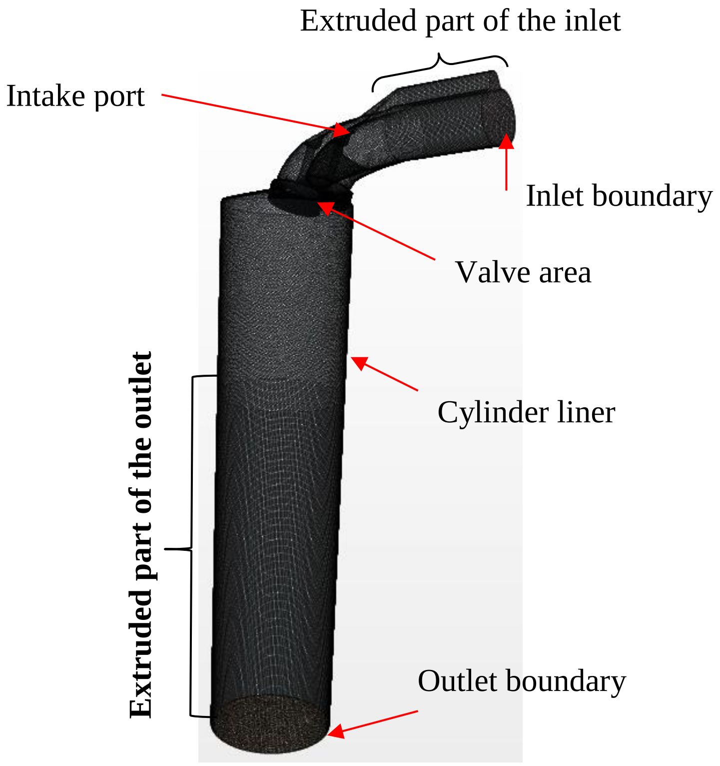

Figure 5.3: Description of the flow computational domain

5.4: The Computational Mesh or Grid

Mesh or grid generation is the significant factor in the accuracy and stability of CFD calculation. The solution domain should be divided into sub domains, which are identified as numerical grid. This defined the spatial discretisation at which variables are to be calculated that is required a discrete representation of the geometric domain on which the problem should be resolved. The numerical grid should be sufficiently refined and adapted so that the flow structure can be resolved. The generated mesh here is polyhedral type due to the complexity of the cylinder head geometry. The mesh sensitivity test was assessed by increasing mesh density as following: low mesh number was 700 thousand unstructured cells, medium mesh number with 1 million unstructured cells, and fine mesh with 1.7 million unstructured cells. The mesh size range is from 1mm in the intake port to 0.5mm in the more critical areas. In the cylinder liner part of the mesh, cells do not exceed 1mm in width.

For practicable computation of three-dimensional flows, the number of computational cells is generally, a compromise between accuracy of solution and computation time. Ideally, a grid size is that gives no significant different results for the quantities of interest after the grid refinement (i.e. grid independent solution). Since the fluid velocities vary throughout the domain, the cell size may vary as well inversely proportional to the local fluid velocities. For instance, very high velocities are encountered through the valve gap, and cylinder liner wall due to the cylinder head was designed to generate strong tumble motion particularly on the side of cylinder liner faced the intake valves. Therefore, a non-structured grid such as polyhedral type (CD-ADAPCO, 2012) can be applied to reduce the number of cells. Moreover, cell distribution density different from part to part. Outlet boundary conditions are defined at the end of the cylinder and was extruded about 250mm to avoid the reverse outlet flow. Two layers of prismatic cells were created next to the wall in order to have good quality boundary layer solution. The wall function (Cebeci and Bradshaw, 1977) applied was the standard wall function, which is valid only for local equilibrium and constant shear assumptions. Figure 5.4 shows the computational mesh arrangements used in this study.

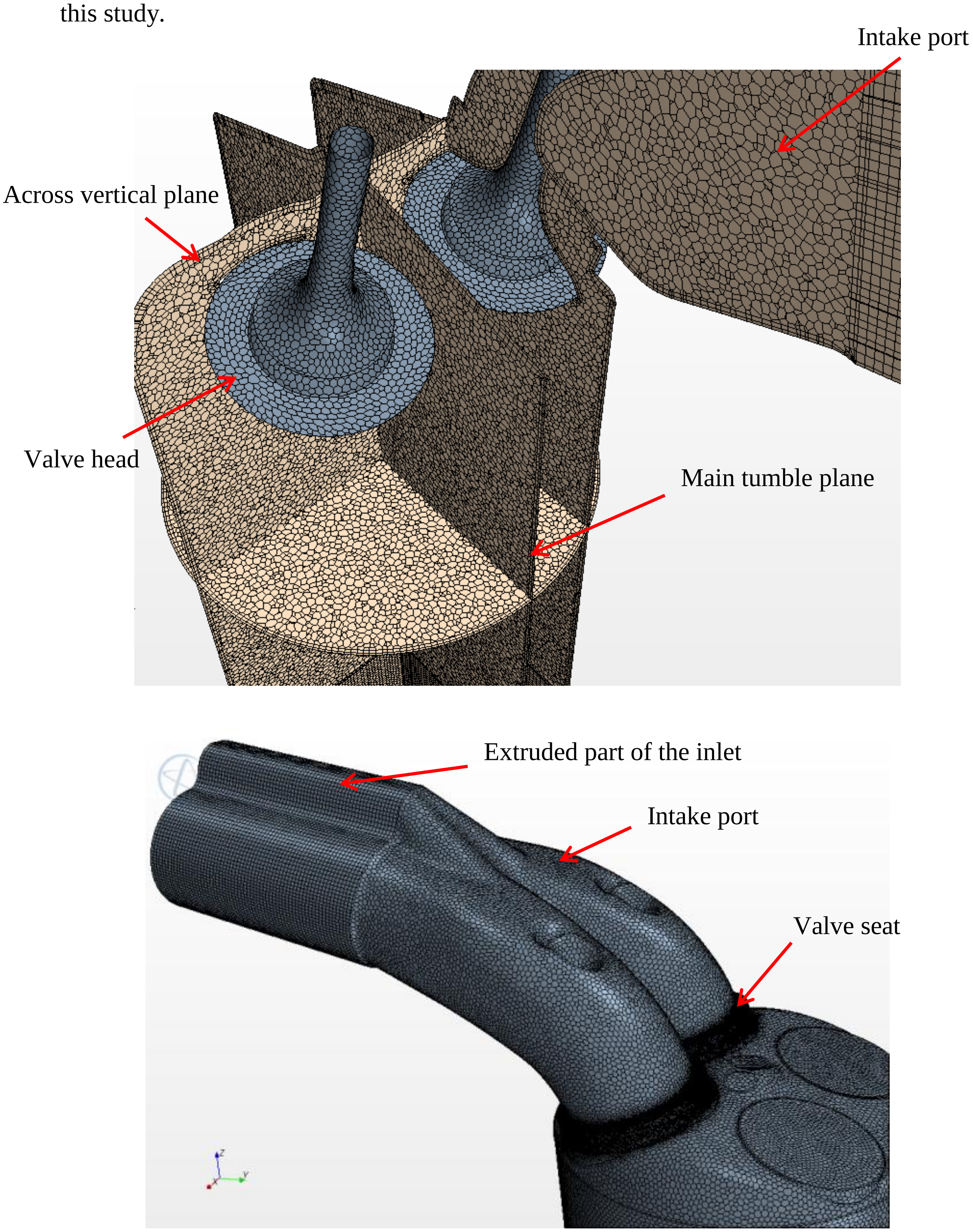

Figure 5.4: Computational meshes for steady-flow rig simulations

5.5: Boundary and Initial Conditions

A set of appropriate boundary conditions is an essential to close the set of non-linear equations. In accordance with the experimental procedure, the prescribed pressure drop boundary condition was used in the flow calculations. There are three boundary types namely: the inlet boundary, the wall boundary, and the outlet boundary.

5.5.1: Inlet Boundary Conditions

The inlet velocity boundary condition was imposed at inlet boundary. The quantity specified at the inlet was a uniform constant velocity as shown in Table 5.1, which was obtained from the airflow rig measurements. The volumetric flow rate was measured by the airflow rig from which the velocity at the inlet port was calculated using the equation $V_{in} = Q/A$ where Q is the volumetric flow rate, V_{in} is the inlet velocity and A is area of the inlet port. Since the turbulence model at the inlet was employed, it is essential to specify the turbulent length scale and the turbulent intensity. Values for the turbulence length scale (l_t) and turbulence intensity (I_t) were specified at the inlet flow boundary for each case as shown also in Table 5.1. The turbulence intensity is defined as the ratio of the fluctuation velocity (u_{RMS}) to the mean velocity (U) as calculated in Equation 5.18. The turbulence intensity at the inlet boundary was initially set to 20% based on measured LDA data that was conducted for the same cylinder head in a horizontal plane 44mm downstream from the cylinder head. The turbulence length scale was set to be the same as the valve lift.

$$I_t = \frac{u_{RMS}}{U} \tag{5.18}$$

Table 5.1: Numerical simulations parameters and initial inlet velocity calculations for all cases

Both valves open		**Pressure drop (mm of H_2O)**	**V_{in}(m/s)**	**u_{RMS} (m/s)**
L_v (mm)	**l_t (mm)**			
2	2	250	10.28	2.05
5	5		25.14	5.03
8	8		37.14	7.43
2	2	635	16.57	3.31
5	5		40.57	8.11
8	8		59.43	11.88

5.5.2: Outlet Boundary Conditions

The flow is assumed to be outwards-directed on the boundary. A pressure outlet boundary condition was specified. The outlet boundary was extruded about 250mm to avoid the reverse outlet flow. There is only one outlet boundary at the bottom of the cylinder. In the computations, the pressure drop was obtained inside the domain by setting the reference pressure as the required pressure drop.

5.6: Summary

In this Chapter, an introduction to the governing equation and numerical model used in this investigation are described and presented. The description of turbulence and selection of turbulence models was presented and discussed. In addition, general descriptions of the computational methods that are employed, the generation of the computational mesh and initial and boundary conditions are described and discussed. The Numerical analysis is discussed in Chapter 7.

Chapter 6

Experimental Analysis of In-cylinder Flows: Results and Discussions

6.1: Introduction

This Chapter presents results from the experimental analysis of the in-cylinder flow structure under steady state conditions utilising Particle Image Velocimetry (PIV) and swirl and torque meters. The experiments have been conducted for a range of valve lifts (1mm-10mm) with increment of 0.5 mm, and for three cases of inlet valve configurations; both inlet valves are opened, right inlet valve is opened only and left inlet valve is opened only. These measurements were carried out at four pressure drops, 127mm, 250mm, 445mm and 635mm of H_2O that correlate with engine speeds of 1750, 2500, 3000 and 4000 RPM respectively. The correlation between pressure drop and engine speed is the estimation provided by Lotus according to real engine studies. The flow characteristic through the intake port was carried out on rapid prototyped cylinder head utilising the airflow rig. The investigation of steady flow valve performance was carried out in order to measure the discrepancy between the real engine head and the rapid prototyped cylinder head. The influence of increasing the valve lift and pressure drops on the mass flow rate and discharge coefficient was discussed and represented.

From the PIV two-dimensional in-cylinder flow measurements, a tumble flow analysis is carried out for six planes parallel to the cylinder axis (0^o, 30^o, 60^o, 90^o, 120^o, 150^o). In addition, a swirl flow analysis is carried out for one horizontal plane perpendicular to the cylinder axis at half bore downstream from the cylinder head (44mm). A swirl and tumble ratios were obtained from both swirl meter and PIV 2-D measurements. The influence of different number of PIV image pairs measurements was presented. Swirl ratios were calculated at a distance about half bore downstream from the cylinder head (44mm) and tumble ratios were calculated for number of vertical planes. The obtained swirl and tumble ratios from the swirl and torque meter measurements were compared with the ratios were calculated from the PIV measurements.

6.2: Steady Flow Intake Valves Performance Analysis

The intake port performance of rapid prototyped cylinder head was tested. The steady flow valve investigation was carried out in order to measure the discrepancy between the real engine head and the rapid prototyped cylinder head. Plasticine was used around the inlet edge of the intake port in order to prevent any flow separation occurring as a result of the sharp edge on the inlet. Figure 6.1 shows the effect of using the plasticine on the mass flow rate. It is observed that the mass flow rate increased by using the plasticine around the intake port edge. The influence of increasing the valve lift, valve configuration, and pressure drops on the mass flow rate and discharge coefficient was discussed in the following Sections.

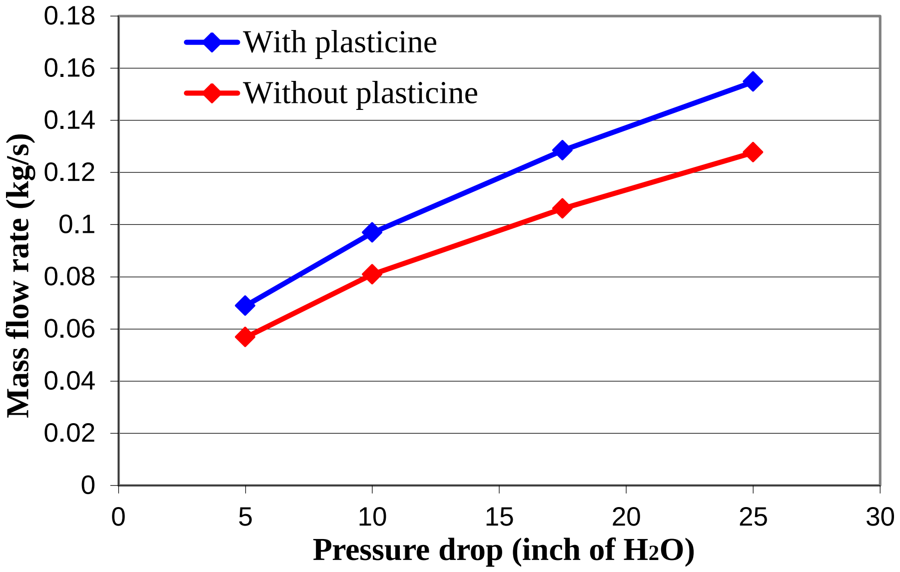

Figure 6.1: Mass flow rate vs. pressure drop to clarify the influence of using plasticine

6.2.1: Effects on Mass Flow Rate

Figure 6.2 shows the mass flow rate through the inlet valves across a range of fixed lifts and at two pressures drops for three cases of inlet valve configurations. It can be seen that the mass flow rate through both valves at the two pressure drops is higher than the single valve configurations. Furthermore, the single valve trends are similar except for a slight change at the higher valve lifts range between 6.5mm – 8mm for 635mm of H_2O pressure drop. It can also be seen that a slight drop in the mass flow rate occurs for the both valves open configuration at (0.057Lv/Dv) (2mm valve lift), 635mm of H_2O which might represent the flow separation from the valve and then forms zones of turbulent recirculation. In general, it was found that increasing the valve lift and test pressure drop can increase the airflow through the intake port but after (0.25 Lv/Dv), the mass flow rate tends to be steady.

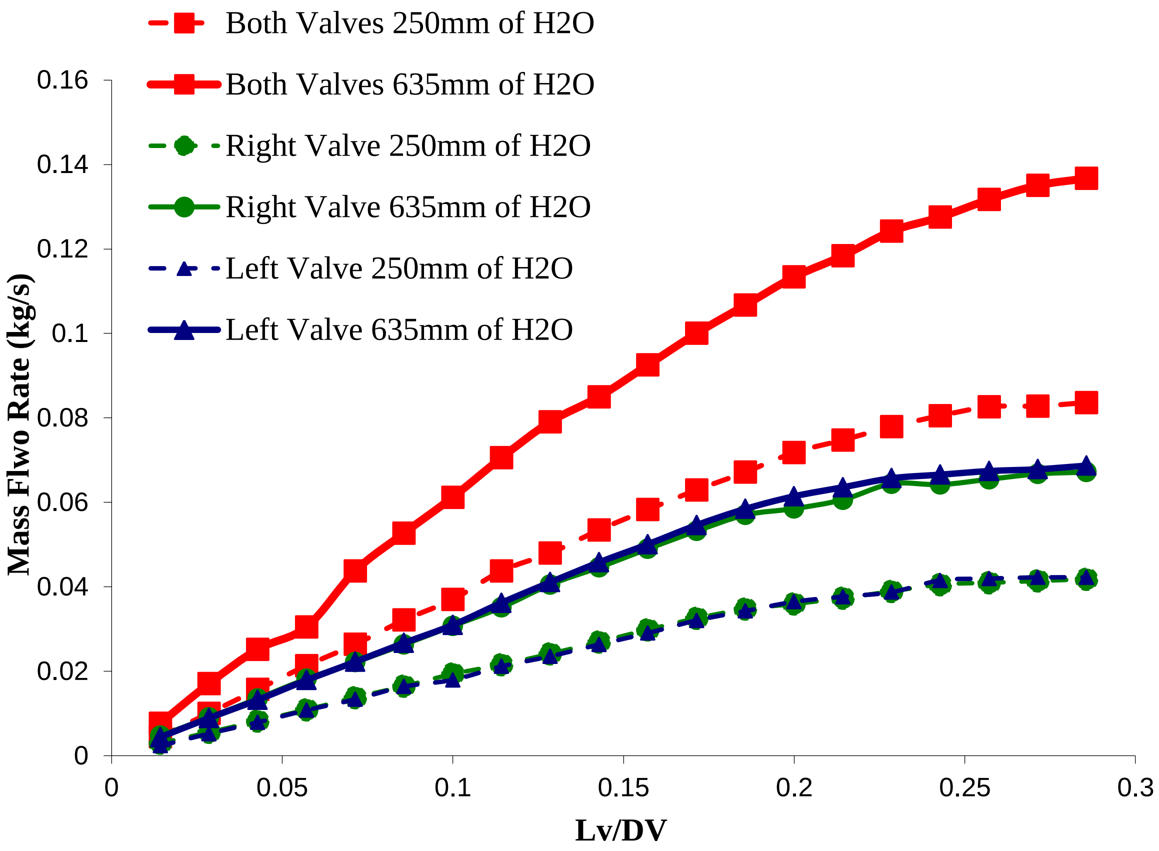

Figure 6.2: Inlet mass flow rate of prototyped head

6.2.2: Effects on Discharged Coefficient

Figure 6.3 shows that the discharge coefficient values are higher for the higher-pressure drop. This is believed to be a result of the reduction in the size of the turbulent boundary layer on the surface due to the higher velocities of the airflow through the port and valve area. There is a drop in the discharge coefficient at (0.057Lv/Dv) (2mm valve lift), 635mm of H_2O. This is as result of the separation point was explained previously in Figure 6.2 which is also due to the fact that discharge coefficient is a function of mass flow rate. Furthermore, it is noticed that the discharge coefficient for the single valve configurations at higher-pressure drop is higher than both valves configuration. This can be caused by the flow restriction between both opened valves which reduces the amount of entering air at this region.

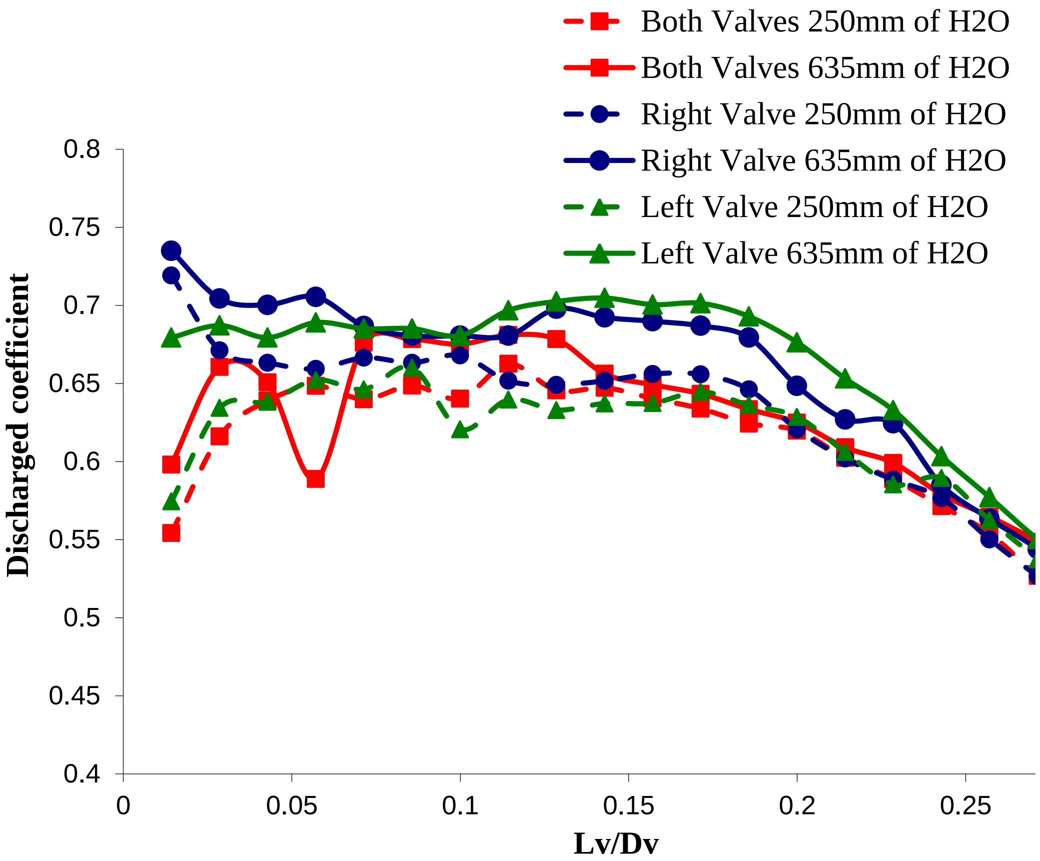

Figure 6.3: Inlet discharge coefficients of prototyped head

Furthermore, it can be noted that at low valve lifts the right valve performs more efficient than the left valve. However, at high valve lifts, the left valve is more efficient than the right valve. Pitcher *et al.* (2010) of Lotus Engineering confirmed this was not considered a design feature of the inlet port. Therefore, it might be due to valve adjustment method, the left valve was opened marginally more than the required. Even an increase of 0.05mm would cause an error in calculating the discharge coefficient. This error could also be attributed to the shape of the plasticine at the inlet port edge. Any non-symmetry in the shape of the plasticine would lead to one valve being more efficient than the other. Possible methods for increasing accuracy would be to measure the valve lift using a more precise method, such as dial gauges in order to take reading at smaller incremental values.

6.2.3: Comparisons between the Manufactured and Prototyped Cylinder Head

It is essential to compare the discharge coefficient of the manufactured and prototyped cylinder heads. It can be seen that slight differences are present between the two heads. Although, the discharge coefficient plots has the same trends but the manufactured cylinder head has higher values as shown in Figure 6.4.

A number of reasons could contribute to the discrepancy. The most noticeable one is the increased surface roughness in the inlet ports (based on visual examination). It is possible that increased surface roughness, which has the effect of causing increased turbulence within the ports, will actually increase flow rate through the valves. This is a result of the formed turbulent boundary layer within the port causing an alteration to the flow path.

Secondly, the shape of the plasticine made on the port edge could also cause some irregularities. It is highly unlikely the shape of the plasticine was identical in the two experiments. This might result in the separation point being at different points within the two experimental set-ups, explaining the difference in flow rates observed.

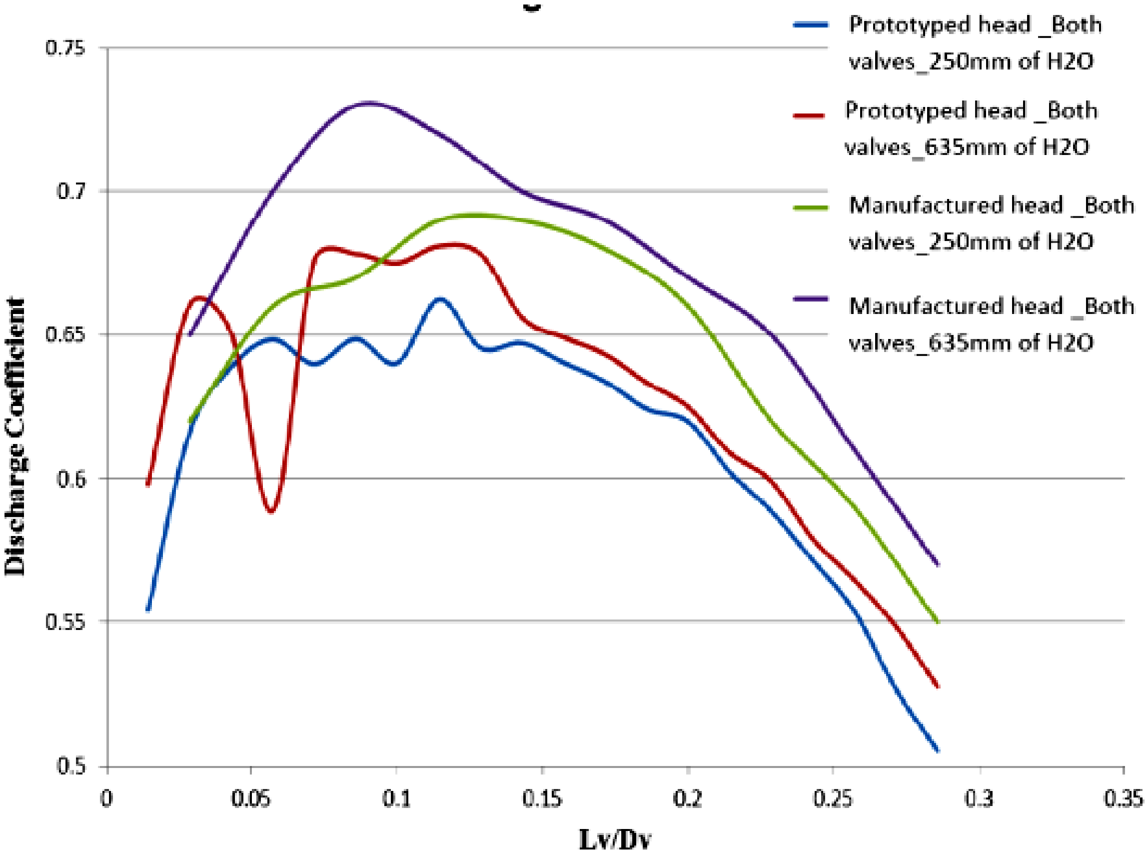

Figure 6.4: Comparison of discharge coefficient between manufactured and prototyped cylinder heads

6.3: PIV Measurements Analysis

In the following Sections, PIV measurements are presented and discussed. The results display vectors representing two components of velocities. Swirl flow motions are obtained from the horizontal plane measurements. While, tumble flow motions are obtained from the vertical plane measurements. Valve locations are represented by two small circles and the active and in-active valve configurations are represented with filled and hollow circles respectively in the swirl Figures.

6.3.1: Horizontal Swirl Plane

Flow Structure Variation as a Function of Valve Configurations

A direct comparison between the flow structures created by each individual valve and both valves being open 5mm is illustrated in Figure 6.5. As shown in Figure 6.5 *(a)* and *(b)* the formed vortices are a mirror image of each other. Positions and shapes of the vortices do show similar characteristics. However, the maximum flow velocity with the right valve open is higher. Figure 6.5 *(c)* shows the flow structure produced with both valves open. It can be seen that the vortices formed are symmetric about an axis between the valves but the right vortex is stronger than the left one due to the maximum flow velocity from the right valve being higher.

Effects of Valve Lift

Figure 6.6 shows the variation in flow structures caused by various valve lifts. The first observation, which can be made, is that the flow velocity is increased when valve lift increased until a certain valve lift is reached. In the current case, as can be seen from Figure 6.6 *(b)* and *(c)* flow velocity did not increase when the valve lift was 10mm as opposed to 8mm. The general patterns seen within the bulk flow motions show little variation with an increase in valve lift. It can be seen that the symmetrical two counter-rotating vortices appeared in all images for high valve lifts except the 2mm lift case as (see Figure 6.6 *(a)*).

For the valve lift opened cases (8mm and 10mm), the velocities around the edge of the cylinder are not seen. This could be due to the high turbulence levels in these areas of the cylinder, which could be interpreted as noise or small changes in focus due to the need to slide the head up the endoscope for the regular liner cleaning process.

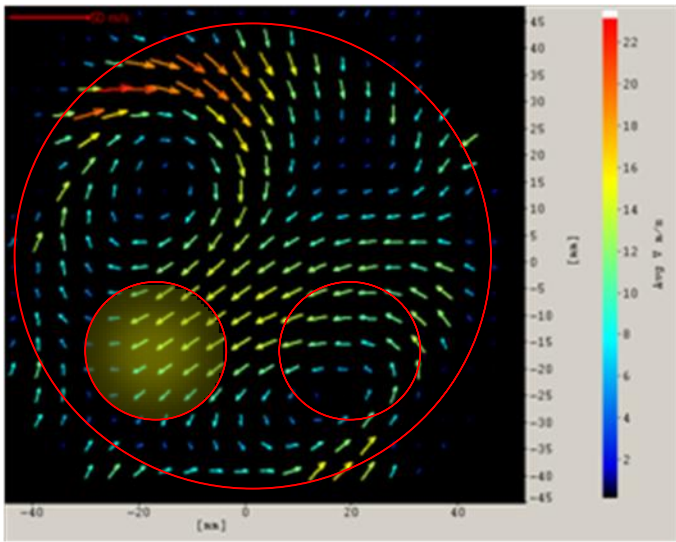

a) 250mm pressure drop, left valve active 5mm

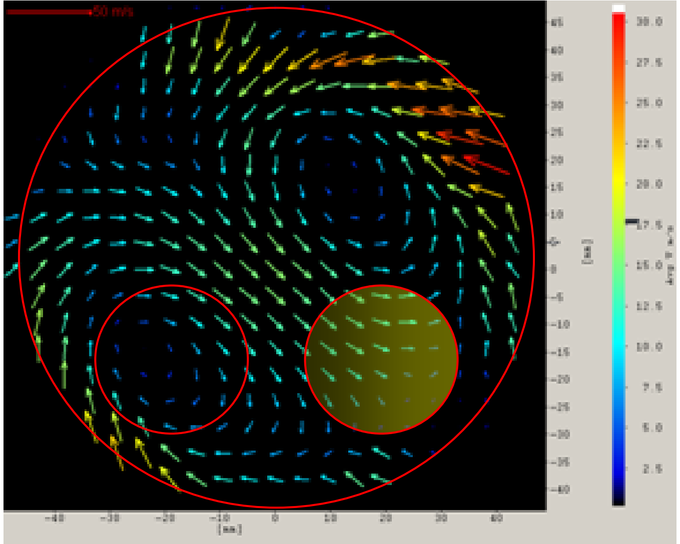

b) 250mm pressure drop, right valve active 5mm

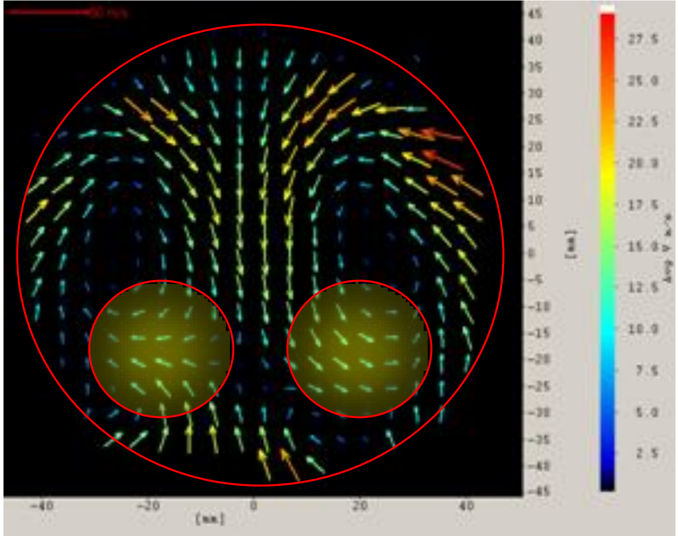

c) 250mm pressure drop, both valves active 5mm

Figure 6.5: Flow structure variations with formed vortices as a function of pressure drop and valve situation

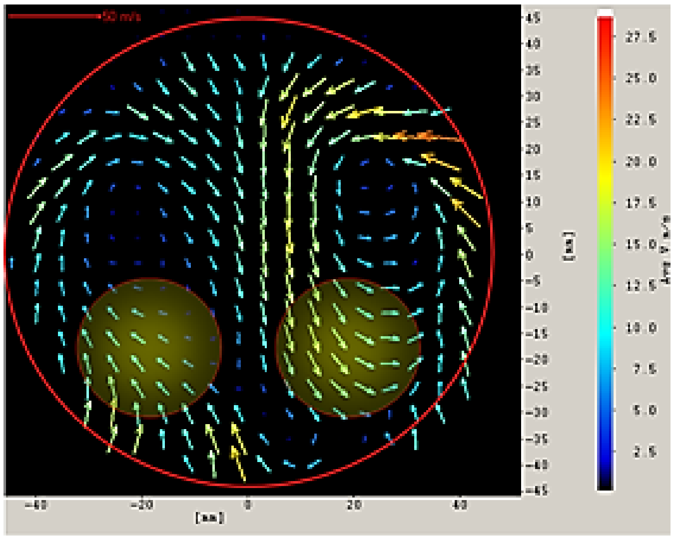

a) 635mm pressure drop, both valves 2mm

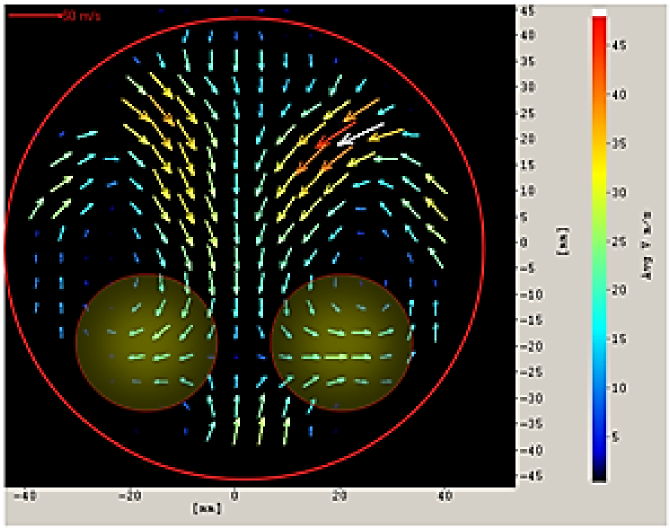

b) 635mm pressure drop, both valves 8mm

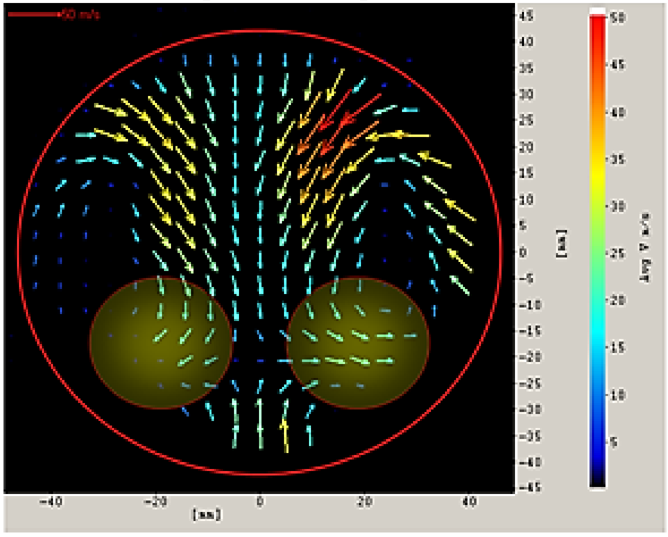

c) 635mm pressure drop, both valves 10mm

Figure 6.6: Effect of valve lift on flow structures

Effects of Increasing Pressure Drop

Figure 6.7 shows the variation in swirl flow structures caused by increasing pressure drop. As can be seen from Figure 6.7 *(a)* and *(b)* the formed vortices preserve their shape in both images. The only change presents in most cases is in the vortex strength, with maximum velocities shown to be approximately 63% larger in the 635mm of H_2O pressure drop case. This correlates well with the Bernoulli calculations for the maximum inlet velocities for 250mm of H_2O pressure drop case is 65 m/sec and for 635mm of H_2O pressure drop case is 103 m/sec.

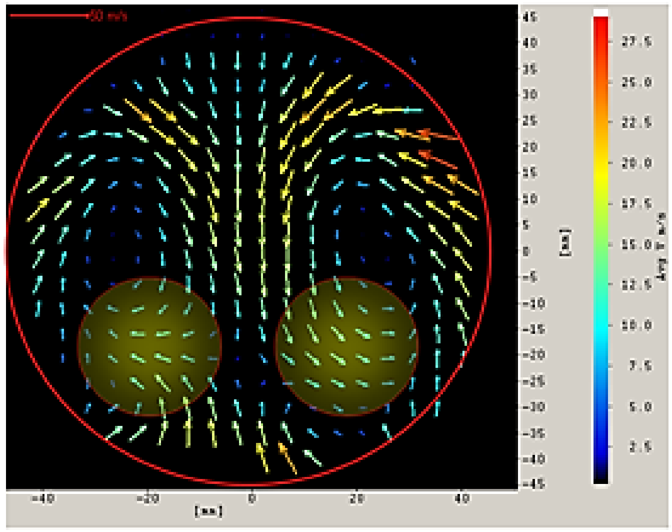

a) 250mm pressure drop, both valves 5mm

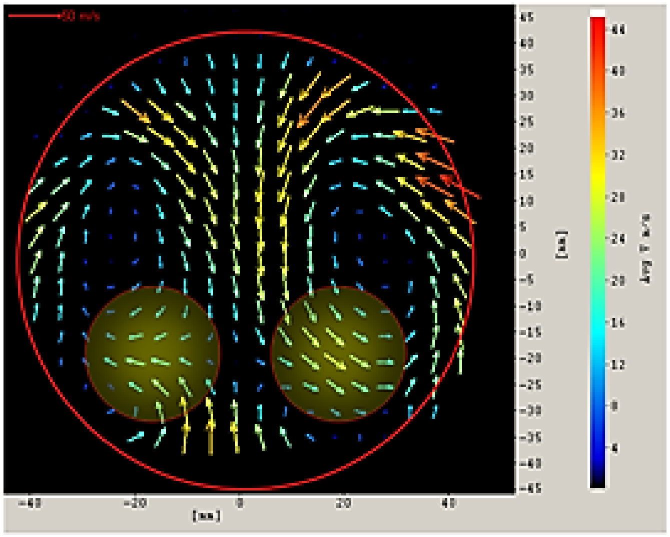

b) 635mm pressure drop, both valves 5mm

Figure 6.7: Swirl flow structure variation as a function of pressure drop

6.3.2: Vertical Tumble Plane

Mass Flow Rate Comparison with Measured Values

The mass flow rate was calculated for both 2mm and 5mm valve lift at 250mm of H_2O pressure drop from the axial velocities of the six PIV vertical measurements at the half bore distance from the head. In the beginning, the volumetric flow rate was calculated for segmented areas in each plane as shown in Figure 6.8 and Equations (6.1-6.4) were used to calculate the total mass flow rate for the six vertical planes. It was found that the calculated mass flow rate from the PIV vectors is less than the measured mass flow rate as shown in the Table 6.1. There are two possible contributors to this apparent loss of mass flow: Firstly, there is a significant amount of optical noise close to the cylinder walls, and removing vectors from the flow field reducing the confidence in these results. As with a tumble flow it is expected that the highest velocities would be close to the walls, the loss of these vectors from the calculation would have a significant effect. Secondly, it is also possible that with a limited number of planes measurements, the highest in-cylinder velocities will lie outside of these planes, again reducing the calculated value for the mass flow rate.

$$\dot{m_i} = Q_i \, \rho \tag{6.1}$$

$$\dot{m_{total}} = \sum \dot{m_i} \tag{6.2}$$

Where,

$$Q_i = U_i \, A_i \tag{6.3}$$

$$A_i = \frac{\pi \, R_i^2 - \pi R_{i-1}^2}{12} \tag{6.4}$$

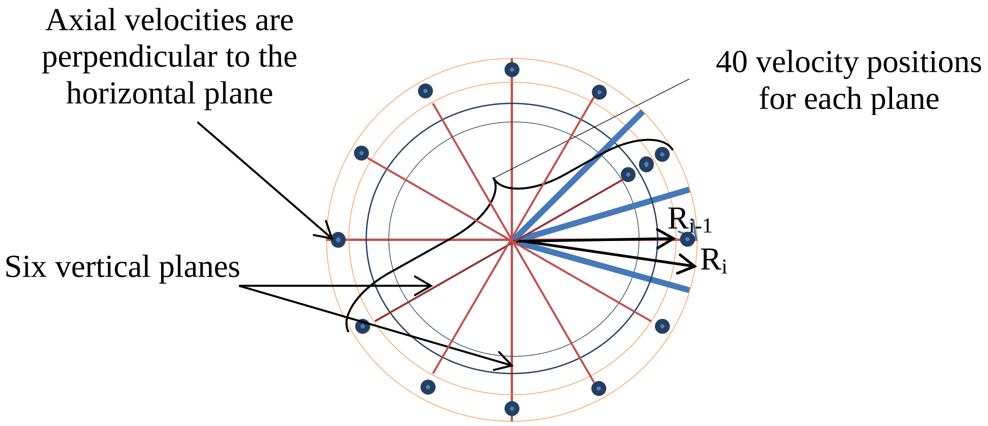

Figure 6.8: Calculated segmented area for each axial velocity

Table 6.1: Mass flow rate calculations

Valve configuration at 250 mm of H_2O	**Mass flow rate (Kg/s)**	
	Measured from air flow rig	**Calculated from PIV vectors**
Both valve 2mm	0.0206	0.0112
Both valve 5mm	0.0498	0.0329

Flow Structure Variation as a Function of Valve Configurations

Figure 6.9 shows the tumble flow structure produced by each individual valve and both valves being open 5mm in the main tumble plane. As can be seen from Figure 6.9 *(a)* and *(b)*, the flow structures caused by each valve individually are identical images and the general shape of the tumble motion is also similar. However, there is a vortex which was formed towards the edge of the cylinder head by activating both valves as can be seen in Figure 6.9 *(c)*.

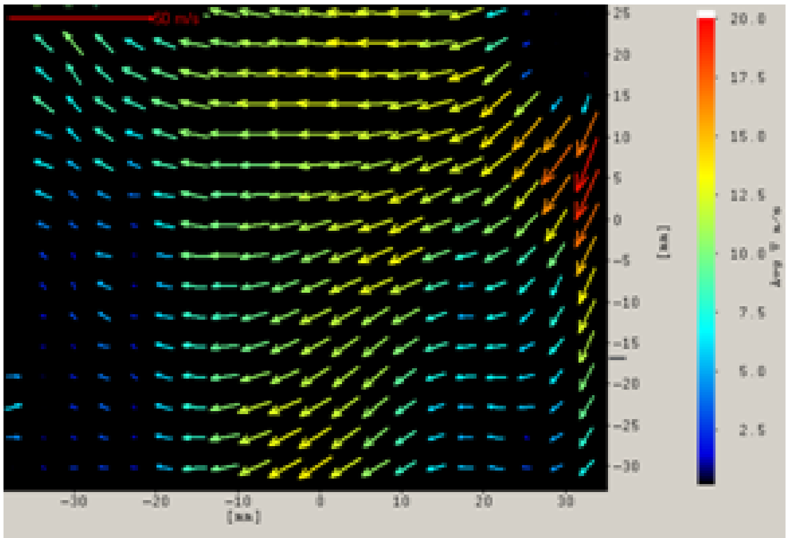

a) 250mm pressure drop, right valve 5mm, 90°

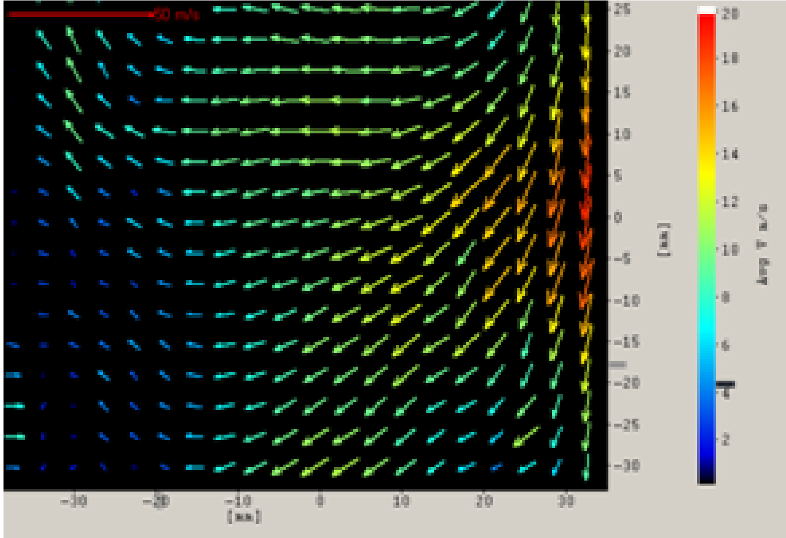

b) 250mm pressure drop, left valve 5mm,90°

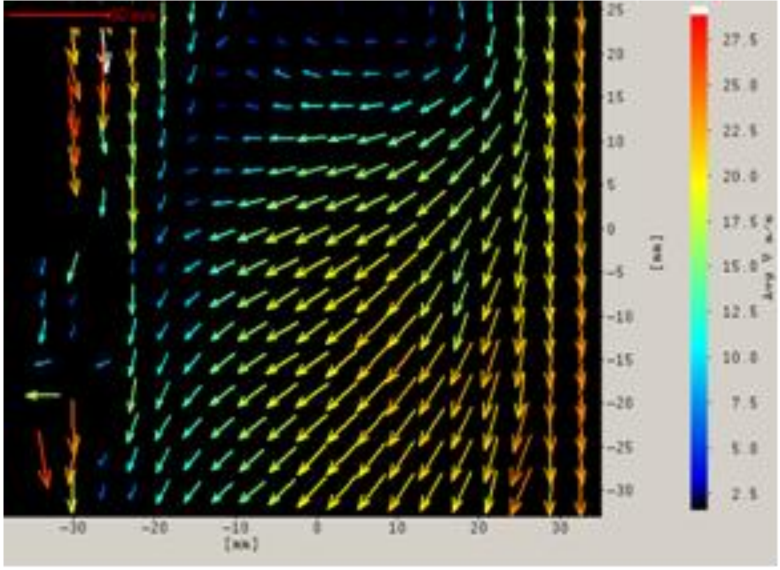

c) 250mm pressure drop, both valves 5mm, 90°

Figure 6.9: Comparison between valve configurations (Tumble flow)

Effects of Valve Lift

Figure 6.10 shows the variations in flow structures created by varying the valve lift. As expected the flow structure remains similar, but the velocities within these structures increase with increasing valve lift. The maximum inlet velocity observed for the 10mm valve lift is actually found to be slightly higher than at the 8mm valve lift. This correlates well with the calculated maximum velocities that were obtained by the measured volumetric flow rate. The obtained maximum inlet velocity for the 10mm valve lift is 48.6 m/s and for the 8mm valve lift is 45.7 m/s. It is also noted that the vortex core found to move slightly closer to the cylinder axis and down far away from the flame face where the valve lift was increased. It can be seen that in the left portion of the cylinder, the vector field is poorly represented. This is believed to be a result of a higher density of seeding particles entering the cylinder, and hence causing an increase in the level of reflected light or the cylinder liner reflection. Thus, the density of seeding particles should be reduced in order to eliminate the level of reflected light.

Effects of Increasing Pressure Drop

The variation in tumble flow structures produced by increasing the pressure drop across the cylinder head from 250mm of H_2O to 635mm of H_2O is shown in Figure 6.11. The flow structures remain of similar orientation. However, the magnitude of the velocities within these flow structures is increased. It was noted that an increase in pressure drop, similar to an increase in valve lift, reduces the area from which vector fields can be produced. This, again, is due to the higher level of seeding within the cylinder, which is causing an increase in scattered light and generating optical flare noise at the cylinder wall. It was noticed also that an increase in pressure drop moves the vortex core slightly closer to the cylinder axis, similar to an increase in valve lift as explained earlier.

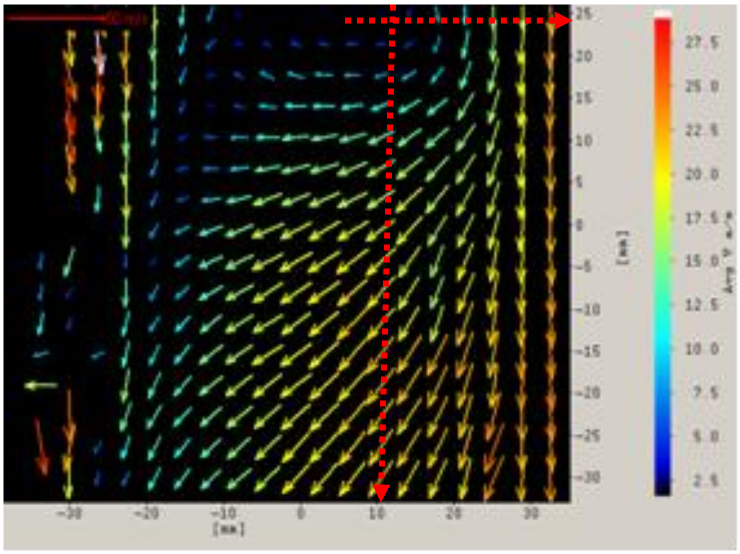

a) 250mm pressure drop, both valves 5mm, 90°

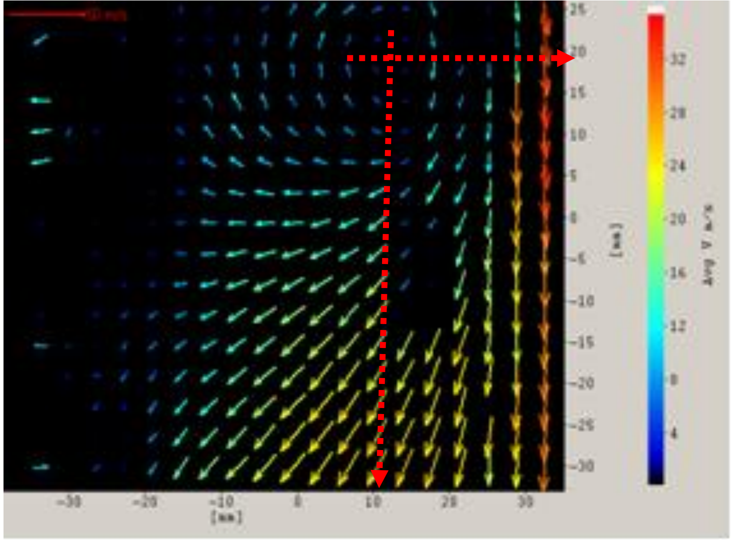

b) 250mm pressure drop, both valves 8mm, 90°

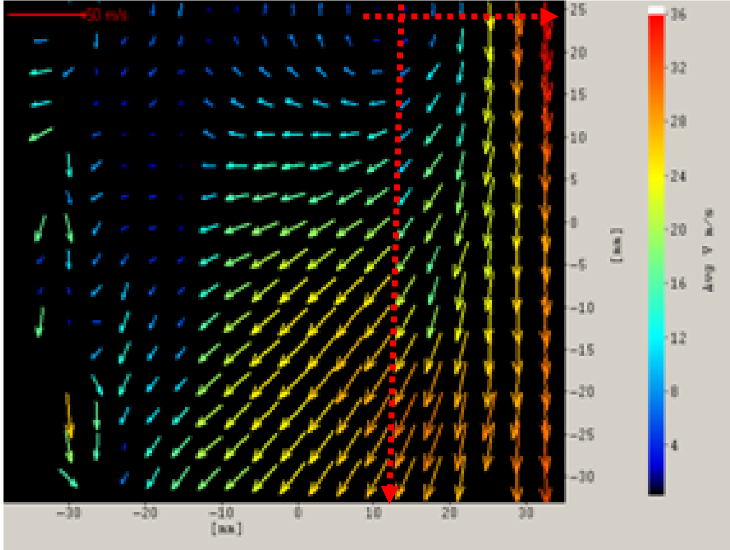

c) 250mm pressure drop, both valves 10mm, 90°

Figure 6.10: Effect of valve lift on flow structures on vertical plane

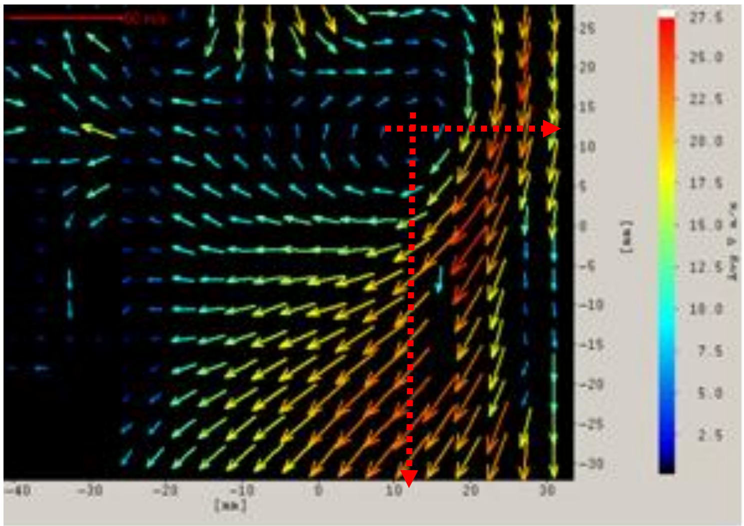

a) 250mm pressure drop, both valves 8mm, 120°

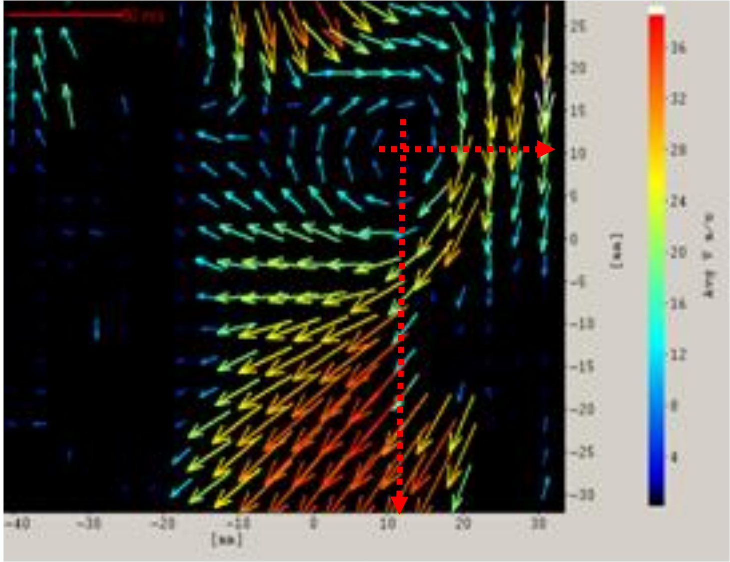

b) 635mm pressure drop, both valves 8mm, 120°

Figure 6.11: Tumble flow structure variation as a function of pressure drop

6.3.3: Swirl and Tumble Ratios

In the current work, the PIV velocity fields are obtained under steady state conditions and used to calculate both the tumble and swirl ratios in order to obtain an indication of the significance of pressure drop and valve lift. Several methods of calculating the tumble and swirl ratios can be used as described in Section 2.2.2. The full vector field of the plane and both axial and radial components of velocity have been involved in the calculations using Equations 2.8 and 2.9.

Swirl ratio was calculated for several valve configurations at two pressure drops as illustrated in Table 6.2. Tumble ratio was also calculated for several valve configurations at two pressure drops and for two planes (120^o, 90^o) as can be seen in Table 6.3. The tumble ratio calculations were obtained from the vertical PIV measurements. While the swirl ratio calculations were obtained from the horizontal PIV measurements. Note that negative values of the swirl and tumble ratios indicate the direction of vortices is anti-clockwise.

Table 6.2: Swirl ratio calculation

Pressure Drop (mm of H2O)	**Left Valve Lift (mm)**	**Right Valve Lift (mm)**	**PIV Swirl ratio**	
			Eq. 2.8	**Eq. 2.9**
250	2	0	-0.005	-0.158
	0	2	-0.138	-0.148
	2	2	0.039	0.089
	5	0	-0.036	-0.248
	0	5	0.184	0.196
	5	5	-0.011	-0.008
	8	0	-0.052	-0.359
	0	8	0.003	0.263
	8	8	-0.012	-0.006
	10	10	-0.068	-0.043
635	2	2	-0.012	-0.079
	5	5	0.041	0.017
	8	0	-0.078	-0.334
	0	8	0.057	0.255
	8	8	0.019	0.008
	10	10	-0.048	-0.037

Table 6.3: Tumble ratio calculation

Pressure Drop (mm of H_2O)	**Plane (degree)**	**Left Valve Lift (mm)**	**Right Valve Lift (mm)**	**PIV Tumble ratio**	
				Eq. 2.8	Eq. 2.9
250	120	8	0	0.354	0.474
		8	8	-0.173	-0.677
	90	10	0	-0.026	-0.212
		2	2	-0.118	0.376
		5	5	-0.238	-0.561
		8	8	0.349	0.944
635	120	8	0	0.161	0.236
		8	8	-0.054	-0.457
	90	2	2	0.263	0.314
		5	5	-0.316	0.899
		8	8	0.383	0.897
		10	0	0.484	-0.264

Figure 6.12 shows that single valve configurations at high valve lifts have higher magnitude of swirl ratios. It can also be noted that there is no significant impact of the pressure drop on the swirl ratios except a slight increase at high pressure drop at high valve lift (Lv/Dv >0.15) for the both valves open configuration. It can be noted that tumble ratios declined when the pressure drop was increased in the plane 120^o, while in plane 90^o, a slight increase of the tumble ratio was obtained as can be seen in Table 6.3. It was found that as the valve lift is increased, an obvious increase was observed for tumble ratio values but the swirl ratio values diminished. The obtained results for tumble ratio are higher than the swirl ratio values. This agreed well with the purpose of designing the engine cylinder head, which is to generate strong tumble structure inside the cylinder.

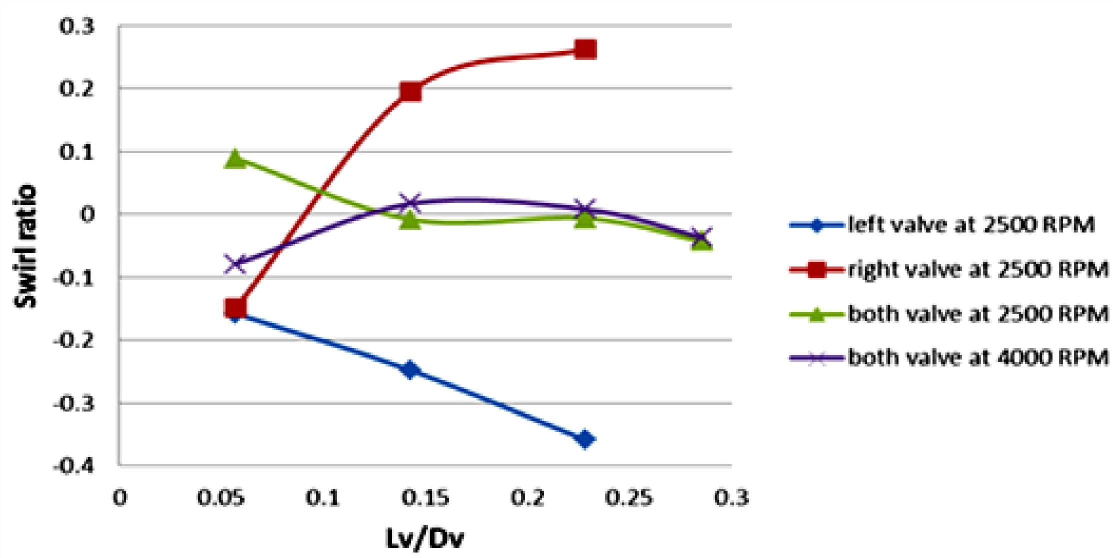

Figure 6.12: Swirl ratios vs. valve lift comparisons at 2500 and 4000 RPM

6.4: Influence of the Number of Image Pairs

In the PIV measurements, such technique is based on recording a specified number of instantaneous velocity fields to calculate either mean flow field or RMS values. The number of image pairs captured plays a significant role that should be enough in order to obtain converging statistics of the unstable flow field. Stansfield (2008) reported that statistical analyses indicate that the required image pairs for the mean flow field is 600 in order to achieve 99% certainty of ±1%. However, the RMS field calculation requires approximately 2400 image pairs or more to reach the same certainty mentioned above as investigated by Hollis (2004). Stansfield (2008) performed a study to confirm the sufficient image pairs that ensure the converged values for mean flow field. He found that 50 image pairs are enough. In the current investigation, a number of image pairs were recorded such as (400, 800 and 1200 image pairs) for the RMS field calculations. The influence of theses on the RMS values was observed as shown in Figures 6.13 and 6.14. It is found that as the number of image pairs increased, changes in the RMS values were detected as can be seen in Figure 6.14. A dramatic drop was observed between the 50 and 400 image pairs and then the deviation of RMS values reduced as the number of image pairs increased. It is anticipated that as the number of image pairs increased, the deviation of RMS values trends to be stable. In the current investigation, 1200 image pairs were used and a comparison with the predicted results with the RSTM turbulence model was obtained. There are several limitations restrict conducting the measurements with more than 1200 image pairs. First, the used laser source in the current investigation had some problematic related to miss firing during the long running. Secondly, the optical liner was smeared due to applying high density of seeding particles in the current experimental setting up.

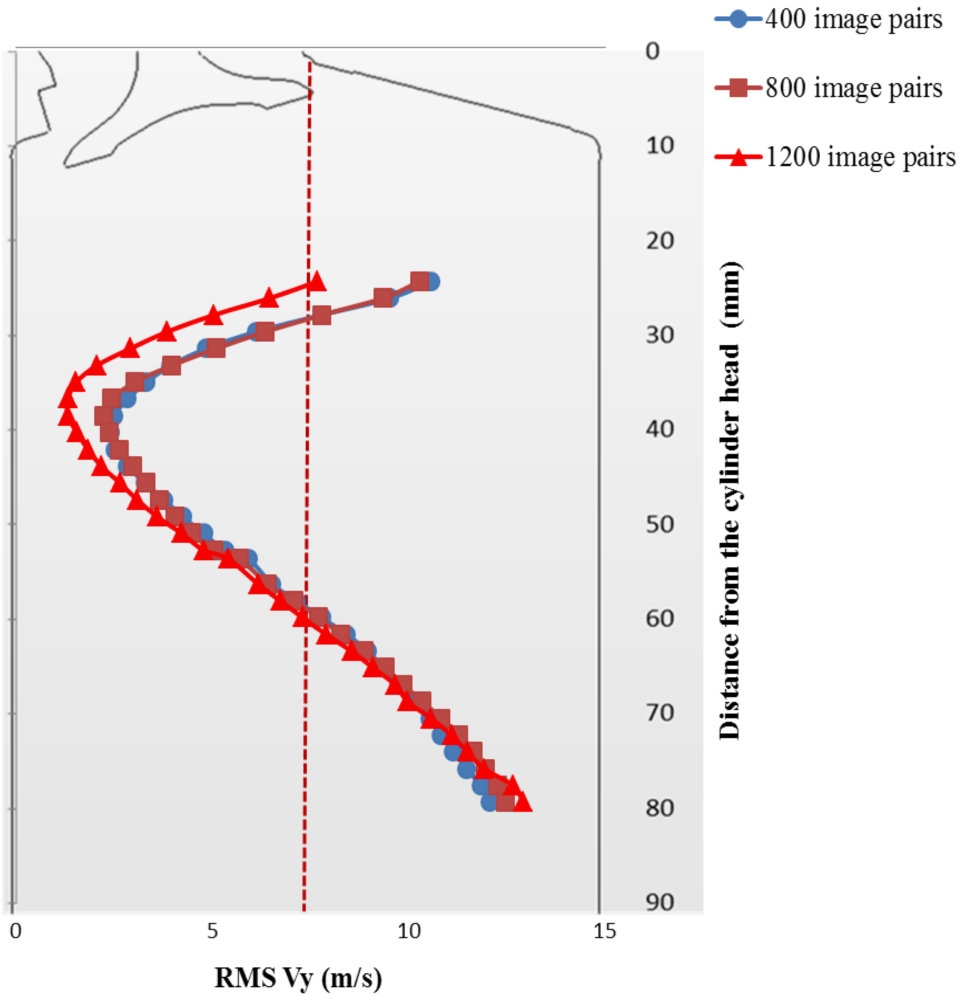

Figure 6.13: Fluctuating velocity in y-direction with different number of image pairs (400, 800 and 1200) for 5mm valve lift and both valves opened and 250mm of H_2O pressure drop

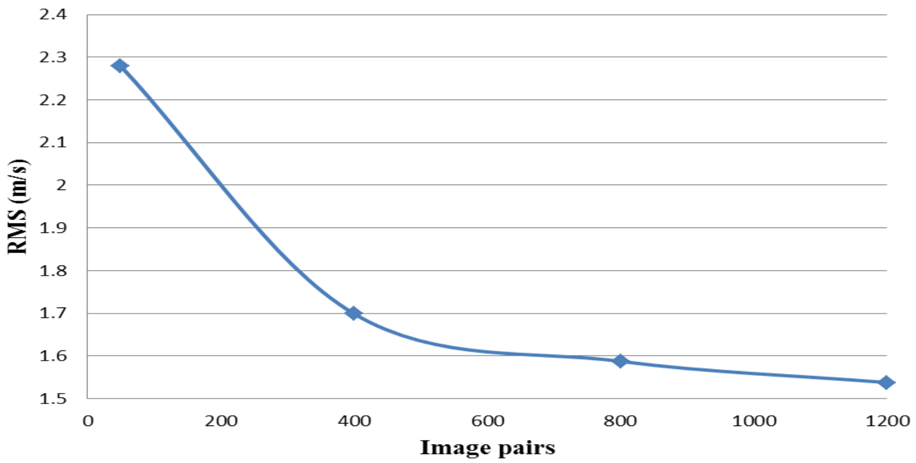

a) RMS values at cylinder centre x=0, y=13.5 mm

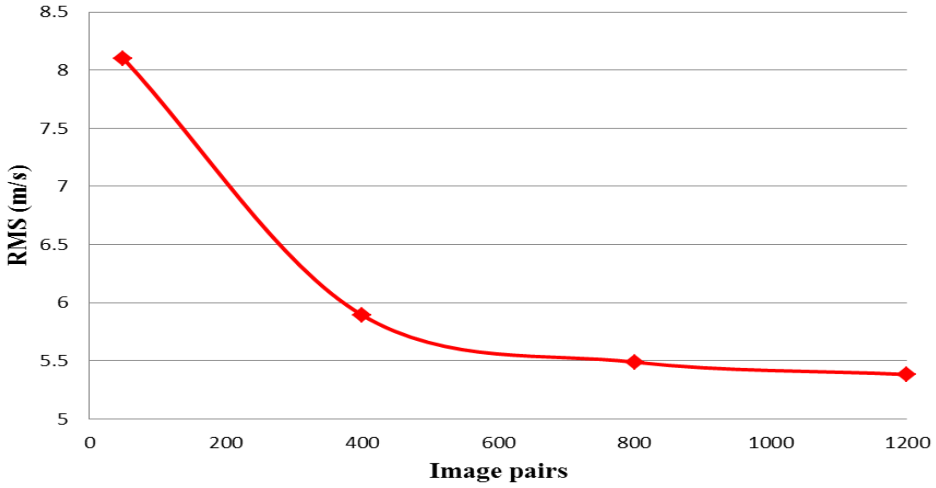

b) RMS values at x=3.6mm, y=21.3mm

Figure 6.14: Fluctuating velocity values in y-direction vs. number of image pairs at different positions

6.5: Swirl and Impulse Torque Meters Analysis

Rotational velocity of the flow N_f (RPM) was recorded directly via a swirl meter. The swirl ratios were then calculated by dividing the angular velocity of the flow ω_f (rad/sec)= $2\pi N_f$ by the engine speed. Figure 6.15 shows that swirl ratios at low valve lifts are small or zeros. However, swirl ratios are increased at high valve lifts. It can be seen that single valve configuration at high lifts has higher swirl ratios magnitude. For both valves opened configuration, the swirl ratio values are small or zero at low valve lifts and tends to be same values at higher valve lifts. Moreover, there is no significant impact of the pressure drop on the swirl ratios except slightly increase at high-pressure drop after high valve lift (Lv/Dv >0.2).

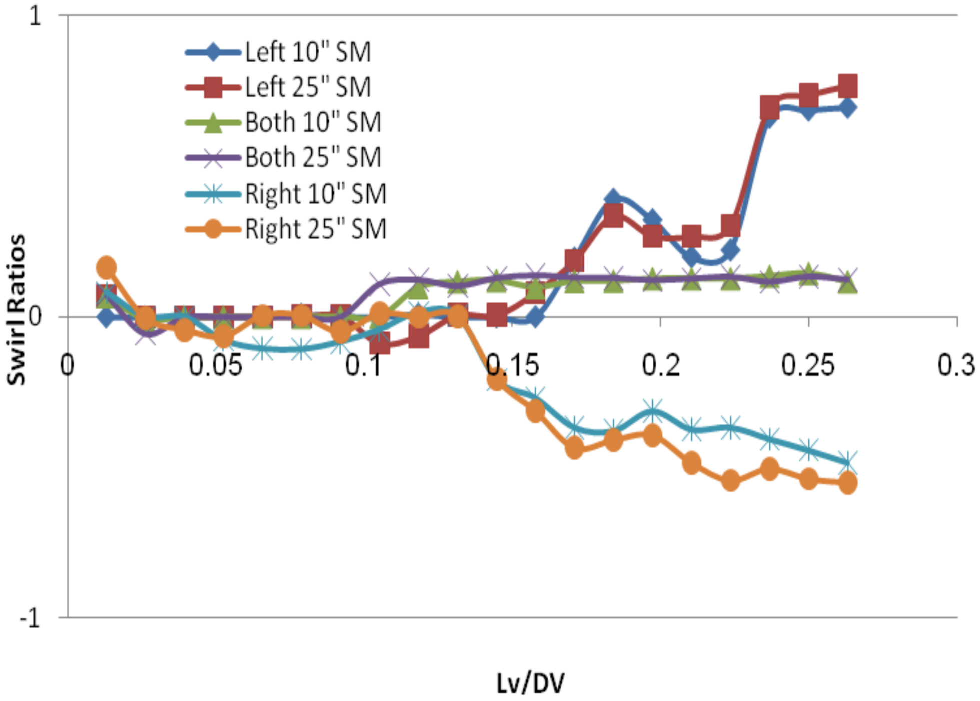

Figure 6.15: Swirl ratios via swirl meter plot

The torque meter was also used to measure the torque generated by the flow and then angular velocity was obtained to calculate the swirl ratios. Figure 6.16 illustrates that swirl ratios at single valve configurations are higher magnitude than both valve configuration. In contrast to swirl meter results, swirl torque meter gives higher magnitude and anti-clockwise swirl ratios. Either this is as result of the calibration of torque meter or it might be mounted in opposite position. The underestimate values of paddle wheel meter are due to the slip between wheel blades as the flow exerts torque on the paddle wheel. Monaghan and Pettifer (1981) suggested that the paddle meter should underestimate swirl by approximately 1.2 to 1.75 times and for the SCORE head, it is approximately 2 to 2.5 times higher at valve lift above 5mm. this is as result of the high axial flow at the outer radii of the cylinder and high recirculation flow close to the cylinder wall.

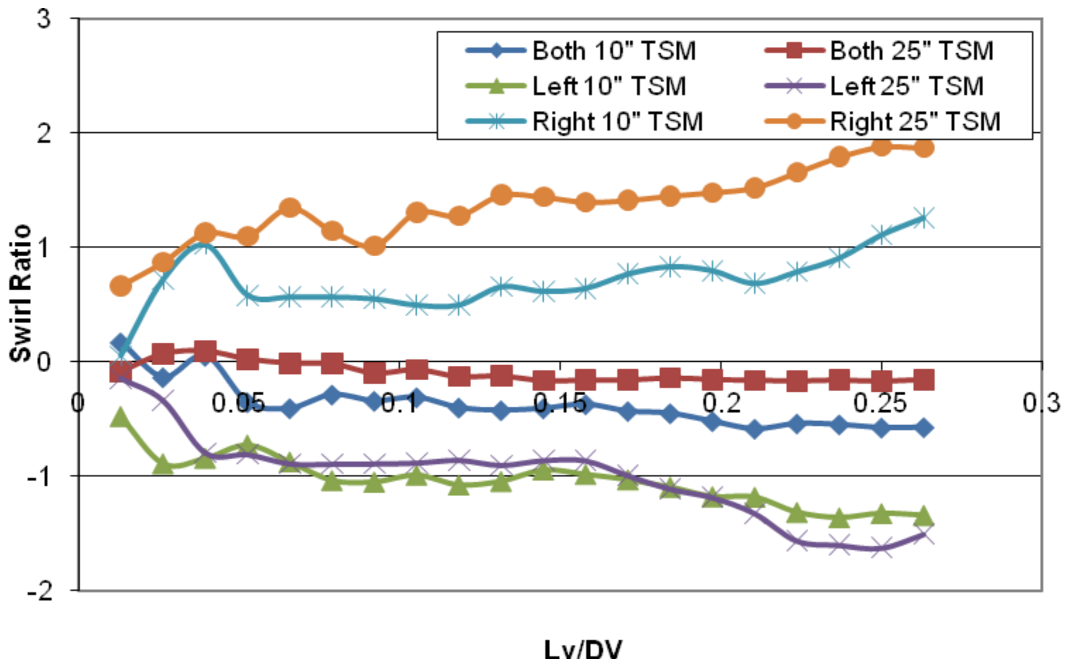

Figure 6.16: Swirl ratios via swirl torque meter plot

6.6: Summary

In this Chapter, results from the experimental analysis of the in-cylinder flow structure under steady state conditions utilising Particle Image Velocimetry (PIV) and swirl and torque meters are presented and discussed. The experiments have been conducted for a range of valve lifts (1mm- 10mm) with increment of 0.5 mm, and for three cases of inlet valve configurations; both inlet valves are opened, right inlet valve is opened only and left inlet valve is opened only. These measurements were carried out at four pressure drops, 127mm, 250mm, 445mm and 635mm of H_2O that correlate with engine speeds of 1750, 2500, 3000 and 4000 RPM respectively. The flow characteristic through the intake port was carried out on rapid prototyped cylinder head utilising the airflow rig. The investigation of steady flow valve performance was carried out in order to measure the discrepancy between the real engine head and the rapid prototyped cylinder head. The influence of increasing the valve lift and pressure drops on the mass flow rate and discharge coefficient was discussed and represented.

From the PIV two-dimensional in-cylinder flow measurements, a tumble flow analysis is carried out for six planes parallel to the cylinder axis (0^o, 30^o, 60^o, 90^o, 120^o, 150^o). In addition, a swirl flow analysis is carried out for one horizontal plane perpendicular to the cylinder axis at half bore downstream from the cylinder head (44mm). A swirl and tumble ratios were obtained from both swirl meter and 2-D PIV measurements. The influence of different number of PIV image pairs measurements was presented. Swirl ratios were calculated at a target distance about at half bore downstream from the cylinder head (44mm) and tumble ratios were calculated for number of vertical planes.

Chapter 7

Numerical Analysis of the In-cylinder Flows: Results and Discussions

7.1: Introduction

Results from the numerical analysis of the flow structure generated inside a single cylinder engine under steady state conditions are presented and discussed in this Chapter. The results are obtained using the finite-volume CFD package, STAR CCM+. Two turbulence models have been examined to simulate the turbulent flow structure in the current study, namely, the Realizable k-ε and Reynolds stress models (RSM) as described in Section 5.2.1. Three-dimensional numerical simulations have been conducted on a single cylinder Lotus engine with a pent-roof type head, as described in Section 4.1.1, for a number of fixed valve lifts (2mm, 5mm and 8mm) at two pressure drops 250mm and 635mm of H_2O that is equivalent to engine speeds of 2500 and 4000 RPM respectively. This correlation between pressure drop and engine speed is provided by Lotus engineering according to real engine studies. Three densities of generated mesh, which is polyhedral type, are examined. Numerical analysis was employed to investigate tumble and swirl flow motions formed within the cylinder under steady state condition utilising RSM for a number of swirl and tumble planes. The nature of the flow structure together with discussions on the influence of the pressure drop and valve lifts parameters on the flow structures are presented and discussed. In the current work, the CFD velocity fields, obtained under steady state conditions, were used to calculate swirl and tumble ratios.

7.2: Modelling Sensitivity

The computational grid or mesh should be sufficiently refined and adapted so that the flow structure can be resolved. The grid used here is polyhedral type and was generated with the STAR CCM+, version 5.06.010. Grid independency tests were carried out by using three cases of grid density. Table 7.1 shows the number of computational cells in each case, and Figure 7.1 shows the three grid densities used in the current investigation. The mesh size range is from 1mm in the intake port to 0.5mm in the more critical areas. In the cylinder liner part of the mesh, cells do not exceed 1mm in width. Mean velocity profiles were obtained along the dotted vertical line in the centre of the cylinder and which the results obtained with different mesh densities will be compared.

Table 7.1: The computational mesh densities cases

Three cases	Low mesh	Medium mesh	Refined mesh
# of cells	700,000	1000,000	1,700,000

A discrepancy was noticed in the predicted x-component of mean velocity in the corresponding to y-component when the grid density increases as can be seen in Figure 7.2 and Figure 7.3. The percentage difference for these x-component and y-component values can be seen in Table 7.2 and Table 7.3 following each of the plots. The difference is seen between mesh density cases in the predicted x-component of mean velocity between 0<L<60mm and in the predicted y-component of mean velocity between 20mm<L<35mm, where L is the distance from the cylinder head. It was noticed that at L>60mm, small discrepancy about 1% is obtained between the three grids density cases (see Table 7.2). This might be due to the flow became fully established in this region.

a) Low mesh with 700,000 cells

b) Medium mesh with 1000,000 cells

c) Refined mesh with 1,700,000 cells

Figure 7.1: Generated mesh with three grid densities

It can be seen that all grids have similar trend and as expected, as the mesh density increases, more accurate results are obtained. The level discrepancies in x-component of mean velocity can be attributed to low velocities in this region. It was found that the results obtained using medium mesh case were close enough to those of the more refined mesh case, i.e. leading to a grid independent solution. Based on the results, the finest mesh was used for all simulations of in-cylinder flow structures.

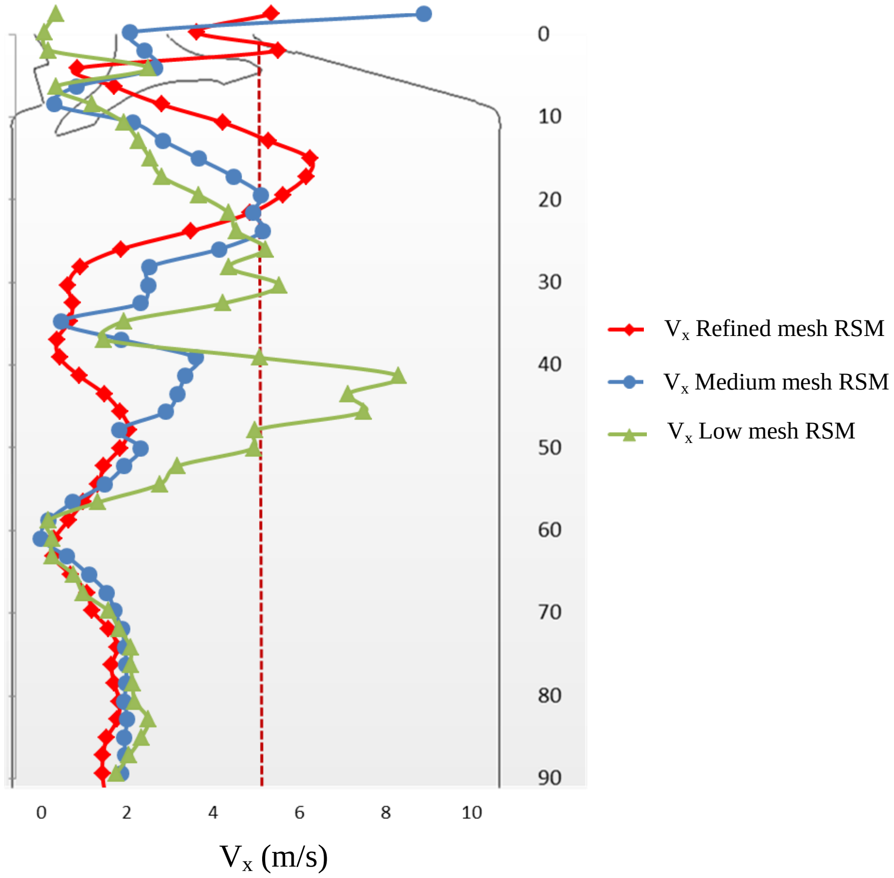

Figure 7.2: Mean velocity profiles of x- component for three mesh densities

Table 7.2: Percentage difference between velocity profiles of x-component for three mesh densities

Grid density case	**Region**		
	0<L<36mm	36mm<L<60mm	L>60mm
Low –medium meshes	2%	43.3%	1%
Medium –Refined meshes	5%	14%	1%

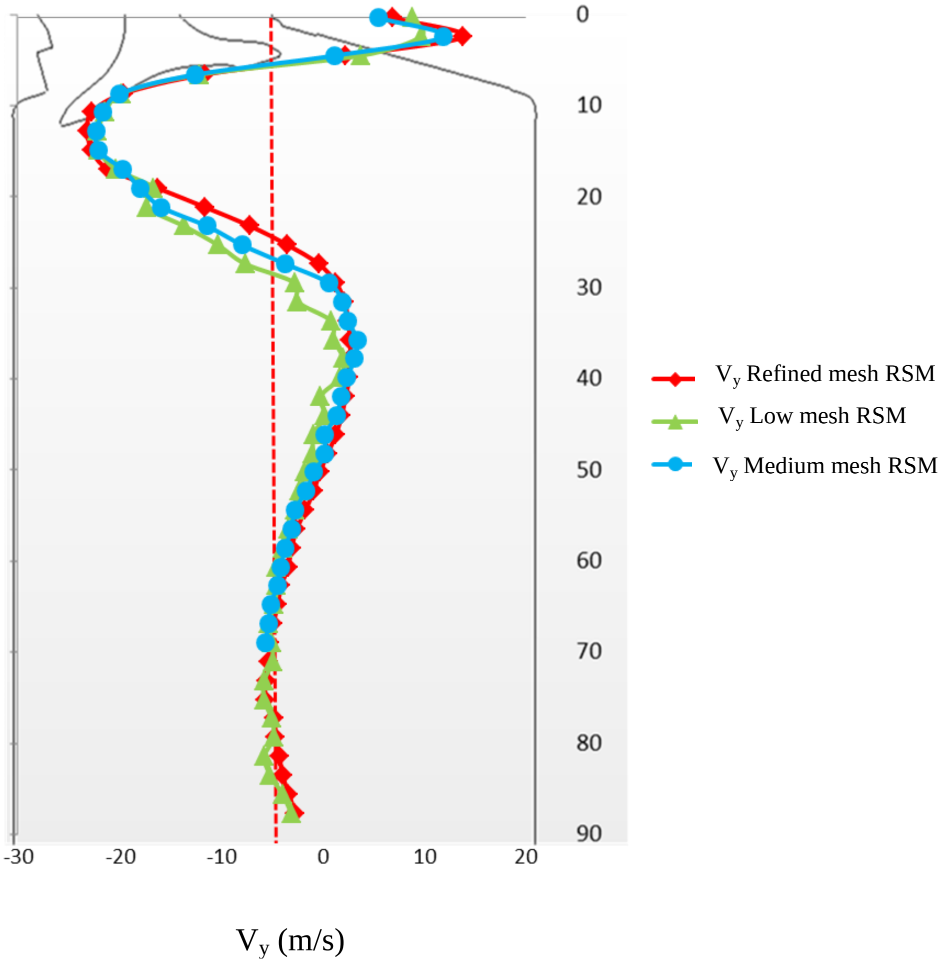

Figure 7.3: Mean velocity profiles of y-component for three mesh densities

Table 7.3: Percentage difference between velocity profiles of y-component for three mesh densities

Grid density case	**Region**
	20<L<35
Low –medium meshes	13.6%
Medium –Refined meshes	8.6%

7.3: Comparisons of Results from Two Turbulence Models

It is well known that there is no single turbulence model can be universally applied to all practical flow configurations. Several considerations must be taken into account when selecting a turbulence model including physics encompassed in the flow, the accuracy, and the availability of computational resources. Two turbulence models have been examined, in this study, in order to predict velocity fields inside the engine cylinder, namely, Realizable k-ε and Reynolds stress models (RSM). The flow velocity and its turbulence kinetic energy profiles were obtained along vertical lines in the centre of cylinder and close the cylinder wall that are shown as dotted lines in Figures 6.4 to 6.7. For the mean x-component velocity at the centre of the cylinder, both models show similar trends however, the Realizable k-ε model predicts significantly different velocity magnitudes as shown in the Figure 7.4. Moreover, similar observation can be seen in Figure 7.5 that shows the mean y-component velocity profile at the cylinder wall. The turbulence kinetic energy profiles at the centre of the cylinder are presented in Figure 7.6. The predicted results by the Realizable k-ε model show similar trends but differ quit significantly in magnitude from the results obtained from RSM model.

Generally, the results obtained by the Realizable k-ε model were less accurate than results obtained from the RSM model. The discrepancy between the RSM model results and those given by the Realizable k-ε model is due to that RSM model takes in account the anisotropic nature of the flow. Individual influences of the fluctuating magnitudes on the flow are important in several types of flows. This gives RSM model the ability to predict complex flows with good accuracy. However, the computational time was increased by applying RSM. The computational time by using a Linux PC contains 3.16GHz, dual Intel Core processors, having 8 Gb of RAM was about 48 hours and 430 hours for the Realizable k-ε and Reynolds stress models (RSM), respectively.

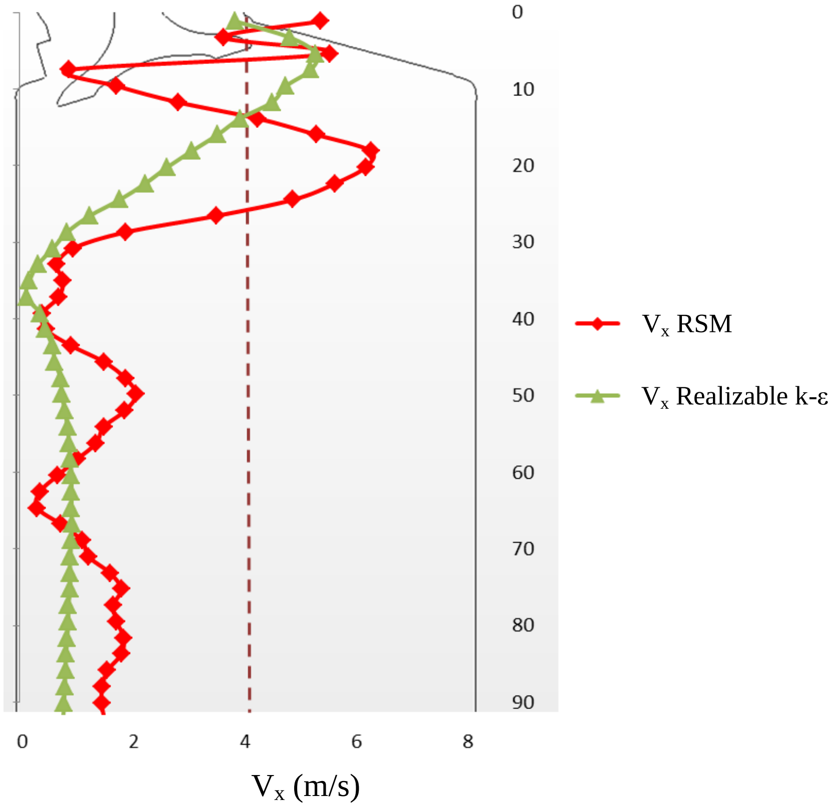

Figure 7.4: Mean velocity profiles of x-component at the centre of cylinder using two turbulence models

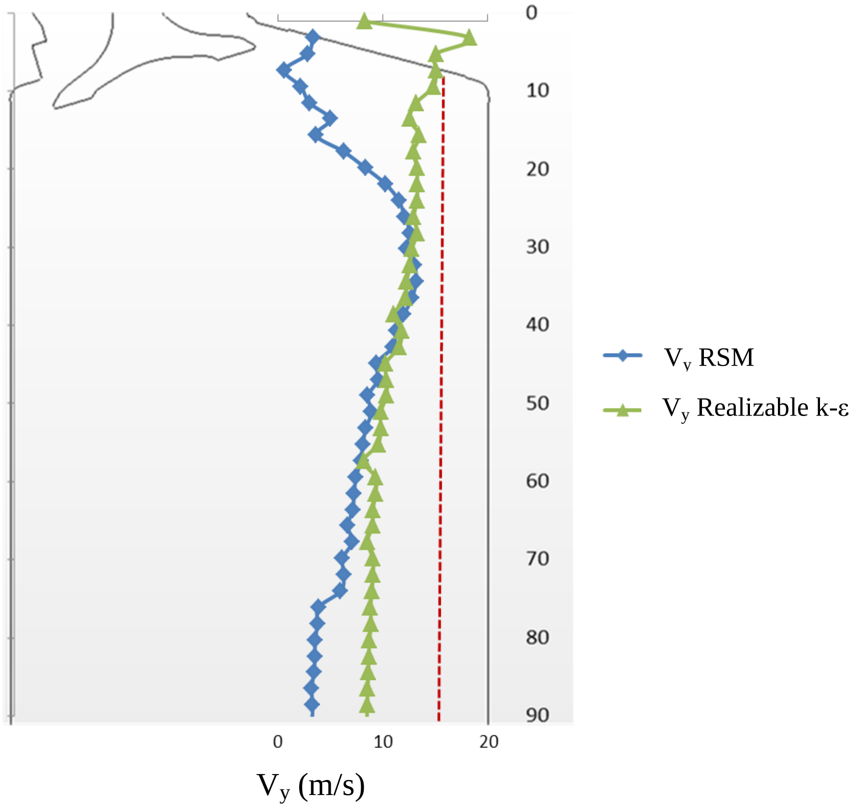

Figure 7.5: Mean velocity profiles of y- component at the cylinder wall using two turbulence models

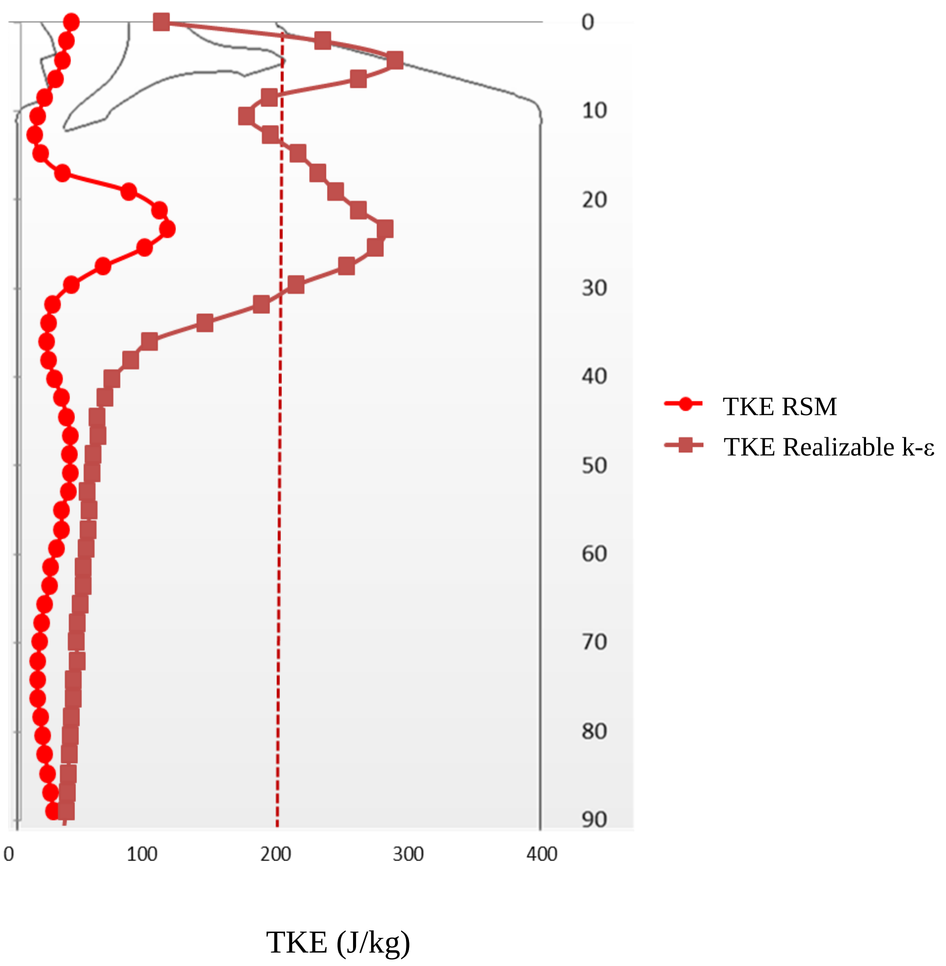

Figure 7.6: Turbulence kinetic energy profiles at the centre of cylinder using two turbulence models

Figure 7.7 shows profiles of the Reynolds stresses and the turbulence kinetic energy at a location close to the cylinder wall. The Reynolds stresses *uu*, *vv*, and *ww* components contribute to the total resolved turbulence kinetic energy level. Nevertheless, the magnitude and location of the peaks of the three components are not the same and this verifies that the flow turbulence is anisotropic in this region. Based on the above comparison between two turbulence models, the RSM model was used to calculate the turbulent flow structure of the flow field inside a single cylinder engine under steady state conditions. The calculated results are then validated with the experimental data as discussed in Chapter 8.

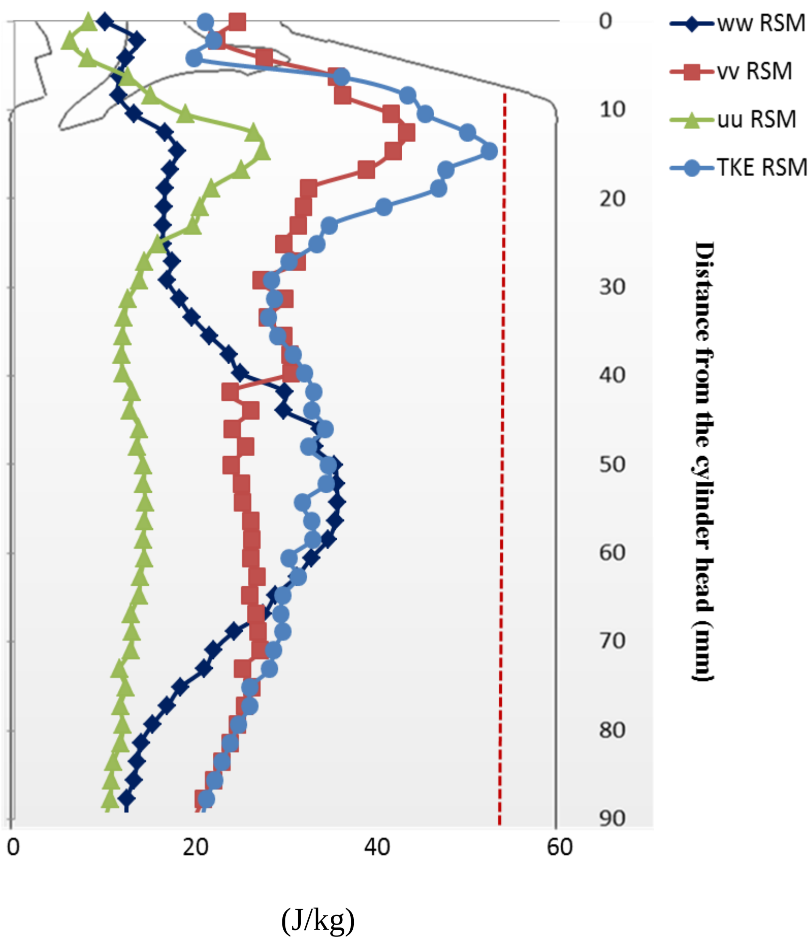

Figure 7.7: Reynolds stresses and TKE at the cylinder wall for both valves opened at 5mm and 25mm of H_2O pressure drop

7.4: Numerical Results for the Flow Structure

In the following sections, numerical results are presented. Swirl motions can be obtained from the horizontal planes. While tumble motions can be obtained from the vertical planes.

7.4.1: Horizontal Swirl Plane

In order to investigate the development of the flow structure in the axial direction along the cylinder, six planes under the cylinder head were considered as shown in Figure 7.8, namely at L=11, 22, 44, 66, 88 and 110 mm where L is the distance from the cylinder head to the plane. Figure 7.9 shows the flow structure produced with both valves open with 5mm and 250mm of H_2O pressure drop for the 6 planes. It can be seen that a number of small vortices are formed in the region close to the cylinder wall at the planes adjacent to the cylinder head as seen at L=11mm and 22mm. These vortices are then merged with each other to form two vortices at the later planes as seen at L=44mm, 66mm, 88mm and 110mm. It can, also, be noted that the right vortex is larger than the left one due to the maximum flow velocity from the right valve is being higher as obtained from PIV results (see Figures 6.5 and 6.6). It can be seen that as the distance from the cylinder head increases, the more established the flow becomes.

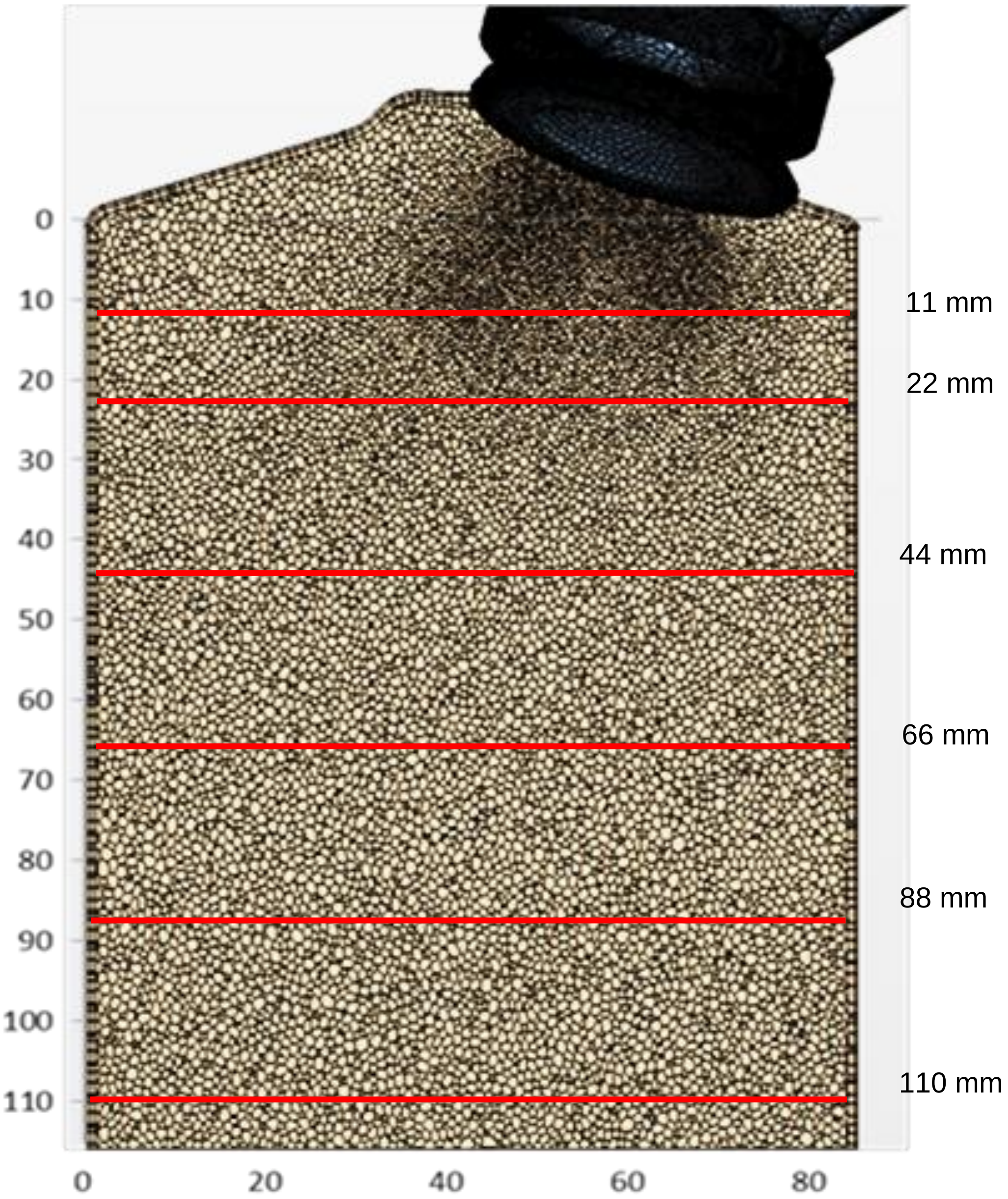

Figure 7.8: Location of horizontal planes

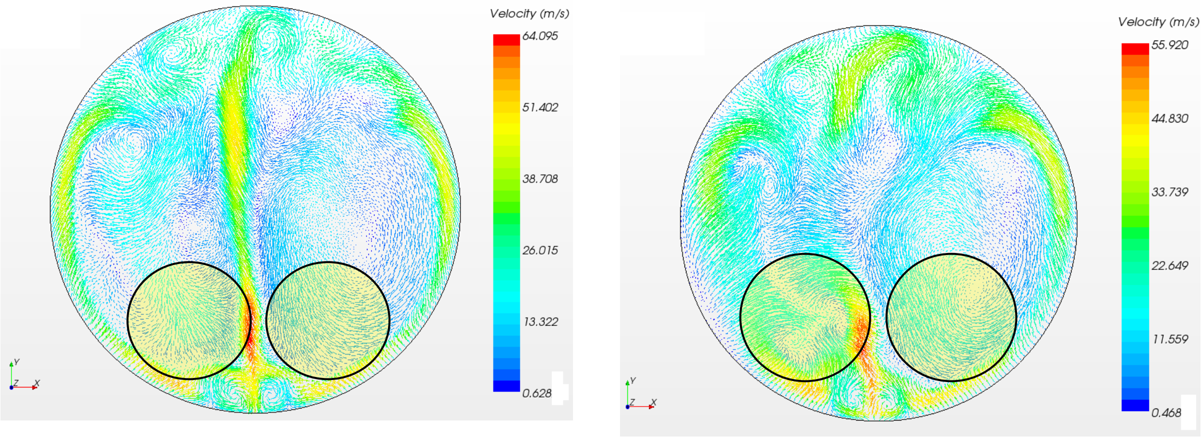

11mm 22mm

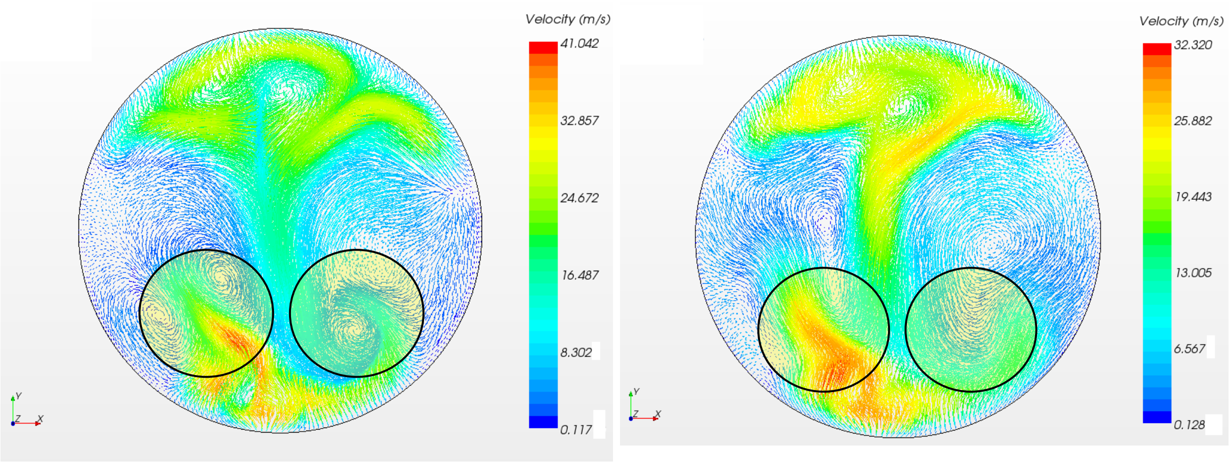

44mm 66mm

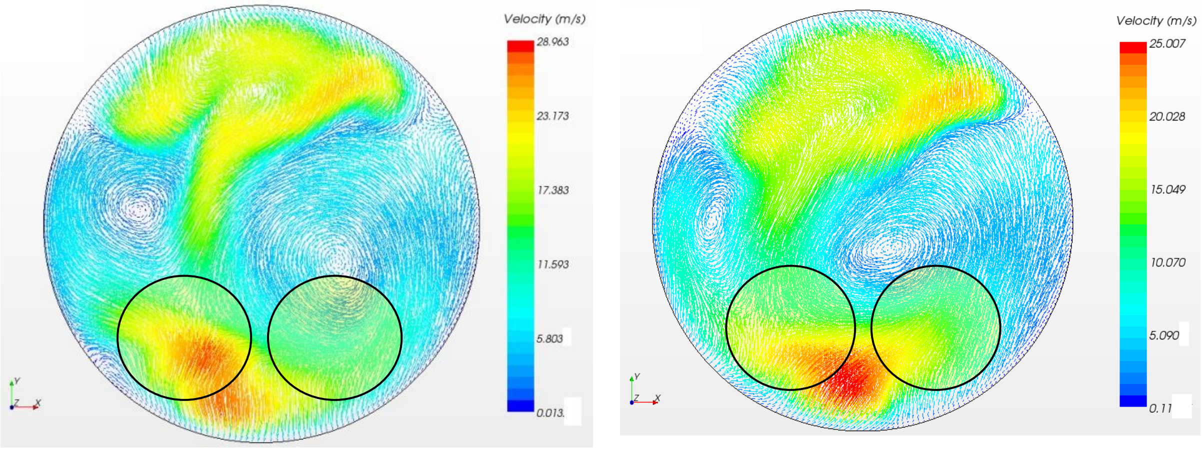

88mm 110mm

Figure 7.9: Sequence of flow structures development in the six swirl planes for 5mm valve lift and 250mm of H_2O pressure drop

Effects of Valve Lift

Variation in flow structures caused by various valve lifts is shown in Figure 7.10. The first observation made was the increase in the flow velocity when the valve lift is increased. The general patterns seen within the bulk flow motion show little variation with an increase in the valve lift. It can also be seen that the two counter-rotating vortices appeared in all images for all valve lifts. The formed vortices at 5mm and 8mm valve lift have the same vortices core as indicated in the Figure 7.10 *(b)* and *(c)* but the right vortex at 5mm valve lift has larger diameter due to the effect of the high jet from the right valve. Formation of small vortices has been observed at the top region close to the cylinder wall for 8mm valve lift. At 2mm valve lift, the two vortices are asymmetrical and the diameter of left vortex is larger from the right one as can be seen in Figure 7.10 *(a)*.

Effects of Increasing Pressure Drop

The variation in swirl flow structures caused by increasing pressure drop is shown in Figure 7.11. As can be seen from Figures 7.11 *(a)* and *(b)* the formed vortices preserve their shape in both images. The only change presents in most cases is in the vortex strength, with maximum velocities shown to be approximately 42% larger in the 635mm pressure drop case. This is slightly over predicted by about 5% compared with the Bernoulli calculations for the maximum inlet velocity with estimations for 250mm of H_2O is 65 m/sec and for 635mm of H_2O is 103 m/sec.

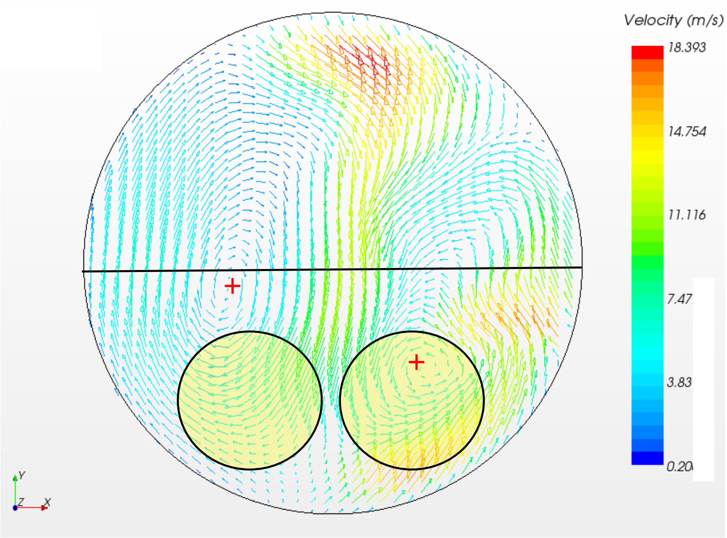

a) 2mm

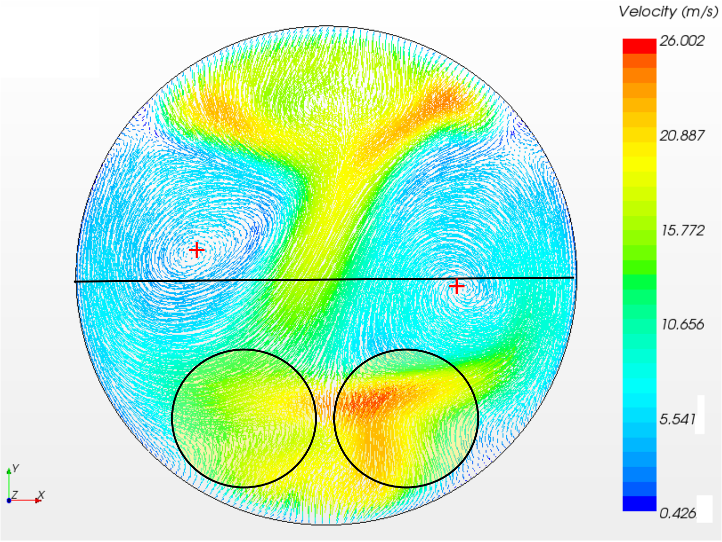

b) 5mm

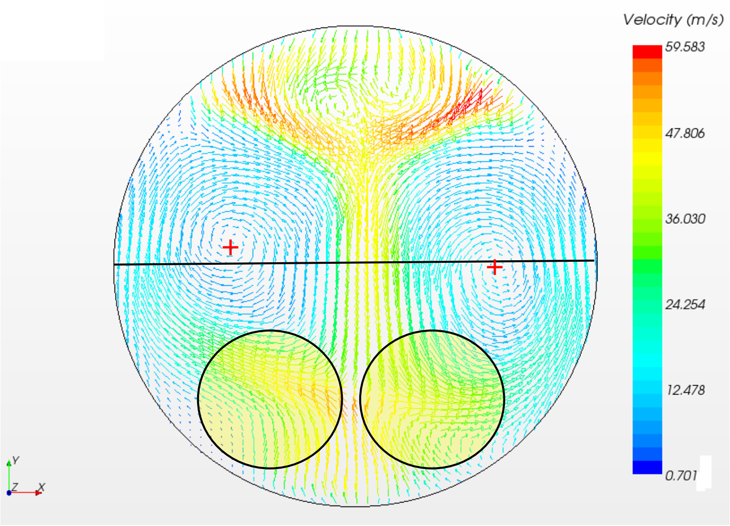

c) 8mm

Figure 7.10: Effect of valve lift on flow structures at L=88mm and 635m of H_2O pressure drop

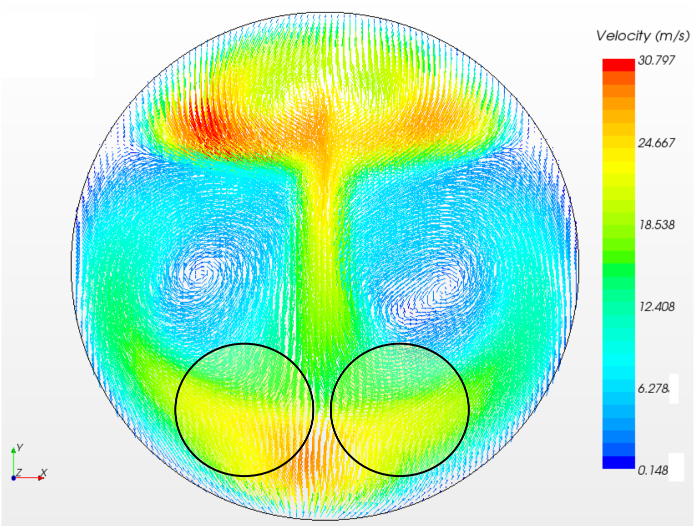

a) 250mm of H_2O

b) 635mm of H_2O

Figure 7.11: Effect of pressure drops on flow structures at L=110mm and 8mm valve lift

7.4.2: Tumble Flow Structure

The vertical planes positions under current analysis are shown in Figure 7.12. These planes are across the valve vertical, main tumble planes and a parallel plane to it on the right valve. Tumble flow structures produced by both valves being opened 2mm, 5mm and 8mm at two pressure drops 250mm of H_2O and 635mm of H_2O. The tumble flow motion analysis on such planes are described with discussion on the influence of the valve lifts and pressure drops parameters on the flow structures in the following Sections.

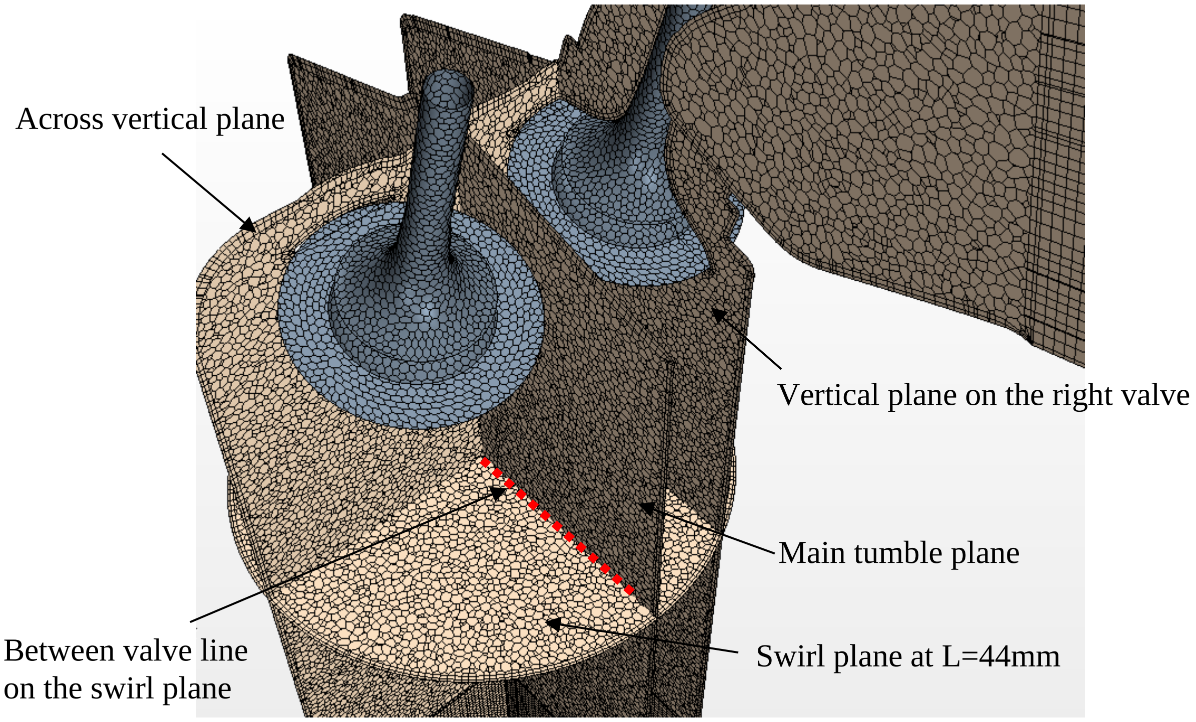

Figure 7.12: Locations of vertical planes and a horizontal plane at L=44mm

Effects of Valve Lift

Variations in flow structures created by varying the valve lift are shown in Figure 7.13. The flow structure is comprised of a single vortex for both cases. The tumble vortex was generated as the result of a strong jet flow, which comes out from the intake valves, on the cylinder wall. In general, the flow structures remain similar but the velocities within these structures increase with increasing valve lift. The vortex core found to move closer to the cylinder axis where the valve lift was increased. The reason of such movement can be explained clearly from the results shown in Figure 7.14, which represents the flow structure in vertical plane on the right valve. It can be seen, evidently, that the jet flow was separated away from the cylinder wall when the valve lift was increased. It can be noticed that the high velocity region appears close to the cylinder wall whereas the low velocity region exists in the cylinder centre. The cross point of the dashed lines shown in Figure 7.13 shows the vortex core and the small “square” in the Figure 7.14 shows the jet flow region.

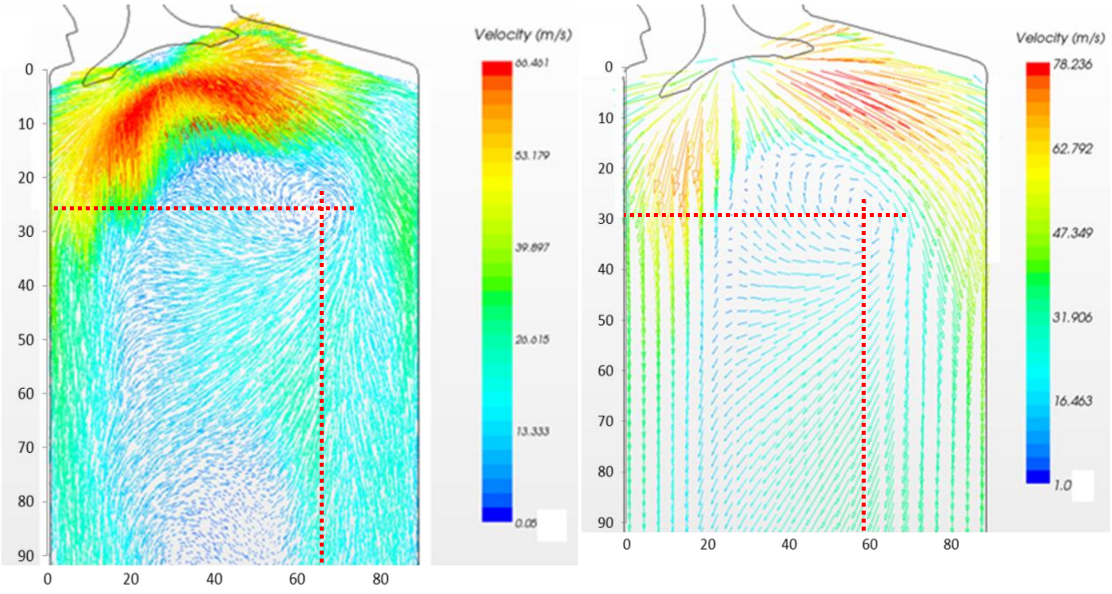

(a) (b)

Figure 7.13: Effect of valve lift on flow structures at 250mm of H_2O pressure drop - main tumble plane *a)* 5mm *b)* 8mm

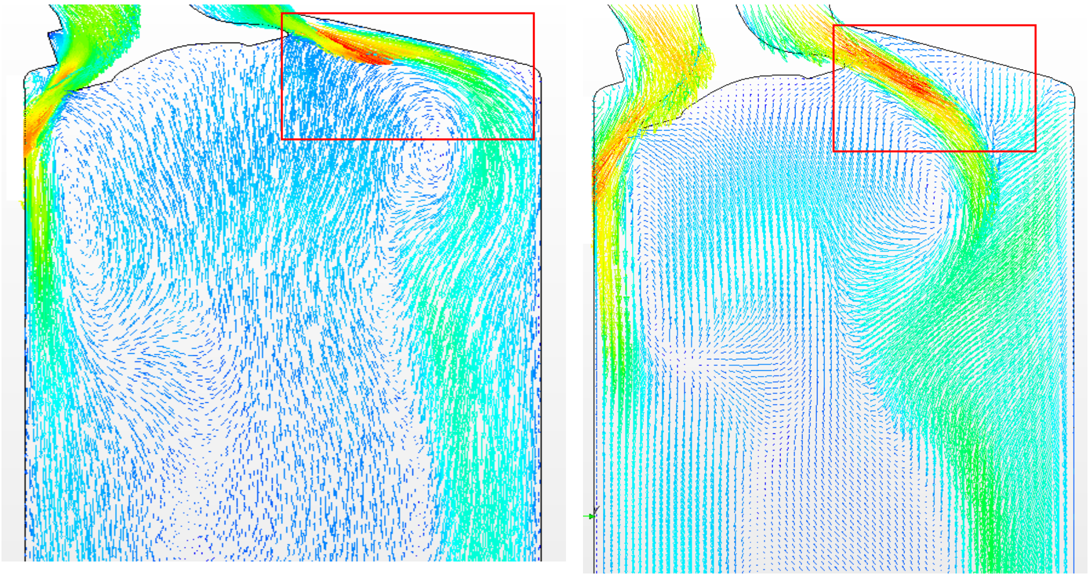

(a) (b)

Figure 7.14: Effect of valve lift on flow structures at 250mm of H_2O pressure drop - vertical plane on the right valve *a)* 5mm and *b)* 8mm

Effects of Increasing Pressure Drop

Variation in tumble flow structures, shown in Figure 7.15, is produced by increasing the pressure drop across the cylinder head from 250mm of H_2O to 635mm of H_2O. The flow structures remain of similar orientation, however, the magnitude of the velocities within these flow structures is increased as can be evidently seen in Figure 7.16 which shows the same flow structures produced in the across valves plane. It was noticed that an increase in pressure drop moves the vortex core closer to the cylinder axis, similar to an increase in valve lift as explained before.

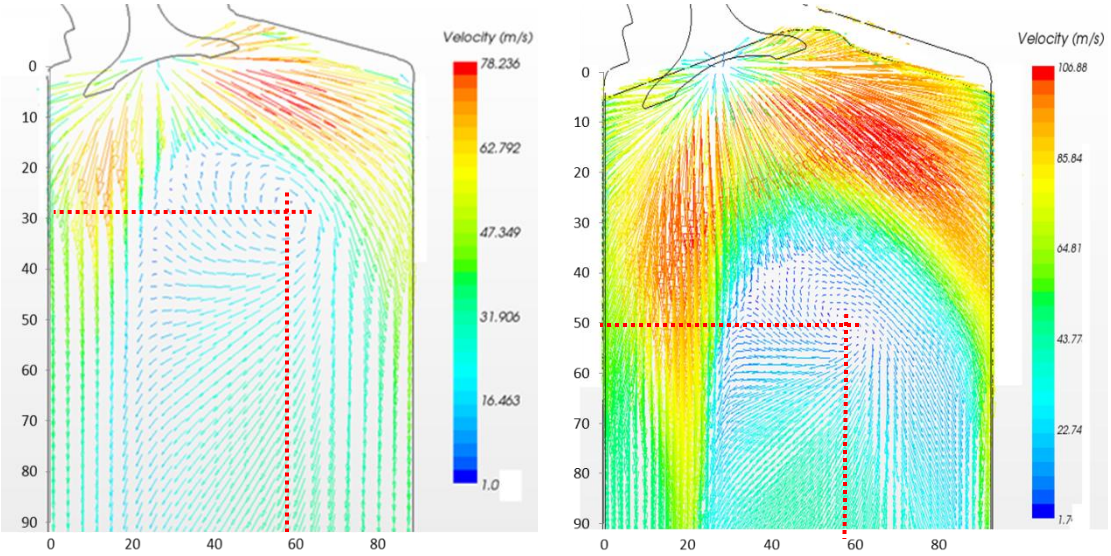

(a) *(b)*

Figure 7.15: Effect of pressure drops on flow structures at 8mm valve lift- between valves planes *a)* 250mm of H_2O and *b)* 635mm of H_2O

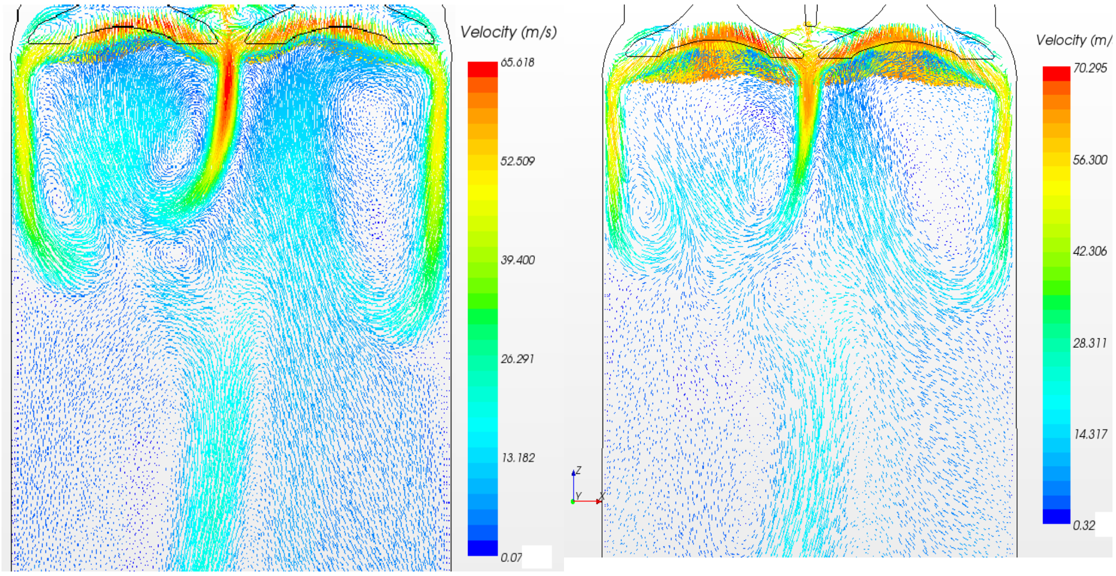

(a) *(b)*

Figure 7.16: Effect of pressure drops on flow structures at 5mm valve lift-across valves plane in the centre *a)* 250mm of H_2O and *b)* 635 mm of H_2O

7.5: Swirl and Tumble Ratios

In the current work, the numerical velocity fields obtained under steady state conditions were used to calculate both the tumble and swirl ratios in order to obtain an indication of the significance of pressure drop and valve lift. The same methods of calculating the tumble and swirl ratios was applied as explained in Section 6.3.2, and the full vector field of the plane and both axial and radial components of velocity have been involved in the calculations. Both swirl and tumble ratios were calculated for both valves opened configuration at two pressure drops as illustrated in Table 7.4. The tumble ratio calculations were obtained from the vertical plane (main tumble plane, 90^{o}). While the swirl ratio calculations were obtained from the horizontal plane placed downstream from the cylinder head at 44mm.

It can be noticed that the tumble ratio has higher values than the swirl ratio, see Table 7.4. This again proved that the tested head is a tumble head. The influence of valve lift was obvious on the tumble ratio when the valve lift is increased, tumble ratio values increased. However, there is no significance change on the swirl ratio values. It can also be noticed that there is no significant impact of the pressure drop on the swirl ratios except a slight increase at high-pressure drop at high valve lift. While, tumble ratio values increased when the pressure drop was increased as can be seen in Table 7.4.

Table 7.4: Calculated swirl and tumble ratios

Both valves opened configuration	**Pressure drop (mm of H_2O)**	**Swirl ratio**	**Tumble ratio**
Lv (mm)			
2	250	0.054	0.065
5		-0.019	0.14
8		-0.038	0.697
2	635	-0.025	0.084
5		-0.063	0.34
8		-0.047	0.782

7.6: Summary

In this Chapter, 3D-dimensional numerical simulations have been conducted under steady state conditions on a single cylinder Lotus engine with a pent-roof type head for a number of fixed valve lifts (2mm, 5mm and 8mm) at two pressure drops 250mm and 635mm of H_2O that is equivalent to engine speeds of 2500 and 4000 RPM respectively. The results are obtained using the finite-volume CFD package, STAR CCM+. Two turbulence models have been examined to simulate the turbulent flow structure in the current study, namely, the Realizable k-ε and Reynolds stress models (RSM). Three densities of generated mesh, which is polyhedral type, are examined. Numerical analysis was employed to investigate tumble and swirl flow motions formed within the cylinder utilising RSM for a number of swirl and tumble planes. The nature of the flow structure together with discussions on the influence of the pressure drop and valve lifts parameters on the flow structures are presented and discussed.

Chapter 8

Validation of Numerical Data with Experimental Data-Results and Discussions

8.1: Introduction

This Chapter presents and discuss validation of the computational results through qualitative and quantitative comparisons with the Particle Image Velocimetry (PIV) and Laser Doppler Anemometry (LDA) experimental measurements on both vertical and horizontal cross sections. Calculated results for the mean and fluctuations velocities (RMS velocity values) and turbulence intensity were validated against measured PIV data in this investigation and previously published experimental LDA data by Thomas (2006) that were completed on the same engine cylinder. Model validation is carried out in three ways: A Correlation coefficient (C) of the flow patterns between measured and calculated CFD data was calculated. The second method is a comparison for a specific data quantity such as the turbulence components or the mean velocity values on the vertical line parallel to the cylinder axis and on horizontal line perpendicular to cylinder axis. The strength of the rotating motions inside the cylinder is also quantified by a dimensionless swirl and tumble ratios, which were calculated and validated. The third method is through visualisation of the velocity vectors qualitatively from a regular zone.

8.2: Validating Calculated Results with PIV Measurements

8.2.1: Mass Flow Rate Validation

Evaluation of the mass flow rate is essential for the in-cylinder flow characterisation. The measurements were conducted for three valve lifts (2mm, 5mm, 8mm) and at two pressure drops of 250mm and 635mm of H_2O. Table 8.1 shows comparisons between the measured and predicted mass flow rate values. The predicted values show a reasonable correlation between the measured and calculated ideal values for medium valve lifts (5mm). At low and high valve lifts (2mm, 8mm), the discrepancy between the measured and the predicted mass flow rate values is increased. A possible contributor to this over predicted mass flow is size and density of generated mesh in the valve gap region that may require to be refined. The ideal mass flow rate values were calculated by using Equation 2.2.

Table 8.1: Mass flow rate comparisons for measured, calculated and ideal values

L_v (mm)	**Pressure drop (mm of H_2O)**	**Measured $\dot{m}$ Air flow rig (kg/s)**	**Calculated $\dot{m}$ (kg/s)**	**Ideal value $\dot{m_{ideal}}$ (kg/s)**	**% between Air flow rig and calculated results**
2	250	0.021	0.029	0.0328	27.5
5		0.051	0.054	0.082	5.5
8		0.075	0.114	0.131	34.2
2	635	0.037	0.044	0.051	15.9
5		0.086	0.083	0.128	3.4
8		0.129	0.188	0.205	31.3

Figure 8.1 shows the mass flow rate through the intake valves across a range of fixed lifts and at two pressures drops. It can be seen that the predicted mass flow rate correlates well with the measured values. In general, it was found that increasing the valve lift and test pressure drop can increase the air flow through the intake port.

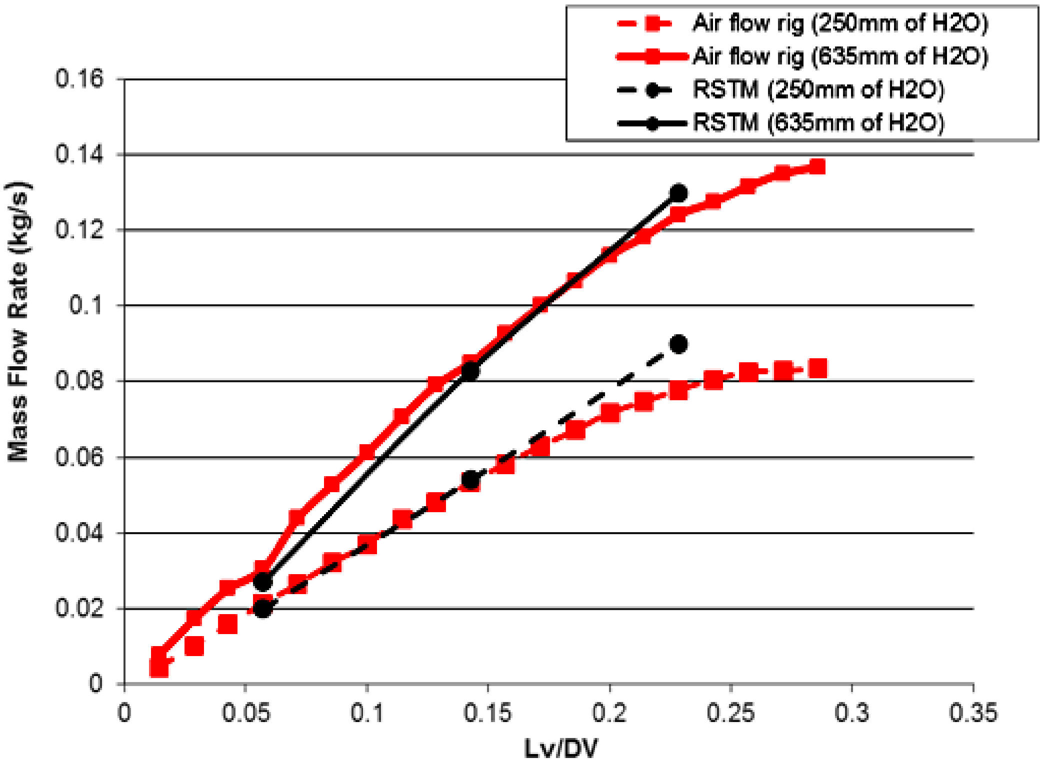

Figure 8.1: Mass flow rate comparisons

8.2.2: Correlation Coefficient Calculation

A quantitative comparison of the flow patterns between the PIV measurements and the calculated CFD data was carried out using a correlation coefficient (C) as suggested by Ishida *et al.* (2011), Equations 8.1-8.3. This was used as a validation of the accuracy of the RSM turbulence model results.

$$C = \frac{\sum_{x,y} \vec{V}_{PIV} \cdot \vec{V}_{CFD}}{\left|\vec{V}_{PIV}\right|\left|\vec{V}_{CFD}\right|} \tag{8.1}$$

$$\vec{V}_{PIV} = (V^1_{PIVx}, V^2_{PIVx}, \ldots, V^n_{PIVx}, V^1_{PIVy}, V^2_{PIVy}, \ldots, V^n_{PIVy}) \tag{8.2}$$

$$\vec{V}_{CFD} = (V^1_{CFDx}, V^2_{CFDx}, \ldots, V^n_{CFDx}, V^1_{CFDy}, V^2_{CFDy}, \ldots, V^n_{CFDy}) \tag{8.3}$$

Where V_{PIVx}, $V_{PIVy,}$ V_{CFDx} and V_{CFDy} are x and y components of the velocity vectors from PIV and CFD respectively. For the purpose of convenient, it is practical to conduct a sensitivity analysis with the correlation coefficient that is applied. The sensitivity coefficient is calculated as shown in Table 8.2.

Table 8.2: Sensitivity calculation

Parameters $(\boldsymbol{x_i})$	$\frac{\boldsymbol{\partial C}}{\boldsymbol{\partial x_i}} =$	**Sensitivity coefficient**
V_{PIV}	$\frac{-\sum_{x,y} V_{CFD}}{\lvert V_{CFD}\rvert \, V_{PIV}^2}$	0.716
V_{CFD}	$\frac{-\sum_{x,y} V_{PIV}}{\lvert V_{PIV}\rvert \, V_{CFD}^2}$	0.759

The calculated correlation coefficients for the mean velocities are shown in Table 8.3 and Figure 8.2. This indicates that the accuracy of the RSM model are good for low and medium valve lifts. At a higher valve lift of 8mm, the prediction accuracy was lower, this is because of the missing data in the PIV images due to high reflection from the cylinder surface. High flare from reflected laser light was reduced by conducting preliminary steps in the experimental set up as mentioned earlier in Section 4.1.6, in order to improve the quality of the raw images. It was found that these steps combined with increasing the number of PIV image pairs contributed to improve the correlation between the data sets at higher valve lift (8mm). It can be observed that the correlation coefficient for the mean velocities is higher for the low-pressure drop case (250mm of H_2O) as shown in Figure 8.2.

Table 8.3: Calculated correlation coefficient

Both valves opened configuration	**# of image pairs**	**Pressure drop (mm of H_2O)**	**Calculated correlation coefficient**
L_v (mm)			
2	50	250	0.78
5	50		0.95
8	50		0.58
8	1200		0.74
2	50	635	0.76
5	50		0.82
8	50		0.38
8	1200		0.68

The correlation coefficient was also calculated for fluctuating velocities at the 5mm valve lift of 250mm of H_2O pressure drop, which was 0.81. This indicates a reasonable prediction accuracy for the RSTM model. It is suggested that the correlation coefficient for the fluctuating velocities can be further optimised by increasing the number image pairs of the PIV measurements to more than 1200 image pairs.

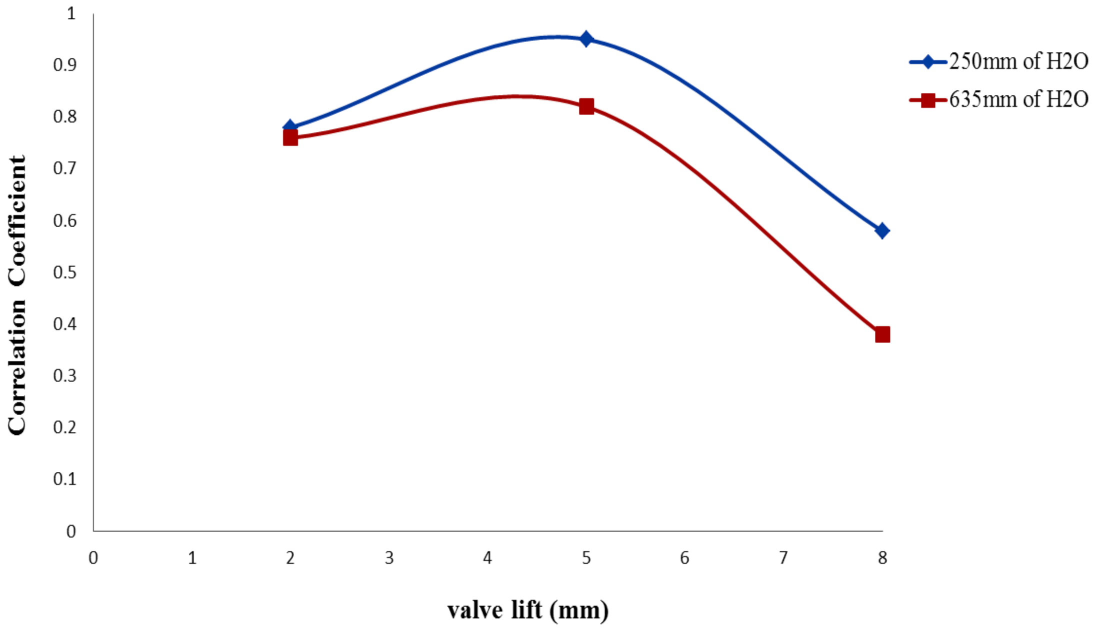

Figure 8.2: Correlation coefficient of flow field between PIV and RSM model

8.2.3: Detailed Velocity Field Predictions

Tumble Plane

Mean velocity profiles obtained along the cylinder axis from both the PIV measurements and CFD predictions are shown in Figures 8.3 and 8.4. These results are for both intake valves opened 5mm and a pressure drop of 250mm of H_2O. The predicted y-component of mean velocity compares well with the PIV data as can be seen in Figure 8.3. However, for the x-component, although there is evidence of similar trends, in some regions the simulations have under- predicted the measurements, Figure 8.4. This may be due to the incompatibility of generated meshes in this region. A 95% confidence interval is approximated for the mean X-component velocity based on the sample mean and sample standard deviation for 50 image pairs as shown in Figure 8.4.

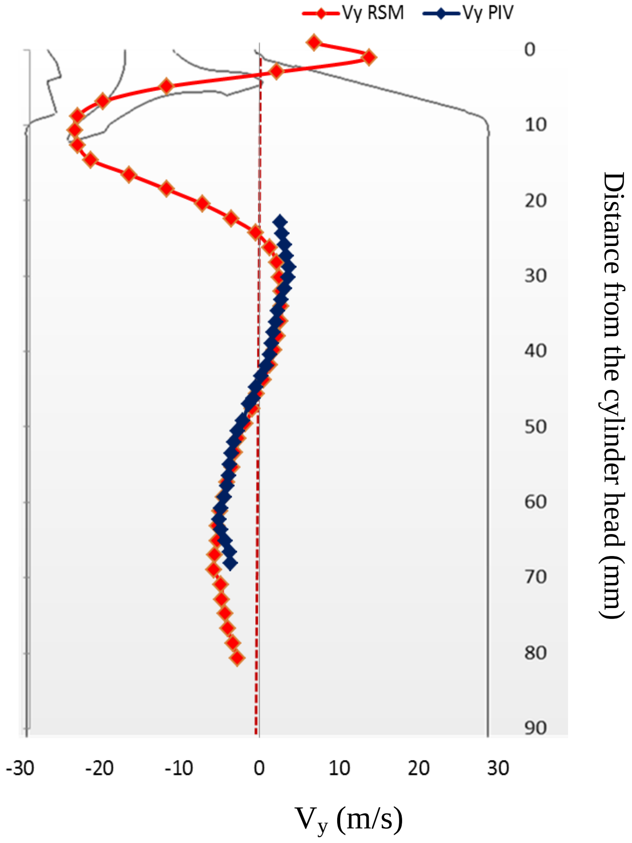

Figure 8.3: Mean Y-component velocities comparisons between PIV and CFD data at the centre of the cylinder for a valve lift of 5mm, both valves opened and 250mm of H2O pressure drop

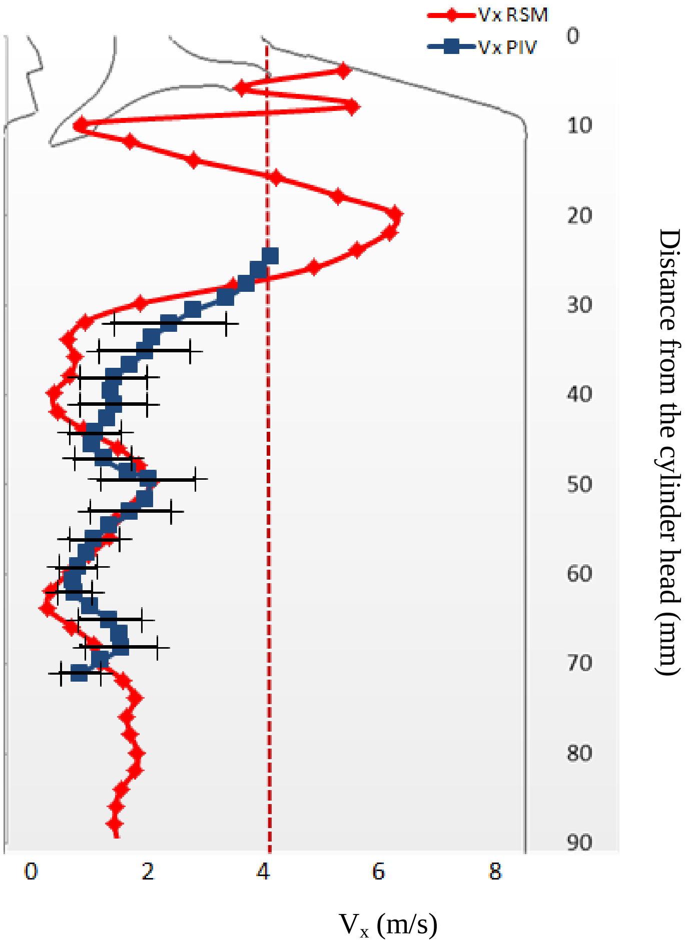

Figure 8.4: Mean X-component velocities comparisons between PIV and CFD data at the centre of the cylinder for a valve lift of 5mm, both valves opened and 250mm of H_2O pressure drop

Figure 8.5 shows the vector maps in the main tumble plane obtained by PIV and CFD results with the RSM turbulence model. These figures show the case for both intake valves with 5mm valve lift and 250mm of H_2O pressure drop. In the PIV result, Figure 8.5*(b)*, half a vortex in the top part of the image was detected. The numerical results show similar flow structures as those of the experimental data as can be seen in the rectangular zone in Figure 8.5*(a)*. However, there is a slight difference about the centre position of the vortex between the PIV and CFD results. It can be seen that in the left portion of the PIV Image, the vector field was poorly represented. This is almost certainly a result of the cylinder liner reflections as shown in the Figure 4.20.

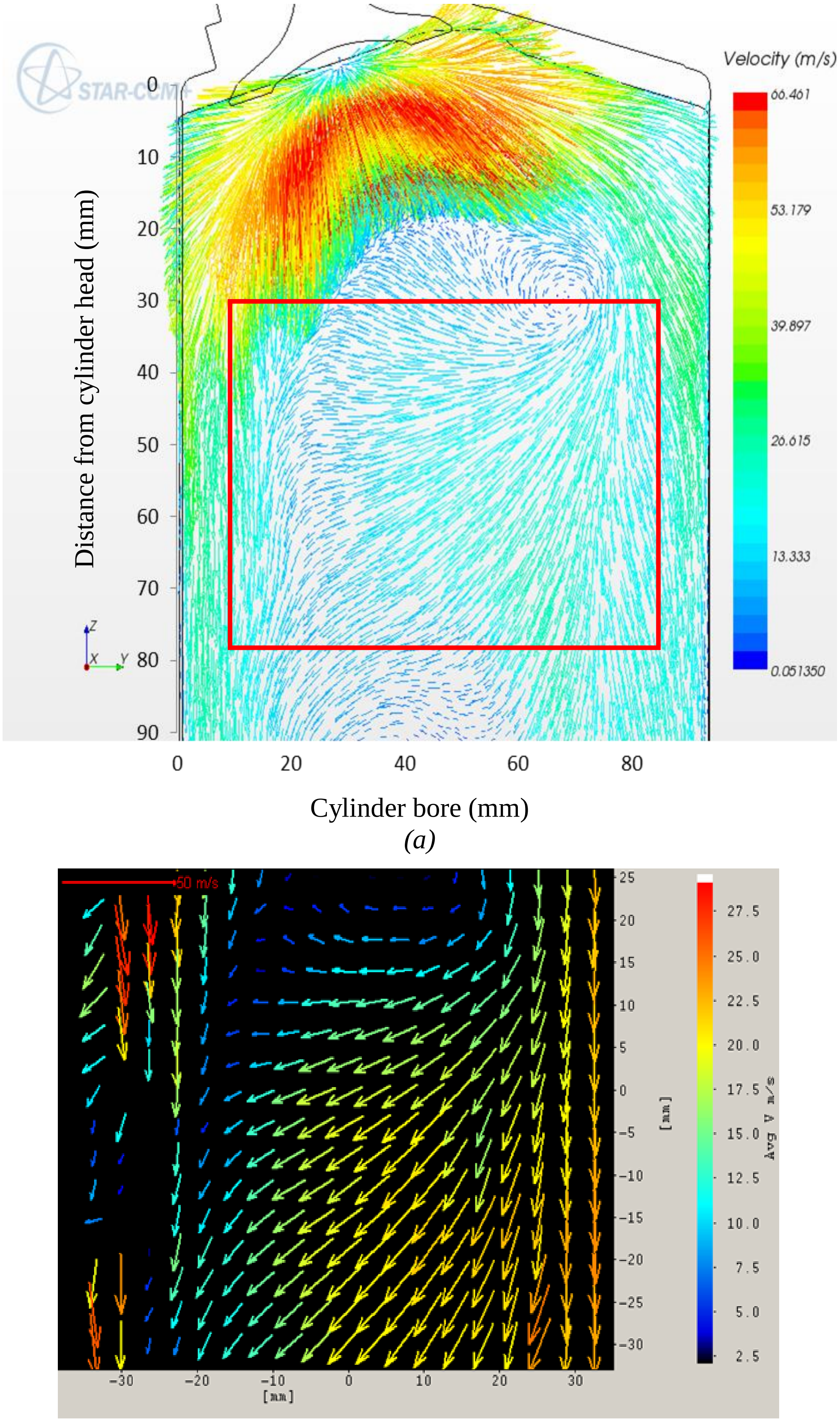

(a)

(b)

Figure 8.5: Flow structure of mean velocity at tumble plane for a valve lift of 5mm, both valves opened and 250mm of H_2O pressure drop *(a)* vectors by RSM model *(b)* vectors by PIV

Swirl Plane

Figure 8.6 shows the distributions of the mean velocity components in the cylinder for both the PIV and CFD analysis in the horizontal plane at 44mm (half of the cylinder bore) from the cylinder head. The PIV measurements at the horizontal plane were carried out on the same cylinder head by using an endoscopic probe and the mean velocity vectors were obtained from 50 image pairs. As can be clearly seen in Figure 8.6, there are two counter-rotating vortices in the swirl plane for both measured and computed data. A line of symmetry is present on the central axis, between the valves of the cylinder. The maximum measured velocity of the vortex on the right hand side of the cylinder is approximately 32.5m/s in the near-wall region and the computed velocity at the same region is approximately 27m/s. The velocity vector fields show good similarities but the computed counter-rotating vortices are asymmetrical as can be seen in Figure 8.6*(a)*. The reason for the asymmetry in the numerical results is the small vortices, which can be observed close to the cylinder wall at the top of image. These small vortices were detected by the numerical simulations because of the anisotropic assumption in the normal stresses of the RSM turbulence model for investigating three dimensional highly rotating flows.

One question that may be asked is that “Why such small vortices were not observed in the PIV measurement in the horizontal plane?”. This may be attributed to the possibility that the averaging process used in the PIV data may remove evidence of any small vortices. The differences between a single flow field and an average of 50 image pairs are shown in Figure 8.7. Looking at the Figure of the mean image with a single image, there are more vortices evident in the single image, which agree with the above statement. Another possible reason could be due to the neglect of the third velocity component in the 2D-PIV measurements. This might have a significant contribution for the generation of small vortices as observed from the numerical simulation (see Figure 8.6(*a*)).

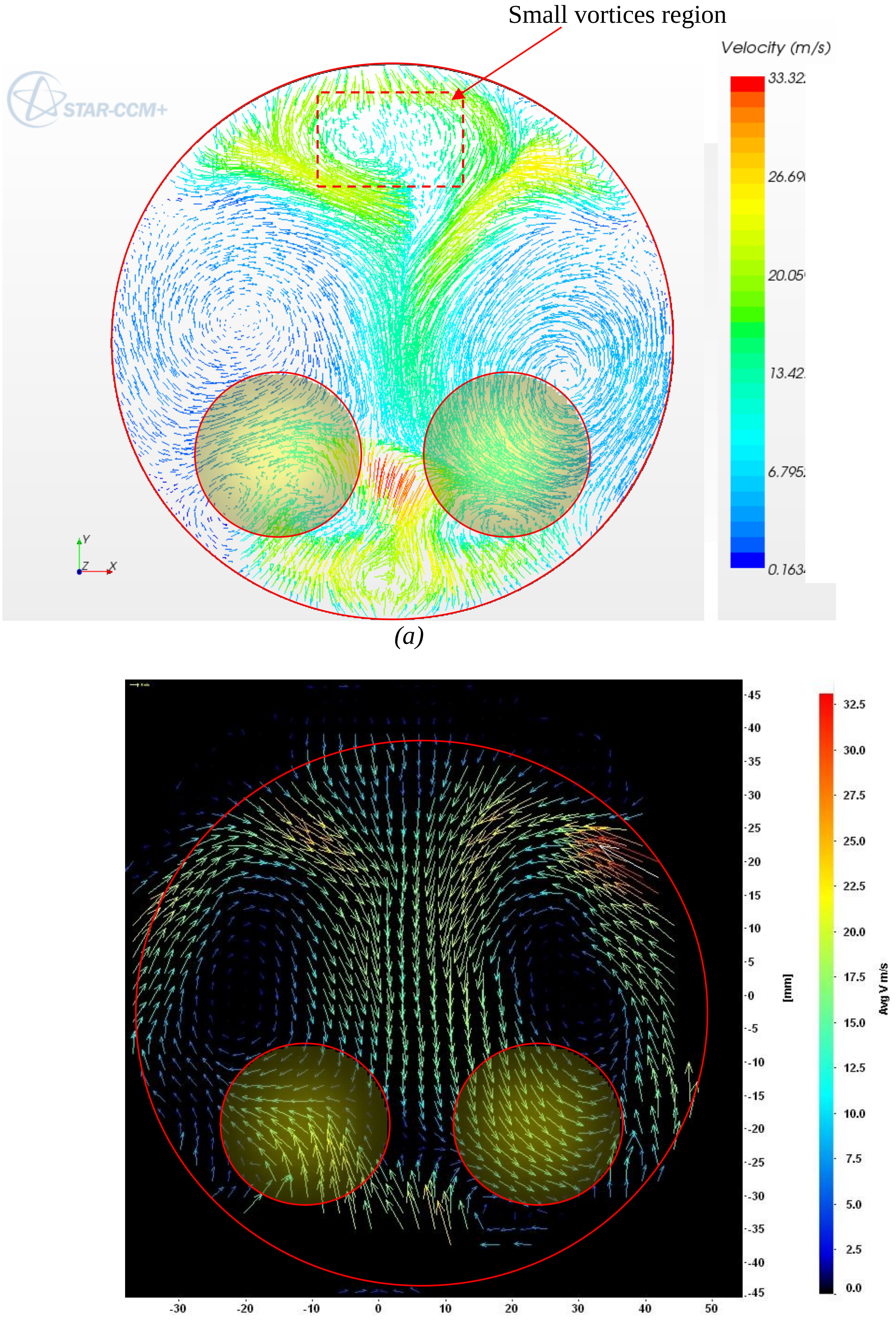

(a)

(b)

Figure 8.6: Flow structures of mean velocity at swirl plane for 5mm valve lift and 250mm of H_2O pressure drop *(a)* vectors by RSM model *(b)* vectors by PIV

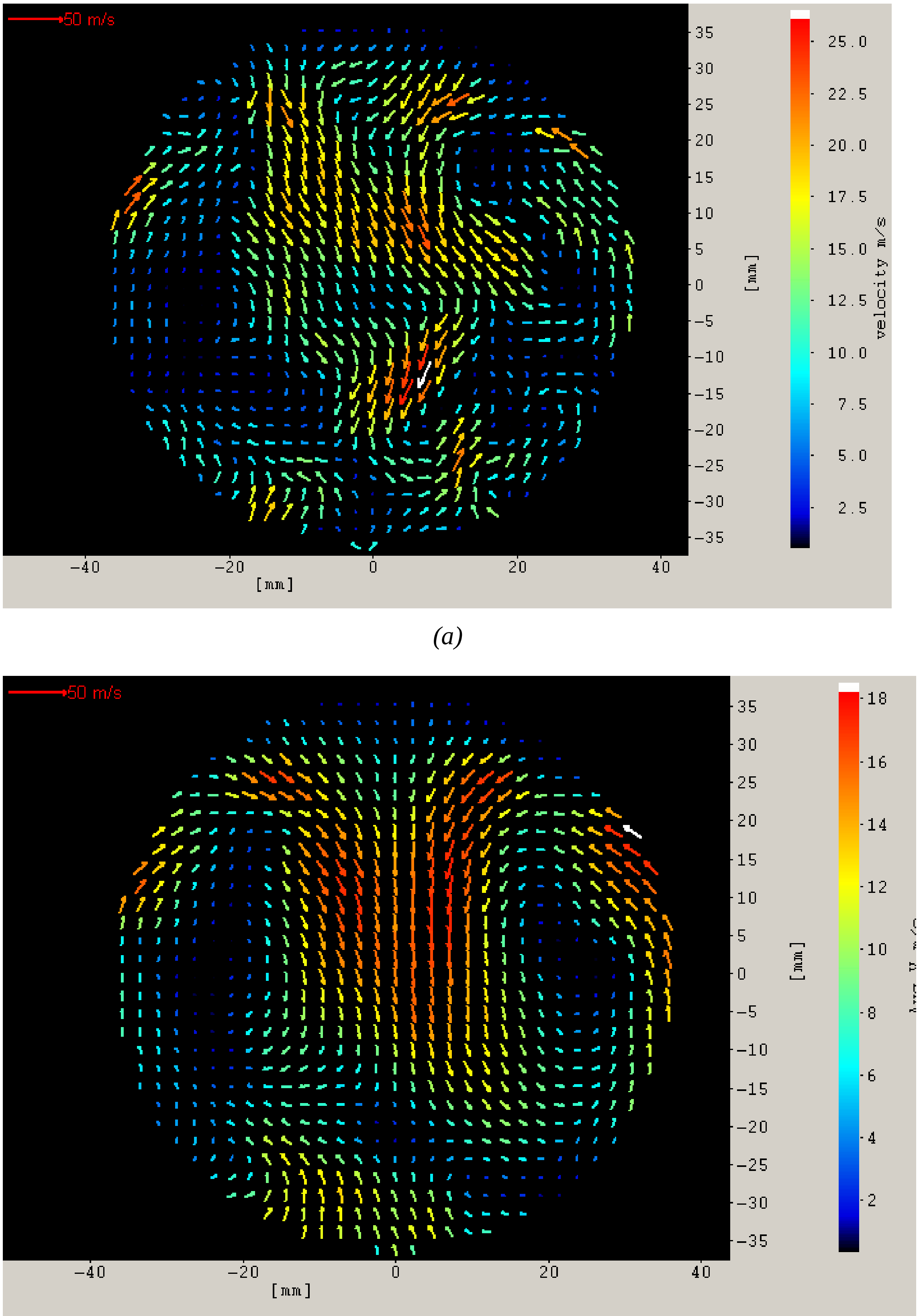

(a)

(b)

Figure 8.7: Effect of capturing 50 images for swirl plane *(a)* single image and *(b)* average of 50 images

Evaluation of Swirl (SR) and Tumble Ratios (TR)

Evaluation of swirl and tumble ratios are essential for the in-cylinder flow characterisation of vehicle engines. In the current work, the measured PIV and calculated CFD values of the horizontal and vertical velocity fields were used to calculate swirl and tumble ratios. Several methods of calculating the swirl and tumble ratios can be used as explained by Pitcher and Wigley (2008). The method applied in this work is a weighted version of the simplest equation where the angular velocity is weighted by the engine speed as shown in Equation 2.8. The comparisons of the predicted and measured swirl and tumble ratios are shown in Tables 8.4 and 8.5 respectively. The numerical simulation results are over predicted values compared with the ratios obtained by PIV calculations. The discrepancy may be attributed to a higher predicted mass flow rate from the numerical simulations. It can be seen that there is an impact of the pressure drop on the swirl and tumble ratios; a slight increase at high pressure drop was detected. The obtained results for tumble ratio are higher than the swirl ratio values.

Table 8.4: Swirl ratio comparisons

Both valves opened configuration	**Pressure drop (mm of H_2O)**	**Swirl ratio PIV**	**Swirl ratio CFD**	**% between the measured and calculated ratios**
L_v (mm)				
2	250	0.039	0.054	27.7
5		-0.011	-0.019	42.1
8		-0.012	-0.038	68.4
2	635	-0.012	-0.025	52
5		0.041	-0.063	34.9
8		0.019	-0.047	59.5

Table 8.5: Tumble ratio comparisons

Both valves opened configuration	**Pressure drop (mm of H_2O)**	**Tumble ratio PIV**	**Tumble ratio CFD**	**% between the measured and calculated ratios**
L_v (mm)				
2	250	-0.118	0.065	44.9
5		-0.238	0.14	41.1
8		0.349	0.697	49.9
2	635	0.263	0.084	68
5		-0.316	0.34	7.5
8		0.383	0.782	48.9

Distribution of Turbulence Parameters

Turbulence kinetic energy (TKE) is associated with eddies in turbulent flow. The TKE is calculated (Roland, 1988) as shown in Equation 8.4 which is characterized by measured velocity fluctuations. The RMS fluctuating velocity in x-direction (u_{RMS}) is the fluctuating component of the instantaneous velocity u_i and is calculated using Equation 8.5 where $\bar{u}$ is the mean velocity, which is calculated as the average velocity of a number of instantaneous velocities as shown in Equation 8.6, where N is the number of vectors. The turbulence intensity (I_t), is defined as the ratio of the fluctuation velocity to the mean velocity as written in Equation 8.7.

$$TKE = \frac{1}{2}\left(u_{RMS}^2 + v_{RMS}^2 + w_{RMS}^2\right) \qquad (8.4)$$

$$u_{RMS} = \sqrt{\frac{1}{(N-1)}\sum_{i=1}^{N}(u_i - \bar{u})^2} \tag{8.5}$$

$$\bar{u} = \frac{\sum_{i=1}^{N} u_i}{N} \tag{8.6}$$

$$I_t = \frac{u_{RMS}}{U} \tag{8.7}$$

In order to compare in detail the results obtained by both the PIV measurements and the CFD data, the RMS values, TKE and turbulence intensity distributions on the cylinder axis were analysed. The RMS values of the simulation results agree well with the PIV data from y= 21 to 44mm for the x-component, as can be seen in the Figure 8.8. However, there were slight differences further down the cylinder with the numerical simulation under predicting RMS values in this region. This discrepancy might be because of the extended part length (250mm in a normal direction to the outlet face), which was generated to simulate the flow rig test. A 95% confidence interval is approximated for the RMS x-component velocity based on the sample mean and sample standard deviation for 1200 image pairs as shown in Figure 8.8. According to these result, it can be noticed that some of the obtained results from the PIV measurements and RSM model are not within a 95% confidence interval for the RMS values. This indicates that the number of image pairs should be more than 1200 for PIV measurements.

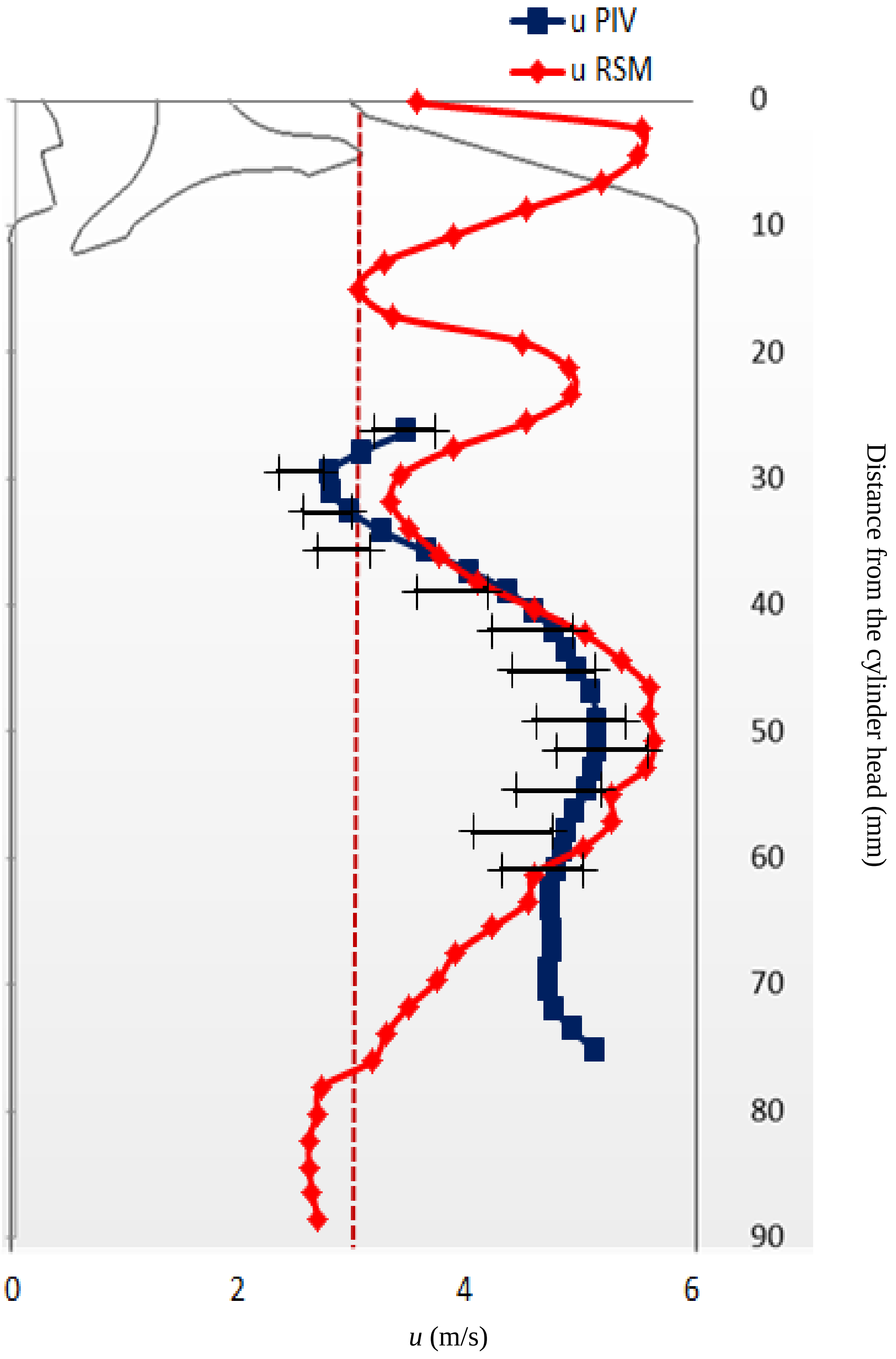

Figure 8.8: RMS velocities comparisons between PIV and CFD data at the centre of the cylinder for a valve lift of 5mm, both valves opened and 250mm of H_2O pressure drop

Figure 8.9 shows the turbulence kinetic energy profiles at different locations. Figure 8.9*(a)* shows the TKE profile at the cylinder centre and Figure 8.9*(b)* shows the TKE profile at the region adjacent to the cylinder wall. It can be noticed that the calculated TKE values are in good agreement with the PIV data. In the 2D-PIV measurements, the TKE was calculated based on a given number of vector fields that have only two components (u_{RMS}, v_{RMS}). Since turbulence is a 3D phenomenon, PIV calculations assumed that the third component behaves like the other two. So each of u_{RMS} and v_{RMS} add a quantity of 1/4(V^2_{RMS}) to the calculated quantity 1/2(V^2_{RMS}). The third component add another 1/4(V^2_{RMS}), so the result of the output value is shown in Equation 8.8 which assumes the turbulence is isotropic (DaVis. 7.2 Manual, 2011). Since the Reynolds stress turbulence model takes in account the anisotropic nature of the flow, Equation 8.9 was defined by assuming that the third component takes the average value of other two components in order to calculate the TKE from the PIV data to close the discrepancy between the data sets. This assumption shows similar trends for the TKE that was calculated from PIV data and RSM turbulence model at the centre of the cylinder, red line in Figure 8.9*(a)*, and at the cylinder wall, red line in Figure 8.9*(b)*. There is a discrepancy in some regions between the data sets and this may be again due to the incompatibility of generated meshes in this regions.

$$TKE = {}^{3}\!/_{4}\left(V_{RMS}^{2}\right) \tag{8.8}$$

$$TKE = {}^{1}\!/_{2}\left(u_{RMS}^{2} + v_{RMS}^{2} + \left(\frac{u_{RMS} + v_{RMS}}{2}\right)^{2}\right) \tag{8.9}$$

——— TKE RSM

TKE PIV Eq. (8.8)

TKE PIV Eq. (8.9)

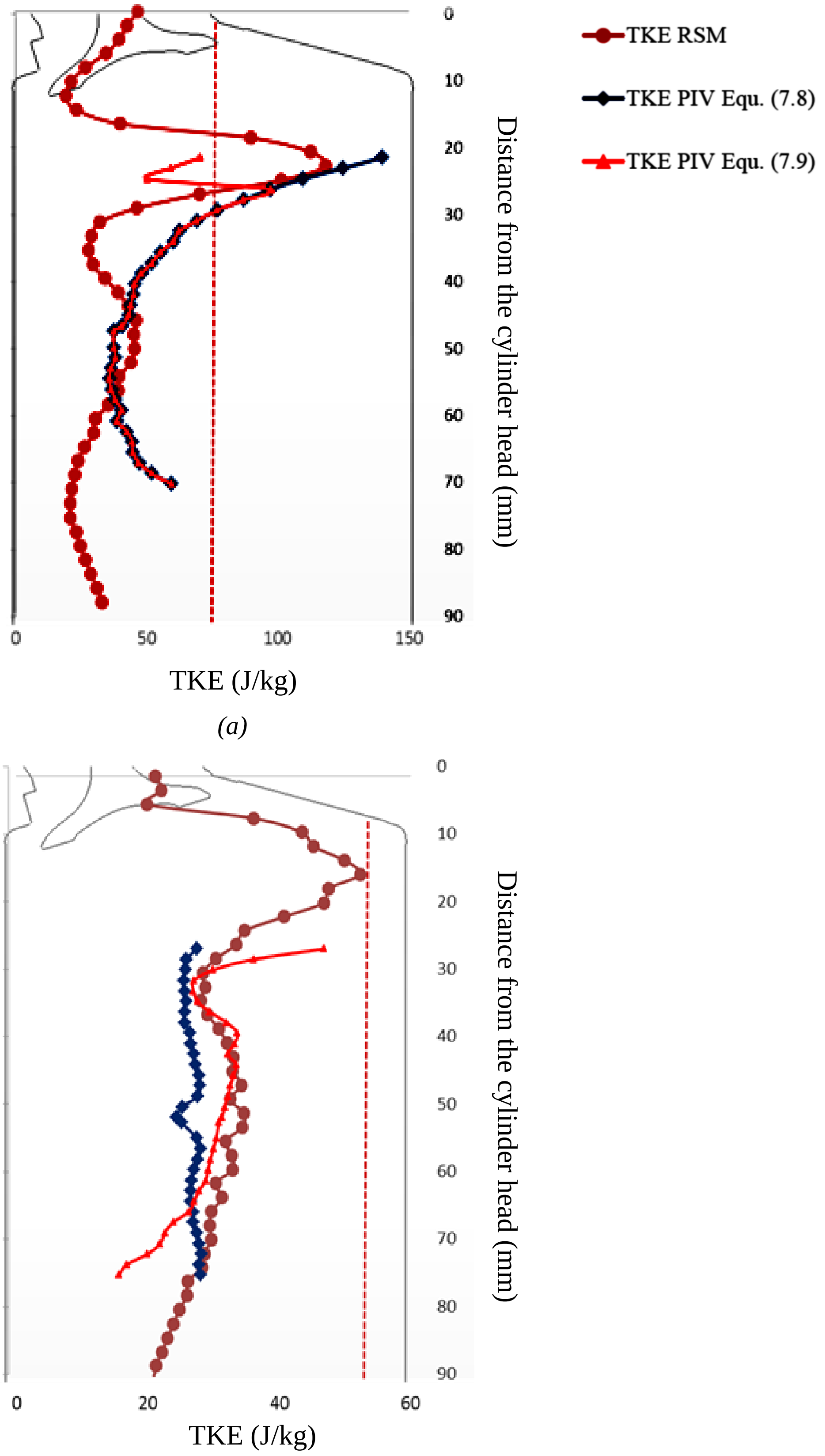

(a)

(b)

Figure 8.9: Turbulent Kinetic Energy comparisons between PIV and RSM data *(a)* at the centre of the cylinder and *(b)* at the cylinder wall for both valves opened at 5mm and 250 mm of H_2O pressure drop.

Figure 8.10 indicates that the numerical simulation with an RSM model shows good turbulence intensity trends. However, the calculated results were over predicting the turbulence intensity. The difference between them was 30% in most of the regions and approximately 65% at the peaks. The reason for such discrepancies are driven by specifying the high turbulence intensity as an initial condition in the numerical run, which was set to be 20% based on a previous LDA experimental study at the horizontal plane placed 44mm down the cylinder head as mentioned before. This indicates that the turbulence intensity should be less than 20% as an initial condition to obtain good results.

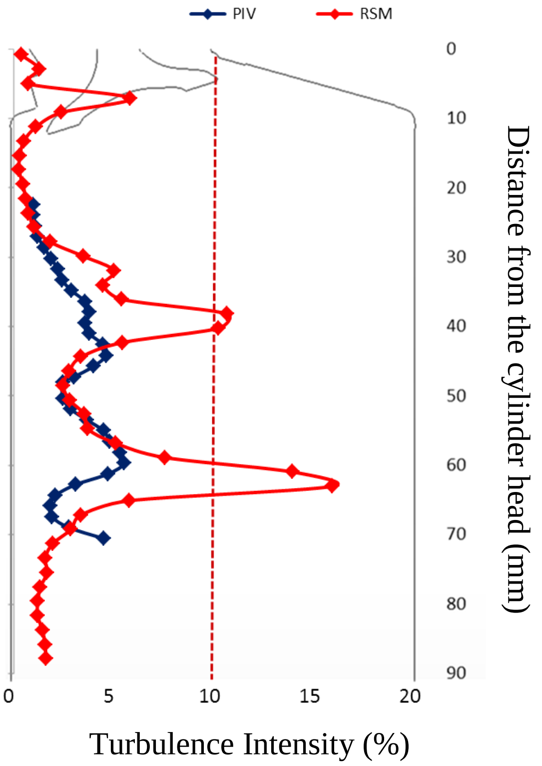

Figure 8.10: Turbulence Intensity comparisons between PIV and RSM data at the centre of the cylinder for both valves opened at 5mm and 250mm of H_2O

8.3: Validating Numerical Data with LDA Measurements

The numerical results obtained from the current study were validated against published experimental measurements. These measurements were obtained from previous investigation on the same cylinder head by Thomas (2006). A quantitative comparisons between experimental and calculated velocity profiles were performed along a line parallel to the horizontal plane at L=44mm. The experimental part applied LDA technique to analyse the flow field created at varying valve lifts and pressures in steady flow conditions. Figure 8.11 shows the mean axial velocity profile obtained along a line between intake valves by both LDA and CFD investigations for the equivalent engine speeds of 2500RPM and dual intake valves opened 5mm. It is shown that the mean axial velocities was well predicted quantitatively along the line by the CFD simulation which has similar trends compared with the LDA data but the predicted velocities in the middle and near to the top cylinder wall regions are in less close in agreement with the experimental data. This may be due to the incompatibility of generated meshes in these regions. A 95% confidence interval is approximated for the mean X-component velocity based on the sample mean and sample standard deviation for 1000 samples as shown in Figure 8.11.

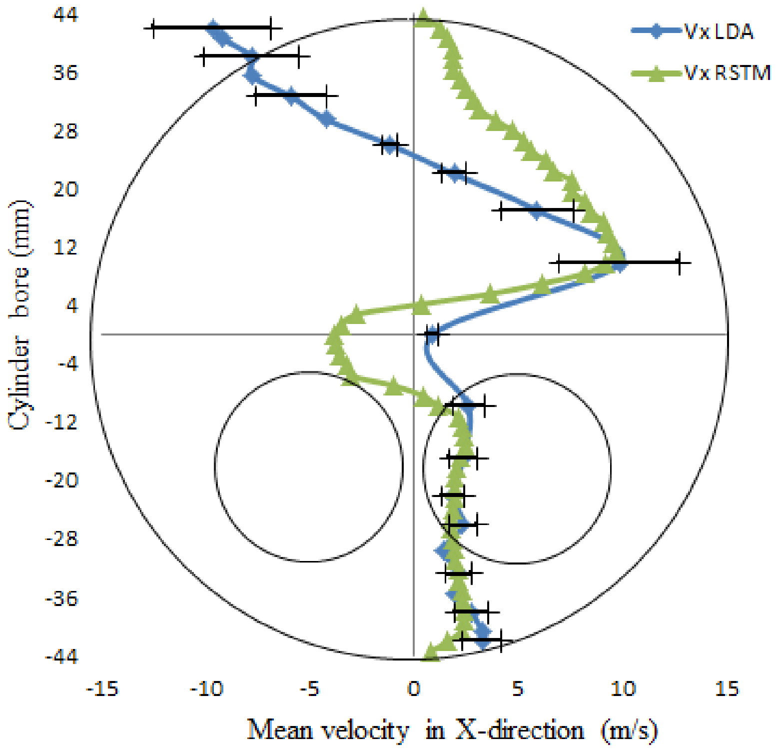

Figure 8.11: Mean velocities comparisons between LDA and CFD data along the line pass between valves for dual valves opened 5mm lift and 250mm of H_2O pressure drop

The fluctuating velocity (u_{RMS}) is the turbulent component of the instantaneous velocity u_i and is calculated by Equation 8.10, where $\bar{u}$ is the mean velocity, which is calculated as the average velocity of number of instantaneous velocities.

$$u_{RMS} = \sqrt{\frac{1}{N}\sum_{i=1}^{N}(u_i - \bar{u})^2} \tag{8.10}$$

The tangential and axial RMS profiles along a line parallel to the horizontal plane at L=44 were analysed. The predicted RMS values of the simulation results agree well with the LDA measurements as can be seen in the Figures 8.12 and 8.13. However, the numerical simulation under predicted the tangential RMS values in some regions and over predicted the axial RMS fluctuating values between valves region. The discrepancy between the numerical and experimental data is within 12%. It can be noticed that the tangential RMS fluctuating is higher where the two vortices mix, but the axial RMS fluctuating is higher close to the cylinder wall behind the valves where the generation of strong tumble motion. A 95% confidence interval is approximated for the RMS X-component velocity based on the sample mean and sample standard deviation for 1000 samples as shown in Figure 8.13. This indicates that the incompatibility of generated meshes in these regions contributes to the discrepancy.

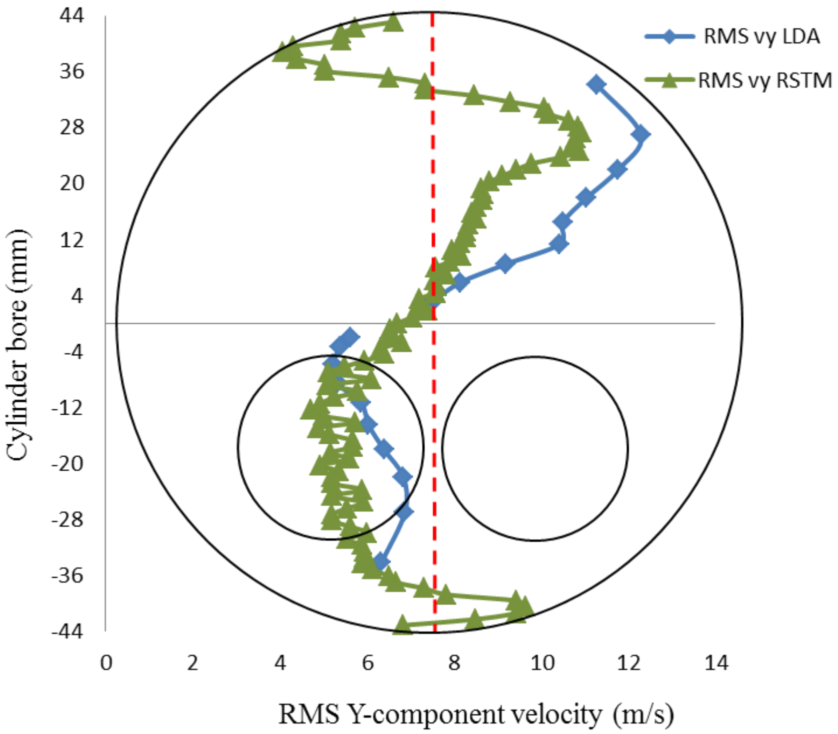

Figure 8.12: Tangential RMS fluctuating comparisons between LDA and CFD data along the line pass between valves for dual valves opened 5mm lift and 250mm of H_2O pressure drop

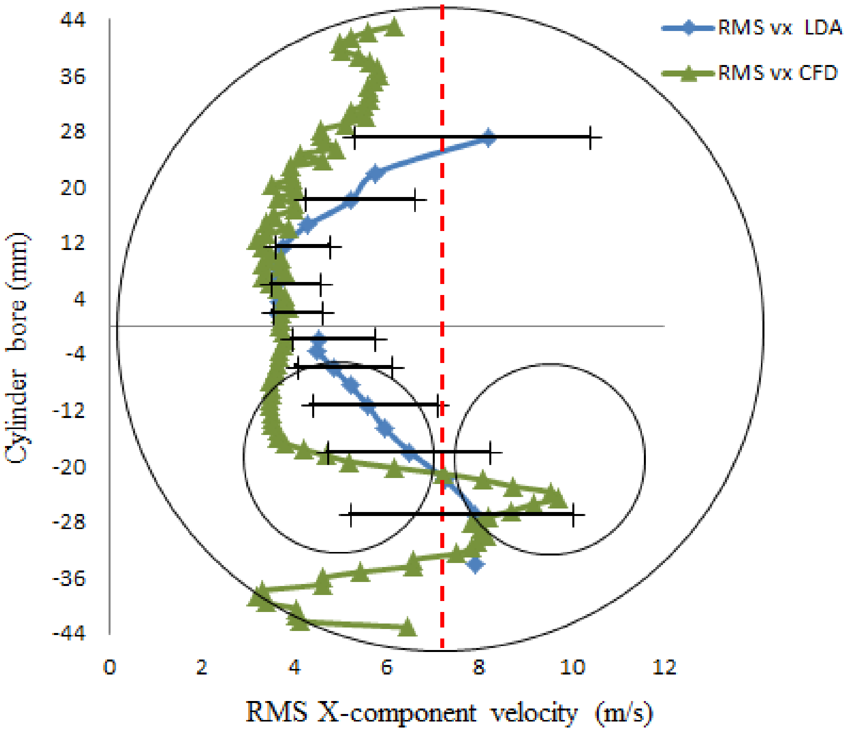

Figure 8.13: Axial RMS velocities comparisons between LDA and CFD data along the line pass between valves for dual valves opened 5mm lift and 250mm of H_2O pressure drop

8.4: Summary

Validation of the computational results through qualitative and quantitative comparisons with the Particle Image Velocimetry (PIV) and Laser Doppler Anemometry (LDA) experimental measurements were presented and discussed on both vertical and horizontal cross sections. Calculated results for the mean and fluctuations velocities (RMS velocity values) and turbulence intensity were validated against measured PIV data as well as previously published experimental LDA data by Thomas (2006) that were completed on the same engine cylinder. Model validation is carried out in three ways: A Correlation coefficient (C) of the flow patterns between measured and calculated CFD data was calculated. The second method is a comparison for a specific data quantity such as the turbulence components or the mean velocity values on the vertical line parallel to the cylinder axis and on horizontal line perpendicular to cylinder axis. The strength of the rotating motions inside the cylinder is also quantified by a dimensionless swirl and tumble ratios, which were calculated and validated. The third method is through visualisation of the velocity vectors qualitatively from a regular zone. The calculated correlation coefficient, which is above 0.6, indicated that a reasonable prediction accuracy for the RSM model. This verifies that the numerical simulation with the RSM model is a useful tool to analyse turbulent flows in complex engine geometries where anisotropic turbulence is created.

Chapter 9

Conclusion and Recommendation for Future Work

9.1: Conclusions

A combined numerical and experimental study has been carried out to examine the structure of the flow field generated inside a 4 valve cylinder head under steady state conditions. In this investigation, Particle Image Velocimetry (PIV) measurements and a finite-volume Computational Fluid Dynamic (CFD) simulations have been used on a single cylinder Lotus engine with a pent-roof head for a number of fixed valve lifts at two pressure drops of 250mm and 635mm of H_2O, equivalent to engine speeds of 2500 and 4000 RPM respectively.

The PIV measurements have been conducted to analyse and visualise flow characteristics created by the prototyped cylinder head for a horizontal plane at half bore downstream (44mm) from the cylinder head and for six vertical planes (0^o, 30^o, 60^o, 90^o, 120^o, 150^o). The measurements have been taken for a number of valve lifts (2mm, 5mm, 8mm, 10mm) for three intake valve open configurations; *(a)* both inlet valves are open, *(b)* right inlet valve only is open and *(c)* left inlet valve only is open. The flow structure variations were discussed as a function of intake valve open configuration, valve lift and pressure drop. The following conclusions are drawn from the PIV measurements:

I. In the horizontal plane, counter-rotating vortices were observed.

II. The general patterns seen within the bulk flow motions, show little variation with an increase in valve lift.

III. The flow velocities did not increase more when the valve lift was opened more than 8mm. This is assumed to be due to flow separations between the valve area reducing the effective flow area and therefore the volume flow rate into the cylinder. Similar occurrences were present with an increase in pressure drop. The difference between the 250mm of H_2O and 635mm of H_2O cases is in terms of the vortex strength. This is as a result of a velocity increase for the higher pressure drop case of approximately 63%.

IV. In the vertical plane, it was observed that measurements at the cylinder wall were not reliable because of the flare noise that was caused by cylinder liner reflections or by higher levels of seeding within the cylinder.

V. High reflection noise on the raw images using a 15 mm thick fused silica can be reduced by using thinner cylinder wall and applying the following steps. First step is to ensure the laser beam alignment with the centre of cylinder. Secondly, ensuring a high enough density of seeded particles, this should distribute uniformly inside the area of interest. Furthermore, painting most of the surrounding parts with a black colour, such as valve heads and cylinder adaptor part on the flow rig, is an essential to eliminate the flare noise.

VI. The main tumble flow was observed from the images. It was shown that as valve lift was increased the strength of the flow motions increased but above 5mm valve lift, this increase was seen to become smaller. This is due to the reduction in the effective flow area, reducing the overall charge motion within the cylinder.

Three-dimensional numerical simulations has been conducted on a single cylinder Lotus engine with a pent-roof type head for both valves opened configuration and fixed valve lifts (2mm, 5mm, 8mm) at two pressure drops. Two turbulence models have been examined to simulate the turbulent flow structure in the current study, namely, Realizable k-ε and Reynolds stress models (RSM). Three densities of generated mesh, which is polyhedral type, are examined. The numerical analysis was employed to investigate both tumble and swirl flow motions formed within the cylinder under steady state condition utilising RSM for a number of swirl and tumble planes. The following summarises the findings from the numerical analysis:

I. In the horizontal planes, the flow structure development was investigated through six planes under the cylinder head: L=11 mm, 22 mm, 44 mm, 66 mm, 88 mm, 110 mm. At planes adjacent to the cylinder head, a number of small vortices were observed in the region close to the cylinder wall. While later planes away from the cylinder head, counter-rotating vortices were observed. This proved that as the distance from the cylinder head increases, the more stable and structured the flow becomes.

II. The general patterns seen within the bulk flow motions in the horizontal planes, show little variation with an increase in valve lift, similar occurrences were present with an increase in pressure drop. The difference between the 250mm of H_2O and 635mm of H_2O cases is in terms of the vortex strength with maximum velocities shown to be approximately 42% larger in the 635mm pressure drop case.

III. In the vertical planes, three vertical planes were considered: across valve vertical plane, main tumble plane and a parallel plane to it on the right valve. The main tumble flow was observed.

IV. In general, it was found that the high velocity region appears close to the cylinder wall whereas the low velocity region exists in the cylinder centre.

V. In case of increasing valve lift, the flow structures remain similar but the velocities within these structures increase.

VI. The vortex core found to move closer to the cylinder axis when the valve lift was increased.

VII. It was found that as pressure drop increases, the flow structures remain of similar orientation, however, the magnitude of the velocities within these flow structures is increased and the vortex core found to move closer to the cylinder axis, similar to an increase in valve lift.

The computational results were validated through qualitative and quantitative comparisons with the PIV experimental measurements on both horizontal and vertical cross sections. Main findings from this validation are:

I. Good agreements are obtained between numerical and experimental outcomes for the mean and RMS velocity values at different locations inside the engine cylinder.

II. It was shown that the mean and RMS fluctuating velocities were well predicted quantitatively by the numerical simulation that has similar trends compared with the LDA data.

III. The mean velocity, RMS values and turbulence intensity were calculated. The strength of the rotating motions inside the cylinder is quantified by a dimensionless swirl ratio.

IV. Good agreement is obtained between the PIV data for the mean and RMS velocities on the cylinder axis inside the cylinder and near the cylinder wall.

V. The predicted mass flow rate values showed good correlation between measured and calculated ideal values for medium valve lifts (5mm).

VI. At low and high valve lifts (2mm, 8mm), the discrepancy between the measured and the predicted mass flow rate values is increased. A possible contributor to this over predicted mass flow is the size and density of generated mesh in the valve gap region that is required to be refined.

VII. The calculated swirl ratios of numerical simulation results are over predicted in value compared with swirl ratios obtained by PIV measurements. The discrepancy may be attributed to an increased mass flow rate that is calculated numerically from CFD.

VIII. It has been found that there is an impact of the pressure drop on the swirl ratios; a slight increase at high-pressure drop was detected.

IX. It is concluded that the numerical CFD simulation data with RSM turbulence model are in good agreements with PIV and LDA data considering the complex flow structure in this study.

X. It was recognised that the numerical simulation with RSM turbulence model provides a useful tool to analyse turbulent flows in complex engine geometries where anisotropic turbulence is created.

9.2: Recommendations for Future Work

This investigation has gathered a vast quantity of numerical and experimental data obtained under steady condition utilising airflow rig. The following are some thoughts that would be of interest for future work:

I. The flow structures seen within this set-up could also be compared to the flow structures seen on the motored Lotus SCORE. This would help confirm the suitability of steady flow laser based testing as a method for future engine design and diagnostic work.

II. It is also suggested that possible methods for reducing the flare are investigated. These could include: a more accurate Laser alignment method, a use of more efficient “light dump” behind the cylinder, which would be closer to the cylinder.

III. In the PIV horizontal plane measurements, it would also be of interest to examine the flow fields at more than just a single horizontal plane. This would allow visualisation of how the flow structures are formed within the cylinder. It would also be of interest to capture more than 50 image pairs so that RMS velocities could be calculated. The intersection between the horizontal and vertical measurement planes provides a line along which there are 3-D statistics. Here it could analyse and compare the anisotropy between the measured and computed turbulence; one example, comparing scatter plots of the off diagonal components of Reynolds stress, this would provide new information on the flow field and reveal how well the anisotropy is captured by the model.

IV. Another possible improvement would be to use stereo PIV measurements technique. This would provide more information of flow motion and eliminate out of plane flow which will distort the vectors in 2-D measurements.

References

Adrian R. and Westerweel J. (2011). Particle Image Velocimetry. *3rd Edition, Cambridge University Press, ISBN* 978-0-521-44008-0.

Adrian, R.J. (1986). Multi-point optical measurements of simultaneous vectors in unsteady flow-a review. *International Journal of Heat and Fluid Flow,* 7(2), pp. 127-145.

Andre, B., Kai, B., Roland, D., Stefan, D., Ansgar, S., and Lutz, S. (2007). Effects of Charge Motion Characteristics on Engine Variables Such as Emission Behavior and Efficiency. *SAE International*, 01-0640.

Angermann, L. (1996). Finite volume schemes as non-conforming Petrov-Galerkin approximations of primal-dual mixed formulations. *Report 181, Institute for Angewandte Mathematik,* Universtat Erlangen-Nurnberg.

Arcoumanis, C., Hu, Z. and Whitelaw, J.H. (1993). Steady flow characterization of tumble-Generating four-valve cylinder heads. *Proceedings of the Institution of Mechanical Engineers, Part D: Journal of Automobile Engineering 1989-1996 (vols 203-210),* 207(34), pp. 203-210.

Arnold, A., Dinkelacker, F., Heitzmann, T., Monkhouse, P., Schäfer, M., Sick, V., Wolfrum, J., Hentschel, W. and Schindler, K. (1992). DI diesel engine combustion visualized by combined laser techniques. *Symposium (International) on Combustion,* 24(1), pp. 1605-1612.

Astarita, T., and Cardone, G. (2005). Analysis of interpolation schemes for image deformation methods in PIV. *Exp. Fluids* 38, 233-243.

Atthey, D.R. (1974). A Finite Difference Scheme for Melting Problems. *J. Inst. Math. Appl.* 13, 353-366.

Bella, G., De maio, A., and Grimaldi, C. N. (2003). Flow Characterization of a High Performance S.I. Engine Intake System Part2-Numerical Analysis. *SAE Technical Paper*, 01-0632.

Beeck, M. and Hentschel, W. (2000). Laser metrology — a diagnostic tool in automotive development processes. *Optics and Lasers in Engineering*, 34(2), pp. 101-120.

Bensler, H., Kapitza, L., Raposo, J. and Reisch, U. (2002). A New Experimental Method for Determining Port-Generated Swirl Flow. *SAE International*, 01-2846.

Bevan, K.E., and Ghandhi, J.B. (2005). PIV Measurements of In-Cylinder Flow in a Four-Stroke Utility Engine and Correlation with Steady Flow Results. *SAE Paper* 2004-32-0005.

Bradshaw, P. (1975). An introduction to turbulence and its measurement. *Pergamon Press*, Oxford, UK.

Bradshaw, P. (1996). The understanding and prediction of turbulent flow. *Engineering Foundation Conference on Turbulent Heat Transfer*, San Diego.

Buchhave, P. (1992). Particle image velocimetry—status and trends. *Experimental Thermal and Fluid Science*, **5**(5), pp. 586-604.

Cao, Z.-M., Nishino, K. , Mizuno, S., Torii, K. (2000). PIV measurement of internal structure of diesel fuel spray. *Exp. In Fluids, 29(1)*, pp. 211-219.

Celik, I., Yavuz, I., Smirnov, A., Smith, J., Amin, E., Gel, A. (1999). Prediction of in-cylinder turbulence for IC engines", *Mediterranean Combustion Symposium*, Antalya, Turkey, June 20-25.

Celik, I., Chattree, M., Singh, S. and French, W.E. (1987). Application of the k-ε turbulence model to swirling flow inside the METC entrained-flow reactor. *in Proc. of Fifth Int. Conf. on Numerical Methods in Laminar and Turbulent Flow*, Montreal, Canada, July 6-10, pp. 2102-2114.

Cebeci, T. and Bradshaw, P. (1977). Momentum transfer in boundary layers. *Hemisphere Publishing/McGraw-Hill*, pp. 176-180.

Chan, V.S. (2000). Velocity measurement inside a motored internal combustion engine using three-component Laser Doppler Anemometry. *Optics and laser technology.,* 32(7-8), pp. 557-8.

Charoenphonphanich, C., Otaka, M., Ennoji, H. and Iijima, T. (1996). In-cylinder fluid motion and mixing of a dual intake valve spark ignition engine. *SAE Paper,* 960266.

Christof Schulz, V.S. (2005). Tracer-LIF Diagnostics: Quantitative measurement of fuel concentration, temperature and air/fuel ratio in practical combustion systems. *Progress in Energy and Combustion Science, 31(1), pp. 75-121.*

Chung, H., Young-June, C., Kyu-Bak, C. and Kern-Yong, K. (1997). Effects of intake ports on in-cylinder flow and lean combustion in a 4-valve engine. *SAE International*, 981048.

Choi, W., Choi, B.-C., Park, H.-K., and Joo, K.-J. (2003). In-cylinder flow field analysis of a single-cylinder DI diesel engine using PIV and CFD. *SAE Technical Paper*, 01-1846.

Choi, J., Lee, S., Shin, H. And Bae, C. (2000). Fuel-spray characteristics of high pressure gasoline injection in flowing fields. *JSME International Journal.Series B, Fluids and Thermal Engineering,* 43(4), pp. 576-581.

Cole, J.B. And Swords, M.D. (1979). Laser Doppler Anemometry measurements in an engine. *Applied Optics*, 18(10/15).

Choudhury, D. (1993). Introduction to the renormalization group method and turbulence modelling. *Fluent Inc. Technical Memorandum TM-107.*

DaVis. 7.2 Software Manual (2011). 1003001_DaVis_D72.pdf , produced by LaVision GmbH, Gottingen.

Dierksheide, U., Meyer, P., Hovestadt, T., Hentschel, W. (2001). Endoscopic 2D-PIV flow field measurements in IC engines. *4th International Symposium on Particle Image Velocimetry,* Göttingen, Germany, September, PIV’01 Paper 1060.

Desantes, J., Pastor, J., and Doudou, A. (2001). Study of the steady flow produced by direct injection diesel engine intake ports. *Proceedings of the Institution of Mechanical Engineers, Part D: Journal of Automobile Engineering,* 215(2), pp. 285-298.

Deardorff, J.W. (1982). A numerical study of three-dimensional turbulent channel flow at large Reynolds number”, *Journal of Fluid Mechanics*. 41, pp 453-480.

Demirdzic, I., Lilek, Z., and Peric, M. (1993). A collocated finite volume method for predicting flows at all speeds. *Int. J. for Numerical Methods in Fluids*, 16, pp. 1029-1050.

Deslandes, W. (2003). PIV measurements of internal aerodynamic of diesel combustion chamber. *SAE transactions.*, 112, 2003-01-3083, pp. 2067-2073.

Durbin, P. A. (1996). On the k-ε stagnation point anomaly. *Int. J. Heat and Fluid Flow*, 17, 89-90.

Elghobashi, S. (1994). On predicting particle-laden turbulent flows. *Applied Scientific Research*, 52, 309–329.

Endres, H., J., neuber, H., and Wurms, R. (1992). Influence of swirl and tumble on economy and emissions of multi valve SI engines. *SAE International*, 24-28.

Engstrom, J., Kaminski, C.F., Alden M., Josefsson, G., and Magnusson, I. (1999). Experimental investigations of flow and temperature fields in an SI engine and comparison with numerical analysis. *SAE International*, 01-3541.

Esirgemez, E., and Olcmen, S.M. (2005). A Spark-Plug LDV Probe for in-cylinder flow analysis of production IC engines", *Measurement Science and Technology*, 16(10), pp. 2038-2047.

Ferziger, J.H., and Peric, M. (2002). Computational methods for fluid dynamics. *3rd rev. ed., Springer-Verlag*, Berlin.

Fujimoto, H., Nakagawa, T., Kudo, H., Wakisaka, T. and Shimamoto, Y. (1995). A study on the formation of vertical vortex in the cylinder of an I.C. engine using CFD: Effect of intake valve closing timing. *JSAE Review*, 16(4), pp. 349-355.

Fujimoto, M. (1993). Effect of swirl rate on mixture formation in a spark ignition engine based on laser 2-D visualization techniques. *SAE Paper*, 102(3), pp. 1781.

Gasparetti, M., Paone, N. And Tomasini, E.P. (1996). Laser Doppler techniques for the combined measurement of inlet flow and valve motion in IC engines. *Measurement Science and Technology,* 7(4), pp. 576-591.

Gault, R.I., (2004). Analysis of the steady flow characteristics through a poppet valve. *SAE Paper,* 113, pp. 1080-1093.

Gibson, M.M., and Launder, B.E. (1978). Ground effects on pressure fluctuations in the atmospheric boundary layer ", *Journal of Fluid Mechanics*. 86. pp. 491-511.

Goryntsev, D.; Sadiki, A. ; Klein, M. ; Janicka, J. (2009). Large Eddy Simulation based analysis of the effects of cycle-to-cycle variations on air-fuel mixing in realistic DISI IC-engines, *In: Proc. Combust. Inst*., 32.

Gold, M.R., Arcoumanis, C., Whitelaw, J.H., Gaade, J. and Wallace, S. (2000). Mixture preparation strategies in an optical four-valve port-injected gasoline engine. *International Journal of Engine Research,* 1(1), pp. 41-56.

Hasegawa, Y. (1993). An experimental investigation on air-fuel mixture formation inside a low- pressure direct injection stratified charge rotary engine. *SAE paper,* 102(3), pp. 927.

Haworth, D.C. (1999). Large-Eddy Simulation of in-cylinder flows. *Oil & Gas Science and Technology, Institut Français du Pétrole.* 54(2), pp. 175-185.

Haworth, D. (1998). Large Eddy Simulation of in-cylinder flows. *International Conference on Multi-dimensional Simulation of Engine Internal Flows, IFP,* Rueil Malmaison, France, Dec. 3-4.

Hai-Wen, GE, Rolf d., Reitz, and Werner, W. (2008). Modelling the effects of in-cylinder flows on HSDI diesel engine performance and emissions. *SAE International Journal of Fuels and Lubricants,* 01-0649.

Heywood, J.B. (1988). Internal combustion engine fundamentals. McGraw-Hill *International Editions*.

Hentschel, W., and Schindler, K. (1996). Flow, spray and combustion analysis by laser techniques in the combustion chamber of a direct-injection diesel engine. *Optics and Lasers in Engineering,* 25(6), pp. 401-413.

Hill, P.G., and Zhang, D. (1994). The effects of swirl and tumble on combustion in spark-ignition engines. *Progress in Energy and Combustion Science,* 20(5), pp. 373-429.

Hongming, X. (2001). Some critical technical issues on the steady flow testing of cylinder heads. *SAE International,* 2001-01-1308.

Hollis, D. (2004). Particle image velocimetry in gas turbine combustor flow fields. PhD thesis, Loughborough University, UK.

Hong, C.W., and Chen, D.G. (1997). Direct measurements of in-cylinder integral length scales of a transparent engine. *Experiments in Fluids,* 23(2), pp. 113-120.

Huang, R.F., Huang, C.W., Chang, S.B., Yang, H.S., Lin, T.W., and Hsu, W.Y. (2005). Topological flow evolutions in cylinder of a motored engine during intake and compression strokes. *Journal of Fluids and Structures,* 20(1), pp. 105-27.

Ismail, A.R., Bakar, R.A. and Semin (2008). An investigation of valve lift effect on air flow and coefficient of discharge of four stroke engines based on experiment. *American Journal of Applied Sciences,* **5**(8), pp. 963-71.

Ishida, R., Nakayama, T., Kaneko, M., and Morikawa, K. (2011). Analysis of in-cylinder flow and fuel vapor concentration distribution in gasoline direct injection engine. *SAE Technical Paper* 2011-01-2052.

Itoh, T., Kakuho, A., Hiray, K., Takahashi, E., and Urushihara, T. (2006). A study of mixture formation processes in direct injection stratified charge gasoline engines by quantitative laser-induced fluorescence imaging and the infrared absorption method. *International Journal of Engine Research.Vol.7,* 7(5), pp. 423-434.

Jay, M.B. (1987). Particle sizing in combustion systems using scattered laser light. *Journal of Quantitative Spectroscopy and Radiative Transfer, Volume 40 (3), pp. 321-330*

John L., Lumley (2001). Early work on fluid mechanics in the IC engine. *Annu. Rev. Fluid Mech. Sibley School of Mechanical and Aerospace Engineering*, New York 14853, pp. 33-319–38.

Josefsson, G., Fischer, J., and Magnusson, I. (2001). Length scale measurements in an engine using PIV and Comparison with LDV. *International Symposium on COMODIA*, pp.653 - 660.

Kakuhou, A., Urushihara, T., Itoh, T., and Takagi, Y. (2000). Characteristics of mixture formation in a direct-injection SI engine with optimized in-cylinder swirl air motion. *Progress In Technology*, pp. 351-360.

Kang, K.Y., and Reitz, R.D. (1999). The effect of intake valve alignment on swirl generation in a DI diesel engine. *Experimental Thermal and Fluid Science,* 20(2), pp. 94-103.

Kang, K.Y., and Baek, J.H. (1998). Turbulence characteristics of tumble flow in a four-valve engine. *Experimental Thermal and Fluid Science,* 18(3), pp. 231-243.

Kang, K.Y., and Baek, J.H. (1995). LDV measurement and analysis of tumble formation and decay in a four-valve engine. *Experimental Thermal and Fluid Science,* 11(2), pp. 181-189.

Keane, R.D., and Adrian R. J. (1992). Theory of cross-correlation analysis of PIV images. *Appl. Sci. Res.* 49, 191-215.

Keane, R.D., and Adrian, R. J. (1991). Optimization of particle image velocimeters. Part II: Multiple pulsed system. *Meas. Sci. Technol.* 2, 963-974.

Keane, R.D., and Adrian, R., J. (1990). Optimization of particle image velocimeters. Part I: Double pulsed system. *Meas. Sci. Technol*. 1, 1202-1215

Klein, M., Sadiki, A., and Janicka, J. (2003). A digital filter based generation of inflow data for spatially developing Direct Numerical or Large Eddy Simulations. J. Comp. Phys. 186, 652-665.

Kohse-Hinghaus, K., and Jeffries, J.B. (2002). Applied combustion diagnostics. *Taylor & Francis,* New York, 480.

Kono, S. (1991). Study of swirl effects on spray formations in DI engines by 3D numerical calculations. *SAE Technical Paper Series,* pp. 10.

Launder, B.E. (1989). Second-Moment Closure: Present and Future. *International Journal of Heat Fluid Flow,* pp 282-300

Launder, B. E., Reece, G. J. and Rodi, W. (1975). Progress in the development of a Reynolds-Stress Turbulent Closure. *Journal of Fluid Mechanics, Vol. 68(3),* pp. 537-566.

Launder, B.E., and Spalding, D.B. (1974). The numerical computation of turbulent flows. *Computer Methods in Applied Mechanics and Engineering,* 3:269–289.

Launder, B.E., and Spalding, D.B. (1972). Lectures in mathematical models of turbulence. *Academic Press.* London, England.

Leschziner, M.A. (1991). Modeling strongly swirling flows with advanced turbulence closure. *In Advances in Numerical Simulations of Turbulent Flows, ASME Publication, FED-Vol. 117,* pp. 1-10, New York.

Lea, C.J., and Watkins, AP. (1997). Differential stress modelling of turbulent flows in model reciprocating engines. *Proc. Instn. Mech. Engrs., 211, part D,* pp. 59-77.

Lee, K. (2007). The effects of tumble and swirl flows on flame propagation in a four-valve S.I. engine. *Applied thermal engineering.,* 27(11-12), pp. 2122-12.

Li, Y. (2004). Characterization of an in-cylinder flow structure in a high-tumble spark ignition engine. *International Journal of Engine Research,* 5(5), pp. 375-400.

Li, Y., Zhao, H., Peng, Z., and Ladommatos, N. (2002). Particle image velocimetry measurement of in-cylinder flow in internal combustion engines—experiment and flow structure analysis. *Proceedings of the Institution of Mechanical Engineers -- Part D -- Journal of Automobile Engineering,* 216(1), pp. 65-81.

Li, Y., Liu, S., Shi, S., Feng, M., and Sui, X. (2001). An investigation of in-cylinder tumbling motion in a four-valve spark ignition engine. *Proceedings of the Institution of*

Mechanical Engineers -- Part D -- Journal of Automobile Engineering, 215(2), pp. 273-284.

Lien, F.S., Chen, W.L., and Leschziner, M.A. (1996). Low-Reynolds number eddy-viscosity modelling based on non-linear stress-strain/vorticity relations. *Proc. 3rd Symp. on Engineering Turbulence Modelling and Measurements,* 27-29 May, Crete, Greece.

Lien, F.S., and Leschziner, M.A. (1994). Assessment of turbulence-transport models including non-linear RNG eddy-viscosity formulation and second-moment closure for flow over a backward-facing step. *Computers Fluids, 23(8),* pp. 983-1004.

Litwiller, D. (2001). CCD vs. CMOS: Facts and Fiction. *Photonics Spectra © Laurin Publishing Co.Inc.*

Lorenz M., and Prescher K. (1990). Cycle-resolved LDV measurement on fired SI-engine at high data rate using conventional modular LDV-system. *Soc. Auto. Eng. SAE paper*. 900054.

Lotus Engine Simulation v5.05 Software Manual (2001).

Lund, T. S., Wu, X., & Squires, K. D. (1998). Generation of turbulent inflow data for spatially-developing boundary layer simulations. *J. Comp. Phys. 140,* 233-258.

Mahrous, A.M. (2007). Computational fluid dynamics simulation of in-cylinder flows in a motored homogeneous charge compression ignition engine cylinder with variable negative valve overlapping. *Proceedings of the Institution of Mechanical Engineers, Part D: Journal of Automobile Engineering,* 221(10), pp. 1295-1304.

Maltsev, A. (2004). Towards the development and assessment of complete CFD models for the simulation of stationary gas turbine combustion processes. PhD thesis, Fachbereich Maschinenbau, Technische Universität Darmstadt.

Melling A. (1997). Tracer particles and seeding for particle image velocimetry. *Meas. Sci. Technol. Volume 8-1406.*

Menter, F.R. (1994). Two-equation eddy-viscosity turbulence models for engineering applications. *AIAA Journal. 8. 32.* pp 1598-1605

Miles, P., Megerle, M., Sick, V., Richards, K., Nagel, Z. And Reitz, R. (2001). Measurement and modeling of large-scale flow structures and turbulence in a high-speed directinjection diesel engine. *Proc.of the Fifth Intl.Symp. on Diagnostics and Modeling of Combustion in IC Engines,* Comodia, pp. 1-4.

Mitsubishi (2005). Mitsubishi Company History. Mitsubishi Motors.

Moin, P., Mahesh K. (1998). Direct numerical simulation: A tool in turbulence research. *Annual Review of Fluid Mechanics, Vol. 30,* pp. 539-578.

Micklow, G.J. (2008). Investigation of the grid and intake-generated tumble on the in-cylinder flow in a compression ignition direct-injection engine. *Proceedings of the Institution of Mechanical Engineers, Part D: Journal of Automobile Engineering,* 222(5), pp. 775-788.

Monaghan, M.L. and Pettifer, H.F. (1981). Air motion and its effect on diesel performance and emissions. *SAE paper 810255*.

Murali Krishna, B., and Mallik Arjuna, J. (2010). Comparative study of in-cylinder tumble flows in an internal combustion engine using different piston shapes-an insight using PIV. *Experiments in Fluids, 48(5),*863-874.

Nomura, T., Takahashi, Y., Ishima, T., and Obokata, T. (2008). LDA and PIV measurements and numerical simulation on in-cylinder flow under steady state flow condition. *SAE international,* 01-1063.

Nomura, T., Takahashi, Y., Ishima, T., and Obokata, T. (2002). Analysis on flow around a rectangular cube by means of LDA, PIV and the numerical simulation by PCC method –In the Case of inclined cube. *Proceedings of 11th International Symposium on Applications of Laser Techniques to Fluid Mechanics, Paper No. 37.4, Lisbon,* pp.1-11.

Nauwerck, A., Gindele, J., Spicher, U., Rosskamp, H., and Landwehr, G. (2000). Investigation of the transient in cylinder flow inside a two-stroke engine with PIV. *SAE International,* 01-0902.

Nino, E. (1993). Two-Color Particle Image Velocimetry in an Engine with Combustion. *S.A.E.transactions.,* 102(3), pp. 1273.

Oliver, D., Thomas, S., and Henry, S. (2009). In-cylinder flow field measurement with doppler global velocimetry in combination with droplet distribution visualization by Mie scattering. *SAE International,* 01-0652.

Ossi, K., Eric, L., Teemu, S., Martti, L. and Pekka, R. (2007). In-cylinder flow field of a diesel engine. *SAE Internatinal,* 01-4046.

Osei-Owusu P. (2008). Numerical studies of charge mixture preparation for HCCI engines. PhD thesis, Loughborough University, UK, 2008.

Payri, F., Benajes, J., Margot, X., and Gil, A. (2004). CFD modeling of the in-cylinder flow in direct-injection diesel engines. *Computers & Fluids,* 33(8), pp. 995-1021.

Petschenig, E., Glanz, R., Sorger, H. (2010). Differential flow field analysis in engine development. *MTZ conference-On-/Off-Highway Engines 2010*, 23,24 November 2010, Mannheim, 05-10-08, Volume 71.

Pitcher, G., Wigley, G. (2008). LDA Analysis of the tumble flow generated in a motored four valve engine. *Report,* Loughborough University, UK.

Pitcher, G., Binjuwair, S., Picton T., Wood, A., Wigley, G., and Hollis, D. (2010). LDA and PIV analyses and comparison of in-cylinder flow structures under steady flow conditions. *15th International Symp. on Applications of Laser Techniques to Fluid Mechanics Lisbon,* Portugal, 1801.

Pope, S.B. (2000). Turbulent flows. *Cambridge University Press,* Cambridge.

Raffel, M., C. Willert, and Kompenhans, J. (1998). Particle Image Velocimetry. A particle guide. Berlin: Springer.

Raffel, M., J. Westerweel, C., Willert, M., Gharib, and Kompenhans, J. (1996). Analytical and experimental investigations of dual-plane particle image velocimetry. *Opt. Eng. 35,* 2067-2074.

Reeves, M., Garner, C. P., Dent, J. C. and Halliwell, N. A. (1996). Particle image velocimetry measure-ments of in-cylinder flow in a multi-valve internal combustion engine. *Proc. Instn Mech. Engrs, Part D: J. Automobile Engineering, 210(D1),* 63–70

Reuss, D.L. (1993). Two-dimensional PIV with electrooptical image shifting in an internal combustion engine. *International Symposium on Optics, imaging, and instrumentation.*,11-16 July 1993. San Diego, ca. SPIE.

Richter, M., Axelsson, B., and Aldén, M., Josefsson, G., Carlsson, L-O., Dahlberg, M., Nisbet J., and Simonsen, H. (1999). Investigation of the fuel distribution and the in-cylinder flow field in a stratified charge engine using laser techniques and comparison with CFD modelling. *SAE International,* 01-3540.

Ricardo (1993). Steady state flow bench port performance measurement and analysis techniques. DP93/0704.

Robert, E., Thierry, G., and Raphaele, H. (2003). Finite volume methods. *Handbook of Numerical Analysis, P.G. Ciarlet, J.L. Lions eds, vol. 7,* pp 713-1020.

Roland, Stull, B. (1988). An introduction to boundary layer meteorology. pp. 45.

Rouland, E. (1997). Particle Image Velocimetry measurements in a high tumble engine for in-cylinder flow structure analysis. *SAE Ppaer,* 106(4), pp. 826.

Rutland, C.J. (1996). Diesel engine model development and experiments. *SAE Paper,* 104(3), pp. 1688.

Sarkar, S., and Balakrishnan, L. (1990). Application of a Reynolds-stress turbulence model to the compressible shear layer. *ICASE Report 90-18, NASA CR 182002.*

Sagaut, P. (2002). Large-eddy simulation for incompressible flows - An introduction. Second edition. *Springer-Verlag, Scientific Computation series.*

Shih, T.-H., Liou, W.W., Shabbir, A., and Zhu, J. (1995). A new k-ε eddy-viscosity model for high Reynolds number turbulent flows - model development and validation, *computers & fluids. Vol. 24, No. 3,* pp. 227-238.

Shojaeefard, M.H., and Noorpoor, A.R. (2008). Flow simulation in engine cylinder with spring mesh. *American Journal of Applied Sciences,* 5(10), pp. 1336-43.

SMMT, 2011-last update, The Society of Motor Manufacturers and Traders U.K. (2006). *[Homepage of the UK Automotive Sector towards Sustainability], [Online] [6/16, 2011].*

Soderberg, F. and Johansson, B. (2002). PIV flow measurements and heat-release analysis in a cross-flow cylinder head. *SAE Paper,*2002-01-2840.

Spalart, P., and Allmaras, S. (1992). A one-equation turbulence model for aerodynamic flows. *American Institute of Aeronautics and Astronautics. AIAA-92-0439.* pp. 5-21

Speziale, C.G., Sarkar, S., and Gatski, T.B. (1991). Modelling the pressure-strain correlation of turbulence: an invariant dynamical systems approach”, *J. Fluid Mech.*, 227, pp. 245-272.

Stansfield P. (2008). Control of unthrottled DISI engine through EIVC. PhD thesis, Loughborough University, UK, 2008.

Stansfield, P., Wigley, G., Catto, J., Pitcher, G. (2007). PIV analysis of in-cylinder flow structures over a range of realistic engine speeds. *Experiments in Fluids,* 43(1), 135-146.

Stucky M.J., Nino E, Gajdeczko, BF., and Felton, PG. (1994). Two-color particle image velocimetry technique for an internal combustion engine. *Experimental. Thermal and Fluid Science Journal, 8 (4),* pp305-314.

STAR-CCM+ v5.06.010 Software Manual, CD-ADAPCO (2012).

Thomas, P. (2006). Steady flow testing of the single cylinder optical research engine (SCORE) Cylinder Head. *Report*, Loughborough University, UK.

Takenaka, Y., Yabe M., Aoyagi, Y., and Shiozaki, T. (1990). Three dimensional computation of in-cylinder flow with intake port in DI diesel engine. *International Symposium COMODIA90:* 425-430.

Thakur, S. and Shyy, W. (1999). Reynolds stress models for flows in complex geometries: Review and application. *30th AIAA Fluid Dynamics Conference, June 28 - July 1, AIAA 99-3782.*

Tabaczynski, R.J. (1976). Turbulence and turbulent combustion in spark-ignition engines. *Progress in Energy and Combustion Science,* 2(3), pp. 143-165.

Tabata, M. (1996). In-cylinder fuel distribution, flow field, and combustion characteristics of a mixture injected SI engine, *SAE Paper*, 104(3), pp. 257.

Tadashi, T., Takeshi, M., Hisashi A., Yuzo, A., Je-Hyung L., Daeyup, L. and Shinichi, G. (2000). Effects of initial in-cylinder flow field on mixture formation in a premixed compression-ignition engine. *SAE International,* 01-0331.

Tsui, Y., and Lee, S. (1992). Calculation of turbulent flow through engine inlet ports. *International Journal of Heat and Fluid Flow,* 13(3), pp. 232-240.

Valentino, G. (1993). Intake valve flow measurements using PIV. *SAE Paper,* 102(4), pp. 1156.

Vucinic, D., Hazarika, B.K., and Dinescu, C. (2001). Visualization and PIV measurements of in-cylinder axisymmetric flows. *SAE Conference Proceedings, 368,* pp. 229-238.

Westerweel, J. (2000b). Theoretical analysis of the measurement precision in particle image velocimetry. *Exp. Fluids 29,* S3-12.

Westerweel, J., Dabiri, D., and Gharib, M. (1997). The effect of a discrete window offset on the accuracy of cross-correlation analysis of digital PIV recording. *Exp. Fluids* 23, 20-28.

Westerweel, J. (1993). Digital Particle Image Velocimetry- theory and application. PhD thesis, Delft University of Technology.

Watkins and Lea, C.J. (1997). Differential stress modelling of turbulent flows in model reciprocating engines. *Proc. Instn. Mech. Engrs., 211, part D,* pp. 59-77.

Watkins, AP., Kanellakopoulos, P., and Lea, e.J. (1990). An assessment of discretisation schemes and turbulence models for in-cylinder flows. *proceedings of International Symposium COMODIA '90,* pp. 499-504.

Wilcox, D.C. (1998). Turbulence modelling for CFD. *DCW Industries, Inc. La* Canada, California.

Wigley G. (2008). Introduction to light scattering and optical diagnostics for the analysis of air flows and fuel sprays. Report, Loughborough University.

Weclas, M., Melling, A., and Durst, F. (1998). Flow separation in the inlet valve gap of piston engines. *Progress in Energy and Combustion Science,* 24(3), pp. 165-195.

Xu, Z.Z., Hu, H., Liu, S.L. And Wang, J. (2003). Experimental study of air flow in cylinder of a 4-valve spark ignition engine. *Tianjin Daxue Xuebao(Journal of Tianjin University of Science and Technology)(China), 36(3),* pp. 380-382.

Xavier, B., and Alain, F. (1997). Investigation of the in-cylinder tumble motion in a multi-valve engine effect of the piston shape. *SAE International,* 971643.

Xu, W., Chen, Q., and Nieuwstadt, F.T.M. (1998). A new turbulence model for near-wall natural convection. *Int. J. Heat Mass Transfer, 41,* pp. 3161-3176.

Yang Y.-X., Liu C.-W., Liu J. and Zhao H., (1998). Study on spatial characteristics of the in-cylinder flow field in an I.C. engine using PIV. *SAE Technical Paper,* 982632.

Yun, J. (2002). New evaluation indices for bulk motion of in-cylinder flow through intake port system in cylinder head. *Proceedings of the Institution of Mechanical Engineers, Part D: Journal of Automobile Engineering*, 216(6), pp. 513-521.

Zhao, H. (1998). Optical diagnostics for in-cylinder mixture formation measurements in IC engines. *Progress in energy and combustion science, 24(4),* pp. 297.

Zhao, F. and HiroYuki, H. (1993). The applications of laser Rayleih scattring to combustion diagnostics. *Progress in Energy and Combustion Science, 19(6),* pp. 447-485.

Zhijun, W. (2001). In-cylinder swirl formation process in a four-valve diesel engine. *Experiments in fluids.,* 31(5), pp. 467.